Winter 2015

Modeling and Simulation of Molecular Couette Flows and Related Flows

Wei Li
Old Dominion University

MODELING AND SIMULATION OF MOLECULAR COUETTE FLOWS AND RELATED FLOWS

by

Wei Li
B.S. in Computing Science at Wuhan University of Technology, China, 2004
M.S. in Applied Mathematics at Wuhan University of Technology, China, 2006

A Dissertation Submitted to the Faculty of
Old Dominion University in Partial Fulfillment of the
Requirements for the Degree of

DOCTOR OF PHILOSOPHY

COMPUTATIONAL AND APPLIED MATHEMATICS

OLD DOMINION UNIVERSITY
December 2015

Approved by:

Li-Shi Luo (Director)

Richard Noren (Member)

Fang Q. Hu (Member)

Yan Peng (Member)

Taehun Lee (Member)

ABSTRACT

MODELING AND SIMULATION OF MOLECULAR COUETTE FLOWS AND RELATED FLOWS

Wei Li
Old Dominion University, 2015
Director: Dr. Li-Shi Luo

In this thesis, molecular Couette flow is clearly defined and the modeling and simulation of this kind of flow is systematically investigated. First, the integral equations for the velocity of gaseous Couette flow and related flows are derived from linearized Boltzmann BGK equation with Maxwell boundary condition and solved with high precision by using Chebyshev collocation and chunk-based collocation methods. The velocity profiles of gaseous Couette flows and related flows with a wide range of Knudsen number and the Maxwell boundary condition of various accommodation ratios are obtained. Moreover, the order of convergence of the numerical methods is also discussed and I obtain better precision. Second, to model the velocity profile, the analysis of Couette flows with pure diffusive boundary condition is given. My results show that the velocity profile is most appropriately approximated by a cubic polynomial. Meanwhile, the analysis also discloses the Knudsen number dependences of microscopic and macroscopic slip velocities and of the half channel mass flow rate. Finally, the modeling and simulation of molecular Couette flow in Navier-Stokes framework is carried out. To obtain density and velocity profiles including the Van der Waals effects near walls, high Knudsen number gaseous Couette flows are simulated by using molecular dynamics simulation (MD). Based on high precision solutions of the integral equations and MD results of velocity and density, macroscopic moments of molecular Couette flows are modeled by using effective radial distribution functions. Then, with these modeled velocity and density profiles, the effective viscosity in the stress tensor of Navier-Stokes equation is constructed. The velocity and density profiles are reproduced by two-relaxation time lattice Boltzmann method in Navier-Stokes framework by the effective viscosity model.

ACKNOWLEDGEMENTS

First, I would like to express my deepest appreciation and gratitude to my advisor, Dr Li-Shi Luo, for providing me the invaluable opportunity to study kinetic theory with him at Old Dominion University, for his insightful suggestions and guidance and for his endless support and encouragement. Over the years, he trained me with his encyclopedic knowledge as an applied mathematician and directed me along the correct path of research with his acute academic perception. Without his guidance, I would not have been able to complete this work.

I would also like to thank my dissertation committee, Dr Richard Noren, Dr Fang Q. Hu, Dr Yan Peng and Dr Taehun Lee from the City College of New York, for their valuable time, for sharing their wealth of knowledge and for their insightful comments and invaluable suggestions to improve my work.

Meanwhile, I am grateful to Dr John Tweed, Dr Shidong Jiang from New Jersey Institute of Technology, Dr Jie Shen from Purdue University and Dr Zhaoli Guo from Huazhong University of Science and Technology in China, for their generous help and guidance when I was learning advanced numerical methods for integral equations and learning the lattice Boltzmann method.

In addition, I gratefully thank all my friends, Dr Wei Liao, Dr Xingwang Chen, Dr Mingkan Zhang, Mr Hao Ji, Ms Jian Huang, Dr Changlong Chen, Dr Ye Ai, Dr Lei Shi, Dr Jixie Zhang, Ms Ruicui Liu, Dr Lin Chen, Dr Tao Huang, Dr Feng Di, Dr Weiming Yang, Dr Shu Liao, Dr Zhunkun Cao, Dr Yu Ma, Dr Dong Si, Mr Chakpong Chung, Ms Wenlu Zhang, Mr Rongjian Li, Mr Daming Feng, Ms Jing Xu, Mr Minhao Dong and Mr Richard Kitt for all the happy times we have enjoyed here. My special thanks go to my three friends – Dr Ning Liao, for his incisive criticism of my weakness in character and for his always being on hand to help, Dr Rui Zhang, for teaching me molecular dynamics simulation at my hardest time, and Dr Weidong Li for his numerous suggestions and help during the modification of my dissertation and beyond.

Finally, I want to thank my family. I am indebted to my wife, Dr Ting Yao, for her love and sacrifice and for enduring six years of separation. I am grateful to my mother and father for the tenacity you instilled to me, for your spiritual support and endless encouragement.

TABLE OF CONTENTS

Page

LIST OF TABLES x

LIST OF FIGURES xvii

Chapter

1. INTRODUCTION 1
   - 1.1 MOTIVATION 1
   - 1.2 PREVIOUS WORK 3
   - 1.3 OUTLINE OF PRESENT WORK 6

2. THE DERIVATION OF THE FREDHOLM EQUATIONS FROM THE BGK EQUATION 8
   - 2.1 THE COUETTE FLOW PROBLEM 8
   - 2.2 THE KRAMERS PROBLEM 18
   - 2.3 THE POISEUILLE FLOW PROBLEM 21

3. HIGH PRECISION SOLUTIONS TO THE FREDHOLM EQUATIONS OF THE SECOND KIND 27
   - 3.1 SOLVING INTEGRAL EQUATION FOR THE COUETTE FLOW PROBLEM WITH CHEBYSHEV COLLOCATION METHOD 27
   - 3.2 SOLVING INTEGRAL EQUATION FOR THE COUETTE FLOW PROBLEM WITH CHUNK BASED COLLOCATION METHOD 42
   - 3.3 SOLVING THE INTEGRAL EQUATION FOR THE POISEUILLE FLOW PROBLEM WITH CHUNK BASED COLLOCATION METHOD 65
   - 3.4 SOLVING THE INTEGRAL EQUATION FOR THE KRAMERS PROBLEM WITH CHUNK BASED COLLOCATION METHOD 77

4. ANALYSIS OF THE COUETTE FLOW 88
   - 4.1 FIRST APPROXIMATION OF VELOCITY 88
   - 4.2 VARIATIONAL APPROACH TO COUETTE FLOW 93
   - 4.3 CUBIC APPROXIMATION TO COUETTE FLOW 97
   - 4.4 THE VELOCITY DEFECT, SLIP VELOCITY AND THE HALF CHANNEL MASS FLOW RATE 99
   - 4.5 DIRICHLET BOUNDARY CONDITION, EFFECTIVE VISCOSITY AND VELOCITY REPRODUCING BY LATTICE BOLTZMANN EQUATION 107

5. MOLECULAR FLOW 115
5.1 THE 2D MOLECULAR DYNAMIC SIMULATION OF RAREFIED COUETTE FLOWS 115
5.2 MODELING THE MACROSCOPIC RESULTS OF THE 2D MOLECULAR DYNAMIC SIMULATION 121
5.3 REPRODUCING MD DATA BY USING LATTICE BOLTZMANN EQUATION 129

6. CONCLUSION 155

BIBLIOGRAPHY 160

APPENDICES

A. THE PROPERTIES AND THE APPROXIMATIONS OF ABRAMOWITZ FUNCTIONS 164

B. NONEXISTENCE OF THE DERIVATIVE OF VELOCITY AT THE BOUNDARIES FOR THE STEADY COUETTE FLOW PROBLEM WITH PURE DIFFUSIVE BOUNDARY CONDITION 168

C. LINEAR TRANSFORM AND INVERSE TRANSFORM BETWEEN GAUSS-LEGENDRE POLYNOMIAL EXPANSION COEFFICIENTS AND THE APPROXIMATED FUNCTION VALUES AT THE CORRESPONDING GAUSS-LEGENDRE ABSCISSAS 170

D. GAUSS-LEGENDRE QUADRATURE 172

E. VELOCITY OF FREE MOLECULAR COUETTE FLOW WITH ARBITRARY ACCOMMODATION RATIOS 174

VITA 176

LIST OF TABLES

Table Page

1. Abscissae and Weights of 40 Order Generalized Gauss quadrature for products of a polynomial and logarithmic function over $[0, 1]$ 34

2. The values of the velocity $\bar{u}_N(y)$ of the Couette flow at $y = 0.1, 0.2$ and 0.3, for $0.003 \leq k \leq 10.0$ and $256 \leq N + 1 \leq 2048$ 37

3. The values of the velocity $\bar{u}_N(y)$ of the Couette flow at $y = 0.4$ and 0.5, for $0.003 \leq k \leq 10.0$ and $256 \leq N + 1 \leq 2048$ 38

4. The Knudsen number k dependence of the velocity $u(1/2)$ at boundary and the channel center velocity derivative $u'(0)$ obtained by the velocity Chebyshev expansion with $N = 2047$ 39

5. The dependence of the rate of convergence for the velocity $\bar{u}_N(y)$ on the Knudsen number k. The rate of convergence α and its standard deviation are computed by using the least-square method. 39

6. The L_2 error of the velocity $\bar{u}_N(y)$ and the rate of convergence α. 41

7. The dependence of the stress T_{xy} and the upper half channel mass flow rate Q on the Knudsen number k 42

8. The values of the approximated velocity $u^N(y)$ of the Couette flow at $y = 0.1, 0.2$ and 0.3, for $0.003 \leq k \leq 10.0$ and $40 \leq N \leq 320$ 47

9. The values of the approximated velocity $u^N(y)$ of the Couette flow at $y = 0.4$ and 0.5, for $0.003 \leq k \leq 10.0$ and $40 \leq N \leq 320$ 48

10. The Knudsen number k dependence of the velocity $u^N(1/2)$ at boundary and the channel center velocity derivative $\frac{du^N}{dy}|_{y=0}$ obtained by the velocity piece-wise Legendre approximation with $N = 320$ 49

11. The dependence of the rate of convergence for the velocity $u^N(y)$ on the Knudsen number k. The rate of convergence α and its standard deviation are computed by using the least-square method. 49

12. The L_2 error of the velocity $u^N(y)$ and the rate of convergence α. 51

13. The dependence of the stress T_{xy} and the upper half channel mass flow rate Q on the Knudsen number k 51

14. The values of the approximated velocity $u^N(y)$ of the Couette flow at $y = -0.5, -0.25$ and 0, for the Knudsen number $k = 0.003$ and $40 \leq N \leq 320$ and $\alpha^{\pm} = 0, 0.1, 0.5, 0.9$ 55

15. The values of the approximated velocity $u^N(y)$ of the Couette flow at $y = 0.25$ and 0.5, for the Knudsen number $k = 0.003$ and $40 \leq N \leq 320$ and $\alpha^{\pm} = 0, 0.1, 0.5, 0.9$ 56

16. The values of the approximated velocity $u^N(y)$ of the Couette flow at $y = -0.5, -0.25$ and 0, for the Knudsen number $k = 0.3$ and $40 \leq N \leq 320$ and $\alpha^{\pm} = 0, 0.1, 0.5, 0.9$ 57

17. The values of the approximated velocity $u^N(y)$ of the Couette flow at $y = 0.25$ and 0.5, for the Knudsen number $k = 0.3$ and $40 \leq N \leq 320$ and $\alpha^{\pm} = 0, 0.1, 0.5, 0.9$ 58

18. The values of the approximated velocity $u^N(y)$ of the Couette flow at $y = -0.5, -0.25$ and 0, for the Knudsen number $k = 1$ and $40 \leq N \leq 320$ and $\alpha^{\pm} = 0, 0.1, 0.5, 0.9$ 59

19. The values of the approximated velocity $u^N(y)$ of the Couette flow at $y = 0.25$ and 0.5, for the Knudsen number $k = 1$ and $40 \leq N \leq 320$ and $\alpha^{\pm} = 0, 0.1, 0.5, 0.9$ 60

20. The values of the approximated velocity $u^N(y)$ of the Couette flow at $y = -0.5, -0.25$ and 0, for the Knudsen number $k = 2$ and $40 \leq N \leq 320$ and $\alpha^{\pm} = 0, 0.1, 0.5, 0.9$ 61

21. The values of the approximated velocity $u^N(y)$ of the Couette flow at $y = 0.25$ and 0.5, for the Knudsen number $k = 2$ and $40 \leq N \leq 320$ and $\alpha^{\pm} = 0, 0.1, 0.5, 0.9$ 62

22. The values of the approximated velocity $u^N(y)$ of the Couette flow at $y = -0.5, -0.25$ and 0, for the Knudsen number $k = 10$ and $40 \leq N \leq 320$ and $\alpha^{\pm} = 0, 0.1, 0.5, 0.9$ 63

23. The values of the approximated velocity $u^N(y)$ of the Couette flow at $y = 0.25$ and 0.5, for the Knudsen number $k = 10$ and $40 \leq N \leq 320$ and $\alpha^{\pm} = 0, 0.1, 0.5, 0.9$ 64

24. The dependence of the stress T_{xy} on the Knudsen number k and various accommodation ratios $\alpha^{\pm}$ for the Couette flow problem 71

25. The dependence of the upper half channel mass flow rate Q^+ on the Knudsen number k and various accommodation ratios $\alpha^{\pm}$ for the Couette flow problem 71

26. The dependence of the lower half channel mass flow rate Q^- on the Knudsen number k and various accommodation ratios $\alpha^{\pm}$ for the Couette flow problem 72

27. The dependence of the channel center stress $T_{xy} - y/2$ on the Knudsen number k and various accommodation ratios $\alpha^{\pm}$ for the Poiseuille flow problem 83

28. The dependence of the upper half channel mass flow rate Q^+ on the Knudsen number k and various accommodation ratios $\alpha^{\pm}$ for the Poiseuille flow problem 83

29. The dependence of the lower half channel mass flow rate Q^- on the Knudsen number k and various accommodation ratios $\alpha^{\pm}$ for the Poiseuille flow problem 84

30. The accommodation ratio α dependence of the slip velocity $q(0)$, the approximated slip coefficient $q(10^7)$ and the shear stress T_{xy} 86

31. Coefficients of the approximation $\tilde{u}(y) = Ay + BF_0(y,k) + CF_1(y,k)$ 92

32. L2 error of the approximation $\tilde{u}_1(y) = Ay + BF_0(y,k) + CF_1(y,k)$ and the shear stress T_{xy} obtained from $\tilde{u}_1(y)$ 92

33. The Knudsen number k dependence of the channel center velocity derivative $u'(0)$ from the chunk based collocation method with $N = 320$ and the Knudsen number k dependence of the coefficient $\boldsymbol{a}$ of the approximating polynomials $u_i(y)(i = 1,3,5)$ 96

34. The Knudsen number k dependence of the shear stress T_{xy} from the chunk based collocation method(CBCM) and from the variational method(VM) for $u_i(y)(i = 1,3,5)$ 96

35. The coefficient a of the cubic term in $\tilde{u}_2(y) = u'(0)y + ay^3$ and L_2 global error of $\tilde{u}_2(y)$ 98

36. The Knudsen number k dependence of $\tilde{u}_2(1/2)$ 99

37. The Knudsen number k dependence of the half channel flow rate Q and the shear stress T_{xy} computed from $\tilde{u}_2(y) = u'(0)y + ay^3$. 99

38. The Knudsen number k dependence of the L_2 error of the approximate solution $\tilde{u}_3(y) = u'(0)y + 4[2u(1/2) - u'(0)]y^3$ 99

39. The Knudsen number k dependence of the half channel mass flow rate Q and the shear stress T_{xy} computed from the approximate solution $\tilde{u}_3(y) = u'(0)y + 4[2u(1/2) - u'(0)]y^3$ 100

40. The values of parameters in the models for the microscopic slip velocity u_s, the fitting range of k for the parameters and the L_2 error of the approximations in the corresponding fitting range of k. 103

41. The values of parameters in the models for the macroscopic slip velocity U_s, the fitting range of k for the parameters and the L_2 error of the approximations in the corresponding fitting range of k. 105

42. The values of parameters in the models for the half channel mass flow rate Q, the fitting range of k for the parameters and the L_2 error of the approximations in the corresponding fitting range of k. 107

43. The L_∞ error and L_2 error of the velocity $\hat{u}_3(y)$ from lattice Boltzmann equation compared to the target velocity $\tilde{u}_3(y)$ and the rate of convergence α of the lattice Boltzmann simulation computed from L_2 error. 114

44. The length L_{MD} and height H_{MD} of the computational domain, the number N of gas molecules in the MD simulations and simulating time ($6 \cdot 10^8$ timesteps) in D/HH/MM/SS for Knudsen number $1.0 \leq k \leq 10.0$ 118

45. The Knudsen number k dependence of the paramters ρ_∞, σ_ρ, a_ρ for the density 126

46. The Knudsen number k dependence of the paramters c_1, c_3, σ_u, a_u for the velocity 126

47. The Knudsen number k dependence of mesh sizes and the parameter β indicating the fraction of bounce back boundary condition in TRT-LBE simulation with 1D wall-gas interaction for the molecular Couette flow. .. 141

48. The simulating times (in seconds) of the 1D wall-gas interaction TRT-LBE simualtions with three sets of nonuniform mesh, the 2D wall-gas interaction TRT-LBE simulations with the coarse nonuniform mesh and the MD simulations 154

49. Coefficients of Chebyshev expansions for f_0, g_0, h_0 and q_0 165

50. Coefficients of Chebyshev expansions for f_1, g_1, h_1 and q_1 166

51. Coefficients of Chebyshev expansions for f_2, g_2, h_2 and q_2 166

LIST OF FIGURES

Figure Page

1. The grid size N dependence of the relative error of the velocity $|\delta u_N(y)|$. The top row, from left to right: $k = 0.01$ at $y = 0.1$ and $k = 0.1$ at $y = 0.2$. The bottom row, from left to right: $k = 1.0$ at $y = 0.3$ and $k = 10.0$ at $y = 0.4$. 40

2. The grid size N dependence of the relative error of the velocity $|\delta u^N(y)|$. The top row, from left to right: $k = 0.01$ at $y = 0.1$ and $k = 0.1$ at $y = 0.2$. The bottom row, from left to right: $k = 1.0$ at $y = 0.3$ and $k = 10.0$ at $y = 0.4$. 50

3. The velocity profiles of the Couette flow problem for $k = 0.003$. Top row, from left to right: $\alpha^+ = 0$, $\alpha^- = 0, 0.1, 0.5, 0.9$ and $\alpha^+ = 0.1$, $\alpha^- = 0.1, 0.5, 0.9$. Bottom row, from left to right: $\alpha^+ = 0.5$, $\alpha^- = 0.1, 0.5, 0.9$ and $\alpha^+ = 0.9$, $\alpha^- = 0.1, 0.5, 0.9$. 65

4. The velocity profiles of the Couette flow problem for $k = 0.3$. Top row, from left to right: $\alpha^+ = 0$, $\alpha^- = 0, 0.1, 0.5, 0.9$ and $\alpha^+ = 0.1$, $\alpha^- = 0.1, 0.5, 0.9$. Bottom row, from left to right: $\alpha^+ = 0.5$, $\alpha^- = 0.1, 0.5, 0.9$ and $\alpha^+ = 0.9$, $\alpha^- = 0.1, 0.5, 0.9$. 66

5. The velocity profiles of the Couette flow problem for $k = 1.0$. Top row, from left to right: $\alpha^+ = 0$, $\alpha^- = 0, 0.1, 0.5, 0.9$ and $\alpha^+ = 0.1$, $\alpha^- = 0.1, 0.5, 0.9$. Bottom row, from left to right: $\alpha^+ = 0.5$, $\alpha^- = 0.1, 0.5, 0.9$ and $\alpha^+ = 0.9$, $\alpha^- = 0.1, 0.5, 0.9$. 67

6. The velocity profiles of the Couette flow problem for $k = 2.0$. Top row, from left to right: $\alpha^+ = 0$, $\alpha^- = 0, 0.1, 0.5, 0.9$ and $\alpha^+ = 0.1$, $\alpha^- = 0.1, 0.5, 0.9$. Bottom row, from left to right: $\alpha^+ = 0.5$, $\alpha^- = 0.1, 0.5, 0.9$ and $\alpha^+ = 0.9$, $\alpha^- = 0.1, 0.5, 0.9$. 68

7. The velocity profiles of the Couette flow problem for $k = 10.0$. Top row, from left to right: $\alpha^+ = 0$, $\alpha^- = 0, 0.1, 0.5, 0.9$ and $\alpha^+ = 0.1$, $\alpha^- = 0.1, 0.5, 0.9$. Bottom row, from left to right: $\alpha^+ = 0.5$, $\alpha^- = 0.1, 0.5, 0.9$ and $\alpha^+ = 0.9$, $\alpha^- = 0.1, 0.5, 0.9$. 69

8. The velocity profiles of the Couette flow problem for $k = 300.0$ and free molecular flow. Top row, from left to right: $\alpha^+ = 0$, $\alpha^- = 0, 0.1, 0.5, 0.9$ and $\alpha^+ = 0.1$, $\alpha^- = 0.1, 0.5, 0.9$. Bottom row, from left to right: $\alpha^+ = 0.5$, $\alpha^- = 0.1, 0.5, 0.9$ and $\alpha^+ = 0.9$, $\alpha^- = 0.1, 0.5, 0.9$. 70

9. The velocity profiles of the Poiseuille flow problem for $k = 0.003$. Top row, from left to right: $\alpha^+ = 0$, $\alpha^- = 0$, 0.1, 0.5, 0.9 and $\alpha^+ = 0.1$, $\alpha^- =$ 0.1, 0.5, 0.9. Bottom row, from left to right: $\alpha^+ = 0.5$, $\alpha^- = 0.1$, 0.5, 0.9 and $\alpha^+ = 0.9$, $\alpha^- = 0.1$, 0.5, 0.9. 73

10. The velocity profiles of the Poiseuille flow problem for $k = 0.3$. Top row, from left to right: $\alpha^+ = 0$, $\alpha^- = 0$, 0.1, 0.5, 0.9 and $\alpha^+ = 0.1$, $\alpha^- =$ 0.1, 0.5, 0.9. Bottom row, from left to right: $\alpha^+ = 0.5$, $\alpha^- = 0.1$, 0.5, 0.9 and $\alpha^+ = 0.9$, $\alpha^- = 0.1$, 0.5, 0.9. 74

11. The velocity profiles of the Poiseuille flow problem for $k = 1.0$. Top row, from left to right: $\alpha^+ = 0$, $\alpha^- = 0$, 0.1, 0.5, 0.9 and $\alpha^+ = 0.1$, $\alpha^- =$ 0.1, 0.5, 0.9. Bottom row, from left to right: $\alpha^+ = 0.5$, $\alpha^- = 0.1$, 0.5, 0.9 and $\alpha^+ = 0.9$, $\alpha^- = 0.1$, 0.5, 0.9. 75

12. The velocity profiles of the Poiseuille flow problem for $k = 2.0$. Top row, from left to right: $\alpha^+ = 0$, $\alpha^- = 0$, 0.1, 0.5, 0.9 and $\alpha^+ = 0.1$, $\alpha^- =$ 0.1, 0.5, 0.9. Bottom row, from left to right: $\alpha^+ = 0.5$, $\alpha^- = 0.1$, 0.5, 0.9 and $\alpha^+ = 0.9$, $\alpha^- = 0.1$, 0.5, 0.9. 76

13. The velocity profiles of the Poiseuille flow problem for $k = 10.0$. Top row, from left to right: $\alpha^+ = 0$, $\alpha^- = 0$, 0.1, 0.5, 0.9 and $\alpha^+ = 0.1$, $\alpha^- =$ 0.1, 0.5, 0.9. Bottom row, from left to right: $\alpha^+ = 0.5$, $\alpha^- = 0.1$, 0.5, 0.9 and $\alpha^+ = 0.9$, $\alpha^- = 0.1$, 0.5, 0.9. 77

14. Comparisons of Poiseuille flow velocities for $k = 0.003$: high precision solution v.s. quadratic profile. Top row, from left to right: $\alpha^+ = \alpha^- = 0$ and $\alpha^+ = \alpha^- = 0.1$. Bottom row, from left to right: $\alpha^+ = \alpha^- = 0.5$ and $\alpha^+ = \alpha^- = 0.9$. 78

15. Comparisons of Poiseuille flow velocities for $k = 0.3$: high precision solution v.s. quadratic profile. Top row, from left to right: $\alpha^+ = \alpha^- = 0$ and $\alpha^+ = \alpha^- = 0.1$. Bottom row, from left to right: $\alpha^+ = \alpha^- = 0.5$ and $\alpha^+ = \alpha^- = 0.9$. 79

16. Comparisons of Poiseuille flow velocities for $k = 1.0$: high precision solution v.s. quadratic profile. Top row, from left to right: $\alpha^+ = \alpha^- = 0$ and $\alpha^+ = \alpha^- = 0.1$. Bottom row, from left to right: $\alpha^+ = \alpha^- = 0.5$ and $\alpha^+ = \alpha^- = 0.9$. 80

17. Comparisons of Poiseuille flow velocities for $k = 2.0$: high precision solution v.s. quadratic profile. Top row, from left to right: $\alpha^+ = \alpha^- = 0$ and $\alpha^+ = \alpha^- = 0.1$. Bottom row, from left to right: $\alpha^+ = \alpha^- = 0.5$ and $\alpha^+ = \alpha^- = 0.9$. 81

18. Comparisons of Poiseuille flow velocities for $k = 10.0$: high precision solution v.s. quadratic profile. Top row, from left to right: $\alpha^+ = \alpha^- = 0$ and $\alpha^+ = \alpha^- = 0.1$. Bottom row, from left to right: $\alpha^+ = \alpha^- = 0.5$ and $\alpha^+ = \alpha^- = 0.9$. 82

19. Shear stress versus the accommodation ratio $\alpha = 0, 0.001, 0.01, 0.1, 0.2, 0.3, 0.4, 0.5, 0.6, 0.7, 0.8, 0.9$. 87

20. The velocity defect of the Kramer flow problem for $\alpha = 0, 0.1, 0.2, 0.3, 0.4, 0.5, 0.6, 0.7, 0.8, 0.9$ with $y \in [0, 2.72703]$. 87

21. The Knudsen number dependence of velocity $u(y)$. Top: The solid and dashed lines corresponds to the numerical solution $u^N(y)$ with $N = 320$ and $u_1^* = u'(0)y$, *i.e.*, the straight line tangent to $u(y)$ at $y = 0$. Bottom: The normalized nonlinear component of the velocity, u_{NL} defined by Equation (115), $u(y)/u(1/2)$. 90

22. The velocity defect $u_{\rm d}(y)$ (top) and the normalized velocity defect $u_{\rm d}(y)/u_{\rm d}(1/2)$ (bottom) for $k = 0.03$, 0.1, 1.0 and 10.0. The normalized velocity defect increases monotonically as k increases. 102

23. The k dependence of the slip velocity u_s. The circles are obtained from the high precision solution of the integral equation (72) given in Table 10. The solid, dash, dot and dash-dot lines are the approximations of u_s by equations (132)-(134) with $C_2 \neq C_1$ and equation (135), respectively. The lines of equations (132)-(133) overlap each other. 104

24. The k dependence of the slip velocity U_s. The circles are obtained from the high precision solution of the integral equation (72) given in Table 10. The solid, dash and dash-dot lines are the approximations of u_s by equations (136)-(138), respectively. The lines of equations (136)-(137) overlap each other when $k \geq 0.3$. 106

25. The k dependence of the normalized half channel mass flow rate Q/Q_0. The circles are obtained from the high precision solution of the integral equation (72) given in Table 13. The solid, dash, dot and dash-dot lines are the approximations of Q/Q_0 by equations (139)-(142), respectively. The lines of equations (139)-(140) overlap each other. 108

26. The cross section of the MD simulation box for the planar gaseous Couette flow. 116

27. The velocity profile (red solid line in the left figures) and density profile (red solid line in the right figures) of MD simulation with Knudsen number $k = 1.0$ and 2.0. The blue dash circle line in the left figures are the correponding high precision solution of velocity from equation (72). From the top row to the bottom row the corresponding value of k increases. The three dashed lines from the top to the bottom on the top of each figure represent the position of centers of the inner most wall molecules, the position of $\sqrt[6]{2}\sigma$ distance from the first dashed line and the position of 3σ distance from the first dashed line, respectively. The three dashed lines on the bottom of each figure are located similarly. 119

28. The velocity profile (red solid line in the left figures) and density profile (red solid line in the right figures) of MD simulation with Knudsen number $k = 3.0$ and 4.0. The blue dash circle line in the left figures are the correponding high precision solution of velocity from equation (72). From the top row to the bottom row the corresponding value of k increases. The three dashed lines from the top to the bottom on the top of each figure represent the position of centers of the inner most wall molecules, the position of $\sqrt[6]{2}\sigma$ distance from the first dashed line and the position of 3σ distance from the first dashed line, respectively. The three dashed lines on the bottom of each figure are located similarly. 120

29. The velocity profile (red solid line in the left figures) and density profile (red solid line in the right figures) of MD simulation with Knudsen number $k = 5.0$, and 6.0. The blue dash circle line in the left figures are the correponding high precision solution of velocity from equation (72). From the top row to the bottom row the corresponding value of k increases. The three dashed lines from the top to the bottom on the top of each figure represent the position of centers of the inner most wall molecules, the position of $\sqrt[6]{2}\sigma$ distance from the first dashed line and the position of 3σ distance from the first dashed line, respectively. The three dashed lines on the bottom of each figure are located similarly. 121

30. The velocity profile (red solid line in the left figures) and density profile (red solid line in the right figures) of MD simulation with Knudsen number $k = 7.0$ and 8.0. The blue dash circle line in the left figures are the correponding high precision solution of velocity from equation (72). From the top row to the bottom row the corresponding value of k increases. The three dashed lines from the top to the bottom on the top of each figure represent the position of centers of the inner most wall molecules, the position of $\sqrt[6]{2}\sigma$ distance from the first dashed line and the position of 3σ distance from the first dashed line, respectively. The three dashed lines on the bottom of each figure are located similarly. 122

31. The velocity profile (red solid line in the left figures) and density profile (red solid line in the right figures) of MD simulation with Knudsen number $k = 9.0$ and 10.0. The blue dash circle line in the left figures are the correponding high precision solution of velocity from equation (72). From the top row to the bottom row the corresponding value of k increases. The three dashed lines from the top to the bottom on the top of each figure represent the position of centers of the inner most wall molecules, the position of $\sqrt[6]{2}\sigma$ distance from the first dashed line and the position of 3σ distance from the first dashed line, respectively. The three dashed lines on the bottom of each figure are located similarly. 123

32. Comparison of the velocity from the model $(c_1 y + c_3 y^3) g_{10,3,u}(1/2 - y)$, the modified MD data $\tilde{u}_{MD}(y)$ and the high precision solution of the integral equation (72) (left) and the comparison of the density from the model $\rho_\infty g_{10,6,\rho}(1/2 - y)$ and the modified MD data $\tilde{\rho}_{MD}(y)$ (right), with Knudsen number $k = 1.0$ and 2.0. 127

33. Comparison of the velocity from the model $(c_1 y + c_3 y^3) g_{10,3,u}(1/2 - y)$, the modified MD data $\tilde{u}_{MD}(y)$ and the high precision solution of the integral equation (72) (left) and the comparison of the density from the model $\rho_\infty g_{10,6,\rho}(1/2 - y)$ and the modified MD data $\tilde{\rho}_{MD}(y)$ (right), with Knudsen number $k = 3.0$ and 4.0. 128

34. Comparison of the velocity from the model $(c_1 y + c_3 y^3) g_{10,3,u}(1/2 - y)$, the modified MD data $\tilde{u}_{MD}(y)$ and the high precision solution of the integral equation (72) (left) and the comparison of the density from the model $\rho_\infty g_{10,6,\rho}(1/2 - y)$ and the modified MD data $\tilde{\rho}_{MD}(y)$ (right), with Knudsen number $k = 5.0$ and 6.0. 129

35. Comparison of the velocity from the model $(c_1 y + c_3 y^3) g_{10,3,u}(1/2 - y)$, the modified MD data $\tilde{u}_{MD}(y)$ and the high precision solution of the integral equation (72) (left) and the comparison of the density from the model $\rho_\infty g_{10,6,\rho}(1/2 - y)$ and the modified MD data $\tilde{\rho}_{MD}(y)$ (right), with Knudsen number $k = 7.0$ and 8.0. 130

36. Comparison of the velocity from the model $(c_1 y + c_3 y^3) g_{10,3,u}(1/2 - y)$, the modified MD data $\tilde{u}_{MD}(y)$ and the high precision solution of the integral equation (72) (left) and the comparison of the density from the model $\rho_\infty g_{10,6,\rho}(1/2 - y)$ and the modified MD data $\tilde{\rho}_{MD}(y)$ (right), with Knudsen number $k = 9.0$ and 10.0. 131

37. Computation of the 1D acceleration by averaging. 133

38. The MD configuration and the LBE computational domain. 134

39. The sketch of the interface of Tier 3 mesh with grid size of $9\delta_x$ and Tier 4 mesh with grid size of $27\delta_x$. The dash line grids are ghost grids. 136

40. Comparison of the streamwise velocity profiles (left) and the comparison of the density profiles (right) for Knudsen number $k = 1$ and 2: from the 1D wall-gas interaction TRT-LBE simulation with different nonuniform mesh given in Table 47, the MD simulation and the high precision solution of the integral equations for velocity. 142

41. Comparison of the streamwise velocity profiles (left) and the comparison of the density profiles (right) for Knudsen number $k = 3$ and 4: from the 1D wall-gas interaction TRT-LBE simulation with different nonuniform mesh given in Table 47, the MD simulation and the high precision solution of the integral equations for velocity. 143

42. Comparison of the streamwise velocity profiles (left) and the comparison of the density profiles (right) for Knudsen number $k = 5$ and 6: from the 1D wall-gas interaction TRT-LBE simulation with different nonuniform mesh given in Table 47, the MD simulation and the high precision solution of the integral equations for velocity. 144

43. Comparison of the streamwise velocity profiles (left) and the comparison of the density profiles (right) for Knudsen number $k = 7$ and 8: from the 1D wall-gas interaction TRT-LBE simulation with different nonuniform mesh given in Table 47, the MD simulation and the high precision solution of the integral equations for velocity. 145

44. Comparison of the streamwise velocity profiles (left) and the comparison of the density profiles (right) for Knudsen number $k = 9$ and 10: from the 1D wall-gas interaction TRT-LBE simulation with different nonuniform mesh given in Table 47, the MD simulation and the high precision solution of the integral equations for velocity. 146

45. The Galilean transform of a grid point in the LBE with 2D wall-gas interaction 147

46. Comparison of the streamwise velocity profiles (left) and the comparison of the density profiles (right) for Knudsen number $k = 1$ and 2: from the 2D wall-gas interaction TRT-LBE simulation at three positions (left $x = l/6$, center $x = l/2$ and right $x = 5l/6$) along x-axis, the MD simulation and the high precision solution of the integral equations for velocity. 149

47. Comparison of the streamwise velocity profiles (left) and the comparison of the density profiles (right) for Knudsen number $k = 3$ and 4: from the 2D wall-gas interaction TRT-LBE simulation at three positions (left $x = l/6$, center $x = l/2$ and right $x = 5l/6$) along x-axis, the MD simulation and the high precision solution of the integral equations for velocity..... 150

48. Comparison of the streamwise velocity profiles (left) and the comparison of the density profiles (right) for Knudsen number $k = 5$ and 6: from the 2D wall-gas interaction TRT-LBE simulation at three positions (left $x = l/6$, center $x = l/2$ and right $x = 5l/6$) along x-axis, the MD simulation and the high precision solution of the integral equations for velocity..... 151

49. Comparison of the streamwise velocity profiles (left) and the comparison of the density profiles (right) for Knudsen number $k = 7$ and 8: from the 2D wall-gas interaction TRT-LBE simulation at three positions (left $x = l/6$, center $x = l/2$ and right $x = 5l/6$) along x-axis, the MD simulation and the high precision solution of the integral equations for velocity..... 152

50. Comparison of the streamwise velocity profiles (left) and the comparison of the density profiles (right) for Knudsen number $k = 9$ and 10: from the 2D wall-gas interaction TRT-LBE simulation at three positions (left $x = l/6$, center $x = l/2$ and right $x = 5l/6$) along x-axis, the MD simulation and the high precision solution of the integral equations for velocity..... 153

CHAPTER 1

INTRODUCTION

During the decade, the applications of microflows in microelectromechanical systems (MEMs) have attracted increasing interest of researchers. As a branch of the microflow study, we are particularly interested in the gaseous Couette flows in planar micro-scale channels, in which the media of the flows consist of finite numbers of gas molecules. Therefore, the flows are also called molecular Couette flows. Quantitative investigation of the hydrodynamic quantities, such as the density profiles and the velocity profiles of the molecular Couette flows, is conducive to the development of the micro-machine manufacturing industry. For instance, it contributes to the design of the microscopic electromechanical devices and the magnetic disc drive units.

1.1 MOTIVATION

The molecular Couette flows are multi-scale gaseous flows. Two typical lengths of different scales coexist in the molecular Couette flows. One of the typical lengths is the mean free path, namely, the average distance traveled by a moving gas molecule between successive collisions with another gas molecule. The mean free path is in the mesoscopic length scale. The ratio of the mean free path to the height of the planar channel defines the Knudsen number of the molecular Couette flow. The domain of the Knudsen number can be divided into four regions, less than 0.001 is the continuous flow region, between 0.001 and 0.1 is the slip flow region, from 0.1 to 10.0 is the transitional flow region, greater than 10.0 is the near free molecular flow region. Although continuous flows and slip flows are usually characterized by the Navier-Stokes equation, the governing equation for gaseous flows in the whole domain of the Knudsen number is the Boltzmann transport equation or its simplified model equations, such as the Boltzmann BGK equation [23]. The derivation of these equations is rooted in the dilute gas limit, namely, when the number of the molecules in the gaseous flow approaches to infinite, the multiplication of the number of the molecules with the square of the diameter of the molecules remains a constant. It is noted that,

in the dilute gas limit, the net volume of the gas molecules is 0, meaning the gas molecules are regarded as point particles and the diameter of the gas molecules is negligible with respect to the mean free path. Assuming the validity of the dilute gas limit is fine as long as one does not consider the van der Waals forces between the gas molecules and the solid walls. However, when the van der Waals forces must be considered, the second typical length, the diameter of the gas molecules, appears. The diameter of the gas molecules is in the microscopic length scale. In the microscopic length scale, the movement of gas molecules follows the Newton's Second Law and the Newton's Second Law based molecular dynamics (MD) simulation is almost the only resort to simulate the flow. The MD simulation corresponds to another gas limit, where the multiplication of the number of the molecules with the cube of the diameter of the molecules is a constant, when the number of molecules approaches to infinite. In this gas limit, the net volume of the gas molecules is a constant. Thus, a single gas molecule can not be regarded as a point particle but rather a ball. In a nutshell, not only are the two typical lengths in totally different length scales, but the governing equations model distinct gas limits. Coupling the Boltzmann equation or its simplified model equations with MD simulation in order to characterize molecular Couette flow under a unified frame is hard. Before a unified model is obtained, solving the Boltzmann equation with high precision and implementing MD simulation to get high quality flow information are not only necessary but also have their self-contained significance.

On the one band, solving the Boltzmann equation for the Couette flow problem can provide accurate solution to the bulk region velocity of the molecular Couette flow, where the bulk region is a distance, around three times of the diameter of the gas molecules, away from the walls. This distance is also called the wall force penetration depth. The full Boltzmann equation is a nonlinear partial differential integral equation for the distribution function in seven variables, one in time, three in space and three in phase velocity. It could be solved by direct simulation Monte Carlo method (DSMC) or first linearized and then solved by discrete ordinate method (DOM). However, DSMC bears intrinsic statistical noise and DOM involves quadratures of a huge number of discrete phase velocities in order to characterize relatively higher Knudsen number flow. Moreover, both methods are impossible to achieve very high precision. Due to the simple geometry, the Boltzmann BGK equation for the Couette flow with proper kinetic boundary condition can be converted into a weakly singular

Fredholm integral equation of the second kind. Numerical investigations to the integral equation for Couette flow has made a great progress. However, the precision of previous solutions have not reached benchmark criterion, due to their failure to properly handle the weak singularity of the kernel of the integral equation and the mild singularity at the boundaries of the solution to the integral equation. Successful treatments to these singularities will substantially improve the quality of the solution to the integral equation for the Couette flow problem.

On the other hand, MD simulation can supplement quantitatively correct velocity profiles and density profiles, which are not able to be obtained by solving the Boltzmann equation, in the the near wall van der Waals force affected region. In fact, Barisik *et al* [44, 45] has implemented MD simulations of molecular Couette flows to discover that the velocity profile in the wall penetration depth is quite different from that obtained by Sone *et al* [24] who solved the linearized Boltzmann equation with the same Knudsen number. But, Barisik *et al*'s work is initiatory and their MD results suffer from strong statistical error when the Knudsen is relatively lower.

In this thesis, one of the objects of the present research is to improve the precision and the computational efficiency in solving the integral equations to obtain benchmark solutions to the molecular Couette flows. The next is to systematically investigate the van der Waals effects near the walls by using MD simulation with low statistical noise. Considering the high cost of MD simulation, our final object is to construct effective viscosity model to simulate the molecular Couette flows by a lattice Boltzmann method (LBM) with low cost.

1.2 PREVIOUS WORK

In order to reduce the difficulty of solving the full Boltzmann equation but to maintain its main property, simplifications have been made to obtain model equations such as the BGK equation [23] and the linearized Boltzmann equation of different models, like the steady state model [24], the S-model [25], the variable collision frequency model [26] and the CES model [27]. The boundary conditions of the Boltzmann equation and its model equations are various prescribed reflective distribution functions at the solid walls, which include, but are not limited to the Maxwell boundary condition [28] with one parameter and the Cercignani-Lampis boundary condition [29] with two parameters. The study of gaseous Couette flow by using

Boltzmann model equation can be divided as the early theoretical analysis and the later numerical investigation. Gross and Cercignani are two pioneers in the theoretical study. Gross *et al* [8] utilized the analysis, which was once used for Milne equation of radiative transfer, to obtain linearize BGK equation. They further converted the linearized BGK equation into an integro-differential equation with purely diffusive boundary condition and derived a series of half range polynomial formal solutions by using a series of full range moment equations of the integro-differential equation. The first half range polynomial solution is a linear function, which serves as the footstone for deriving more delicate approximations to the velocity profile of the gaseous Couette flow. Another class of analysis of the gaseous Couette flow was done by Cercignani [30], who applied the method of elementary solutions to two different Fredholm integral equations, both of them are derived from the BGK equation. By using this method, he obtained two solutions to the velocity of gaseous Couette flow in term of two convergent series expansions, one expansion for small Knudsen number case and the other for big Knudsen number case. Besides, Cercignani [31] further applied the method of elementary solutions to the variable collision frequency model for general shear flows. The significance of Gross *et al* and Cercignani's analytical works lies in their mathematical closeness. They provided a series of analytic approximations to the velocity profiles of gaseous Couette flows with increased precision from different starting points. However, as the order of approximation increases the complexity of expressions in both approaches becomes prohibitive for practical usage. Hence, numerical solution of the problem is necessary. The numerical solutions for gaseous Couette flow are mainly obtained by numerically solving an integral equation converted from the BGK equation or other linearized Boltzmann model equations with pure diffusive boundary condition, of which the rarity is characterized by the Knudsen number. For instance, Willis [32] used Nyström method to solve the integral equation derived from the linearized BGK equation with four digits of precision. Loyalka *et al* [33] used the successive iteration method to solve Cercignani's Fredholm equation [30] derived from the BGK equation with various Knudsen numbers. They obtained five digits of precision. Sone *et al* [24] used their own designed finite difference method to solve the steady linearized Boltzmann equation with Knudsen number ranging from 0.1 to 10.0. Their solution has four digits of procision. Siewert [34] used a polynomial expansion technique [35] and the analytical discrete ordinates method [36] to solve the linearized Boltzmann equation in

the CES model with three different Knudsen numbers. His method has five digits of precision. Yap and Sader [37] used uniform chunk based Nyström method to solve Fredholm equations of the second kind derived from the oscillatory and the steady BGK equations with at most six and eight digits of precision, respectively. These numerical solutions to the velocities of the gaseous Couette flows are accurate enough in engineering fields. However, they have not reached the enough precision to serve as benchmark results. As a benchmark solution, the accuracy should be close to the double precision. Recalling the literatures, the model equations for the gaseous Couette flow fall into two classes, the integro-differential equation and the Fredholm equation of the second kind. It is hard to obtain very accurate numerical solution to the integro-differential equation with unbounded phase domain. However, it is easier to solve the Fredholm equation of the second kind with quite high precision. Very recently, a state-of-the-art solution was obtained by Jiang and Luo [38], who used the singular region adaptively refined chunk based collocation method to solve the steady case integral equation discussed by Yap and Sader with at least 14 digits of precision in a wide range of Knudsen numbers. Hence, their results serve as a benchmark. Jiang and Luo's method is based on the recent works [39, 40, 41] in solving integral equations with singular kernels and corner singularities. The integral equation derived from the linearized BGK equation falls into this category. On the one hand, the kernel, a composite Abramowitz function, is weakly singular with a logrithmic and an absolute value singularity. On the other hand, it is proved that the solution to the integral equation has a mild singularity on each of the end points. Jiang and Luo utilized a piecewise low order spectral polynomial expansion to approximate the solution. They used generalized Gaussian quadratures [42, 43] to approximate the integrals associated with the weakly singular kernel to a prescribed precision. For the boundary singularity of the solution, they used adaptively refined subintervals towards the boundaries to decompose the whole interval, such that the end points are contained in the shortest subintervals, where the highest numerical precision is obtained.

The initiatory investigation of the molecular Couette flow by MD simulation is done by Barisik *et al* [44, 45], who implemented MD simuation by using what they call a 'smart wall algorithm'. The density profiles from Barisik *et al*'s MD simulation illustrate nearly uniform density outside the wall force penetration depth and a gradually increased density in the wall force penetration depth. The density profiles reach a

peak at the position of about one molecule diameter away from the wall molecules and abruptly drop to zero at the solid wall. Barisik *et al* also discussed the velocity profiles from their MD simulation. Although the velocity profiles have relatively stronger statistical noise when the Knudsen number of the Couette flow is getting lower, Barisik *et al* asserted that, outside the wall force penetration depth, their velocity profiles match well with Sone *et al*'s numerical solutions to the linearized Boltzmann equation [24] with the same Knudsen number. But in the attractive wall force region which is inside the wall force penetration depth, Barisik *et al*'s velocity profiles have an apparently overshoot with respect to Sone *et al*'s solutions to the linearized Boltzmann equation. In the repulsive force region, Barisik *et al*'s velocity profiles are random and vanish at the wall. The peak values of Barisik *et al*'s velocity are located at approximately the same peak positions as those of the corresponding density profiles.

1.3 OUTLINE OF PRESENT WORK

In this thesis, we carry out our numerical investigation for the molecular Couette flow in three steps. First we solve the Fredholm integral equations of the second kind from the linearized BGK equation of the molecular Couette flows with high precision. Then, we analyze the high precision solution for the velocities by providing high quality approximations. These approximations store the velocity profiles with different Knudsen numbers in simple pattern functions with optimal cofficients subject to various criteria. At last, we implement MD simulation for the molecular Couette flow, model the density profiles and velocity profiles of the molecular Couette flows by using the high precision solutions to the integral equations and the results from MD simulation and finally reproduce the density profiles and velocity profiles by using lattice Boltzmann equation (LBE).

On balance, this thesis is organized as follows. Chapter two gives the derivation of the integral equations for the Couette flow, Poiseuille flow and the Kramers problem with arbitrary Knudsen number and with the Maxwell boundary condition. Chapter three solves the integral equation for steady Couette flow by using the Chebyshev collocation method and the nonuniform chunk based collocation method, respectively, with high precision. As side products, we also solve the integral equations

for Poiseuille flow and Kramers problem in this chapter. Chapter four discusses various approximations to the velocities of the Couette flows, as well as the Knudsen number dependence of the microscopic slip velocity, the marcroscopic slip velocity and the half region mass flow rate. Chapter five implements the MD simulation of the molecular Couette flow, models the density profiles and velocity profiles and reproduce these profiles by using TRT-LBE simulation with one dimensional and two dimensional gas-wall interaction, respective. Chapter six summarizes the work in this thesis and discusses the prospects of furture work.

CHAPTER 2

THE DERIVATION OF THE FREDHOLM EQUATIONS FROM THE BGK EQUATION

In this chapter, we give the derivation of Fredholm integral equations of the 2nd Kind for ocillatory Couette flow, the Kramers problem and Poiseuille flow, respectively, from the Boltzmann BGK equation with arbitrary accommodation ratio in the Maxwell boundary condition. In all of the problems, the derivations are exact except for the linearization of the BGK equation with low Mach number assumption, where the Mach number terms of order 2 and higher are omitted.

2.1 THE COUETTE FLOW PROBLEM

The BGK approximation of the Boltzmann equation is

$$\frac{\partial f}{\partial t} + \boldsymbol{\xi} \cdot \nabla f = -\frac{1}{\tau}(f - f_{LM}) \tag{1}$$

where $f = f(\boldsymbol{r}, \boldsymbol{\xi}, t)$ is the distribution function and $f_{LM} = f_{LM}(\boldsymbol{r}, \boldsymbol{\xi}, t)$ is the local Maxwellian distribution function. The relaxation time, particle position, particle velocity and temporal variable are $\tau, \boldsymbol{r}, \boldsymbol{\xi}$ and t, respectively.
In the present case, we consider the local density ρ and the local temperature T to be constants. The function f can be written as

$$f(\boldsymbol{r}, \boldsymbol{\xi}, t) = \pi^{-3/2} \rho \xi_m^{-3} e^{-|\boldsymbol{\xi}/\xi_m|^2} \left[1 + \frac{U_0}{\xi_m} g(\boldsymbol{r}, \boldsymbol{\xi}, t)\right], \tag{2}$$

and f_{LM} can be written as

$$\begin{aligned} f_{LM}(\boldsymbol{r}, \boldsymbol{\xi}, t) &= \pi^{-3/2} \rho \xi_m^{-3} \exp\left[-\frac{|\boldsymbol{\xi} - \boldsymbol{U}(\boldsymbol{r}, t)|^2}{\xi_m^2}\right] \\ &= \pi^{-3/2} \rho \xi_m^{-3} e^{-|\boldsymbol{\xi}/\xi_m|^2} \exp\left[\frac{2\boldsymbol{\xi} \cdot \boldsymbol{U}(\boldsymbol{r}, t) - |\boldsymbol{U}(\boldsymbol{r}, t)|^2}{\xi_m^2}\right], \end{aligned}$$

where $\boldsymbol{U}, U_0, \xi_m$ are the local flow velocity, the maximum velocity difference of the plates, and the most probable particle speed, respectively. The function g is the

perturbation of f from the absolute Maxwellian, $\pi^{-3/2}\rho\xi_m^{-3}e^{-|\boldsymbol{\xi}/\xi_m|^2}$. Let m be the particle mass and k_b be the Boltzmann constant, then $\xi_m = \sqrt{2k_bT/m}$ is also a constant.

We set up Cartesian coordinates for the oscillatory planar Couette flow problem. Let the stream-wise direction point in the direction of the positive x-axis, the outer normal direction of the lower plate point in the direction of the positive y-axis and the span-wise direction point in the direction of z-axis. The two parallel plates are separated by distance d with the lower one placed at the plane $y = -d/2$ and the upper one placed at the plane $y = d/2$. The upper plate is moving with the velocity $\boldsymbol{U}_w = (U_0\cos(\omega t)/2, 0, 0)$, where ω is the oscillatory frequency. When $\omega = 0$, the flow reduces to steady Couette flow. The lower plate is moving with the velocity $-\boldsymbol{U}_w$. Equiped with the Cartesian coordinates, we have

$$\begin{aligned}\boldsymbol{U}(\boldsymbol{r},t) &= (u(y,t),0,0),\\ f(\boldsymbol{r},\boldsymbol{\xi},t) &= f(y,\boldsymbol{\xi},t),\\ g(\boldsymbol{r},\boldsymbol{\xi},t) &= g(y,\xi_x,\xi_y,t).\end{aligned}$$

and

$$f_{LM}(\boldsymbol{r},\boldsymbol{\xi},t) = \pi^{-3/2}\rho\xi_m^{-3}e^{-|\boldsymbol{\xi}/\xi_m|^2}\left[1+\frac{2\xi_x u(y,t)}{\xi_m^2}+O\left(\frac{u^2(y,t)}{\xi_m^2}\right)\right]. \tag{3}$$

Substituting equations (2)–(3) into equation (1) and neglecting the 2nd order infinitesimal, we have the linearized BGK equation

$$\frac{\partial g}{\partial t}+\xi_y\frac{\partial g}{\partial y} = \frac{1}{\tau}\left[\frac{2\xi_x u(y,t)}{\xi_m U_0}-g\right]. \tag{4}$$

Using the scaling

$$\begin{cases} t\to t\omega,\\ \tau\to\tau\omega,\\ y\to yd^{-1},\\ \boldsymbol{\xi}\to\boldsymbol{\xi}\xi_m^{-1},\\ u\to uU_0^{-1},\\ \boldsymbol{U}_w\to(\cos(\omega t)/2,0,0),\end{cases}$$

equation (4), after rearrangement, is normalized as

$$\frac{\partial g}{\partial t}+\frac{\xi_m\xi_y}{d\omega}\frac{\partial g}{\partial y} = \frac{2\xi_x u-g}{\tau}. \tag{5}$$

We seek a 2π periodic solution with respect to t for the dimensionless equation (5). In order to do so, we consider $g(y, \xi_x, \xi_y, t)$ and $u(y, t)$ as the real parts of two complex valued functions, namely,

$$g(y, \xi_x, \xi_y, t) = \mathrm{Re}\{\tilde{g}(y, \xi_x, \xi_y) \exp(-it)\} = \tilde{g}_R \cos t + \tilde{g}_I \sin t, \tag{6}$$

$$u(y, t) = \mathrm{Re}\{\tilde{u}(y) \exp(-it)\} = \tilde{u}_R \cos t + \tilde{u}_I \sin t, \tag{7}$$

where $\tilde{g}(y, \xi_x, \xi_y) = \tilde{g}_R + i\tilde{g}_I$ and $\tilde{u}(y) = \tilde{u}_R + i\tilde{u}_I$ are complex value functions, $\tilde{g}_R$ and $\tilde{u}_R$ are the real parts and $\tilde{g}_I$ and $\tilde{u}_I$ are the imaginary parts.
Substituting equations (6)–(7) into equation (5) results in the equation below

$$\begin{aligned}&\tilde{g}_R(-\sin t) + \tilde{g}_I \cos t + \frac{\xi_m \xi_y}{d\omega} \frac{\partial \tilde{g}_R}{\partial y} \cos t + \frac{\xi_m \xi_y}{d\omega} \frac{\partial \tilde{g}_I}{\partial y} \sin t \\ =&\frac{2\xi_x \tilde{u}_R \cos t + 2\xi_x \tilde{u}_I \sin t - \tilde{g}_R \cos t - \tilde{g}_I \sin t}{\tau}.\end{aligned}$$

Equating the coefficients of $\sin t$ and the coefficients of $\cos t$ on both sides of the equation respectively, leads to the equations

$$\begin{aligned}\frac{\xi_m \xi_y}{d\omega} \frac{\partial \tilde{g}_R}{\partial y} + \frac{\tilde{g}_R}{\tau} + \tilde{g}_I &= \frac{2\xi_x \tilde{u}_R}{\tau}, \\ \frac{\xi_m \xi_y}{d\omega} \frac{\partial \tilde{g}_I}{\partial y} - \tilde{g}_R + \frac{\tilde{g}_I}{\tau} &= \frac{2\xi_x \tilde{u}_I}{\tau}.\end{aligned}$$

We can use these equations to recover an equation for $\tilde{g}$ and $\tilde{u}$, namely

$$\xi_y \frac{\partial \tilde{g}}{\partial y} + \frac{d\omega(1 - i\tau)}{\xi_m \tau} \tilde{g} = \frac{2\xi_x d\omega \tilde{u}}{\xi_m \tau}.$$

Let λ be the mean free path, then Knudsen number writes $k = \frac{\lambda}{d} = \frac{\xi_m \tau}{d\omega}$. The above equation can be written as the steady complex value linearized BGK equation

$$\xi_y \frac{\partial \tilde{g}}{\partial y} + \frac{1 - i\tau}{k} \tilde{g} = \frac{2\xi_x \tilde{u}}{k}. \tag{8}$$

We introduce the reduced perturbation function $\tilde{\Phi}(y, \xi_y)$ to remove the dependence of ξ_x in equation (8),

$$\tilde{\Phi}(y, \xi_y) = \pi^{-1/2} \int_{-\infty}^{\infty} \xi_x e^{-\xi_x^2} \tilde{g}(y, \xi_x, \xi_y) \, \mathrm{d}\xi_x. \tag{9}$$

Multiplying equation (9) by $\pi^{-1/2} \xi_x e^{-\xi_x^2}$ and then integrating with respect to ξ_x from $-\infty$ to ∞ leads to

$$\xi_y \frac{\partial \tilde{\Phi}}{\partial y} + \frac{1 - i\tau}{k} \tilde{\Phi} = \frac{\tilde{u}}{k}. \tag{10}$$

equation (10) has the solution

$$\tilde{\Phi}(y,\xi_y) = \frac{1}{\xi_y k}\int_{-1/2}^{y} \tilde{u}(s)e^{-\frac{1-i\tau}{\xi_y k}(y-s)}\,\mathrm{d}s + \tilde{\Phi}(-1/2,\xi_y)e^{-\frac{1-i\tau}{\xi_y k}(y+1/2)} \tag{11}$$

$$= -\frac{1}{\xi_y k}\int_{y}^{1/2} \tilde{u}(s)e^{-\frac{1-i\tau}{\xi_y k}(y-s)}\,\mathrm{d}s + \tilde{\Phi}(1/2,\xi_y)e^{\frac{1-i\tau}{\xi_y k}(1/2-y)}. \tag{12}$$

The next thing we will do is write $\tilde{u}(y)$ in terms of $\tilde{\Phi}(y,\xi_y)$ by using the first order moment of f. First

$$\begin{aligned} u(y,t) =& \frac{\int \xi_m^4 \xi_x f(y,\boldsymbol{\xi},t)\,\mathrm{d}\boldsymbol{\xi}}{\rho U_0} \\ =& \pi^{-1}\int_{-\infty}^{\infty}\int_{-\infty}^{\infty} \xi_x e^{-\xi_x^2} g(y,\xi_x,\xi_y,t)e^{-\xi_y^2}\,\mathrm{d}\xi_x\,\mathrm{d}\xi_y. \end{aligned}$$

This means

$$\mathrm{Re}\{\tilde{u}(y)e^{-it}\} = \mathrm{Re}\left\{\pi^{-1}\int_{-\infty}^{\infty}\int_{-\infty}^{\infty} \xi_x e^{-\xi_x^2}\tilde{g}(y,\xi_x,\xi_y)e^{-it}e^{-\xi_y^2}\,\mathrm{d}\xi_x\,\mathrm{d}\xi_y\right\}$$

for all $t \in \mathbb{R}$. So,

$$\begin{aligned} \mathrm{Im}\{\tilde{u}(y)e^{-it}\} &= \mathrm{Re}\{\tilde{u}(y)e^{-i(t+\pi/2)}\} \\ &= \mathrm{Re}\left\{\pi^{-1}\int_{-\infty}^{\infty}\int_{-\infty}^{\infty} \xi_x e^{-\xi_x^2}\tilde{g}(y,\xi_x,\xi_y)e^{-i(t+\pi/2)}e^{-\xi_y^2}\,\mathrm{d}\xi_x\,\mathrm{d}\xi_y\right\} \\ &= \mathrm{Im}\left\{\pi^{-1}\int_{-\infty}^{\infty}\int_{-\infty}^{\infty} \xi_x e^{-\xi_x^2}\tilde{g}(y,\xi_x,\xi_y)e^{-it}e^{-\xi_y^2}\,\mathrm{d}\xi_x\,\mathrm{d}\xi_y\right\}. \end{aligned}$$

Thus, we have

$$\begin{aligned} \tilde{u}(y) &= \pi^{-1/2}\int_{-\infty}^{\infty} e^{-\xi_y^2}\left[\pi^{-1/2}\int_{-\infty}^{\infty} \xi_x e^{-\xi_x^2}\tilde{g}(y,\xi_x,\xi_y)\,\mathrm{d}\xi_x\right]\mathrm{d}\xi_y \\ &= \pi^{-1/2}\int_{-\infty}^{\infty} e^{-\xi_y^2}\tilde{\Phi}(y,\xi_y)\,\mathrm{d}\xi_y. \end{aligned} \tag{13}$$

Substitute equations (11)-(12) into equation (13) to get

$$\begin{aligned}
\tilde{u}(y) = &\pi^{-1/2}\int_0^\infty e^{-\xi_y^2}\frac{1}{\xi_y k}\int_{-1/2}^{y}\tilde{u}(s)e^{-\frac{1-i\tau}{\xi_y k}(y-s)}\,\mathrm{d}s\,\mathrm{d}\xi_y \\
&+\pi^{-1/2}\int_0^\infty e^{-\xi_y^2}\tilde{\Phi}(-1/2,\xi_y)e^{-\frac{1-i\tau}{\xi_y k}(y+1/2)}d\xi_y \\
&-\pi^{-1/2}\int_{-\infty}^0 e^{-\xi_y^2}\frac{1}{\xi_y k}\int_{y}^{1/2}\tilde{u}(s)e^{-\frac{1-i\tau}{\xi_y k}(y-s)}\,\mathrm{d}s\,\mathrm{d}\xi_y \\
&+\pi^{-1/2}\int_{-\infty}^0 e^{-\xi_y^2}\tilde{\Phi}(1/2,\xi_y)e^{\frac{1-i\tau}{\xi_y k}(1/2-y)}\,\mathrm{d}\xi_y \\
=&\,\pi^{-1/2}k^{-1}\int_{-1/2}^{1/2}\tilde{u}(s)\int_0^\infty \xi_y^{-1}e^{-\xi_y^2-\frac{1-i\tau}{\xi_y k}|y-s|}\,\mathrm{d}\xi_y\,\mathrm{d}s \\
&+\pi^{-1/2}\int_0^\infty \tilde{\Phi}(-1/2,\xi_y)e^{-\xi_y^2-\frac{1-i\tau}{\xi_y k}(y+1/2)}\,\mathrm{d}\xi_y \\
&+\pi^{-1/2}\int_0^\infty \tilde{\Phi}(1/2,-\xi_y)e^{-\xi_y^2-\frac{1-i\tau}{\xi_y k}(1/2-y)}\,\mathrm{d}\xi_y. \qquad (14)
\end{aligned}$$

Equation (14) is a generic integral equation for velocity. The quantities $\tilde{\Phi}(-1/2,\xi_y)$ and $\tilde{\Phi}(1/2,-\xi_y)$ with $\xi_y > 0$ are to be determined by boundary conditions to give a closed form of the integral equation.

The same idea can be used to discuss shear stress. Let the shear stress normalized by $\rho\xi_m U_0$ be $T_{xy}(y,t)$, which can be written as the real part of a complex value function,

$$T_{xy}(y,t) = \mathrm{Re}\{\tilde{T}_{xy}(y)\exp(-it)\}. \qquad (15)$$

$\tilde{T}_{xy}$ can be written in terms of $\tilde{\Phi}(y,\xi_y)$ by using a second order moment of f,

$$\begin{aligned}
\tilde{T}_{xy}(y,t) =&\frac{\int \xi_m^5\xi_x\xi_y f(y,\boldsymbol{\xi},t)\,\mathrm{d}\boldsymbol{\xi}}{\rho\xi_m U_0} \\
=&\pi^{-1}\int_{-\infty}^\infty\int_{-\infty}^\infty \xi_x\xi_y e^{-\xi_x^2-\xi_y^2}g(y,\xi_x,\xi_y,t)\,\mathrm{d}\xi_x\,\mathrm{d}\xi_y.
\end{aligned}$$

This means

$$\mathrm{Re}\{\tilde{T}_{xy}(y)e^{-it}\} = \mathrm{Re}\left\{\pi^{-1}\int_{-\infty}^\infty\int_{-\infty}^\infty \xi_y e^{-\xi_y^2}\tilde{g}(y,\xi_x,\xi_y)e^{-it}\xi_x e^{-\xi_x^2}\,\mathrm{d}\xi_x\,\mathrm{d}\xi_y\right\}.$$

By using the same method as we do for the velocity, we have

$$\mathrm{Im}\{\tilde{T}_{xy}(y)e^{-it}\} = \mathrm{Im}\{\pi^{-1}\int_{-\infty}^\infty\int_{-\infty}^\infty \xi_y e^{-\xi_y^2}\tilde{g}(y,\xi_x,\xi_y)e^{-it}\xi_x e^{-\xi_x^2}\,\mathrm{d}\xi_x\,\mathrm{d}\xi_y\},$$

so

$$\begin{aligned}
\tilde{T}_{xy}(y) =&\pi^{-1}\int_{-\infty}^\infty\int_{-\infty}^\infty \xi_y e^{-\xi_y^2}\tilde{g}(y,\xi_x,\xi_y)\xi_x e^{-\xi_x^2}\,\mathrm{d}\xi_x\,\mathrm{d}\xi_y \\
=&\pi^{-1/2}\int_{-\infty}^\infty \xi_y e^{-\xi_y^2}\tilde{\Phi}(y,c_y)\,\mathrm{d}\xi_y. \qquad (16)
\end{aligned}$$

Substitute equations (11)-(12) into equation (16), we have

$$\begin{aligned}
\tilde{T}_{xy}(y) =&\pi^{-1/2}\int_0^\infty \xi_y e^{-\xi_y^2}\frac{1}{\xi_y k}\int_{-1/2}^{y}\tilde{u}(s)e^{-\frac{1-i\tau}{\xi_y k}(y-s)}\,\mathrm{d}s\,\mathrm{d}\xi_y\\
&+\pi^{-1/2}\int_0^\infty \xi_y e^{-\xi_y^2}\tilde{\Phi}(-1/2,\xi_y)e^{-\frac{1-i\tau}{\xi_y k}(y+1/2)}\,\mathrm{d}\xi_y\\
&-\pi^{-1/2}\int_{-\infty}^0 \xi_y e^{-\xi_y^2}\frac{1}{\xi_y k}\int_{y}^{1/2}\tilde{u}(s)e^{-\frac{1-i\tau}{\xi_y k}(y-s)}\,\mathrm{d}s\,\mathrm{d}\xi_y\\
&+\pi^{-1/2}\int_{-\infty}^0 \xi_y e^{-\xi_y^2}\tilde{\Phi}(1/2,\xi_y)e^{\frac{1-i\tau}{\xi_y k}(1/2-y)}\,\mathrm{d}\xi_y\\
=&\pi^{-1/2}k^{-1}\int_0^\infty \tilde{u}(s)\int_{-1/2}^{1/2}\mathrm{sgn}(y-s)e^{-\xi_y^2-\frac{1-i\tau}{\xi_y k}|y-s|}\,\mathrm{d}s\,\mathrm{d}\xi_y\\
&+\pi^{-1/2}\int_0^\infty \tilde{\Phi}(-1/2,\xi_y)\xi_y e^{-\xi_y^2-\frac{1-i\tau}{\xi_y k}(y+1/2)}\,\mathrm{d}\xi_y\\
&-\pi^{-1/2}\int_0^\infty \tilde{\Phi}(1/2,-\xi_y)\xi_y e^{-\xi_y^2-\frac{1-i\tau}{\xi_y k}(1/2-y)}\,\mathrm{d}\xi_y. \qquad (17)
\end{aligned}$$

Now we discuss the boundary conditions of the Couette flow problem. The natural boundary conditions are given by the distribution function $f(y,\boldsymbol{\xi},t)$ at the lower and the upper plates. Our goal is to present the boundary conditions in the form of equations for $\tilde{\Phi}(-1/2,\xi_y)$ and $\tilde{\Phi}(1/2,-\xi_y)$ with $\xi_y>0$, respectively.

We follow the process of Dadzie [46] to get our boundary conditions. First, the pure diffusive boundary condition applied at the lower and the upper plates is given by

$$f_D(\pm 1/2,\boldsymbol{\xi},t)=\pi^{-3/2}\rho\xi_m^{-3}e^{-|\boldsymbol{\xi}\mp U_0(\cos(\omega t)/2,0,0)/\xi_m|^2},\quad \boldsymbol{\xi}\cdot\boldsymbol{n}>0, \qquad (18)$$

where $\boldsymbol{n}$ is the unit normal vector of the boundary plate pointing inside the channel. The diffusive speculative reflection combined boundary condition is given by

$$f(\pm 1/2,\boldsymbol{\xi},t)=(1-\alpha^{\pm})f_D(\pm 1/2,\boldsymbol{\xi},t)+\alpha^{\pm}f(\pm 1/2,\boldsymbol{\xi}_{in},t),\quad \boldsymbol{\xi}\cdot\boldsymbol{n}>0, \qquad (19)$$

where $\boldsymbol{\xi}_{in}$ is the incident velocity at boundary, $\boldsymbol{\xi}$ is the corresponding speculative reflecting velocity, $\alpha^{\pm}$ are the accommodation ratio of the lower and the upper plates, indicating the percentage of the speculative reflection at the corresponding boundary. The relation between the incident velocity and the reflecting velocity is $\boldsymbol{\xi}_{in}=\boldsymbol{\xi}-2(\boldsymbol{\xi}\cdot\boldsymbol{n})\boldsymbol{n}$.

Substitute equation (2) and equation (18) into equation (19); we have

$$\begin{aligned}
&1+\frac{U_0}{\xi_m}g(\pm 1/2,\xi_x,\xi_y,t)\\
=&(1-\alpha^{\pm})e^{-|\boldsymbol{\xi}\mp U_0(\cos t/2,0,0)/\xi_m|^2+|\boldsymbol{\xi}|^2}+\alpha^{\pm}\left[1+\frac{U_0}{\xi_m}g(\pm 1/2,\xi_x,-\xi_y,t)\right],
\end{aligned}$$

where $\xi_y < 0$ when $y = 1/2$ and $\xi_y > 0$ when $y = -1/2$.
This is equivalent to

$$g(\pm 1/2, \xi_x, \xi_y, t) = \frac{(1-\alpha^{\pm})\xi_m}{U_0}\left[e^{\pm\frac{\xi_x U_0 \cos t}{\xi_m} - \frac{U_0^2 \cos^2 t}{4\xi_m^2}} - 1\right] + \alpha^{\pm} g(\pm 1/2, \xi_x, -\xi_y, t). \tag{20}$$

So,

$$\begin{aligned}\mathrm{Re}\{\tilde{g}(\pm 1/2, \xi_x, \xi_y)e^{-it}\} =& \frac{(1-\alpha^{\pm})\xi_m}{U_0}\left[e^{\pm\frac{\xi_x U_0 \cos t}{\xi_m} - \frac{U_0^2 \cos^2 t}{4\xi_m^2}} - 1\right] \\ &+ \alpha^{\pm}\,\mathrm{Re}\{\tilde{g}(\pm 1/2, \xi_x, -\xi_y)e^{-it}\}\end{aligned}$$

and

$$\begin{aligned}&\mathrm{Im}\{\tilde{g}(\pm 1/2, \xi_x, \xi_y)e^{-it}\} = \mathrm{Re}\{\tilde{g}(\pm 1/2, \xi_x, \xi_y)e^{-i(t+\pi/2)}\} \\ =&\frac{(1-\alpha^{\pm})\xi_m}{U_0}\left[e^{\frac{\pm\xi_x U_0 \cos(t+\pi/2)}{\xi_m} - \frac{U_0^2 \cos^2(t+\pi/2)}{4\xi_m^2}} - 1\right] + \alpha^{\pm}\,\mathrm{Re}\{\tilde{g}(\pm 1/2, \xi_x, -\xi_y)e^{-i(t+\pi/2)}\} \\ =&\frac{(1-\alpha^{\pm})\xi_m}{U_0}\left[e^{\mp\frac{\xi_x U_0 \sin t}{\xi_m} - \frac{U_0^2 \sin^2 t}{4\xi_m^2}} - 1\right] + \alpha^{\pm}\,\mathrm{Im}\{\tilde{g}(\pm 1/2, \xi_x, -\xi_y)e^{-it}\},\end{aligned}$$

leading to

$$\begin{aligned}&\tilde{g}(\pm 1/2, \xi_x, \xi_y) \\ =&\frac{(1-\alpha^{\pm})\xi_m e^{it}}{U_0}\left[\left(e^{\pm\frac{\xi_x U_0 \cos t}{\xi_m} - \frac{U_0^2 \cos^2 t}{4\xi_m^2}} - 1\right) + i\left(e^{\mp\frac{\xi_x U_0 \sin t}{\xi_m} - \frac{U_0^2 \sin^2 t}{4\xi_m^2}} - 1\right)\right] \\ &+ \alpha^{\pm}\tilde{g}(\pm 1/2, \xi_x, -\xi_y).\end{aligned}$$

Using the above equation and equation (9), we can derive

$$\tilde{\Phi}(1/2, \xi_y) = (1-\alpha^{+})/2 + \alpha^{+}\tilde{\Phi}(1/2, -\xi_y), \quad \xi_y < 0, \tag{21}$$

$$\tilde{\Phi}(-1/2, \xi_y) = -(1-\alpha^{-})/2 + \alpha^{-}\tilde{\Phi}(-1/2, -\xi_y), \quad \xi_y > 0. \tag{22}$$

Equation (21) is equivalent to

$$\tilde{\Phi}(1/2, -\xi_y) = (1-\alpha^{+})/2 + \alpha^{+}\tilde{\Phi}(1/2, \xi_y), \quad \xi_y > 0, \tag{23}$$

Plugging $(1/2, \xi_y)$ and $(1/2, -\xi_y)$, respectively, into equation (11), we get

$$\tilde{\Phi}(1/2, \xi_y) = \frac{1}{\xi_y k}\int_{-1/2}^{1/2} \tilde{u}(s)e^{-\frac{1-i\tau}{\xi_y k}(1/2-s)}\,\mathrm{d}s + \tilde{\Phi}(-1/2, \xi_y)e^{-\frac{1-i\tau}{\xi_y k}} \tag{24}$$

and

$$\tilde{\Phi}(1/2,-\xi_y) = -\frac{1}{\xi_y k}\int_{-1/2}^{1/2} \tilde{u}(s) e^{\frac{1-i\tau}{\xi_y k}(1/2-s)}\,\mathrm{d}s + \tilde{\Phi}(-1/2,-\xi_y)e^{\frac{1-i\tau}{\xi_y k}}. \tag{25}$$

Under the condition that $\xi_y > 0$, we solve for $\tilde{\Phi}(-1/2,\xi_y)$ and $\tilde{\Phi}(1/2,-\xi_y)$ from equations (22)-(25) to get

$$\begin{aligned}\tilde{\Phi}(-1/2,\xi_y) = &-\frac{(1-\alpha^-)-\alpha^-(1-\alpha^+)e^{-\frac{1-i\tau}{\xi_y k}}}{1-\alpha^-\alpha^+e^{-\frac{2(1-i\tau)}{\xi_y k}}}\frac{1}{2} \\ &+\frac{\alpha^-}{\xi_y k}\int_{-1/2}^{1/2}\frac{e^{-\frac{1-i\tau}{\xi_y k}(1/2+s)}+\alpha^+e^{-\frac{1-i\tau}{\xi_y k}(3/2-s)}}{1-\alpha^-\alpha^+e^{-\frac{2(1-i\tau)}{\xi_y k}}}\tilde{u}(s)\,\mathrm{d}s\end{aligned} \tag{26}$$

and

$$\begin{aligned}\tilde{\Phi}(1/2,-\xi_y) = &\frac{(1-\alpha^+)-\alpha^+(1-\alpha^-)e^{-\frac{1-i\tau}{\xi_y k}}}{1-\alpha^-\alpha^+e^{-\frac{2(1-i\tau)}{\xi_y k}}}\frac{1}{2} \\ &+\frac{\alpha^+}{\xi_y k}\int_{-1/2}^{1/2}\frac{e^{-\frac{1-i\tau}{\xi_y k}(1/2-s)}+\alpha^-e^{-\frac{1-i\tau}{\xi_y k}(3/2+s)}}{1-\alpha^-\alpha^+e^{-\frac{2(1-i\tau)}{\xi_y k}}}\tilde{u}(s)\,\mathrm{d}s.\end{aligned} \tag{27}$$

We denote the n^{th} order Abramowitz function as

$$I_n(x) = \int_0^\infty s^n e^{-s^2-x/s}\,\mathrm{d}s \tag{28}$$

and the n^{th} order modified Abramowitz function as

$$J_n(\alpha,\beta,x) = \int_0^\infty \frac{s^n}{1-\alpha e^{-2\beta/s}} e^{-s^2-\beta x/s}\,\mathrm{d}s. \tag{29}$$

Substituting equation (26) and equation (27) into equation (14), we obtain

$$\begin{aligned}\tilde{u}(y) =& \frac{1}{\pi^{1/2}k}\int_{-1/2}^{1/2}\tilde{u}(s)I_{-1}\left(\frac{1-i\tau}{k}|y-s|\right)\mathrm{d}s \\ &- \frac{1-\alpha^-}{2\pi^{1/2}}J_0\left(\alpha^-\alpha^+,\frac{1-i\tau}{k},y+1/2\right) \\ &+ \frac{\alpha^-(1-\alpha^+)}{2\pi^{1/2}}J_0\left(\alpha^-\alpha^+,\frac{1-i\tau}{k},y+3/2\right) \\ &+ \frac{1-\alpha^+}{2\pi^{1/2}}J_0\left(\alpha^-\alpha^+,\frac{1-i\tau}{k},1/2-y\right) \\ &- \frac{\alpha^+(1-\alpha^-)}{2\pi^{1/2}}J_0\left(\alpha^-\alpha^+,\frac{1-i\tau}{k},3/2-y\right) \\ &+ \frac{\alpha^-}{\pi^{1/2}k}\int_{-1/2}^{1/2}\tilde{u}(s)J_{-1}\left(\alpha^-\alpha^+,\frac{1-i\tau}{k},1+y+s\right)\mathrm{d}s \\ &+ \frac{\alpha^-\alpha^+}{\pi^{1/2}k}\int_{-1/2}^{1/2}\tilde{u}(s)J_{-1}\left(\alpha^-\alpha^+,\frac{1-i\tau}{k},2+y-s\right)\mathrm{d}s \\ &+ \frac{\alpha^+}{\pi^{1/2}k}\int_{-1/2}^{1/2}\tilde{u}(s)J_{-1}\left(\alpha^-\alpha^+,\frac{1-i\tau}{k},1-y-s\right)\mathrm{d}s \\ &+ \frac{\alpha^-\alpha^+}{\pi^{1/2}k}\int_{-1/2}^{1/2}\tilde{u}(s)J_{-1}\left(\alpha^-\alpha^+,\frac{1-i\tau}{k},2-y+s\right)\mathrm{d}s. \end{aligned} \tag{30}$$

Equation (30) is an integral of the second kind for $\tilde{u}$ in closed form. Once solving this equation, one can recover the velocity profile by using equation (7).

Before we apply similar analysis on $\tilde{T}_{xy}$, an interesting discovery is derived by multiplying $\pi^{-1/2}e^{-}\xi_y^2$ on both sides of equation (10) and integration with respect to ξ_y from $-\infty$ to ∞,

$$\frac{\mathrm{d}\tilde{T}_{xy}}{\mathrm{d}y} = \frac{i\tau}{k}\tilde{u}. \tag{31}$$

Substituting equation (26) and equation (27) into equation (16), we obtain

$$\begin{aligned}
\tilde{T}_{xy}(y) =& \frac{1}{\pi^{1/2}k}\int_{-1/2}^{1/2}\tilde{u}(s)\,\mathrm{sgn}(y-s)I_0\left(\frac{1-i\tau}{k}|y-s|\right)\mathrm{d}s \\
&- \frac{1-\alpha^-}{2\pi^{1/2}}J_1\left(\alpha^-\alpha^+,\frac{1-i\tau}{k},y+1/2\right) \\
&+ \frac{\alpha^-(1-\alpha^+)}{2\pi^{1/2}}J_1\left(\alpha^-\alpha^+,\frac{1-i\tau}{k},y+3/2\right) \\
&- \frac{1-\alpha^+}{2\pi^{1/2}}J_1\left(\alpha^-\alpha^+,\frac{1-i\tau}{k},1/2-y\right) \\
&+ \frac{\alpha^+(1-\alpha^-)}{2\pi^{1/2}}J_1\left(\alpha^-\alpha^+,\frac{1-i\tau}{k},3/2-y\right) \\
&+ \frac{\alpha^-}{\pi^{1/2}k}\int_{-1/2}^{1/2}\tilde{u}(s)J_0\left(\alpha^-\alpha^+,\frac{1-i\tau}{k},1+y+s\right)\mathrm{d}s \\
&+ \frac{\alpha^-\alpha^+}{\pi^{1/2}k}\int_{-1/2}^{1/2}\tilde{u}(s)J_0\left(\alpha^-\alpha^+,\frac{1-i\tau}{k},2+y-s\right)\mathrm{d}s \\
&- \frac{\alpha^+}{\pi^{1/2}k}\int_{-1/2}^{1/2}\tilde{u}(s)J_0\left(\alpha^-\alpha^+,\frac{1-i\tau}{k},1-y-s\right)\mathrm{d}s \\
&- \frac{\alpha^-\alpha^+}{\pi^{1/2}k}\int_{-1/2}^{1/2}\tilde{u}(s)J_0\left(\alpha^-\alpha^+,\frac{1-i\tau}{k},2-y+s\right)\mathrm{d}s. \qquad (32)
\end{aligned}$$

Equation (32) is a functional of $\tilde{u}$. From equation (31), we know if the plates keep uniform velocity, i.e., $\omega = 0$ (which will cause the normalized τ to vanish), then $T_{xy} = \tilde{T}_{xy}$ is independent of the spatial variable y. In this special case, we have

$$\begin{aligned}
T_{xy} =& -\frac{1}{\pi^{1/2}k}\int_{-1/2}^{1/2}u(s)\,\mathrm{sgn}(s)I_0\left(\frac{|s|}{k}\right)\mathrm{d}s \\
&- \frac{2-\alpha^--\alpha^+}{2\pi^{1/2}}J_1\left(\alpha^-\alpha^+,\frac{1}{k},1/2\right) \\
&+ \frac{\alpha^-+\alpha^+-2\alpha^-\alpha^+}{2\pi^{1/2}}J_1\left(\alpha^-\alpha^+,\frac{1}{k},3/2\right) \\
&+ \frac{\alpha^-}{\pi^{1/2}k}\int_{-1/2}^{1/2}u(s)J_0\left(\alpha^-\alpha^+,\frac{1}{k},1+s\right)\mathrm{d}s \\
&+ \frac{\alpha^-\alpha^+}{\pi^{1/2}k}\int_{-1/2}^{1/2}u(s)J_0\left(\alpha^-\alpha^+,\frac{1}{k},2-s\right)\mathrm{d}s \\
&- \frac{\alpha^+}{\pi^{1/2}k}\int_{-1/2}^{1/2}u(s)J_0\left(\alpha^-\alpha^+,\frac{1}{k},1-s\right)\mathrm{d}s \\
&- \frac{\alpha^-\alpha^+}{\pi^{1/2}k}\int_{-1/2}^{1/2}u(s)J_0\left(\alpha^-\alpha^+,\frac{1}{k},2+s\right)\mathrm{d}s \qquad (33)
\end{aligned}$$

or

$$
\begin{aligned}
T_{xy} =& \frac{1}{2\pi^{1/2}k}\int_{-1/2}^{1/2} u(s)F_0(s,k)\,\mathrm{d}s \\
&- \frac{2-\alpha^- -\alpha^+}{4\pi^{1/2}}\left[J_1\left(\alpha^-\alpha^+,\frac{1}{k},0\right)+J_1\left(\alpha^-\alpha^+,\frac{1}{k},1\right)\right] \\
&+ \frac{\alpha^- +\alpha^+ -2\alpha^-\alpha^+}{4\pi^{1/2}}\left[J_1\left(\alpha^-\alpha^+,\frac{1}{k},1\right)+J_1\left(\alpha^-\alpha^+,\frac{1}{k},2\right)\right] \\
&+ \frac{\alpha^-}{2\pi^{1/2}k}\int_{-1/2}^{1/2} u(s)\left[J_0\left(\alpha^-\alpha^+,\frac{1}{k},3/2+s\right)+J_0\left(\alpha^-\alpha^+,\frac{1}{k},1/2+s\right)\right]\mathrm{d}s \\
&+ \frac{\alpha^-\alpha^+}{2\pi^{1/2}k}\int_{-1/2}^{1/2} u(s)\left[J_0\left(\alpha^-\alpha^+,\frac{1}{k},5/2-s\right)+J_0\left(\alpha^-\alpha^+,\frac{1}{k},3/2-s\right)\right]\mathrm{d}s \\
&- \frac{\alpha^+}{2\pi^{1/2}k}\int_{-1/2}^{1/2} u(s)\left[J_0\left(\alpha^-\alpha^+,\frac{1}{k},3/2-s\right)+J_0\left(\alpha^-\alpha^+,\frac{1}{k},1/2-s\right)\right]\mathrm{d}s \\
&- \frac{\alpha^-\alpha^+}{2\pi^{1/2}k}\int_{-1/2}^{1/2} u(s)\left[J_0\left(\alpha^-\alpha^+,\frac{1}{k},5/2+s\right)+J_0\left(\alpha^-\alpha^+,\frac{1}{k},3/2+s\right)\right]\mathrm{d}s.
\end{aligned}
\tag{34}
$$

2.2 THE KRAMERS PROBLEM

We start from the steady BGK Equation,

$$\boldsymbol{\xi}\cdot\nabla f = -\frac{1}{\tau}(f - f_{LM}). \tag{35}$$

In this case, we also consider the local density ρ and local temperature T as constants. The distribution function, f, can be written as

$$f(\boldsymbol{r},\boldsymbol{\xi}) = \pi^{-3/2}\rho\xi_m^{-3}e^{-|\boldsymbol{\xi}/\xi_m|^2}[1+\dot{\gamma}\tau g(\boldsymbol{r},\boldsymbol{\xi})] \tag{36}$$

where $\dot{\gamma}$ is the shear rate, g is the perturbation of f from the absolution Maxwellian. f_{LM} can be written as

$$
\begin{aligned}
f_{LM}(\boldsymbol{r},\boldsymbol{\xi}) &= \pi^{-3/2}\rho\xi_m^{-3}e^{-|\boldsymbol{\xi}/\xi_m|^2}\exp\left[\frac{2\boldsymbol{\xi}\cdot\boldsymbol{U}(\boldsymbol{r})-|\boldsymbol{U}(\boldsymbol{r})|^2}{\xi_m^2}\right] \\
&= \pi^{-3/2}\rho\xi_m^{-3}e^{-|\boldsymbol{\xi}/\xi_m|^2}\left[1+\frac{2\boldsymbol{\xi}\cdot\boldsymbol{U}(\boldsymbol{r})}{\xi_m^2}+O\left(\frac{\boldsymbol{U}^2(\boldsymbol{r})}{\xi_m^2}\right)\right].
\end{aligned}
\tag{37}
$$

We set up Cartesian coordinates for the Kramers problem. Let the stream-wise direction point in the direction of the positive x-axis, the outer normal direction of the plate point in the direction of the positive y-axis and the span-wise direction

point in the direction of the z-axis. The plate placed at the plane $y = 0$ is at rest. The flow velocity at the location y is $\boldsymbol{U}(\boldsymbol{r}) = (\dot{\gamma}(y + q(y)), 0, 0)$.
In the Cartesian coordinate, we have

$$f(\boldsymbol{r}, \boldsymbol{\xi}) = f(y, \boldsymbol{\xi}),$$
$$g(\boldsymbol{r}, \boldsymbol{\xi}) = g(y, \xi_x, \xi_y).$$

Substituting equations (36)-(37) into equation (35) and neglecting the 2nd order infinitesimal, we have the linearized BGK equation

$$\xi_y \frac{\partial g}{\partial y} = \frac{1}{\tau}\left[\frac{2\xi_x(y + q(y))}{\xi_m^2 \tau} - g\right]. \tag{38}$$

The mean free path is defined by $\lambda = \xi_m \tau$. Using the scaling

$$\begin{cases} y \to y\lambda^{-1}, \\ q \to q\lambda^{-1}, \\ \boldsymbol{\xi} \to \boldsymbol{\xi}\xi_m^{-1}, \end{cases}$$

we rearrange equation (38) and normalize it as

$$\xi_y \frac{\partial g}{\partial y} = 2\xi_x(y + q) - g. \tag{39}$$

We define

$$\Phi(y, \xi_y) = \pi^{-1/2} \int_{-\infty}^{\infty} \xi_x e^{-\xi_x^2} g(y, \xi_x, \xi_y)\, \mathrm{d}\xi_x \tag{40}$$

and assume g is small enough as $y \gg 1$, such that $|\Phi|$ is bounded by a constant C_Φ. Multiplying equation (39) by $\pi^{-1/2}\xi_x e^{-\xi_x^2}$ and then integrating with respect to ξ_x from $-\infty$ to ∞ leads to

$$\xi_y \frac{\partial \Phi}{\partial y} + \Phi = y + q. \tag{41}$$

Equation (41) has the solution

$$\Phi(y, \xi_y) = \xi_y^{-1} \int_0^y (s + q(s)) e^{(s-y)/\xi_y}\, \mathrm{d}s + \Phi(0, \xi_y) e^{-y/\xi_y} \tag{42}$$

$$= -\xi_y^{-1} \int_y^{y^*} (s + q(s)) e^{(s-y)/\xi_y}\, \mathrm{d}s + \Phi(y^*, \xi_y) e^{(y^*-y)/\xi_y} \tag{43}$$

Using equations (42)-(43) and the fact

$$\left| \int_0^\infty \Phi(y^*, -\xi_y) \xi_y^n e^{-\xi_y^2 - (y^* \pm y)/\xi_y}\, \mathrm{d}\xi_y \right| \le C_\Phi I_n(y^* \pm y) \to 0, \quad \text{as} \quad y^* \to \infty,$$

and the first order moment of f, we write $q(y)$ in terms of $\Phi(y,\xi_y)$,

$$\begin{aligned}
q(y) =& \frac{\int \xi_m^4 \xi_x f(y,\boldsymbol{\xi})\,\mathrm{d}\boldsymbol{\xi}}{\rho\dot{\gamma}\lambda} - y \\
=& \pi^{-1}\int_{-\infty}^{\infty}\int_{-\infty}^{\infty} \xi_x e^{-\xi_x^2} g(y,\xi_x,\xi_y) e^{-\xi_y^2}\,\mathrm{d}\xi_x\,\mathrm{d}\xi_y - y \\
=& \pi^{-1/2}\int_{-\infty}^{\infty} \Phi(y,\xi_y) e^{-\xi_y^2}\,\mathrm{d}\xi_y - y \\
=& \pi^{-1/2}\int_0^{y^*} (s+q(s)) I_{-1}(|y-s|)\,\mathrm{d}s + \pi^{-1/2}\int_0^{\infty} \Phi(0,\xi_y) e^{-\xi_y^2 - y/\xi_y}\,\mathrm{d}\xi_y \\
&+ \pi^{-1/2}\int_0^{\infty} \Phi(y^*,-\xi_y) e^{-\xi_y^2-(y^*-y)/\xi_y}\,\mathrm{d}\xi_y - y \\
\to& \pi^{-1/2}\left[\int_0^{\infty} (s+q(s)) I_{-1}(|y-s|)\,\mathrm{d}s + \int_0^{\infty} \Phi(0,\xi_y) e^{-\xi_y^2 - y/\xi_y}\,\mathrm{d}\xi_y\right] - y, y^* \to \infty \\
=& \pi^{-1/2}\left[\int_0^{\infty} q(s) I_{-1}(|y-s|)\,\mathrm{d}s + I_1(y) + \int_0^{\infty} \Phi(0,\xi_y) e^{-\xi_y^2 - y/\xi_y}\,\mathrm{d}\xi_y\right]. \qquad (44)
\end{aligned}$$

Similarly, the diffusive speculative reflection combined boundary condition is given by

$$f(0,\boldsymbol{\xi}) = (1-\alpha)\pi^{-3/2}\rho\xi_m^{-3} e^{-|\boldsymbol{\xi}|^2} + \alpha f(0,\boldsymbol{\xi}_{in}), \quad \boldsymbol{\xi}\cdot\boldsymbol{n} > 0 \qquad (45)$$

with $\boldsymbol{\xi}_{in} = \boldsymbol{\xi} - 2(\boldsymbol{\xi}\cdot\boldsymbol{n})\boldsymbol{n}$.

This equivalent to

$$\Phi(0,\xi_y) = \alpha\Phi(0,-\xi_y), \quad \xi_y > 0. \qquad (46)$$

Plugging $(0,-\xi_y)$ into equation (43) and using equation (46), we have

$$\begin{aligned}
&\int_0^{\infty} \Phi(0,\xi_y) e^{-\xi_y^2 - y/\xi_y}\,\mathrm{d}\xi_y \\
=& \alpha\int_0^{\infty} \Phi(0,-\xi_y) e^{-\xi_y^2 - y/\xi_y}\,\mathrm{d}\xi_y \\
=& \alpha\int_0^{\infty} \left[\xi_y^{-1}\int_0^{y^*} (s+q(s)) e^{-s/\xi_y}\,\mathrm{d}s + \Phi(y^*,-\xi_y) e^{-y^*/\xi_y}\right] e^{-\xi_y^2 - y/\xi_y}\,\mathrm{d}\xi_y \\
=& \alpha\left[\int_0^{y^*} (s+q(s)) I_{-1}(y+s)\,\mathrm{d}s + \int_0^{\infty} \Phi(y^*,-\xi_y) e^{-\xi_y^2-(y^*+y)/\xi_y}\,\mathrm{d}\xi_y\right] \\
\to& \alpha\int_0^{\infty} (s+q(s)) I_{-1}(y+s)\,\mathrm{d}s, \quad (y^* \to \infty) \\
=& \alpha\left[I_1(y) + \int_0^{\infty} q(s) I_{-1}(y+s)\,\mathrm{d}s\right].
\end{aligned}$$

Substituting the above equation into equation (44), we obtain

$$q(y) = \pi^{-1/2}\left[\int_0^{\infty} q(s) I_{-1}(|y-s|)\,\mathrm{d}s + (1+\alpha) I_1(y) + \alpha\int_0^{\infty} q(s) I_{-1}(y+s)\,\mathrm{d}s\right]. \qquad (47)$$

Equation (47) is an integral equation of the 2nd kind for q in the closed form. Solving this equation, we can recover the velocity profile of the Kramers problem.
Then, we discuss the shear stress of the Kramers problem. Let the shear stress normalized by $\rho\dot{\gamma}\lambda\xi_m$ be T_{xy}. From the derivation of equation (44), we have

$$\pi^{-1/2}\int_{-\infty}^{\infty}\Phi(y,\xi_y)e^{-\xi_y^2}\,\mathrm{d}\xi_y = q(y)+y. \tag{48}$$

On the one hand, using equation (48) and multiplying equation (41) by $\pi^{-1/2}e^{-\xi_y^2}$ and then integrating the resultant equation with respect to ξ_y from $-\infty$ to ∞ leads to

$$\pi^{-1/2}\frac{\mathrm{d}}{\mathrm{d}y}\int_{-\infty}^{\infty}\Phi(y,\xi_y)\xi_y e^{-\xi_y^2}\,\mathrm{d}\xi_y = 0.$$

On the other hand, $T_{xy}(y)$ can be written in terms of $\Phi(y,\xi_y)$ by using a second order moment of f, namely,

$$\begin{aligned}T_{xy}(y) =& \frac{\int \xi_m^5\xi_x\xi_y f(y,\boldsymbol{\xi})\,\mathrm{d}\boldsymbol{\xi}}{\rho\dot{\gamma}\lambda\xi_m}\\ =&\pi^{-1/2}\int_{-\infty}^{\infty}\Phi(y,\xi_y)\xi_y e^{-\xi_y^2}\,\mathrm{d}\xi_y.\end{aligned}$$

The above two equations show that T_{xy} is independent of the spatial variable y. Plugging $(0,-\xi_y)$ into Equation (43), we get

$$\Phi(0,-\xi_y) = \xi_y^{-1}\int_0^{y^*}(s+q(s))e^{-s/\xi_y}\,\mathrm{d}s + \Phi(y^*,-\xi_y)e^{-y^*/\xi_y}.$$

Using the above equation and Equation (46), T_{xy} can be written as

$$\begin{aligned}T_{xy} =&\pi^{-1/2}\int_{-\infty}^{\infty}\Phi(0,\xi_y)\xi_y e^{-\xi_y^2}\,\mathrm{d}\xi_y\\ =&-\pi^{-1/2}(1-\alpha)\int_0^{\infty}\Phi(0,-\xi_y)\xi_y e^{-\xi_y^2}\,\mathrm{d}\xi_y\\ =&-\pi^{-1/2}(1-\alpha)\left[\int_0^{y^*}(s+q(s))I_0(s)\,\mathrm{d}s + \int_0^{\infty}\Phi(y^*,-\xi_y)\xi_y e^{-\xi_y^2-y^*/\xi_y}\,\mathrm{d}\xi_y\right]\\ \to&-\pi^{-1/2}(1-\alpha)\int_0^{\infty}(s+q(s))I_0(s)\,\mathrm{d}s, \quad (y^*\to\infty).\end{aligned} \tag{49}$$

2.3 THE POISEUILLE FLOW PROBLEM

First, we set up Cartesian coordinates for the planar Poiseuille flow problem. Let the stream-wise direction point in the direction of the positive x-axis, the outer

normal direction of the lower plate point in the direction of the positive y-axis and the span-wise direction point in the direction of the z-axis. The two parallel plates are separated by the distance, d, with lower one placed at the plane $y = -d/2$ and the upper one placed at the plane $y = d/2$. Both of the plates are at rest. We focus on the cross section of the channel where $x = 0$. We assume that the cross section has uniform density ρ and constant temperature T and is subject to uniform density gradient $\nabla\rho = (\frac{\mathrm{d}\rho}{\mathrm{d}x}, 0, 0)$. The local flow velocity is $\boldsymbol{U}(y) = (u(y), 0, 0)$.
Recall the steady BGK equation (35). In the present case, the distribution function, f, can be written as

$$f(x, y, \boldsymbol{\xi}) = \pi^{-3/2}\rho\xi_m^{-3}e^{-|\boldsymbol{\xi}/\xi_m|^2}\left[1 + \frac{\xi_x}{\xi_m}g(y, \xi_y) + \frac{\mathrm{d}\rho}{\mathrm{d}x}\frac{x}{\rho}\right], \tag{50}$$

where f_{LM} can be written as

$$\begin{aligned} f_{LM}(x, y, \boldsymbol{\xi}) =& \pi^{-3/2}\rho\xi_m^{-3}e^{-|\boldsymbol{\xi}-\boldsymbol{U}|^2/\xi_m^2}\left(1 + \frac{\mathrm{d}\rho}{\mathrm{d}x}\frac{x}{\rho}\right) \\ =& \pi^{-3/2}\rho\xi_m^{-3}e^{-|\boldsymbol{\xi}/\xi_m|^2}\left[1 + \frac{\mathrm{d}\rho}{\mathrm{d}x}\frac{x}{\rho} + \frac{2\xi_x u}{\xi_m^2} + O\left(\frac{u^2}{\xi_m^2}\right)\right]. \end{aligned} \tag{51}$$

Substituting equations (50)–(51) into equation $\left(\frac{2u}{\xi_m^2} - \frac{g}{\xi_m}\right)$eglecting the 2nd order infinitesimal, we have

$$\frac{\mathrm{d}\rho}{\mathrm{d}x}\frac{1}{\rho} + \frac{\xi_y}{\xi_m}\frac{\partial g}{\partial y} = \frac{1}{\tau}\left(\frac{2u}{\xi_m^2} - \frac{g}{\xi_m}\right). \tag{52}$$

The Knudsen number is defined as $k = \frac{\xi_m\tau}{d}$. Using the scaling

$$\begin{cases} x \to xd^{-1}, \\ y \to yd^{-1}, \\ \boldsymbol{\xi} \to \boldsymbol{\xi}\xi_m^{-1}, \\ u \to -u\rho\left(\xi_m\frac{\mathrm{d}\rho}{\mathrm{d}x}\right)^{-1}, \end{cases}$$

equation (52) can be rewritten as the linearized BGK equation

$$\xi_y\frac{\partial g}{\partial y} + \frac{g}{k} = -\frac{\mathrm{d}\rho}{\mathrm{d}x}\frac{2u + k}{k\rho}. \tag{53}$$

Equation (53) has the solution

$$g(y, \xi_y) = -\frac{\mathrm{d}\rho}{\mathrm{d}x}\frac{1}{\rho\xi_y}\int_{-1/2}^{y}(2u(s)/k + 1)e^{(s-y)/(\xi_y k)}\,\mathrm{d}s + g(-1/2, \xi_y)e^{-(y+1/2)/(\xi_y k)} \tag{54}$$

$$= \frac{\mathrm{d}\rho}{\mathrm{d}x}\frac{1}{\rho\xi_y}\int_{y}^{1/2}(2u(s)/k + 1)e^{(s-y)/(\xi_y k)}\,\mathrm{d}s + g(1/2, \xi_y)e^{-(y-1/2)/(\xi_y k)}. \tag{55}$$

Using equations (54)–(55) and the first order moment of f, we write $u(y)$ in terms of $g(y,\xi_y)$, namely,

$$\begin{aligned} u(y) =& -\frac{\int \xi_m^4 \xi_x f(x,y,\boldsymbol{\xi})\,\mathrm{d}\boldsymbol{\xi}}{\xi_m \frac{\mathrm{d}\rho}{\mathrm{d}x}} \\ =& -\frac{\rho}{2\pi^{1/2}\frac{\mathrm{d}\rho}{\mathrm{d}x}} \int_{-\infty}^{\infty} g(y,\xi_y) e^{-\xi_y^2}\,\mathrm{d}\xi_y \\ =& \frac{1}{2\pi^{1/2}} \int_{-1/2}^{1/2} (2u(s)/k+1) I_{-1}\left(\frac{|y-s|}{k}\right) \mathrm{d}s \\ & -\frac{\rho}{2\pi^{1/2}\frac{\mathrm{d}\rho}{\mathrm{d}x}} \int_0^{\infty} g(-1/2,\xi_y) e^{-(y+1/2)/(\xi_y k)-\xi_y^2}\,\mathrm{d}\xi_y \\ & -\frac{\rho}{2\pi^{1/2}\frac{\mathrm{d}\rho}{\mathrm{d}x}} \int_0^{\infty} g(1/2,-\xi_y) e^{-(1/2-y)/(\xi_y k)-\xi_y^2}\,\mathrm{d}\xi_y. \end{aligned} \tag{56}$$

The diffusive speculative reflection combined boundary condition is given by

$$f(0,\pm 1/2,\boldsymbol{\xi}) = (1-\alpha^{\pm})\pi^{-3/2}\rho\xi_m^{-3} e^{-|\boldsymbol{\xi}|^2} + \alpha^{\pm} f(0,\pm 1/2,\boldsymbol{\xi}_{in}), \quad \boldsymbol{\xi}\cdot\boldsymbol{n} > 0 \tag{57}$$

with $\boldsymbol{\xi}_{in} = \boldsymbol{\xi} - 2(\boldsymbol{\xi}\cdot\boldsymbol{n})\boldsymbol{n}$.

This is equivalent to

$$g(1/2,\xi_y) = \alpha^{+} g(1/2,-\xi_y), \quad \xi_y < 0 \tag{58}$$

and

$$g(-1/2,\xi_y) = \alpha^{-} g(-1/2,-\xi_y), \quad \xi_y > 0. \tag{59}$$

Equation (58) can be written as

$$g(1/2,-\xi_y) = \alpha^{+} g(1/2,\xi_y), \quad \xi_y > 0. \tag{60}$$

Plugging $(1/2,\xi_y)$ and $(1/2,-\xi_y)$, respectively, into equation (54), we get

$$g(1/2,\xi_y) = -\frac{\mathrm{d}\rho}{\mathrm{d}x}\frac{1}{\rho\xi_y} \int_{-1/2}^{1/2} (2u(s)/k+1) e^{-\frac{1/2-s}{\xi_y k}}\,\mathrm{d}s + g(-1/2,\xi_y) e^{-\frac{1}{\xi_y k}} \tag{61}$$

and

$$g(1/2,-\xi_y) = \frac{\mathrm{d}\rho}{\mathrm{d}x}\frac{1}{\rho\xi_y} \int_{-1/2}^{1/2} (2u(s)/k+1) e^{\frac{1/2-s}{\xi_y k}}\,\mathrm{d}s + g(-1/2,-\xi_y) e^{\frac{1}{\xi_y k}}. \tag{62}$$

Under the condition, $\xi_y > 0$, we solve for $g(1/2,-\xi_y)$ and $g(-1/2,\xi_y)$ from equations (59)–(62) to get

$$\begin{aligned} & g(-1/2,\xi_y) \\ =& -\frac{\alpha^{-}\frac{\mathrm{d}\rho}{\mathrm{d}x}\left[\int_{-1/2}^{1/2}(2u(s)/k+1)e^{-\frac{1/2+s}{\xi_y k}}\,\mathrm{d}s + \alpha^{+}\int_{-1/2}^{1/2}(2u(s)/k+1)e^{-\frac{3/2-s}{\xi_y k}}\,\mathrm{d}s\right]}{\rho\xi_y\left(1-\alpha^{-}\alpha^{+}e^{-\frac{2}{\xi_y k}}\right)} \end{aligned} \tag{63}$$

and

$$
\begin{aligned}
&g(1/2,-\xi_y)\\
&=-\frac{\alpha^+\frac{\mathrm{d}\rho}{\mathrm{d}x}\left[\int_{-1/2}^{1/2}(2u(s)/k+1)e^{-\frac{1/2-s}{\xi_y k}}\,\mathrm{d}s+\alpha^-\int_{-1/2}^{1/2}(2u(s)/k+1)e^{-\frac{3/2+s}{\xi_y k}}\,\mathrm{d}s\right]}{\rho\xi_y\left(1-\alpha^-\alpha^+e^{-\frac{2}{\xi_y k}}\right)}. \qquad (64)
\end{aligned}
$$

Substituting equation (63) and equation (64) into equation (56), we obtain

$$
\begin{aligned}
u(y)=&\frac{1}{2\pi^{1/2}}\int_{-1/2}^{1/2}(2u(s)/k+1)I_{-1}\left(\frac{|y-s|}{k}\right)\mathrm{d}s\\
&+\frac{\alpha^-}{2\pi^{1/2}}\int_{-1/2}^{1/2}(2u(s)/k+1)J_{-1}(\alpha^-\alpha^+,1/k,1+y+s)\,\mathrm{d}s\\
&+\frac{\alpha^-\alpha^+}{2\pi^{1/2}}\int_{-1/2}^{1/2}(2u(s)/k+1)J_{-1}(\alpha^-\alpha^+,1/k,2+y-s)\,\mathrm{d}s\\
&+\frac{\alpha^+}{2\pi^{1/2}}\int_{-1/2}^{1/2}(2u(s)/k+1)J_{-1}(\alpha^-\alpha^+,1/k,1-y-s)\,\mathrm{d}s\\
&+\frac{\alpha^-\alpha^+}{2\pi^{1/2}}\int_{-1/2}^{1/2}(2u(s)/k+1)J_{-1}(\alpha^-\alpha^+,1/k,2-y+s)\,\mathrm{d}s. \qquad (65)
\end{aligned}
$$

Denote $w(y)=2u(y)/k+1$, equation (65) can be written as

$$
\begin{aligned}
w(y)=&\frac{1}{\pi^{1/2}k}\int_{-1/2}^{1/2}w(s)I_{-1}\left(\frac{|y-s|}{k}\right)\mathrm{d}s+1\\
&+\frac{\alpha^-}{\pi^{1/2}k}\int_{-1/2}^{1/2}w(s)J_{-1}(\alpha^-\alpha^+,1/k,1+y+s)\,\mathrm{d}s\\
&+\frac{\alpha^-\alpha^+}{\pi^{1/2}k}\int_{-1/2}^{1/2}w(s)J_{-1}(\alpha^-\alpha^+,1/k,2+y-s)\,\mathrm{d}s\\
&+\frac{\alpha^+}{\pi^{1/2}k}\int_{-1/2}^{1/2}w(s)J_{-1}(\alpha^-\alpha^+,1/k,1-y-s)\,\mathrm{d}s\\
&+\frac{\alpha^-\alpha^+}{\pi^{1/2}k}\int_{-1/2}^{1/2}w(s)J_{-1}(\alpha^-\alpha^+,1/k,2-y+s)\,\mathrm{d}s. \qquad (66)
\end{aligned}
$$

Equation (66) is a Fredholm integral equation of the second kind for w in the closed form. Solving this equation, we can recover the velocity profile of the Poiseuille flow problem. Then, we consider the shear stress of the Poiseuille flow problem. Let the shear stress normalized by $-\xi_m^2\frac{\mathrm{d}\rho}{\mathrm{d}x}$ be T_{xy}, which can be written in terms of $g(y,\xi_y)$

by using a second order moment of f, namely,

$$T_{xy}(y) = -\frac{\int \xi_m^5 \xi_x \xi_y f(x,y,\boldsymbol{\xi})\,\mathrm{d}\boldsymbol{\xi}}{\xi_m^2 \frac{\mathrm{d}\rho}{\mathrm{d}x}} = -\frac{\rho}{2\pi^{1/2}\frac{\mathrm{d}\rho}{\mathrm{d}x}} \int_{-\infty}^{\infty} g(y,\xi_y)\xi_y e^{-\xi_y^2}\,\mathrm{d}\xi_y. \tag{67}$$

Using equations (54)–(55) and equations (63)–(64), equation (67) is rewritten as

$$\begin{aligned}
T_{xy}(y) =& \frac{1}{2\pi^{1/2}} \int_{-1/2}^{1/2} (2u(s)/k+1)\,\mathrm{sgn}(y-s) I_0\left(\frac{|y-s|}{k}\right)\mathrm{d}s \\
&- \frac{\rho}{2\pi^{1/2}\frac{\mathrm{d}\rho}{\mathrm{d}x}} \int_0^{\infty} \left[g(-1/2,\xi_y)\xi_y e^{-\xi_y^2 - \frac{y+1/2}{\xi_y k}} - g(1/2,-\xi_y)\xi_y e^{-\xi_y^2 - \frac{1/2-y}{\xi_y k}} \right] \mathrm{d}\xi_y \\
=& \frac{1}{2\pi^{1/2}} \int_{-1/2}^{1/2} (2u(s)/k+1)\,\mathrm{sgn}(y-s) I_0\left(\frac{|y-s|}{k}\right)\mathrm{d}s \\
&+ \frac{\alpha^-}{2\pi^{1/2}} \int_{-1/2}^{1/2} (2u(s)/k+1) J_0(\alpha^-\alpha^+, 1/k, 1+y+s)\,\mathrm{d}s \\
&+ \frac{\alpha^-\alpha^+}{2\pi^{1/2}} \int_{-1/2}^{1/2} (2u(s)/k+1) J_0(\alpha^-\alpha^+, 1/k, 2+y-s)\,\mathrm{d}s \\
&- \frac{\alpha^+}{2\pi^{1/2}} \int_{-1/2}^{1/2} (2u(s)/k+1) J_0(\alpha^-\alpha^+, 1/k, 1-y-s)\,\mathrm{d}s \\
&- \frac{\alpha^-\alpha^+}{2\pi^{1/2}} \int_{-1/2}^{1/2} (2u(s)/k+1) J_0(\alpha^-\alpha^+, 1/k, 2-y+s)\,\mathrm{d}s.
\end{aligned} \tag{68}$$

From the derivation of equation (56), we have

$$u(y) = -\frac{\rho}{2\pi^{1/2}\frac{\mathrm{d}\rho}{\mathrm{d}x}} \int_{-\infty}^{\infty} g(y,\xi_y) e^{-\xi_y^2}\,\mathrm{d}\xi_y. \tag{69}$$

Using equation (67) and equation (69) and multiplying equation (53) by $\pi^{-1/2}e^{-\xi_y^2}$ then integrating the resultant equation with respect to ξ_y from $-\infty$ to ∞ leads to

$$\frac{\mathrm{d}T_{xy}}{\mathrm{d}y} = \frac{1}{2}. \tag{70}$$

From equation (68) and equation (70), we obtain the shear stress of the Poiseuille

flow problem

$$
\begin{aligned}
T_{xy}(y) =& \frac{y}{2} + T_{xy}(0) \\
=& \frac{y}{2} - \frac{1}{\pi^{1/2}k} \int_{-1/2}^{1/2} u(s)\,\mathrm{sgn}(s) I_0\left(\frac{|s|}{k}\right) \mathrm{d}s \\
&+ \frac{k(\alpha^- - \alpha^+)}{2\pi^{1/2}} \left[J_1(\alpha^-\alpha^+, 1/k, 1/2) - J_1(\alpha^-\alpha^+, 1/k, 3/2)\right] \\
&+ \frac{\alpha^-}{\pi^{1/2}k} \int_{-1/2}^{1/2} u(s) J_0(\alpha^-\alpha^+, 1/k, 1+s)\,\mathrm{d}s \\
&+ \frac{\alpha^-\alpha^+}{\pi^{1/2}k} \int_{-1/2}^{1/2} u(s) J_0(\alpha^-\alpha^+, 1/k, 2-s)\,\mathrm{d}s \\
&- \frac{\alpha^+}{\pi^{1/2}k} \int_{-1/2}^{1/2} u(s) J_0(\alpha^-\alpha^+, 1/k, 1-s)\,\mathrm{d}s \\
&- \frac{\alpha^-\alpha^+}{\pi^{1/2}k} \int_{-1/2}^{1/2} u(s) J_0(\alpha^-\alpha^+, 1/k, 2+s)\,\mathrm{d}s. \qquad (71)
\end{aligned}
$$

CHAPTER 3

HIGH PRECISION SOLUTIONS TO THE FREDHOLM EQUATIONS OF THE SECOND KIND

In this chapter, we first use the Chebyshev collocation method to solve the Fredholm equation for the steady Couette flow with purely diffusive boundary condition. This method utilizes high order Chebyshev expansion to approximate the solution to the integral equation. It outperforms the Nyström method in handling the weakly singular kernel and the boundary singularity of the solution by modifying the expansion coefficients near the boundary. We list the numerical solution at sample positions, discuss the rate of convergence, and provide shear stress and half channel mass flow rate with high precision. The velocity obtained from the Chebyshev collocation method has least 11 digits of precision when the Knudsen number is as low as 0.003 and has 13 digits of precision when the Knudsen number is higher. However, this method needs to evaluate highly oscillatory integrals due to the in high order terms in the Chebyshev expansion of the solution, which is time consuming. Jiang and Luo [38] propose a better method free from evaluating oscillatory integrals. Their method is the singular region adaptively refined chunk based collocation method, which uses nonuniform subintervals to mitigate the influence of the boundary singularity. On each subinterval, the solution is approximated by a low order spectral polynomial expansion. We modify their chunk based collocation method by replacing their process of approximating the weakly singular kernel with our own easier operation and apply the modified method to solve the same Fredholm equation as we did by using the Chebyshev collocation method once again. We will analyze the rate of convergence of the method and give quantitative shear stress and half channel mass flow rate as well to compare with the counterparts of the Chebyshev collocation method. We further apply this method to solve the Fredholm equation for the steady Couette flow with arbitrary accommodation ratio Maxwell boundary condition. As a side product, we will use the same method to solve the Fredholm equation for the Poiseuille flow and the Kramers problem with an arbitrary accommodation ratio in the Maxwell boundary condition.

3.1 SOLVING INTEGRAL EQUATION FOR THE COUETTE FLOW PROBLEM WITH CHEBYSHEV COLLOCATION METHOD

In this section, we solve the steady Couette flow problem with purely diffusive boundary condition and Knudsen number k by using the Chebyshev collocation method. The corresponding equation to solve is a simplified version of equation (30) with $\tau = 0$ and $\alpha^{\pm} = 0$:

$$u(y) - \frac{1}{\pi^{1/2}k}\int_{-1/2}^{1/2} I_{-1}\left(\frac{|y-s|}{k}\right) u(s)\,\mathrm{d}s = \frac{1}{2\pi^{1/2}}\left[I_0\left(\frac{1/2-y}{k}\right) - I_0\left(\frac{y+1/2}{k}\right)\right]. \tag{72}$$

Solving equation (72) requires evaluating Abramowitz functions of order -1 and order 0 precisely. By using Macleod's [1] method of Chebyshev expansion, we are able to compute Abramowitz functions of order $0, 1$ and 2 with 20 decimal digits of precision. Meanwhile, the accurate value of the Abramowitz function of order -1 can be derived from those of order 0 and order 2. The details of the properties of the Abramowitz functions, the results of Macloed's method and our approximation for Abramowitz function of order -1 are given in Appendix A. From the properties of Abramowitz function of order -1, one knows the kernel of the integral operator has a logarithmic singularity along the diagonal $y = s$. This singularity can be mitigated by the singularity deduction technique [6] and equation (72) is converted to

$$G_0(y,k)u(y) - \frac{1}{k}\int_{-1/2}^{1/2} I_{-1}\left(\frac{|y-s|}{k}\right)[u(s)-u(y)]\,\mathrm{d}s = \frac{1}{2}F_0(y,k) \tag{73}$$

where

$$G_n(y,k) = I_n\left(\frac{1/2-y}{k}\right) + I_n\left(\frac{1/2+y}{k}\right),$$
$$F_n(y,k) = I_n\left(\frac{1/2-y}{k}\right) - I_n\left(\frac{1/2+y}{k}\right),$$

Since the velocity $u(y)$ is antisymmetric about the channel center line $y = 0$, we expand it in terms of the odd-order Chebyshev polynomial T_n with $n = 2j-1$,

$$u_N(y) = \sum_{j=1}^{N} c_n T_n(2y), \quad n = 2j-1. \tag{74}$$

Then equation (73) becomes a system of equations for the coefficients $\{c_n | n = 2j-1, 1 \le j \le N\}$,

$$\sum_{j=1}^{N} c_n A_n(y) = F_0(y,k)/2, \tag{75}$$

where

$$A_n(y) = G_0(y,k)T_n(2y) - \frac{1}{k}\int_{-1/2}^{1/2} I_{-1}\left(\frac{|y-s|}{k}\right)[T_n(2s) - T_n(2y)]\,\mathrm{d}s.$$

Equation (75) can be solve by a collocation method or a Galerkin method. We choose a collocation method for its computational efficiency. Choosing N collocation points $\{y_m | m = 2i-1, 1 \le i \le N\}$ and plugging in Equation (75), we have a linear system for $\{c_n\}$

$$\boldsymbol{A}\cdot\boldsymbol{c} = \boldsymbol{b}, \tag{76}$$

where $\boldsymbol{A}$ is a $N \times N$ matrix with entries $A_{mn} = A_n(y_m)$, $\boldsymbol{b}$ and $\boldsymbol{c}$ are N-tuple column vectors with entries $b_m = F_0(y_m,k)/2$ and c_n, respectively, where $m = 2i-1, n = 2j-1, 1 \le i,j \le N$.

If the solution to Equation (73) is analytic, the Chebyshev-Gauss collocation points or the Chebyshev-Gauss-Lobatto collocation points can be used to achieve exponential rate of convergence. However, we can show (in Appendix B) that the velocity derivative $u'(y)$ blows up at the boundary, *i.e.*, $\lim_{y\to\pm 1/2} u'(y) \to \pm\infty$. This means the spectral collocation method can only provide an at most polynomial rate of convergence. Moreover, the Chebyshev-Gauss collocation points which do not include endpoints outperforms the Chebyshev-Gauss-Lobatto points which includes endpoints in this problem, since if one adopts the latter collocation points the endpoint $y = \pm 1/2$ singularity of the solution will pollute the whole domain. Hence, we choose the Chebyshev Gauss collocation points. The number of collocation points determines the number of linearly independent functions in the expansion basis. In Equation (74), the expansion consists of N linearly independent odd Chebyshev functions. So, we need N collocation points to correspond to the N odd Chebyshev functions. The $(2N)^{th}$ order Chebyshev collocation point set is $\{x_i | 0 \le i \le 2N-1\}$, where $x_i = \cos\left(\frac{2i+1}{4N}\pi\right)$. The set $\{x_i\}$ can be divided into two subsets, the odd collocation point subset and the even collocation point subset according to whether i is an odd number or an even number. Since the collocation points should be consistent with expansion functions, we actually begin with the odd collocation point subset $\{x_m | m = 2i-1, 1 \le i \le N\}$ and scale it to the interval $[-1/2, 1/2]$. Hence the first collocation point set we use is

$$P_1 = \{y_m \,|\, y_m = \frac{1}{2}\cos\theta_m,\ \theta_m = \frac{(2m+1)\pi}{4N},\ m = 2i-1,\ 1 \le i \le N\}. \tag{77}$$

With the collocation points P_1, we observe the velocity $u_N(y)$ is more accurate in the interval $[y_{2N-1}, -y_{2N-1}] \subset [-1/2, 1/2]$ than in the sets $[-1/2, y_{2N-1}) \cup (-y_{2N-1}, 1/2]$.

More specifically, through numerical experiment, the rate of convergence of $u_N(y)$ on $[y_{2N-1}, -y_{2N-1}]$ is two times that on $[-1/2, y_{2N-1}) \cup (-y_{2N-1}, 1/2]$. To overcome this deficiency, we include one endpoint $y = 1/2$ in the first collocation point set. We name the augmented set of collocation points the second collocation point set,

$$P_2 = \{y_0 | y_0 = 1/2\} \cup \{y_m | y_m = \frac{1}{2}\cos\theta_m,\ \theta_m = \frac{(2m+1)\pi}{4N},\ m = 2i-1,\ 1 \le i \le N\}. \tag{78}$$

With the collocation points P_2, the velocity $u(y)$ is expanded in $N+1$ terms of odd–order Chebyshev polynomials

$$\tilde{u}_{N+1}(y) = \sum_{j=1}^{N+1} \tilde{c}_n T_n(2y), \quad n = 2j-1. \tag{79}$$

The derived linear system is

$$\tilde{A} \cdot \tilde{c} = \tilde{b} \tag{80}$$

where $\tilde{A}$ is a $(N+1) \times (N+1)$ with A as its submatrix, *i.e.*,

$$\tilde{A} = \begin{pmatrix} \tilde{A}_{0,1} & \tilde{A}_{0,3} & \cdots & \tilde{A}_{0,2N+1} \\ \tilde{A}_{1,1} & & & \\ \vdots & & A & \\ \tilde{A}_{2N-1,1} & & & \end{pmatrix} = \begin{pmatrix} \tilde{A}_{0,1} & \tilde{A}_{0,3} & \cdots & \tilde{A}_{0,2N+1} \\ \tilde{A}_{1,1} & A_{1,1} & \cdots & A_{1,2N-1} \\ \vdots & \vdots & \ddots & \vdots \\ \tilde{A}_{2N-1,1} & A_{2N-1,1} & \cdots & A_{2N-1,2N-1} \end{pmatrix},$$

$\tilde{b}$ and $\tilde{c}$ are $(N+1)$-tuple column vectors with entries $\tilde{b}_m = F_0(y_m, k)/2$ and $\tilde{c}_n$, respectively, where $m = 0$ when $i = 0$ and $m = 2i-1$ when $1 \le i \le N$ and $n = 2j-1, 1 \le j \le N+1$.

In the numerical experiment, we observe the accuracy of the velocity on the sets $[-1/2, y_{2N-1}) \cup (-y_{2N-1}, 1/2]$ is enhanced with the new approximation $\tilde{u}_{N+1}(y)$. Numerical experiment shows the rate of convergence and accuracy on $[-1/2, y_{2N-1}) \cup (-y_{2N-1}, 1/2]$ by using the collocation points P_2 is approximately the same as the rate of convergence and accuracy on $[y_{2N-1}, -y_{2N-1}]$ by using the collocation points P_1. However, with the collocation points P_2, the accuracy of the velocity in the interior deteriorates. Due to the above discovery, we use the first collocation point set P_1 for $[y_{2N-1}, -y_{2N-1}]$ and the second collocation point set P_2 for $[-1/2, y_{2N-1}) \cup (-y_{2N-1}, 1/2]$ to obtain uniform accuracy of $u(y)$ on the entire interval $[-1/2, 1/2]$. On balance, our N^{th} order approximation of $u(y)$ is:

$$\bar{u}_N(y) = \begin{cases} \sum_{j=1}^{N} c_n T_n(2y), & n = 2j-1, \quad y \in [y_{2N-1}, -y_{2N-1}] \\ \sum_{j=1}^{N+1} \tilde{c}_n T_n(2y), & n = 2j-1, \quad y \in [-1/2, y_{2N-1}) \cup (-y_{2N-1}, 1/2] \end{cases} \tag{81}$$

where $y_{2N-1} = -\frac{1}{2}\cos\frac{\pi}{4N}$. The coefficients $\boldsymbol{c}$ and $\tilde{\boldsymbol{c}}$ are obtained from equation (76) and equation (80), respectively.

To solve equation (76) and equation (80), we need to compute the coefficient matrix $\tilde{A}$ and the right hand side column vector $\tilde{\boldsymbol{b}}$. The key is to evaluate the entries $\tilde{A}_{mn}$ accurately. We have

$$\tilde{A}_{mn} = G_0(y_m, k)T_n(2y_m) - \frac{1}{k}\int_{-1/2}^{1/2} I_{-1}\left(\frac{|y_m - s|}{k}\right)[T_n(2s) - T_n(2y_m)]\,\mathrm{d}s.$$

We denote the integral in $\tilde{A}_{mn}$ by $\Psi_{ij}(k)$, *i.e.*,

$$\begin{aligned}\Psi_{ij}(k) &= \int_{-1/2}^{1/2} I_{-1}\left(\frac{|y_m - s|}{k}\right)[T_n(2s) - T_n(2y_m)]\,\mathrm{d}s \\ &= \begin{cases} \int_{-1/2}^{1/2} I_{-1}\left(\frac{|1/2-s|}{k}\right)[T_{2j-1}(2s) - 1]\,\mathrm{d}s, & i = 0, \\ \int_{-1/2}^{1/2} I_{-1}\left(\frac{|y_{2i-1}-s|}{k}\right)[T_{2j-1}(2s) - T_{2j-1}(2y_{2i-1})]\,\mathrm{d}s, & 1 \le i \le N. \end{cases}\end{aligned}$$

Let

$$\theta_i = \begin{cases} 1, & i = 0, \\ \cos\theta_i, & i = 1, 2, \cdots, N, \end{cases}$$

$\Psi_{ij}(k)$ can be written as

$$\Psi_{ij}(k) = \int_0^{\pi} K_{ij}(\theta, k)\,\mathrm{d}\theta \tag{82}$$

with

$$K_{ij}(\theta, k) = I_{-1}\left(\frac{|\cos\theta - \cos\theta_i|}{2k}\right)[\cos(2j+1)\theta - \cos(2j+1)\theta_i]\sin\theta. \tag{83}$$

The integrand $K_{ij}(\theta, k)$ is highly oscillatory when $j \gg 1$ and has a deducted singularity at θ_i, since I_{-1} has a $\ln x$ singularity at $x = 0$. To address the numerical difficulties caused by oscillatory, we divide the interval of integration, $[0, \pi]$ into $2(j+1)$ subintervals for $1 \le j \le N$, such that two adjacent subinterval, excluding two subintervals at two ends, cover exactly one period of $\cos(2j+1)\theta$. So, the integrand in the subintervals are slow varying. Also the singularity of I_{-1} occurs at $\theta = \theta_i$, which is an end-point of two subintervals. Since the abscissae of the quadrature we use do not include the end points, this mitigated the numerical difficulty caused by the singularity.

The interval $[0, \pi]$ has to be divided in two ways depending on both i and j. Denote

l^* and r as the integer and remainder of $(4i-1)(2j+1)/(4N)$, *i.e.*,

$$l^* = \left\lfloor \frac{(4i-1)(2j+1)}{4N} \right\rfloor,$$
$$r = \frac{(4i-1)(2j+1)}{4N} - l^*,$$

where $i = 1, 2, \cdots, N$ and $j = 0, 1, \cdots, N$. We further introduce the following notations:

$$\bar{r} = 1 - r,$$
$$\varphi_j = \frac{\pi}{2j+1}.$$

For even and odd l^*, the integration interval $[0, \pi]$ is divided into $2(j+1)$ subintervals as follows:

$$[0,\pi] = [0, r\varphi_j] \cup \cup_{l=0}^{j-1} \{[l_1 - \bar{r}, l_1 + \bar{r}] \cup [l_2 - r, l_2 + r]\}\varphi_j \cup [\pi - \bar{r}\varphi_j, \pi],\ l^* \text{ even},$$
$$[0,\pi] = [0, \bar{r}\varphi_j] \cup \cup_{l=0}^{j-1} \{[l_1 - r, l_1 + r] \cup [l_2 - \bar{r}, l_2 + \bar{r}]\}\varphi_j \cup [\pi - r\varphi_j, \pi],\ l^* \text{ odd},$$

where $l_1 = 2l + 1$ and $l_2 = 2(l+1)$. The interval $[l_1 - \bar{r}, l_1 + \bar{r}]\varphi$ has the endpoints $(2l + 1 \pm \bar{r})\varphi_j$. The interval $[l_2 - r, l_2 + r]\varphi_j$ has the endpoints $(2l + 2 \pm r)\varphi_j$. Clearly, in the above divisions any two adjacent subintervals, excluding the two subintervals at the two ends which cover the length of $2\varphi_j = 2\pi/(2j+1)$, which is exactly one period of $\cos(2j+1)\theta$ for $\theta \in [0, 2\pi]$.

For even l^*, the integrals on the subintervals are:

$$\begin{aligned}
&\int_0^{r\varphi_j} K_{ij}(\theta, k)\, \mathrm{d}\theta \\
=& r\varphi_j \int_{-1}^{1} I_{-1}\left(\frac{1}{k}\left|\sin\left[\frac{(1+s)r\varphi_j}{4} + \frac{\theta_i}{2}\right]\sin\left[\frac{(1+s)r\varphi_j}{4} - \frac{\theta_i}{2}\right]\right|\right) \\
&\sin\frac{(3+s)r\pi}{4}\sin\frac{(1-s)r\pi}{4}\sin\frac{(1+s)r\varphi_j}{2}\,\mathrm{d}s, \qquad (84) \\
&\int_{(l_1-\bar{r})\varphi_j}^{(l_1+\bar{r})\varphi_j} K_{ij}(\theta, k)\, \mathrm{d}\theta \\
=& -2\bar{r}\varphi_j \int_{-1}^{1} I_{-1}\left(\frac{1}{k}\left|\sin\left[\frac{(l_1+\bar{r}s)\varphi_j}{2} + \frac{\theta_i}{2}\right]\sin\left[\frac{(l_1+\bar{r}s)\varphi_j}{2} - \frac{\theta_i}{2}\right]\right|\right) \\
&\sin\frac{(1+s)\bar{r}\pi}{2}\sin\frac{(1-s)\bar{r}\pi}{2}\sin[(l_1+\bar{r}s)\varphi_j]\,\mathrm{d}s, \qquad (85)
\end{aligned}$$

$$\int_{(l_2-r)\varphi_j}^{(l_2+r)\varphi_j} K_{ij}(\theta,k)\,\mathrm{d}\theta$$

$$= 2r\varphi_j \int_{-1}^{1} I_{-1}\left(\frac{1}{k}\left|\sin\left[\frac{(l_2+rs)\varphi_j}{2}+\frac{\theta_i}{2}\right]\sin\left[\frac{(l_2+rs)\varphi_j}{2}-\frac{\theta_i}{2}\right]\right|\right)$$
$$\sin\frac{(1+s)r\pi}{2}\sin\frac{(1-s)r\pi}{2}\sin[(l_2+rs)\varphi_j]\,\mathrm{d}s, \tag{86}$$

$$\int_{\pi-\bar{r}\varphi_j}^{\pi} K_{ij}(\theta,k)\,\mathrm{d}\theta$$

$$= -\bar{r}\varphi_j \int_{-1}^{1} I_{-1}\left(\frac{1}{k}\left|\cos\left[\frac{(1-s)\bar{r}\varphi_j}{4}+\frac{\theta_i}{2}\right]\cos\left[\frac{(1-s)\bar{r}\varphi_j}{4}-\frac{\theta_i}{2}\right]\right|\right)$$
$$\sin\frac{(1+s)\bar{r}\pi}{4}\sin\frac{(3-s)\bar{r}\pi}{4}\sin\frac{(1-s)\bar{r}\varphi_j}{2}\,\mathrm{d}s. \tag{87}$$

Similarly, for odd l^*, the integrals on the subintervals are:

$$\int_{0}^{\bar{r}\varphi_j} K_{ij}(\theta,k)\,\mathrm{d}\theta$$

$$= \bar{r}\varphi_j \int_{-1}^{1} I_{-1}\left(\frac{1}{k}\left|\sin\left[\frac{(1+s)\bar{r}\varphi_j}{4}+\frac{\theta_i}{2}\right]\sin\left[\frac{(1+s)\bar{r}\varphi_j}{4}-\frac{\theta_i}{2}\right]\right|\right)$$
$$\sin\frac{(3+s)\bar{r}\pi}{4}\sin\frac{(1-s)\bar{r}\pi}{4}\sin\frac{(1+s)\bar{r}\varphi_j}{2}\,\mathrm{d}s, \tag{88}$$

$$\int_{(l_1-r)\varphi_j}^{(l_1+r)\varphi_j} K_{ij}(\theta,k)\,\mathrm{d}\theta$$

$$= -2r\varphi_j \int_{-1}^{1} I_{-1}\left(\frac{1}{k}\left|\sin\left[\frac{(l_1+rs)\varphi_j}{2}+\frac{\theta_i}{2}\right]\sin\left[\frac{(l_1+rs)\varphi_j}{2}-\frac{\theta_i}{2}\right]\right|\right)$$
$$\sin\frac{(1+s)r\pi}{2}\sin\frac{(1-s)r\pi}{2}\sin[(l_1+rs)\varphi_j]\,\mathrm{d}s, \tag{89}$$

$$\int_{(l_2-\bar{r})\varphi_j}^{(l_2+\bar{r})\varphi_j} K_{ij}(\theta,k)\,\mathrm{d}\theta$$

$$= 2\bar{r}\varphi_j \int_{-1}^{1} I_{-1}\left(\frac{1}{k}\left|\sin\left[\frac{(l_2+\bar{r}s)\varphi_j}{2}+\frac{\theta_i}{2}\right]\sin\left[\frac{(l_2+\bar{r}s)\varphi_j}{2}-\frac{\theta_i}{2}\right]\right|\right)$$
$$\sin\frac{(1+s)\bar{r}\pi}{2}\sin\frac{(1-s)\bar{r}\pi}{2}\sin[(l_2+\bar{r}s)\varphi_j]\,\mathrm{d}s, \tag{90}$$

$$\int_{\pi-r\varphi_j}^{\pi} K_{ij}(\theta,k)\,\mathrm{d}\theta$$

$$= -r\varphi_j \int_{-1}^{1} I_{-1}\left(\frac{1}{k}\left|\cos\left[\frac{(1-s)r\varphi_j}{4}+\frac{\theta_i}{2}\right]\cos\left[\frac{(1-s)r\varphi_j}{4}-\frac{\theta_i}{2}\right]\right|\right)$$
$$\sin\frac{(1+s)r\pi}{4}\sin\frac{(3-s)r\pi}{4}\sin\frac{(1-s)r\varphi_j}{2}\,\mathrm{d}s. \tag{91}$$

The integrals given by equations (84)-(87) and equations (88)-(91) are evaluated by using adaptive quadrature with a specific absolute tolerance $\epsilon = 10^{-15}$. In particular,

as the kernel of the adaptive quadrature, we use the generalized Gaussian quadrature [42] for products of a polynomial and logarithmic function over the interval $[0, 1]$, *i.e.*, $\int_0^1 f(x)\,\mathrm{d}x = \sum_{i=1}^{40} w_i f(x_i)$. The nodes and weights are listed in Table 1.

TABLE 1: Abscissae and Weights of 40 Order Generalized Gauss quadrature for products of a polynomial and logarithmic function over $[0, 1]$

i	Abscissae x_i	Weights w_i	i	Abscissae x_i	Weights w_i
1	0.237684143879143D-5	0.908716648479552D-5	21	0.274657164616264D0	0.403530031221956D-1
2	0.357941198659536D-4	0.708096570276615D-4	22	0.316369047605705D0	0.430195644057483D-1
3	0.178564191524854D-3	0.236107924249676D-3	23	0.360582741027397D0	0.453456033756603D-1
4	0.558572352357276D-3	0.552941324982586D-3	24	0.406925414636825D0	0.472673103983455D-1
5	0.134949361265519D-2	0.106471907669186D-2	25	0.454963103785795D0	0.487264791953468D-1
6	0.276558618788719D-2	0.180898827559081D-2	26	0.504207051427098D0	0.496719629360194D-1
7	0.505522381417743D-2	0.281624906827513D-2	27	0.554121436898801D0	0.500609861199254D-1
8	0.849332816182978D-2	0.410894500639753D-2	28	0.604132331112845D0	0.498602805316812D-1
9	0.133728905726761D-1	0.570065525023859D-2	29	0.653637688015750D0	0.490470175905769D-1
10	0.199957958342846D-1	0.759550947534350D-2	30	0.702018156811904D0	0.476095141198307D-1
11	0.286631788855304D-1	0.978784093517871D-2	31	0.748648479051785D0	0.455476938170290D-1
12	0.396655579573064D-1	0.122620873954733D-1	32	0.792909219783803D0	0.428732923992053D-1
13	0.532729943956627D-1	0.149929436836712D-1	33	0.834198572923854D0	0.396098004030230D-1
14	0.697255301257928D-1	0.179457635281876D-1	34	0.871943978073835D0	0.357921438452470D-1
15	0.892241483693333D-1	0.210772023407832D-1	35	0.905613289425416D0	0.314661094009314D-1
16	0.111922491943615D0	0.243360867646222D-1	36	0.934725247515507D0	0.266875279291532D-1
17	0.137919556510407D0	0.276644913094057D-1	37	0.958859023272801D0	0.215212411445673D-1
18	0.167253553899293D0	0.309989973545750D-1	38	0.977662642064842D0	0.160399123812805D-1
19	0.199897113629064D0	0.342721053423017D-1	39	0.990860246620079D0	0.103230260805101D-1
20	0.235753959625130D0	0.374137672104434D-1	40	0.998259972471242D0	0.446223271379884D-2

Evaluating $\tilde{A}$ near double precision needs $N = 2047$. After evaluating $\tilde{A}$ and $\tilde{b}$, one can solve equation (76) and equation (80). Since the size of the coefficient matrices are moderate, at most 2048×2048 in the present work, we use direct method to solve the two linear system of equations. In order to achieve at least double precision accuracy, we implement the algorithm for the LU decomposition with pivoting and the forward elimination backward substitution by using C++ with arbitrary precision package. Balancing the effectiveness and efficiency we use 40 digits of decimal precision.

After obtaining $\tilde{c}$, in order to reduce the risk of augmenting round off error, when computing the Chebyshev expansion at position y, we use Clenshaw's algorithm with Reinsch's modification [47] to evaluate equation (81).

For the first branch of equation (81), we have:

when $-\frac{1}{2}\cos\frac{\pi}{4N} \leq y < -\delta$,

1) $b_{2N}(y) = d_{2N}(y) = 0$
2) for j from N to 1
   $d_{2j-1}(y) = c_{2j-1} + 2(2y+1)b_{2j}(y) - d_{2j}(y)$
   $b_{2j-1}(y) = d_{2j-1}(y) - b_{2j}(y)$
   $d_{2j-2}(y) = 2(2y+1)b_{2j-1}(y) - d_{2j-1}(y)$
   $b_{2j-2}(y) = d_{2j-2}(y) - b_{2j-1}(y)$
3) $\bar{u}_N(y) = (d_0(y) - d_1(y))/2$

when $|y| \leq \delta$,

1) $b_{2N}(y) = b_{2N+1}(y) = 0$
2) for j from N to 1
   $b_{2j-1}(y) = c_{2j-1} + 4yb_{2j}(y) - b_{2j+1}(y)$
   $b_{2j-2}(y) = 4yb_{2j-1}(y) - b_{2j}(y)$
3) $\bar{u}_N(y) = (b_0(y) - b_2(y))/2$

when $\delta < y \leq \frac{1}{2}\cos\frac{\pi}{4N}$,

1) $b_{2N}(y) = d_{2N}(y) = 0$
2) for j from N to 1
   $d_{2j-1}(y) = c_{2j-1} + 2(2y-1)b_{2j}(y) - d_{2j}(y)$
   $b_{2j-1}(y) = d_{2j-1}(y) + b_{2j}(y)$
   $d_{2j-2}(y) = 2(2y-1)b_{2j-1}(y) - d_{2j-1}(y)$
   $b_{2j-2}(y) = d_{2j-2}(y) + b_{2j-1}(y)$
3) $\bar{u}_N(y) = (d_0(y) + d_1(y))/2$

For the second branch of Equation (81), we have when $-\frac{1}{2} \leq y < -\frac{1}{2}\cos\frac{\pi}{4N}$,

1) $b_{2N+2}(y) = d_{2N+2}(y) = 0$

2) for j from N+1 to 1

$$d_{2j-1}(y) = \tilde{c}_{2j-1} + 2(2y+1)b_{2j}(y) - d_{2j}(y)$$

$$b_{2j-1}(y) = d_{2j-1}(y) - b_{2j}(y)$$

$$d_{2j-2}(y) = 2(2y+1)b_{2j-1}(y) - d_{2j-1}(y)$$

$$b_{2j-2}(y) = d_{2j-2}(y) - b_{2j-1}(y)$$

3) $\bar{u}_N(y) = (d_0(y) - d_1(y))/2$

when $\frac{1}{2}\cos\frac{\pi}{4N} < y \leq \frac{1}{2}$,

1) $b_{2N+2}(y) = d_{2N+2}(y) = 0$

2) for j from N+1 to 1

$$d_{2j-1}(y) = \tilde{c}_{2j-1} + 2(2y-1)b_{2j}(y) - d_{2j}(y)$$

$$b_{2j-1}(y) = d_{2j-1}(y) + b_{2j}(y)$$

$$d_{2j-2}(y) = 2(2y-1)b_{2j-1}(y) - d_{2j-1}(y)$$

$$b_{2j-2}(y) = d_{2j-2}(y) + b_{2j-1}(y)$$

3) $\bar{u}_N(y) = (d_0(y) + d_1(y))/2$

The parameter δ determines the thickness of the boundary in which the Reinsch's modification should be adopted. In this study, we choose $\delta = 0.3$.

Numerically, we solve equation (72) for the Couette flow with a wide range of Knudsen number k, *i.e.*, $0.003 \leq k \leq 10.0$, which cover four decimal digits. We vary the order of equation (80), namely $N+1 = 2^n$ with $4 \leq n \leq 11$, *i.e.*, $15 \leq N \leq 2047$, to ensure the convergence of the results. Table 2 and Table 3 give the value of $\bar{u}_N(y)$ at $y = 0.1, 0.2, 0.3, 0.4$ and 0.5 for various values of k and N. At channel center $y = 0$, $\bar{u}_N(0) = 0$ for all values of k. When $N = 2047$, the results of $\bar{u}_N(y)$ in Table 2 and Table 3 are accurate for at least 11 significant digits. From equation (81), the derivative of velocity at the channel center, $u'(0)$, is approximated by

$$\bar{u}'_N(0) = 2\sum_{j=1}^{N} c_{2j-1}(-1)^{j+1}$$

Table 4 gives the boundary velocity $u(1/2)$ and the derivative of the channel center velocity for various values of k with $N = 2047$.

TABLE 2: The values of the velocity $\bar{u}_N(y)$ of the Couette flow at $y = 0.1, 0.2$ and 0.3, for $0.003 \leq k \leq 10.0$ and $256 \leq N+1 \leq 2048$

y	0.1	0.2	0.3
$N+1$		$k = 0.003$	
256	$9.93939802817675 \cdot 10^{-2}$	$1.98787960563724 \cdot 10^{-1}$	$2.98181940854607 \cdot 10^{-1}$
512	$9.93939801575752 \cdot 10^{-2}$	$1.98787960322574 \cdot 10^{-1}$	$2.98181940467945 \cdot 10^{-1}$
1024	$9.93939801487210 \cdot 10^{-2}$	$1.98787960304567 \cdot 10^{-1}$	$2.98181940443658 \cdot 10^{-1}$
2048	$9.93939801484713 \cdot 10^{-2}$	$1.98787960303896 \cdot 10^{-1}$	$2.98181940442773 \cdot 10^{-1}$
$N+1$		$k = 0.01$	
256	$9.80081002587778 \cdot 10^{-2}$	$1.96016201408749 \cdot 10^{-1}$	$2.94024342763042 \cdot 10^{-1}$
512	$9.80081002254805 \cdot 10^{-2}$	$1.96016201348442 \cdot 10^{-1}$	$2.94024342646767 \cdot 10^{-1}$
1024	$9.80081002231047 \cdot 10^{-2}$	$1.96016201342903 \cdot 10^{-1}$	$2.94024342640619 \cdot 10^{-1}$
2048	$9.80081002229763 \cdot 10^{-2}$	$1.96016201342550 \cdot 10^{-1}$	$2.94024342640308 \cdot 10^{-1}$
$N+1$		$k = 0.03$	
256	$9.42551023448203 \cdot 10^{-2}$	$1.88515596522206 \cdot 10^{-1}$	$2.82808471818603 \cdot 10^{-1}$
512	$9.42551023372640 \cdot 10^{-2}$	$1.88515596512985 \cdot 10^{-1}$	$2.82808471779802 \cdot 10^{-1}$
1024	$9.42551023364727 \cdot 10^{-2}$	$1.88515596510692 \cdot 10^{-1}$	$2.82808471778404 \cdot 10^{-1}$
2048	$9.42551023363842 \cdot 10^{-2}$	$1.88515596510505 \cdot 10^{-1}$	$2.82808471778333 \cdot 10^{-1}$
$N+1$		$k = 0.1$	
256	$8.35610402937810 \cdot 10^{-2}$	$1.67349050225909 \cdot 10^{-1}$	$2.51810807114286 \cdot 10^{-1}$
512	$8.35610402944326 \cdot 10^{-2}$	$1.67349050232477 \cdot 10^{-1}$	$2.51810807101969 \cdot 10^{-1}$
1024	$8.35610402942453 \cdot 10^{-2}$	$1.67349050231428 \cdot 10^{-1}$	$2.51810807102181 \cdot 10^{-1}$
2048	$8.35610402942564 \cdot 10^{-2}$	$1.67349050231355 \cdot 10^{-1}$	$2.51810807102247 \cdot 10^{-1}$
$N+1$		$k = 0.3$	
256	$6.64543006930748 \cdot 10^{-2}$	$1.33570950940784 \cdot 10^{-1}$	$2.02360723344343 \cdot 10^{-1}$
512	$6.64543006949853 \cdot 10^{-2}$	$1.33570950948607 \cdot 10^{-1}$	$2.02360723339400 \cdot 10^{-1}$
1024	$6.64543006949260 \cdot 10^{-2}$	$1.33570950947971 \cdot 10^{-1}$	$2.02360723339812 \cdot 10^{-1}$
2048	$6.64543006949395 \cdot 10^{-2}$	$1.33570950947927 \cdot 10^{-1}$	$2.02360723339879 \cdot 10^{-1}$
$N+1$		$k = 1.0$	
256	$4.45319411508086 \cdot 10^{-2}$	$8.97629000550284 \cdot 10^{-2}$	$1.36669180693308 \cdot 10^{-1}$
512	$4.45319411521308 \cdot 10^{-2}$	$8.97629000599260 \cdot 10^{-2}$	$1.36669180691337 \cdot 10^{-1}$
1024	$4.45319411521130 \cdot 10^{-2}$	$8.97629000596012 \cdot 10^{-2}$	$1.36669180691618 \cdot 10^{-1}$
2048	$4.45319411521217 \cdot 10^{-2}$	$8.97629000595787 \cdot 10^{-2}$	$1.36669180691658 \cdot 10^{-1}$
$N+1$		$k = 2.0$	
256	$3.28317510127771 \cdot 10^{-2}$	$6.62008086650869 \cdot 10^{-2}$	$1.00839934023394 \cdot 10^{-1}$
512	$3.28317510136486 \cdot 10^{-2}$	$6.62008086682613 \cdot 10^{-2}$	$1.00839934022253 \cdot 10^{-1}$
1024	$3.28317510136395 \cdot 10^{-2}$	$6.62008086680595 \cdot 10^{-2}$	$1.00839934022438 \cdot 10^{-1}$
2048	$3.28317510136450 \cdot 10^{-2}$	$6.62008086680455 \cdot 10^{-2}$	$1.00839934022465 \cdot 10^{-1}$
$N+1$		$k = 3.0$	
256	$2.67884225065252 \cdot 10^{-2}$	$5.40076130212065 \cdot 10^{-2}$	$8.22393190026562 \cdot 10^{-2}$
512	$2.67884225071785 \cdot 10^{-2}$	$5.40076130235737 \cdot 10^{-2}$	$8.22393190018391 \cdot 10^{-2}$
1024	$2.67884225071721 \cdot 10^{-2}$	$5.40076130234255 \cdot 10^{-2}$	$8.22393190019777 \cdot 10^{-2}$
2048	$2.67884225071763 \cdot 10^{-2}$	$5.40076130234154 \cdot 10^{-2}$	$8.22393190019973 \cdot 10^{-2}$
$N+1$		$k = 5.0$	
256	$2.02181035056891 \cdot 10^{-2}$	$4.07451054936705 \cdot 10^{-2}$	$6.19942703911553 \cdot 10^{-2}$
512	$2.02181035061279 \cdot 10^{-2}$	$4.07451054952536 \cdot 10^{-2}$	$6.19942703906268 \cdot 10^{-2}$
1024	$2.02181035061240 \cdot 10^{-2}$	$4.07451054951556 \cdot 10^{-2}$	$6.19942703907201 \cdot 10^{-2}$
2048	$2.02181035061269 \cdot 10^{-2}$	$4.07451054951488 \cdot 10^{-2}$	$6.19942703907331 \cdot 10^{-2}$
$N+1$		$k = 7.0$	
256	$1.65589614002174 \cdot 10^{-2}$	$3.33595222277592 \cdot 10^{-2}$	$5.07233582368858 \cdot 10^{-2}$
512	$1.65589614005492 \cdot 10^{-2}$	$3.33595222289539 \cdot 10^{-2}$	$5.07233582364927 \cdot 10^{-2}$
1024	$1.65589614005463 \cdot 10^{-2}$	$3.33595222288803 \cdot 10^{-2}$	$5.07233582365632 \cdot 10^{-2}$
2048	$1.65589614005484 \cdot 10^{-2}$	$3.33595222288753 \cdot 10^{-2}$	$5.07233582365731 \cdot 10^{-2}$
$N+1$		$k = 10.0$	
256	$1.32484005418904 \cdot 10^{-2}$	$2.66795457529754 \cdot 10^{-2}$	$4.05357403215398 \cdot 10^{-2}$
512	$1.32484005421342 \cdot 10^{-2}$	$2.66795457538518 \cdot 10^{-2}$	$4.05357403212547 \cdot 10^{-2}$
1024	$1.32484005421322 \cdot 10^{-2}$	$2.66795457537980 \cdot 10^{-2}$	$4.05357403213064 \cdot 10^{-2}$
2048	$1.32484005421337 \cdot 10^{-2}$	$2.66795457537942 \cdot 10^{-2}$	$4.05357403213135 \cdot 10^{-2}$

We compute the local relative error of the velocity $u(y)$ at a specific location y and a given value of k:

$$|\delta u_N(y)| = \frac{|\bar{u}_N(y) - u_*(y)|}{|u_*(y)|}$$

where the reference solution $u_*(y)$ is obtained with $N = 2047$. We compute $|\delta u_N(y)|$ at $y = 0.1, 0.2, 0.3, 0.4$ and 0.5 and $0.003 \leq k \leq 10.0$. Figure 1 shows the log-log plots of N-dependence of $|\delta u_N|$ at $y = 0.1$ and $k = 0.01$, $y = 0.2$ and $k = 0.1$, $y = 0.3$

TABLE 3: The values of the velocity $\bar{u}_N(y)$ of the Couette flow at $y = 0.4$ and 0.5, for $0.003 \leq k \leq 10.0$ and $256 \leq N + 1 \leq 2048$

y	0.4	0.5
$N+1$	$k = 0.003$	
256	$3.97575921205698 \cdot 10^{-1}$	$4.97891532817256 \cdot 10^{-1}$
512	$3.97575920708319 \cdot 10^{-1}$	$4.97891535105931 \cdot 10^{-1}$
1024	$3.97575920673503 \cdot 10^{-1}$	$4.97891535267197 \cdot 10^{-1}$
2048	$3.97575920671607 \cdot 10^{-1}$	$4.97891535278427 \cdot 10^{-1}$
$N+1$	$k = 0.01$	
256	$3.92035572153263 \cdot 10^{-1}$	$4.93069779961988 \cdot 10^{-1}$
512	$3.92035572014922 \cdot 10^{-1}$	$4.93069780717902 \cdot 10^{-1}$
1024	$3.92035572003626 \cdot 10^{-1}$	$4.93069780770369 \cdot 10^{-1}$
2048	$3.92035572002762 \cdot 10^{-1}$	$4.93069780773982 \cdot 10^{-1}$
$N+1$	$k = 0.03$	
256	$3.77352560943944 \cdot 10^{-1}$	$4.80005867993200 \cdot 10^{-1}$
512	$3.77352560907856 \cdot 10^{-1}$	$4.80005868257133 \cdot 10^{-1}$
1024	$3.77352560903030 \cdot 10^{-1}$	$4.80005868275276 \cdot 10^{-1}$
2048	$3.77352560902472 \cdot 10^{-1}$	$4.80005868276515 \cdot 10^{-1}$
$N+1$	$k = 0.1$	
256	$3.38368406078662 \cdot 10^{-1}$	$4.41224640891364 \cdot 10^{-1}$
512	$3.38368406075732 \cdot 10^{-1}$	$4.41224640966721 \cdot 10^{-1}$
1024	$3.38368406073280 \cdot 10^{-1}$	$4.41224640971868 \cdot 10^{-1}$
2048	$3.38368406072997 \cdot 10^{-1}$	$4.41224640972217 \cdot 10^{-1}$
$N+1$	$k = 0.3$	
256	$2.75170669357004 \cdot 10^{-1}$	$3.67212569528701 \cdot 10^{-1}$
512	$2.75170669360757 \cdot 10^{-1}$	$3.67212569548601 \cdot 10^{-1}$
1024	$2.75170669359285 \cdot 10^{-1}$	$3.67212569549952 \cdot 10^{-1}$
2048	$2.75170669359094 \cdot 10^{-1}$	$3.6721256955004 \cdot 10^{-1}$
$N+1$	$k = 1.0$	
256	$1.87233642995143 \cdot 10^{-1}$	$2.51861339985755 \cdot 10^{-1}$
512	$1.87233642998431 \cdot 10^{-1}$	$2.51861339989221 \cdot 10^{-1}$
1024	$1.87233642997678 \cdot 10^{-1}$	$2.51861339989455 \cdot 10^{-1}$
2048	$1.87233642997577 \cdot 10^{-1}$	$2.51861339989471 \cdot 10^{-1}$
$N+1$	$k = 2.0$	
256	$1.38179710139242 \cdot 10^{-1}$	$1.85246299372828 \cdot 10^{-1}$
512	$1.38179710141497 \cdot 10^{-1}$	$1.85246299373941 \cdot 10^{-1}$
1024	$1.38179710141030 \cdot 10^{-1}$	$1.85246299374016 \cdot 10^{-1}$
2048	$1.38179710140967 \cdot 10^{-1}$	$1.85246299374021 \cdot 10^{-1}$
$N+1$	$k = 3.0$	
256	$1.12600645437724 \cdot 10^{-1}$	$1.50428244498615 \cdot 10^{-1}$
512	$1.12600645439436 \cdot 10^{-1}$	$1.50428244499167 \cdot 10^{-1}$
1024	$1.12600645439093 \cdot 10^{-1}$	$1.50428244499204 \cdot 10^{-1}$
2048	$1.12600645439046 \cdot 10^{-1}$	$1.50428244499207 \cdot 10^{-1}$
$N+1$	$k = 5.0$	
256	$8.47465578276147 \cdot 10^{-2}$	$1.12635188029221 \cdot 10^{-1}$
512	$8.47465578287766 \cdot 10^{-2}$	$1.12635188029443 \cdot 10^{-1}$
1024	$8.47465578285502 \cdot 10^{-2}$	$1.12635188029458 \cdot 10^{-1}$
2048	$8.47465578285188 \cdot 10^{-2}$	$1.12635188029459 \cdot 10^{-1}$
$N+1$	$k = 7.0$	
256	$6.92533624010780 \cdot 10^{-2}$	$9.17168961350864 \cdot 10^{-2}$
512	$6.92533624019604 \cdot 10^{-2}$	$9.17168961352056 \cdot 10^{-2}$
1024	$6.92533624017904 \cdot 10^{-2}$	$9.17168961352137 \cdot 10^{-2}$
2048	$6.92533624017670 \cdot 10^{-2}$	$9.17168961352143 \cdot 10^{-2}$
$N+1$	$k = 10.0$	
256	$5.52678934659797 \cdot 10^{-2}$	$7.29221129932192 \cdot 10^{-2}$
512	$5.52678934666303 \cdot 10^{-2}$	$7.29221129932804 \cdot 10^{-2}$
1024	$5.52678934665059 \cdot 10^{-2}$	$7.29221129932845 \cdot 10^{-2}$
2048	$5.52678934664887 \cdot 10^{-2}$	$7.29221129932848 \cdot 10^{-2}$

and $k = 1.0$ and $y = 0.4$ and $k = 10.0$. The results indicate that

$$\ln \frac{|\delta u_N(y)|}{|\delta u_M(y)|} \sim -\alpha \ln \frac{N}{M}$$

where $N \neq M < 2047$.

Table 5 shows the dependence of α and its standard deviation $|\Delta\alpha|$ on k. By observation, we discover that the rate of convergence α is independent of the position y and is only dependent on the Knudsen number k. For small value of k, *i.e.*, $k < 1.0$, the

TABLE 4: The Knudsen number k dependence of the velocity $u(1/2)$ at boundary and the channel center velocity derivative $u'(0)$ obtained by the velocity Chebyshev expansion with $N = 2047$

k	$u(1/2)$	$u'(0)$
0.003	$4.97891535278427 \cdot 10^{-1}$	0.993939801103754
0.01	$4.93069780773982 \cdot 10^{-1}$	0.980081001908009
0.03	$4.80005868276515 \cdot 10^{-1}$	0.942545599824700
0.1	$4.41224640972217 \cdot 10^{-1}$	0.835285765647133
0.3	$3.67212569550043 \cdot 10^{-1}$	0.663530077027944
1.0	$2.51861339989471 \cdot 10^{-1}$	0.444228469746625
2.0	$1.85246299374021 \cdot 10^{-1}$	0.327474576937359
3.0	$1.50428244499207 \cdot 10^{-1}$	0.267207005940212
5.0	$1.12635188029459 \cdot 10^{-1}$	0.201694431817770
7.0	$9.17168961352143 \cdot 10^{-2}$	0.165208634795606
10.0	$7.29221129932848 \cdot 10^{-2}$	0.13219579051697

rate of convergence α increases as k rises. After $k \geq 1.0$, α exceeds 4.0 and remains constant. The reason that small values of k converge slightly slower than greater values of k is that the Knudsen layer of the Couette flow attenuates as k becomes increasingly smaller. Thus many more collocation points near the boundary points $y = \pm 1/2$ are needed to resolve the Knudsen layer as the Knudsen number k approaches to 0. To address the k dependence on the thickness of the Knudsen layer, we focus on the source term of equation (73), $\frac{1}{2}F_0(y,k) = \frac{1}{2}\left[I_0\left(\frac{1/2-y}{k}\right) - I_0\left(\frac{1/2+y}{k}\right)\right]$. Near the boundary $y = \pm 1/2$, the property of $u(y)$ is mainly determined by the behavior of the source term. From the asymptotic property of Abramowitz functions $I_n(x)$ in Appendix A, we know $I_0(x)$ is a fast decaying function as x is away from 0. The source term $\frac{1}{2}F_0(y,k)$ maintains the fast decaying property as y is away from $\pm 1/2$. However, when k is small, the fast decaying effect is amplified, resulting in the attenuation of the Knudsen layer of $u(y)$; when k is big, the fast decaying effect is mitigated, resulting in the thickening of the Knudsen layer of $u(y)$.

TABLE 5: The dependence of the rate of convergence for the velocity $\bar{u}_N(y)$ on the Knudsen number k. The rate of convergence α and its standard deviation are computed by using the least-square method.

k	0.003	0.01	0.03	0.1	1.0
$\alpha \pm \Delta\alpha$	3.5559 ± 0.0821	3.7229 ± 0.0586	3.8682 ± 0.0978	3.9660 ± 0.2486	4.1325 ± 0.1567
k	2.0	3.0	5.0	7.0	10.0
$\alpha \pm \Delta\alpha$	4.0949 ± 0.1580	4.0844 ± 0.1668	4.0705 ± 0.1793	4.0709 ± 0.1829	4.0651 ± 0.1881

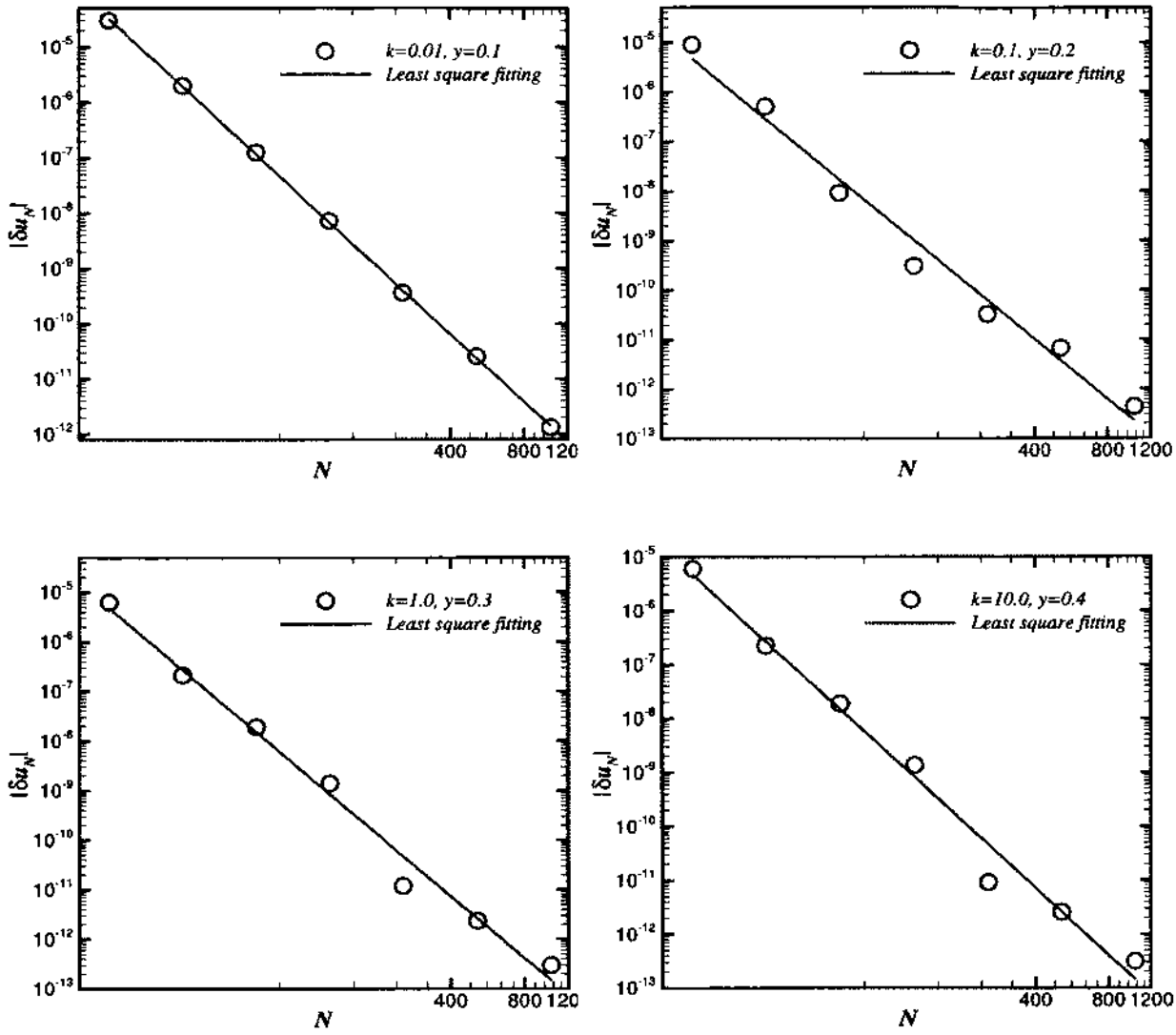

FIG. 1: The grid size N dependence of the relative error of the velocity $|\delta u_N(y)|$. The top row, from left to right: $k = 0.01$ at $y = 0.1$ and $k = 0.1$ at $y = 0.2$. The bottom row, from left to right: $k = 1.0$ at $y = 0.3$ and $k = 10.0$ at $y = 0.4$.

We also compute the L_2 error of the velocity $\bar{u}_N(y)$,

$$\|\delta u_N\|_2 = \frac{\left[\int_{-1/2}^{1/2} |\bar{u}_N(y) - u_*(y)|^2 \, \mathrm{d}y\right]^{1/2}}{\left[\int_{-1/2}^{1/2} |u_*(y)|^2 \, \mathrm{d}y\right]^{1/2}},$$

where the reference solution $u_*(y)$ is obtained with $N = 2047$. The results of $\|\delta u_N\|_2$

with $k = 0.003, 0.01, 0.03, 0.1, 1.0$ and 10.0 are shown in Table 6. The L_2 error $\|\delta u_N\|_2$ shows very weak dependence on k. For various values of $0.003 \leq k \leq 10.0$, the rate of convergence $\alpha > 3$. Both the point-wise relative error and the L_2 error indicate the scheme is of high order.

TABLE 6: The L_2 error of the velocity $\bar{u}_N(y)$ and the rate of convergence α.

k	N	$\|\delta u_N\|_2$	k	N	$\|\delta u_N\|_2$
0.003	16	$9.073159564311592 \cdot 10^{-5}$	0.01	16	$6.850638233262458 \cdot 10^{-5}$
	32	$1.173595294063363 \cdot 10^{-5}$		32	$1.158034979497339 \cdot 10^{-5}$
	64	$1.998332365494139 \cdot 10^{-6}$		64	$2.040512264077090 \cdot 10^{-6}$
	128	$3.555748458719578 \cdot 10^{-7}$		128	$3.589887685163785 \cdot 10^{-7}$
	256	$6.318807893148573 \cdot 10^{-8}$		256	$6.336243964057072 \cdot 10^{-8}$
	512	$1.167675652196907 \cdot 10^{-8}$		512	$1.168038817604225 \cdot 10^{-8}$
	1024	$2.398181505564065 \cdot 10^{-9}$		1024	$2.396621872127319 \cdot 10^{-9}$
	α	3.3570		α	3.4584
0.03	16	$6.906363108665610 \cdot 10^{-5}$	0.1	16	$7.023168944878657 \cdot 10^{-5}$
	32	$1.186616010647807 \cdot 10^{-5}$		32	$1.176707411570782 \cdot 10^{-5}$
	64	$2.056433398329269 \cdot 10^{-6}$		64	$2.015858660824019 \cdot 10^{-6}$
	128	$3.588564081981813 \cdot 10^{-7}$		128	$3.503976368566796 \cdot 10^{-7}$
	256	$6.316031862395808 \cdot 10^{-8}$		256	$6.159685518862506 \cdot 10^{-8}$
	512	$1.163297719138161 \cdot 10^{-8}$		512	$1.134097387572629 \cdot 10^{-8}$
	1024	$2.386153226120782 \cdot 10^{-9}$		1024	$2.325951729127107 \cdot 10^{-9}$
	α	3.4554		α	3.4494
1.0	16	$5.455348234878563 \cdot 10^{-5}$	10.0	16	$3.217798103809692 \cdot 10^{-5}$
	32	$8.956151509566837 \cdot 10^{-6}$		32	$5.264751883741950 \cdot 10^{-6}$
	64	$1.524372937533699 \cdot 10^{-6}$		64	$8.952332255181793 \cdot 10^{-7}$
	128	$2.644513283117079 \cdot 10^{-7}$		128	$1.552658662784406 \cdot 10^{-7}$
	256	$4.646189890073849 \cdot 10^{-8}$		256	$2.727892020475305 \cdot 10^{-8}$
	512	$8.553006371558081 \cdot 10^{-9}$		512	$5.021210272459947 \cdot 10^{-9}$
	1024	$1.754065729796481 \cdot 10^{-9}$		1024	$1.029752165284958 \cdot 10^{-9}$
	α	3.5405		α	3.7309

The accurate solution of $\bar{u}_N(y)$ enables one to obtain accurate shear stress T_{xy} and the upper half channel mass flow rate Q. Corresponding to the present case: steady Couette flow problem with pure diffusive boundary condition, we set $\alpha^{\pm}$ in equation (33) equal to 0 and use the antisymmetric property of $u(y)$ to obtain

$$T_{xy} = -\pi^{-1/2} \left[\frac{2}{k} \int_0^{1/2} I_0 \left(\frac{s}{k} \right) u(s) \, \mathrm{d}s + I_1 \left(\frac{1}{2k} \right) \right]. \tag{92}$$

Substituting $\bar{u}_N(s)$ for $u(s)$ in equation (92), the shear stress T_{xy} is computed with 2048^{th} order Gauss-Legendre quadrature and $N = 2047$ for various values of $0.003 \leq k \leq 10.0$. When $k \to \infty$, $T_{xy} \to -\frac{\pi^{-1/2}}{2} \approx -0.282094792$; when $k \to 0+$, $T_{xy} \to 0$. The upper half channel mass flow rate is define by

$$Q = \int_0^{1/2} u(y) \, \mathrm{d}y. \tag{93}$$

With the Chebyshev expansion of $u(y)$ given by equation (81), the upper half channel

TABLE 7: The dependence of the stress T_{xy} and the upper half channel mass flow rate Q on the Knudsen number k

k	T_{xy}	Q
0.003	$-1.490909702173263 \cdot 10^{-3}$	$1.242445655358978 \cdot 10^{-1}$
0.01	$-4.900405009668500 \cdot 10^{-3}$	$1.225330275294396 \cdot 10^{-1}$
0.03	$-1.413798601517447 \cdot 10^{-2}$	$1.180147037185861 \cdot 10^{-1}$
0.1	$-4.155607782559217 \cdot 10^{-2}$	$1.057028408172310 \cdot 10^{-1}$
0.3	$-9.344983511356993 \cdot 10^{-2}$	$8.560111699820641 \cdot 10^{-2}$
1.0	$-1.694625753368235 \cdot 10^{-1}$	$5.804708735555424 \cdot 10^{-2}$
2.0	$-2.083322536749378 \cdot 10^{-1}$	$4.281659776113900 \cdot 10^{-2}$
3.0	$-2.266437497658086 \cdot 10^{-1}$	$3.489298506190797 \cdot 10^{-2}$
5.0	$-2.446632678455995 \cdot 10^{-1}$	$2.627042060967372 \cdot 10^{-2}$
7.0	$-2.536943539674480 \cdot 10^{-1}$	$2.147460412330824 \cdot 10^{-2}$
10.0	$-2.611624603488405 \cdot 10^{-1}$	$1.714449048590636 \cdot 10^{-2}$

mass flow rate is approximated by

$$\begin{aligned}
Q =& \sum_{j=1}^{N} c_{2j-1} \int_0^{\frac{1}{2}\cos\frac{\pi}{4N}} T_{2j-1}(y)\,\mathrm{d}y + \sum_{j=1}^{N+1} \tilde{c}_{2j-1} \int_{\frac{1}{2}\cos\frac{\pi}{4N}}^{\pi/2} T_{2j-1}(y)\,\mathrm{d}y \\
=& \frac{c_1}{8}\left(\cos\frac{\pi}{2N}+1\right) + \frac{\tilde{c}_1}{8}\left(1-\cos\frac{\pi}{2N}\right) \\
&+ \frac{1}{8}\sum_{j=2}^{N} c_{2j-1}\left[\frac{\cos\frac{j\pi}{2N}-(-1)^j}{j} + \frac{(-1)^{j-1}-\cos\frac{(j-1)\pi}{2N}}{j-1}\right] \\
&+ \frac{1}{8}\sum_{j=2}^{N+1} \tilde{c}_{2j-1}\left[\frac{1-\cos\frac{j\pi}{2N}}{j} + \frac{\cos\frac{(j-1)\pi}{2N}-1}{j-1}\right].
\end{aligned}$$

Table 7 shows the approximated values of T_{xy} and Q. The results in the table are consistent with the most recent and accurate results for steady Couette flow with purely diffusive boundary condition. Meanwhile, our results are more accurate, with at least 11 digits of accuracy.

3.2 SOLVING INTEGRAL EQUATION FOR THE COUETTE FLOW PROBLEM WITH CHUNK BASED COLLOCATION METHOD

In this section, we solve the steady Couette flow problem with purely diffusive boundary condition and the combined diffusive and speculative reflection boundary condition and Knudsen number k with chunk based collocation method. First, we reconsider equation (72) for the case of purely diffusive boundary condition. The integration interval $[-1/2, 1/2]$ is decomposed into N disjoint subintervals $\cup_{j=1}^{N} E_j$. On each of the subinterval $E_j = [y_{j-1}, y_j] \subset [y_0, y_N] = [-1/2, 1/2], (j = 1, 2, \cdots, N)$,

$u(y)$ is approximated by a $(M-1)^{th}$ order expansion of scaled and shifted Gauss-Legendre polynomials with support E_j,

$$u_j^N(y) = \begin{cases} \sum_{m=1}^{M} c_{j,m} L_{j,m-1}(y),\ y \in E_j \\ 0,\ y \notin E_j, \end{cases} \tag{94}$$

where $L_{j,m-1}(y)$ is the scaled and shifted $(m-1)^{th}$ order Gauss-Legendre polynomial on the subinterval E_j and $c_{j,m}$ is the expansion coefficient with respect to $L_{j,m-1}(y)$. Let $L_m(y)$ be the m^{th} order Gauss-Legendre polynomial, $L_{j,m}(y)$ is written as

$$L_{j,m}(y) = L_m\left(\frac{2y - y_{j-1} - y_j}{y_j - y_{j-1}}\right),\ y \in [y_{j-1}, y_j].$$

Hence, the velocity $u(y)$ on the whole interval $[-1/2, 1/2]$ is approximated by

$$u^N(y) = \sum_{j=1}^{N} u_j^N(y),\ y \in [-1/2, 1/2]. \tag{95}$$

We substitute equation (95) into equation (72) and use equation (94) to obtain

$$u_i^N(y) - \frac{1}{\pi^{1/2}k} \sum_{j=1}^{N} \sum_{m=1}^{M} c_{j,m} \int_{E_j} I_{-1}\left(\frac{|y-s|}{k}\right) L_{j,m-1}(s)\,\mathrm{d}s = \frac{1}{2\pi^{1/2}} F_0(y,k),\ y \in E_i. \tag{96}$$

Let $\{x_m | 1 \le m \le M\}$ be the set of M^{th} order Gauss-Legendre abscissas. Then, $\{y_{j,m} | y_{j,m} = y_{j-1} + (x_m + 1)(y_j - y_{j-1})/2,\ 1 \le m \le M\}$ is the set of M^{th} order scaled and shifted Gauss-Legendre abscissas on the subinterval E_j. We choose $\{y_{j,m}\}_{m=1}^{M}$ as the collocation point set on E_j and denote by $u_{j,m} = u_j^N(y_{j,m})$ the $(M-1)^{th}$ degree approximation of $u(y)$ on this collocation point set. According to the linear relation between $\{c_{j,m}\}_{m=1}^{M}$ and $\{u_{j,m}\}_{m=1}^{M}$ in Appendix C, *i.e.*, $\boldsymbol{c}_j = P\boldsymbol{u}_j$, where $\boldsymbol{c}_j$ and $\boldsymbol{u}_j$ are M-tuple column vectors with entries, $c_{j,m}$ and $u_{j,m}$, respectively, equation (96) can be written as

$$u_i^N(y) - \frac{1}{\pi^{1/2}} \sum_{j=1}^{N} \boldsymbol{\Psi}_j^T(y) P \boldsymbol{u}_j = \frac{1}{2\pi^{1/2}} F_0(y,k),\ y \in E_i, \tag{97}$$

where $\boldsymbol{\Psi}_j(y)$ is an M-tuple column vector with entries

$$\Psi_{j,m}(y) = \frac{1}{k} \int_{E_j} I_{-1}\left(\frac{|y-s|}{k}\right) L_{j,m-1}(s)\,\mathrm{d}s,\ m = 1, 2, \cdots, M. \tag{98}$$

We plug $y = y_{i,n}$ with $n = 1, 2, \cdots, M$, into equation (97), respectively, to obtain a linear system of M equations for $\boldsymbol{u}_i$. To simplify the form of the linear system, we

denote an $M \times M$ matrix $\boldsymbol{\Psi}_{j,i}$ by

$$\boldsymbol{\Psi}_{j,i} = (\boldsymbol{\Psi}_j(y_{i,1})\, \boldsymbol{\Psi}_j(y_{i,2}) \cdots \boldsymbol{\Psi}_j(y_{i,M}))$$

and an M-tuple column vector, $\boldsymbol{F}_{0,i}$, by

$$\boldsymbol{F}_{0,i} = (F_0(y_{i,1},k)\, F_0(y_{i,2},k) \cdots F_0(y_{i,M},k))^T.$$

Then, the linear system reads

$$\boldsymbol{u}_i - \frac{1}{\pi^{1/2}} \sum_{j=1}^{N} \boldsymbol{\Psi}_{j,i}^T \boldsymbol{P} \boldsymbol{u}_j = \frac{1}{2\pi^{1/2}} \boldsymbol{F}_{0,i}. \tag{99}$$

Now we focus on the matrix $\boldsymbol{\Psi}_{j,i}$. The m^{th} row and n^{th} column entry reads,

$$\begin{aligned}
\mathrm{ent}_{mn}\, \Psi_{j,i} &= \frac{1}{k} \int_{E_j} I_{-1}\left(\frac{|y_{i,n}-s|}{k}\right) L_{j,m-1}(s)\, \mathrm{d}s \\
&= \begin{cases}
I_0\left(\frac{y_{i,n}-y_j}{k}\right) + (-1)^m I_0\left(\frac{y_{i,n}-y_{j-1}}{k}\right) - \int_{y_{j-1}}^{y_j} I_0\left(\frac{y_{i,n}-s}{k}\right) L'_{j,m-1}(s)\, \mathrm{d}s, & j < i, \\
\pi^{1/2} L_{i,m-1}(y_{i,n}) + (-1)^m I_0\left(\frac{y_{i,n}-y_{i-1}}{k}\right) - I_0\left(\frac{y_i-y_{i,n}}{k}\right) & \\
\quad - \int_{y_{i-1}}^{y_{i,n}} I_0\left(\frac{y_{i,n}-s}{k}\right) L'_{i,m-1}(s)\, \mathrm{d}s + \int_{y_{i,n}}^{y_i} I_0\left(\frac{s-y_{i,n}}{k}\right) L'_{i,m-1}(s)\, \mathrm{d}s, & j = i, \\
(-1)^{m+1} I_0\left(\frac{y_{j-1}-y_{i,n}}{k}\right) - I_0\left(\frac{y_j-y_{i,n}}{k}\right) + \int_{y_{j-1}}^{y_j} I_0\left(\frac{s-y_{i,n}}{k}\right) L'_{j,m-1}(s)\, \mathrm{d}s, & j > i.
\end{cases}
\end{aligned}$$

From Appendix C, we observe that the m^{th} row and n^{th} column entry of the inverse matrix $\boldsymbol{Q} = \boldsymbol{P}^{-1}$ is $L_{i,n-1}(y_{i,m})$. Hence, the matrix $\boldsymbol{\Psi}_{j,i}$ can be decomposed as

$$\boldsymbol{\Psi}_{j,i} = \pi^{1/2} \delta_{ij} \boldsymbol{Q}^T - \boldsymbol{\Phi}_{i,j}^T. \tag{100}$$

The m^{th} row and n^{th} column entry of $\Phi_{i,j}$ reads,

$$
\begin{aligned}
&\mathrm{ent}_{mn}\,\Phi_{i,j}\\
&= \begin{cases}
-I_0\left(\frac{y_{i,m}-y_j}{k}\right) + (-1)^{n+1} I_0\left(\frac{y_{i,m}-y_{j-1}}{k}\right) + \int_{y_{j-1}}^{y_j} I_0\left(\frac{y_{i,m}-s}{k}\right) L'_{j,n-1}(s)\,\mathrm{d}s, & j<i,\\[2ex]
(-1)^{n+1} I_0\left(\frac{y_{i,m}-y_{i-1}}{k}\right) + I_0\left(\frac{y_i-y_{i,m}}{k}\right)\\
\quad + \int_{y_{i-1}}^{y_{i,m}} I_0\left(\frac{y_{i,m}-s}{k}\right) L'_{i,n-1}(s)\,\mathrm{d}s - \int_{y_{i,m}}^{y_i} I_0\left(\frac{s-y_{i,m}}{k}\right) L'_{i,n-1}(s)\,\mathrm{d}s, & j=i,\\[2ex]
(-1)^{n} I_0\left(\frac{y_{j-1}-y_{i,m}}{k}\right) + I_0\left(\frac{y_j-y_{i,m}}{k}\right) - \int_{y_{j-1}}^{y_j} I_0\left(\frac{s-y_{i,m}}{k}\right) L'_{j,n-1}(s)\,\mathrm{d}s, & j>i,
\end{cases}\\
&= \begin{cases}
-I_0\left(\frac{y_{i,m}-y_j}{k}\right) + (-1)^{n+1} I_0\left(\frac{y_{i,m}-y_{j-1}}{k}\right) + \int_{-1}^{1} I_0\left(\frac{y_{i,m}-y_{j,s}}{k}\right) L'_{n-1}(s)\,\mathrm{d}s, & j<i,\\[2ex]
(-1)^{n+1} I_0\left(\frac{y_{i,m}-y_{i-1}}{k}\right) + I_0\left(\frac{y_i-y_{i,m}}{k}\right)\\
\quad + \int_{-1}^{x_m} I_0\left(\frac{x_m-s}{2k}|E_i|\right) L'_{n-1}(s)\,\mathrm{d}s - \int_{x_m}^{1} I_0\left(\frac{s-x_m}{2k}|E_i|\right) L'_{n-1}(s)\,\mathrm{d}s, & j=i,\\[2ex]
(-1)^{n} I_0\left(\frac{y_{j-1}-y_{i,m}}{k}\right) + I_0\left(\frac{y_j-y_{i,m}}{k}\right) - \int_{-1}^{1} I_0\left(\frac{y_{j,s}-y_{i,m}}{k}\right) L'_{n-1}(s)\,\mathrm{d}s, & j>i.
\end{cases}
\end{aligned}
\tag{101}
$$

where $|E_j| = y_j - y_{j-1}$, $y_{j,s} = y_{j-1} + \frac{s+1}{2}|E_j|$.
Substituting equation (100) into equation (99), we obtain

$$\sum_{j=1}^{N} \boldsymbol{\Phi}_{i,j} P \boldsymbol{u}_j = \boldsymbol{F}_{0,i}/2. \tag{102}$$

Equation (102) is equivalent to the linear system

$$\boldsymbol{A}\boldsymbol{u} = \boldsymbol{F}, \tag{103}$$

where

$$\boldsymbol{A} = \begin{pmatrix} \boldsymbol{\Phi}_{1,1}P & \boldsymbol{\Phi}_{1,2}P & \cdots & \boldsymbol{\Phi}_{1,N}P \\ \boldsymbol{\Phi}_{2,1}P & \boldsymbol{\Phi}_{2,2}P & \cdots & \boldsymbol{\Phi}_{2,N}P \\ \cdots & \cdots & \cdots & \cdots \\ \boldsymbol{\Phi}_{N,1}P & \boldsymbol{\Phi}_{N,2}P & \cdots & \boldsymbol{\Phi}_{N,N}P \end{pmatrix},$$

$$\boldsymbol{u} = (\boldsymbol{u}_1^T\, \boldsymbol{u}_2^T \cdots \boldsymbol{u}_N^T)^T,$$

and

$$\boldsymbol{F} = \frac{1}{2}(\boldsymbol{F}_{0,1}^T\, \boldsymbol{F}_{0,2}^T \cdots \boldsymbol{F}_{0,N}^T)^T.$$

To compute A and F precisely, one needs to evaluate the Abramowitz function of order 0 with high precision. Again, we use Macleod's [1] method of Chebyshev expansion. Meanwhile, one needs evaluate the four integrals in equation (101) with equally high precision. This is much easier to implement here than to do in the Chebyshev collocation method. Unlike approximating $u(y)$ on the whole interval $[-1/2, 1/2]$, now $u(y)$ is approximated on the subintervals by using much lower degree of piece-wise polynomials. *i.e.*, we use $M = 10$ and on each of the subintervals. $u(y)$ is approximated by a 9^{th} degree polynomial. In order to evaluate $\Phi_{i,j}$, we use adaptive Gauss-Legendre quadrature with absolute tolerance $\epsilon = 10^{-33}$ to compute the four integrals in equation (101). As the kernel of the adaptive quadrature, we use 16^{th} order Gauss-Legendre quadrature. The details about evaluating the abscissas and weights are listed in Appendix D.

The division of the interval $[-1/2, 1/2]$ into subintervals is another crux of the chunk based collocation method. Recalling from Appendix B that $u'(x)$ doesn't exist at boundaries ± 1, one needs to adopt refined subintervals at the boundaries, in order to mitigate the influence of the boundary singularity. Actually, we use $N/2$ uniform subintervals in the middle of $[-1/2, 1/2]$ and gradually halve the length of subintervals on the two lateral directions. Specifically, when $j \leq N/4$, the subinterval is $E_j = [y_{j-1}, y_j]$ with $y_j = y_{j-1} + 2^{j-1-\frac{N}{4}}/(N/2 + 2\sum_{i=1}^{N/4} 2^{-i})$; when $N/4 < j \leq 3N/4$, the subinterval is $E_j = [y_{j-1}, y_j]$ with $y_j = y_{j-1} + 1/(N/2 + 2\sum_{i=1}^{N/4} 2^{-i})$; when $3N/4 \leq j \leq N$, the subinterval is $E_j = [y_{j-1}, y_j]$ with $y_j = y_{j-1} + 2^{j-\frac{3N}{4}}/(N/2 + 2\sum_{i=1}^{N/4} 2^{-i})$, where $1 \leq j \leq N, y_0 = -1/2, y_N = 1/2$.

Numerically, we solve equation (103) for the Couette flow with the same range of Knudsen number k as we do in Chebyshev collocation method, *i.e.*, $0.003 \leq k \leq 10.0$. We use quadruple precision to ensure accuracy. Meanwhile, we vary the order of equation (103) by changing N with $40 \leq N \leq 320$, to ensure the convergence of the results. Table 8 and Table 9 give the value of $u(y)$ at $y = 0.1, 0.2, 0.3, 0.4$ and 0.5 for various values of k and N. As in the Chebyshev collocation method, we also have $u = 0$ at the channel center, for all values of k. When $N = 320$, the results of $u(y)$ in Table 8 and Table 9 are accurate for at least 13 significant digits. From equation (94) and equation (95) the derivative of velocity at channel center $u'(0)$ is approximated by

$$\frac{\mathrm{d}u_{j^*}^N}{\mathrm{d}y}|_{y=0} = \frac{2}{|E_{j^*}|}\sum_{m=1}^{M} c_{j^*,m} L'_m\left(-\frac{y_{j^*-1} + y_{j^*}}{|E_{j^*}|}\right), 0 \in E_{j^*}.$$

TABLE 8: The values of the approximated velocity $u^N(y)$ of the Couette flow at $y = 0.1, 0.2$ and 0.3, for $0.003 \leq k \leq 10.0$ and $40 \leq N \leq 320$

y	0.1	0.2	0.3
N		$k = 0.003$	
40	$9.939398013577058 \cdot 10^{-2}$	$1.987879602715412 \cdot 10^{-1}$	$2.981819404073140 \cdot 10^{-1}$
80	$9.939398014202010 \cdot 10^{-2}$	$1.987879602840402 \cdot 10^{-1}$	$2.981819404260625 \cdot 10^{-1}$
160	$9.939398014207161 \cdot 10^{-2}$	$1.987879602841432 \cdot 10^{-1}$	$2.981819404262171 \cdot 10^{-1}$
320	$9.939398014207885 \cdot 10^{-2}$	$1.987879602841577 \cdot 10^{-1}$	$2.981819404262388 \cdot 10^{-1}$
N		$k = 0.01$	
40	$9.800810022099017 \cdot 10^{-2}$	$1.960162013383582 \cdot 10^{-1}$	$2.940243426343889 \cdot 10^{-1}$
80	$9.800810022280497 \cdot 10^{-2}$	$1.960162013419878 \cdot 10^{-1}$	$2.940243426398333 \cdot 10^{-1}$
160	$9.800810022280901 \cdot 10^{-2}$	$1.960162013419959 \cdot 10^{-1}$	$2.940243426398454 \cdot 10^{-1}$
320	$9.800810022280944 \cdot 10^{-2}$	$1.960162013419967 \cdot 10^{-1}$	$2.940243426398467 \cdot 10^{-1}$
N		$k = 0.03$	
40	$9.425510233653742 \cdot 10^{-2}$	$1.885155965103996 \cdot 10^{-1}$	$2.828084717775777 \cdot 10^{-1}$
80	$9.425510233708961 \cdot 10^{-2}$	$1.885155965115043 \cdot 10^{-1}$	$2.828084717792371 \cdot 10^{-1}$
160	$9.425510233708989 \cdot 10^{-2}$	$1.885155965115049 \cdot 10^{-1}$	$2.828084717792379 \cdot 10^{-1}$
320	$9.425510233708992 \cdot 10^{-2}$	$1.885155965115049 \cdot 10^{-1}$	$2.828084717792380 \cdot 10^{-1}$
N		$k = 0.1$	
40	$8.356104029412244 \cdot 10^{-2}$	$1.673490502310847 \cdot 10^{-1}$	$2.518108071018377 \cdot 10^{-1}$
80	$8.356104029425423 \cdot 10^{-2}$	$1.673490502313504 \cdot 10^{-1}$	$2.518108071022446 \cdot 10^{-1}$
160	$8.356104029425424 \cdot 10^{-2}$	$1.673490502313504 \cdot 10^{-1}$	$2.518108071022446 \cdot 10^{-1}$
320	$8.356104029425424 \cdot 10^{-2}$	$1.673490502313505 \cdot 10^{-1}$	$2.518108071022446 \cdot 10^{-1}$
N		$k = 0.3$	
40	$6.645430069490896 \cdot 10^{-2}$	$1.335709509478632 \cdot 10^{-1}$	$2.023607233397821 \cdot 10^{-1}$
80	$6.645430069493927 \cdot 10^{-2}$	$1.335709509479253 \cdot 10^{-1}$	$2.023607233398804 \cdot 10^{-1}$
160	$6.645430069493927 \cdot 10^{-2}$	$1.335709509479253 \cdot 10^{-1}$	$2.023607233398804 \cdot 10^{-1}$
320	$6.645430069493927 \cdot 10^{-2}$	$1.335709509479253 \cdot 10^{-1}$	$2.023607233398804 \cdot 10^{-1}$
N		$k = 1.0$	
40	$4.453194115211670 \cdot 10^{-2}$	$8.976290005956775 \cdot 10^{-2}$	$1.366691806916429 \cdot 10^{-1}$
80	$4.453194115212171 \cdot 10^{-2}$	$8.976290005957814 \cdot 10^{-2}$	$1.366691806916597 \cdot 10^{-1}$
160	$4.453194115212171 \cdot 10^{-2}$	$8.976290005957814 \cdot 10^{-2}$	$1.366691806916597 \cdot 10^{-1}$
320	$4.453194115212171 \cdot 10^{-2}$	$8.976290005957814 \cdot 10^{-2}$	$1.366691806916597 \cdot 10^{-1}$
N		$k = 2.0$	
40	$3.283175101364344 \cdot 10^{-2}$	$6.620080866804171 \cdot 10^{-2}$	$1.008399340224601 \cdot 10^{-1}$
80	$3.283175101364504 \cdot 10^{-2}$	$6.620080866804505 \cdot 10^{-2}$	$1.008399340224655 \cdot 10^{-1}$
160	$3.283175101364504 \cdot 10^{-2}$	$6.620080866804505 \cdot 10^{-2}$	$1.008399340224655 \cdot 10^{-1}$
320	$3.283175101364504 \cdot 10^{-2}$	$6.620080866804505 \cdot 10^{-2}$	$1.008399340224655 \cdot 10^{-1}$
N		$k = 3.0$	
40	$2.678842250717560 \cdot 10^{-2}$	$5.400761302341321 \cdot 10^{-2}$	$8.223931900199492 \cdot 10^{-2}$
80	$2.678842250717640 \cdot 10^{-2}$	$5.400761302341487 \cdot 10^{-2}$	$8.223931900199767 \cdot 10^{-2}$
160	$2.678842250717640 \cdot 10^{-2}$	$5.400761302341487 \cdot 10^{-2}$	$8.223931900199767 \cdot 10^{-2}$
320	$2.678842250717640 \cdot 10^{-2}$	$5.400761302341487 \cdot 10^{-2}$	$8.223931900199767 \cdot 10^{-2}$
N		$k = 5.0$	
40	$2.021810350612648 \cdot 10^{-2}$	$4.074510549514783 \cdot 10^{-2}$	$6.199427039073221 \cdot 10^{-2}$
80	$2.021810350612680 \cdot 10^{-2}$	$4.074510549514850 \cdot 10^{-2}$	$6.199427039073332 \cdot 10^{-2}$
160	$2.021810350612680 \cdot 10^{-2}$	$4.074510549514850 \cdot 10^{-2}$	$6.199427039073332 \cdot 10^{-2}$
320	$2.021810350612680 \cdot 10^{-2}$	$4.074510549514850 \cdot 10^{-2}$	$6.199427039073332 \cdot 10^{-2}$
N		$k = 7.0$	
40	$1.655896140054828 \cdot 10^{-2}$	$3.335952222887468 \cdot 10^{-2}$	$5.072335823657267 \cdot 10^{-2}$
80	$1.655896140054846 \cdot 10^{-2}$	$3.335952222887504 \cdot 10^{-2}$	$5.072335823657328 \cdot 10^{-2}$
160	$1.655896140054846 \cdot 10^{-2}$	$3.335952222887504 \cdot 10^{-2}$	$5.072335823657328 \cdot 10^{-2}$
320	$1.655896140054846 \cdot 10^{-2}$	$3.335952222887504 \cdot 10^{-2}$	$5.072335823657328 \cdot 10^{-2}$
N		$k = 10.0$	
40	$1.324840054213361 \cdot 10^{-2}$	$2.667954575379395 \cdot 10^{-2}$	$4.053574032131352 \cdot 10^{-2}$
80	$1.324840054213370 \cdot 10^{-2}$	$2.667954575379414 \cdot 10^{-2}$	$4.053574032131383 \cdot 10^{-2}$
160	$1.324840054213370 \cdot 10^{-2}$	$2.667954575379414 \cdot 10^{-2}$	$4.053574032131383 \cdot 10^{-2}$
320	$1.324840054213370 \cdot 10^{-2}$	$2.667954575379414 \cdot 10^{-2}$	$4.053574032131383 \cdot 10^{-2}$

Table 10 gives the boundary velocity $u^N(1/2)$ and the channel center velocity derivative for various values of k with $N = 320$.

We compute the local relative error of the velocity $u(y)$ at a specific location y and a given value of k,

$$\left|\delta u^N(y)\right| = \frac{\left|u^N(y) - u^*(y)\right|}{\left|u^*(y)\right|},$$

where the reference solution is obtained with $N = 320$. We compute $\left|\delta u^N(y)\right|$ at

TABLE 9: The values of the approximated velocity $u^N(y)$ of the Couette flow at $y = 0.4$ and 0.5, for $0.003 \leq k \leq 10.0$ and $40 \leq N \leq 320$

y	0.4	0.5
N	$k = 0.003$	
40	$3.975759206318977 \cdot 10^{-1}$	$4.978910361032047 \cdot 10^{-1}$
80	$3.975759206568961 \cdot 10^{-1}$	$4.978915350232522 \cdot 10^{-1}$
160	$3.975759206571021 \cdot 10^{-1}$	$4.978915352789675 \cdot 10^{-1}$
320	$3.975759206571311 \cdot 10^{-1}$	$4.978915352789715 \cdot 10^{-1}$
N	$k = 0.01$	
40	$3.920355719950599 \cdot 10^{-1}$	$4.930692881065874 \cdot 10^{-1}$
80	$3.920355720023037 \cdot 10^{-1}$	$4.930697805220819 \cdot 10^{-1}$
160	$3.920355720023198 \cdot 10^{-1}$	$4.930697807742204 \cdot 10^{-1}$
320	$3.920355720023215 \cdot 10^{-1}$	$4.930697807742211 \cdot 10^{-1}$
N	$k = 0.03$	
40	$3.773525609007822 \cdot 10^{-1}$	$4.800053943421772 \cdot 10^{-1}$
80	$3.773525609029753 \cdot 10^{-1}$	$4.800058680342067 \cdot 10^{-1}$
160	$3.773525609029763 \cdot 10^{-1}$	$4.800058682766827 \cdot 10^{-1}$
320	$3.773525609029764 \cdot 10^{-1}$	$4.800058682766829 \cdot 10^{-1}$
N	$k = 0.1$	
40	$3.383684060724656 \cdot 10^{-1}$	$4.412242229655252 \cdot 10^{-1}$
80	$3.383684060729897 \cdot 10^{-1}$	$4.412246407584054 \cdot 10^{-1}$
160	$3.383684060729897 \cdot 10^{-1}$	$4.412246409722420 \cdot 10^{-1}$
320	$3.383684060729897 \cdot 10^{-1}$	$4.412246409722421 \cdot 10^{-1}$
N	$k = 0.3$	
40	$2.751706693589889 \cdot 10^{-1}$	$3.672122547463328 \cdot 10^{-1}$
80	$2.751706693590908 \cdot 10^{-1}$	$3.672125693890145 \cdot 10^{-1}$
160	$2.751706693590906 \cdot 10^{-1}$	$3.672125695500503 \cdot 10^{-1}$
320	$2.751706693590906 \cdot 10^{-1}$	$3.672125695500504 \cdot 10^{-1}$
N	$k = 1.0$	
40	$1.872336429975775 \cdot 10^{-1}$	$2.518611635056980 \cdot 10^{-1}$
80	$1.872336429975761 \cdot 10^{-1}$	$2.518613398991954 \cdot 10^{-1}$
160	$1.872336429975760 \cdot 10^{-1}$	$2.518613399894732 \cdot 10^{-1}$
320	$1.872336429975760 \cdot 10^{-1}$	$2.518613399894732 \cdot 10^{-1}$
N	$k = 2.0$	
40	$1.381797101409755 \cdot 10^{-1}$	$1.852461874424392 \cdot 10^{-1}$
80	$1.381797101409663 \cdot 10^{-1}$	$1.852462993167649 \cdot 10^{-1}$
160	$1.381797101409662 \cdot 10^{-1}$	$1.852462993740218 \cdot 10^{-1}$
320	$1.381797101409662 \cdot 10^{-1}$	$1.852462993740218 \cdot 10^{-1}$
N	$k = 3.0$	
40	$1.126006454390551 \cdot 10^{-1}$	$1.504281616234751 \cdot 10^{-1}$
80	$1.126006454390461 \cdot 10^{-1}$	$1.504282444568137 \cdot 10^{-1}$
160	$1.126006454390460 \cdot 10^{-1}$	$1.504282444992074 \cdot 10^{-1}$
320	$1.126006454390460 \cdot 10^{-1}$	$1.504282444992075 \cdot 10^{-1}$
N	$k = 5.0$	
40	$8.474655782852562 \cdot 10^{-2}$	$1.126351329280281 \cdot 10^{-1}$
80	$8.474655782851844 \cdot 10^{-2}$	$1.126351880012729 \cdot 10^{-1}$
160	$8.474655782851842 \cdot 10^{-2}$	$1.126351880294592 \cdot 10^{-1}$
320	$8.474655782851842 \cdot 10^{-2}$	$1.126351880294592 \cdot 10^{-1}$
N	$k = 7.0$	
40	$6.925336240177241 \cdot 10^{-2}$	$9.171685465163046 \cdot 10^{-2}$
80	$6.925336240176662 \cdot 10^{-2}$	$9.171689611399412 \cdot 10^{-2}$
160	$6.925336240176661 \cdot 10^{-2}$	$9.171689613521434 \cdot 10^{-2}$
320	$6.925336240176661 \cdot 10^{-2}$	$9.171689613521435 \cdot 10^{-2}$
N	$k = 10.0$	
40	$5.526789346649298 \cdot 10^{-2}$	$7.292208261801611 \cdot 10^{-2}$
80	$5.526789346648852 \cdot 10^{-2}$	$7.292211297774700 \cdot 10^{-2}$
160	$5.526789346648851 \cdot 10^{-2}$	$7.292211299328495 \cdot 10^{-2}$
320	$5.526789346648851 \cdot 10^{-2}$	$7.292211299328496 \cdot 10^{-2}$

$y = 0.1$, 0.2, 0.3, 0.4 and 0.5 and $0.003 \leq k \leq 10$. Figure 2 shows the log-log plots of N-dependence of $|\delta u^N|$ at $y = 0.1$ and $k = 0.01$, $y = 0.2$ and $k = 0.1$, $y = 0.3$ and $k = 1.0$ and $y = 0.4$ and $k = 10.0$. The results indicate that

$$\ln \frac{|\delta u^N(y)|}{|\delta u^M(y)|} \sim -\alpha \ln \frac{N}{M},$$

where $N \neq M < 320$.

Table 11 shows the dependence of α on k at the positions: $k = 0.1$, 0.2, 0.3, 0.4 and

TABLE 10: The Knudsen number k dependence of the velocity $u^N(1/2)$ at boundary and the channel center velocity derivative $\frac{du^N}{dy}|_{y=0}$ obtained by the velocity piece-wise Legendre approximation with $N = 320$

k	$u^N(1/2)$	$\frac{du^N}{dy}\|_{y=0}$
0.003	$4.978915352789715 \cdot 10^{-1}$	0.9939398014207865
0.01	$4.930697807742211 \cdot 10^{-1}$	0.9800810020043022
0.03	$4.800058682766829 \cdot 10^{-1}$	0.9425456003244038
0.1	$4.412248409722421 \cdot 10^{-1}$	0.8352857656469437
0.3	$3.672125695500504 \cdot 10^{-1}$	0.6635300770297095
1.0	$2.518613399894732 \cdot 10^{-1}$	0.4442284697467991
2.0	$1.852462993740218 \cdot 10^{-1}$	0.3274745769375015
3.0	$1.504282444992075 \cdot 10^{-1}$	0.2672070059395808
5.0	$1.126351880294592 \cdot 10^{-1}$	0.2016944318181619
7.0	$9.171689613521435 \cdot 10^{-2}$	0.1652086347955840
10.0	$7.292211299328496 \cdot 10^{-2}$	0.1321955790519311

0.5. The rate of convergence is both dependent on the value of k and the position. Fixing position, the rate of convergence increases as the value of k rises. On the other hand, for each value of the k, the rate of convergence varies at different the positions. Near the channel center, the rate of convergence is higher than that at other positions. It is almost the same value when $y \in [0.2, 0.4]$. Due to the singularity, the rate of convergence is the lowest at the boundary. However, the lowest rate of convergence for in the table is as high as 5.7647, demonstrating the high efficiency of the scheme.

TABLE 11: The dependence of the rate of convergence for the velocity $u^N(y)$ on the Knudsen number k. The rate of convergence α and its standard deviation are computed by using the least-square method.

k			0.003	0.01	0.03	0.1	1.0
y	0.1	α	7.0773	7.9845	8.8459	9.7154	11.1634
	0.2		5.9906	6.4555	6.9060	7.4036	8.3477
	0.3		6.0110	6.4842	6.9423	7.4450	8.3835
	0.4		6.0176	6.4936	6.9549	7.4598	8.3392
	0.5		5.7647	6.1665	6.5513	6.9636	7.6833
k			2.0	3.0	5.0	7.0	10.0
y	0.1	α	11.5725	11.8126	12.1271	12.3609	12.7543
	0.2		8.6338	8.8006	9.0095	9.1491	9.3234
	0.3		8.6553	8.8104	9.0018	9.1273	9.2762
	0.4		8.5243	8.6497	8.8094	8.9168	9.0467
	0.5		7.8390	7.9438	8.0774	8.1670	8.2749

We also compute the L_2 error of the velocity $u(y)$,

$$\left\|\delta u^N\right\|_2 = \frac{\left[\int_{-1/2}^{1/2} \left|u^N(y) - u^*(y)\right|^2 \mathrm{d}y\right]^{1/2}}{\left[\int_{-1/2}^{1/2} \left|u^*(y)\right|^2 \mathrm{d}y\right]^{1/2}},$$

where the reference solution is obtained with $N = 320$. The results of $\|\delta u^N\|_2$ with

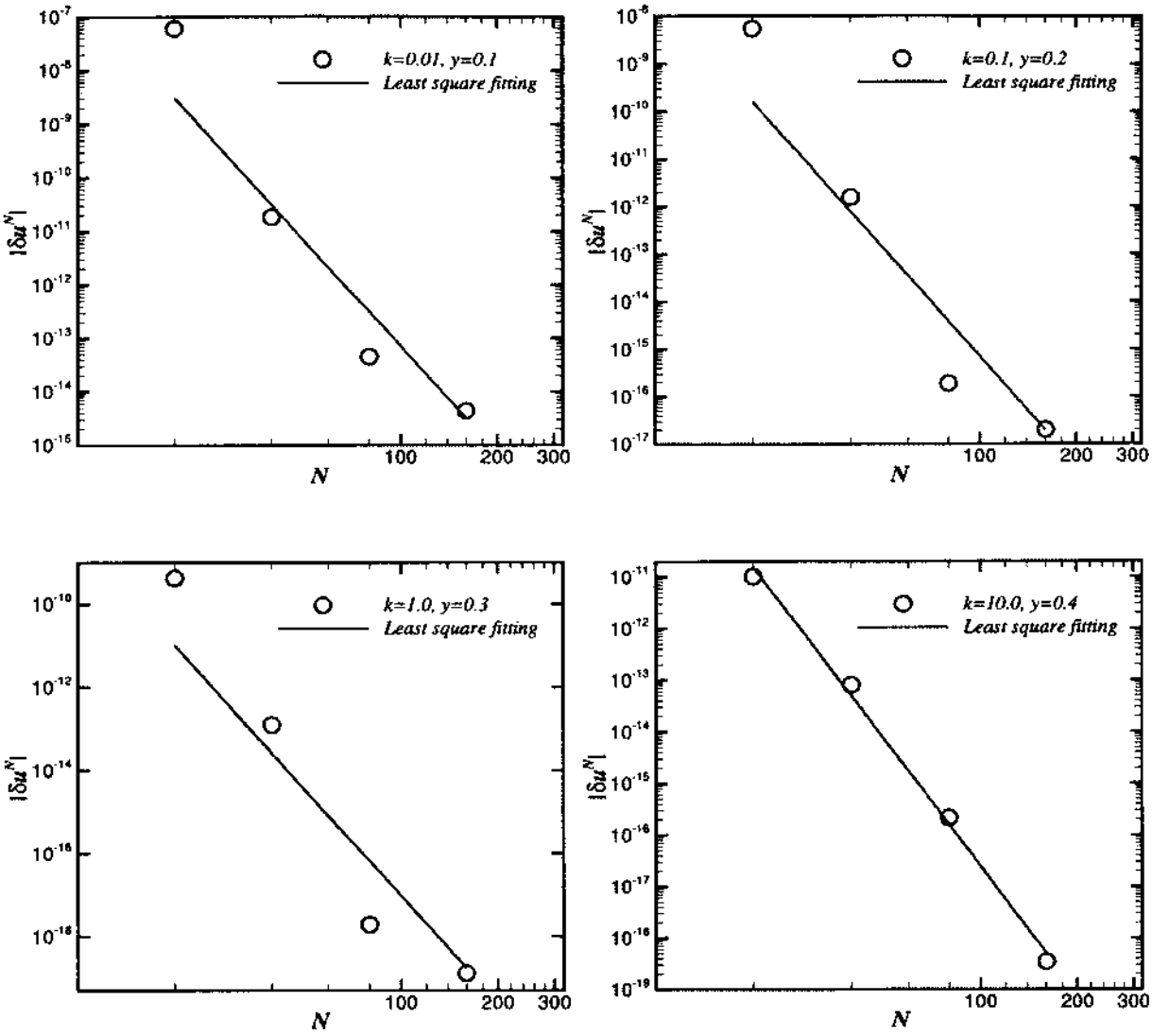

FIG. 2: The grid size N dependence of the relative error of the velocity $|\delta u^N(y)|$. The top row, from left to right: $k = 0.01$ at $y = 0.1$ and $k = 0.1$ at $y = 0.2$. The bottom row, from left to right: $k = 1.0$ at $y = 0.3$ and $k = 10.0$ at $y = 0.4$.

$k = 0.003, 0.01, 0.03, 0.1, 1.0$ and 10.0 are shown in Table 12. The L_2 error $\|\delta u^N\|_2$ shows very weak dependence on k. For various values of $0.003 \leq k \leq 10.0$, the rate of convergence $\alpha > 6.4$. Both the point-wise relative error and the L_2 error indicate the scheme is of high order.

We compute the shear stress T_{xy} and the upper half channel mass flow rate Q

TABLE 12: The L_2 error of the velocity $u^N(y)$ and the rate of convergence α.

k	N	$\|\delta u_N\|_2$	k	N	$\|\delta u_N\|_2$
0.003	20	$5.386917153001316 \cdot 10^{-7}$	0.01	20	$5.249666697031284 \cdot 10^{-7}$
	40	$1.192312561219479 \cdot 10^{-9}$		40	$1.192018845945770 \cdot 10^{-9}$
	80	$1.124408823443008 \cdot 10^{-12}$		80	$1.941661651226171 \cdot 10^{-12}$
	160	$5.218689452049895 \cdot 10^{-13}$		160	$8.244243155989926 \cdot 10^{-13}$
	α	6.9982		α	6.7103
0.03	20	$5.279882275251043 \cdot 10^{-7}$	0.1	20	$5.210626004272502 \cdot 10^{-7}$
	40	$1.189942448531462 \cdot 10^{-9}$		40	$1.168346183980707 \cdot 10^{-9}$
	80	$2.568225262112139 \cdot 10^{-12}$		80	$2.915074774412864 \cdot 10^{-12}$
	160	$1.002197366107061 \cdot 10^{-12}$		160	$1.084157308286381 \cdot 10^{-12}$
	α	6.5877		α	6.5270
1.0	20	$3.987628654884834 \cdot 10^{-7}$	10.0	20	$2.329671201308771 \cdot 10^{-7}$
	40	$8.917068673629308 \cdot 10^{-10}$		40	$5.207687300192405 \cdot 10^{-10}$
	80	$2.416563689297493 \cdot 10^{-12}$		80	$1.429279987857289 \cdot 10^{-12}$
	160	$8.719793709280467 \cdot 10^{-13}$		160	$5.131661120516864 \cdot 10^{-13}$
	α	6.4936		α	6.4886

TABLE 13: The dependence of the stress T_{xy} and the upper half channel mass flow rate Q on the Knudsen number k

k	T_{xy}	Q
0.003	$-1.490917161735522 \cdot 10^{-3}$	$1.242445655299160 \cdot 10^{-1}$
0.01	$-4.900405672137432 \cdot 10^{-3}$	$1.225330275292622 \cdot 10^{-1}$
0.03	$-1.413798608606268 \cdot 10^{-2}$	$1.180147037188893 \cdot 10^{-1}$
0.1	$-4.155607783123266 \cdot 10^{-2}$	$1.057028408172292 \cdot 10^{-1}$
0.3	$-9.344983511406519 \cdot 10^{-2}$	$8.560111699820618 \cdot 10^{-2}$
1.0	$-1.694625753368526 \cdot 10^{-1}$	$5.804708735555459 \cdot 10^{-2}$
2.0	$-2.083322536749430 \cdot 10^{-1}$	$4.281659776113917 \cdot 10^{-2}$
3.0	$-2.266437497658104 \cdot 10^{-1}$	$3.489298506190833 \cdot 10^{-2}$
5.0	$-2.446632678455999 \cdot 10^{-1}$	$2.627042060967383 \cdot 10^{-2}$
7.0	$-2.536943539674481 \cdot 10^{-1}$	$2.147460412330841 \cdot 10^{-2}$
10.0	$-2.611624603488406 \cdot 10^{-1}$	$1.714449048590649 \cdot 10^{-2}$

by using equation (93) and equation (92), respectively, where the integrals in the equations are evaluated piece-wisely on each subinterval E_j by a 10^{th} order shifted and scaled Gauss-Legendre quadrature. Table 13 shows the approximated values of T_{xy} and Q. The results in the table are consistent with our earlier results using the Chebyshev collocation method and are more accurate.

Next, we reconsider the steady case of equation (30) for the pure diffusive speculative reflection combined boundary condition. The equation we solve in this case simplifies

to equation (104):

$$\begin{aligned}
u(y) =& \frac{1}{\pi^{1/2}k}\int_{-1/2}^{1/2} u(s) I_{-1}\left(\frac{|y-s|}{k}\right) \mathrm{d}s \\
&- \frac{1-\alpha^-}{2\pi^{1/2}} J_0\left(\alpha^-\alpha^+, 1/k, y+1/2\right) \\
&+ \frac{\alpha^-(1-\alpha^+)}{2\pi^{1/2}} J_0\left(\alpha^-\alpha^+, 1/k, y+3/2\right) \\
&+ \frac{1-\alpha^+}{2\pi^{1/2}} J_0\left(\alpha^-\alpha^+, 1/k, 1/2-y\right) \\
&- \frac{\alpha^+(1-\alpha^-)}{2\pi^{1/2}} J_0\left(\alpha^-\alpha^+, 1/k, 3/2-y\right) \\
&+ \frac{\alpha^-}{\pi^{1/2}k}\int_{-1/2}^{1/2} u(s) J_{-1}\left(\alpha^-\alpha^+, 1/k, 1+y+s\right) \mathrm{d}s \\
&+ \frac{\alpha^-\alpha^+}{\pi^{1/2}k}\int_{-1/2}^{1/2} u(s) J_{-1}\left(\alpha^-\alpha^+, 1/k, 2+y-s\right) \mathrm{d}s \\
&+ \frac{\alpha^+}{\pi^{1/2}k}\int_{-1/2}^{1/2} u(s) J_{-1}\left(\alpha^-\alpha^+, 1/k, 1-y-s\right) \mathrm{d}s \\
&+ \frac{\alpha^-\alpha^+}{\pi^{1/2}k}\int_{-1/2}^{1/2} u(s) J_{-1}\left(\alpha^-\alpha^+, 1/k, 2-y+s\right) \mathrm{d}s. \qquad (104)
\end{aligned}$$

We take the same subdivision $\cup_{j=1}^{N} E_j$ of the interval $[-1/2, 1/2]$. We use the same order piece-wise, scaled and shifted Gauss-Legendre polynomial expansion from equation (95) to approximate $u(y)$. We end up with a linear system of the same form as equation (103) to solve. In the current case, as before $\Phi_{i,j}$ should be replaced by

$\boldsymbol{\Phi}_{i,j} + \delta\boldsymbol{\Phi}_{i,j}$, where the m^{th} row and n^{th} column entry of $\delta\boldsymbol{\Phi}_{i,j}$ reads

$$
\begin{aligned}
&\mathrm{ent}_{mn}\,\delta\Phi_{i,j}\\
=&\alpha^-\big[J_0(\alpha^-\alpha^+,1/k,1+y_{i,m}+y_j)+(-1)^nJ_0(\alpha^-\alpha^+,1/k,1+y_{i,m}+y_{j-1})\\
&-\int_{-1}^{1}J_0(\alpha^-\alpha^+,1/k,1+y_{i,m}+y_{j,s})L'_{n-1}(s)\,\mathrm{d}s\big]\\
&+\alpha^-\alpha^+\big[-J_0(\alpha^-\alpha^+,1/k,2+y_{i,m}-y_j)+(-1)^{n+1}J_0(\alpha^-\alpha^+,1/k,2+y_{i,m}-y_{j-1})\\
&+\int_{-1}^{1}J_0(\alpha^-\alpha^+,1/k,2+y_{i,m}-y_{j,s})L'_{n-1}(s)\,\mathrm{d}s\big]\\
&+\alpha^+\big[-J_0(\alpha^-\alpha^+,1/k,1-y_{i,m}-y_j)+(-1)^{n+1}J_0(\alpha^-\alpha^+,1/k,1-y_{i,m}-y_{j-1})\\
&+\int_{-1}^{1}J_0(\alpha^-\alpha^+,1/k,1-y_{i,m}-y_{j,s})L'_{n-1}(s)\,\mathrm{d}s\big]\\
&+\alpha^-\alpha^+\big[J_0(\alpha^-\alpha^+,1/k,2-y_{i,m}+y_j)+(-1)^nJ_0(\alpha^-\alpha^+,1/k,2-y_{i,m}+y_{j-1})\\
&-\int_{-1}^{1}J_0(\alpha^-\alpha^+,1/k,2-y_{i,m}+y_{j,s})L'_{n-1}(s)\,\mathrm{d}s\big],
\end{aligned}
\tag{105}
$$

where $|E_j| = y_j - y_{j-1}$, $y_{j,s} = y_{j-1} + \frac{s+1}{2}|E_j|$.
Meanwhile, $\boldsymbol{F}$ is modified as

$$\boldsymbol{F} = \frac{1}{2}(\tilde{\boldsymbol{F}}_{0,1}^T\,\tilde{\boldsymbol{F}}_{0,2}^T\cdots\tilde{\boldsymbol{F}}_{0,N}^T)^T,$$

in which $\tilde{\boldsymbol{F}}_{0,i}$ is an M-tuple column vector,

$$\tilde{\boldsymbol{F}}_{0,i} = (\tilde{F}_0(y_{i,1},k)\,\tilde{F}_0(y_{i,2},k)\cdots\tilde{F}_0(y_{i,M},k))^T,$$

and the function $\tilde{F}_0$ is defined by

$$
\begin{aligned}
&\tilde{F}_0(y,k)\\
=&(1-\alpha^+)J_0(\alpha^-\alpha^+,1/k,1/2-y)-(1-\alpha^-)J_0(\alpha^-\alpha^+,1/k,y+1/2)\\
&+\alpha^-(1-\alpha^+)J_0(\alpha^-\alpha^+,1/k,y+3/2)-\alpha^+(1-\alpha^-)J_0(\alpha^-\alpha^+,1/k,3/2-y).
\end{aligned}
$$

This time, in order to compute the coefficient matrix A and the RHS term $\boldsymbol{F}$ precisely, we need to evaluate both I_0 and J_0 with high precision. For I_0, we use Macleod's [1] method of Chebyshev expansion. For J_0, we use a truncated geometric series to express J_0 in terms of linear combinations of I_0. The general series expansion reads:

$$J_n(\alpha,\beta,x) = \sum_{j=0}^{\infty}\alpha^j I_n(\beta(x+2j)). \tag{106}$$

Equation (106) converges exponentially as long as $0 < \alpha < 1$.
Hence, to control the error the approximation,

$$J_0(\alpha, \beta, x) \approx \sum_{j=0}^{J-1} \alpha^j I_0(\beta(x + 2j)),$$

within ϵ_0, one only need to require $\alpha^J I_0(2\beta J) < \epsilon_0$.
Numerically, we choose $\epsilon_0 = 10^{-17}$ and solve J, so that J_0 will be evaluated with at least double precision. We solve equation (103) for the Couette flow with diffusive speculative combined boundary condition for Knudsen number $k =$ 0.003, 0.3, 1.0, 2.0, 10.0. The dimension of each subblock $\Phi_{i,j}P$ of the matrix A is as before, *i.e.*, $M = 10$. We use quadruple precision to ensure accuracy. Meanwhile, we vary the order of equation (103) by changing N with $40 \leq N \leq 320$, to ensure the convergence of the results. Table 14-23 gives the value of $u(y)$ at $y = -0.5, -0.25, 0, 0.25$ and 0.5 for various values of k, N and accommodation ratio $\alpha^{\pm}$. When $N = 320$, the results of $u(y)$ in Table 14-23 are accurate for at least 13 significant digits. Figure 3-7 show the velocity profiles of the Couette flow problem for $k = 0.003$, 0.3, 1.0, 2.0, 10.0 with various accommodation ratios at the upper and lower walls.
As the value of k increases to a big enough value, the Couette flow becomes free molecular flow. The velocity $u = \frac{\alpha^- - \alpha^+}{2(1-\alpha^-\alpha^+)}$ of free molecular Couette flow is derived in the Appendix E. Figure 8 shows the comparison between velocity profiles of the Couette flow for $k = 300$ and velocity profiles of the free molecular flow for various accommodation ratios. The agreement of profiles shows that when $k \geq 30$, the Couette flow can be viewed as free molecular flow.
We also computed the shear stress T_{xy}, the upper and lower half channel mass flow rates $Q^{\pm}$ of the Couette flow with various accommodation ratios by using equation (33), equation (107) and equation (108), respectively,

$$Q^+ = \int_0^{1/2} u(y)\,\mathrm{d}y, \tag{107}$$

$$Q^- = \int_{-1/2}^{0} u(y)\,\mathrm{d}y. \tag{108}$$

The integrals in the equations are computed piece-wise over each subinterval E_j by using a shifted and scaled 10^{th} order Gauss-Legendre quadrature. Table 24-26 give the value of T_{xy}, Q^- and Q^+ for $k = 0.003$, 0.3, 1.0, 2.0, 10.0 and various values of accommodation ratios $\alpha^{\pm}$, respectively.

TABLE 14: The values of the approximated velocity $u^N(y)$ of the Couette flow at $y = -0.5, -0.25$ and 0, for the Knudsen number $k = 0.003$ and $40 \leq N \leq 320$ and $\alpha^{\pm} = 0, 0.1, 0.5, 0.9$

y	-0.5	-0.25	0
N	$\alpha^- = 0.1, \alpha^+ = 0$		
40	$-4.973653565832297 \cdot 10^{-1}$	$-2.480143122501520 \cdot 10^{-1}$	$3.143938225217815 \cdot 10^{-4}$
80	$-4.973659175104077 \cdot 10^{-1}$	$-2.480143122751279 \cdot 10^{-1}$	$3.143938162678488 \cdot 10^{-4}$
160	$-4.973659177979278 \cdot 10^{-1}$	$-2.480143122752810 \cdot 10^{-1}$	$3.143938162515527 \cdot 10^{-4}$
320	$-4.973659177979334 \cdot 10^{-1}$	$-2.480143122753030 \cdot 10^{-1}$	$3.143938162489209 \cdot 10^{-4}$
N	$\alpha^- = 0.5, \alpha^+ = 0$		
40	$-4.929577678781215 \cdot 10^{-1}$	$-2.443897247635092 \cdot 10^{-1}$	$2.735676631881614 \cdot 10^{-3}$
80	$-4.929586007463435 \cdot 10^{-1}$	$-2.443897248845903 \cdot 10^{-1}$	$2.735676561377301 \cdot 10^{-3}$
160	$-4.929586011733882 \cdot 10^{-1}$	$-2.443897248848695 \cdot 10^{-1}$	$2.735676561276409 \cdot 10^{-3}$
320	$-4.929586011734089 \cdot 10^{-1}$	$-2.443897248849146 \cdot 10^{-1}$	$2.735676561258242 \cdot 10^{-3}$
N	$\alpha^- = 0.9, \alpha^+ = 0$		
40	$-4.531616813263772 \cdot 10^{-1}$	$-2.142247660429099 \cdot 10^{-1}$	$2.288635481647301 \cdot 10^{-2}$
80	$-4.531627902571524 \cdot 10^{-1}$	$-2.142247671704920 \cdot 10^{-1}$	$2.288635407318921 \cdot 10^{-2}$
160	$-4.531627908258160 \cdot 10^{-1}$	$-2.142247671712804 \cdot 10^{-1}$	$2.288635407274468 \cdot 10^{-2}$
320	$-4.531627908259885 \cdot 10^{-1}$	$-2.142247671714509 \cdot 10^{-1}$	$2.288635407264231 \cdot 10^{-2}$
N	$\alpha^- = 0.1, \alpha^+ = 0.1$		
40	$-4.973670121734446 \cdot 10^{-1}$	$-2.481726581713780 \cdot 10^{-1}$	0
80	$-4.973675727481073 \cdot 10^{-1}$	$-2.481726581931904 \cdot 10^{-1}$	0
160	$-4.973675730354466 \cdot 10^{-1}$	$-2.481726581933352 \cdot 10^{-1}$	0
320	$-4.973675730354522 \cdot 10^{-1}$	$-2.481726581933559 \cdot 10^{-1}$	0
N	$\alpha^- = 0.5, \alpha^+ = 0.1$		
40	$-4.929621717342966 \cdot 10^{-1}$	$-2.445495705154726 \cdot 10^{-1}$	$2.421291139374552 \cdot 10^{-3}$
80	$-4.929630040815979 \cdot 10^{-1}$	$-2.445495706333211 \cdot 10^{-1}$	$2.421291075123571 \cdot 10^{-3}$
160	$-4.929630045083754 \cdot 10^{-1}$	$-2.445495706335918 \cdot 10^{-1}$	$2.421291075038974 \cdot 10^{-3}$
320	$-4.929630045083960 \cdot 10^{-1}$	$-2.445495706336356 \cdot 10^{-1}$	$2.421291075023438 \cdot 10^{-3}$
N	$\alpha^- = 0.9, \alpha^+ = 0.1$		
40	$-4.531897854229757 \cdot 10^{-1}$	$-2.143962379276408 \cdot 10^{-1}$	$2.257261066335325 \cdot 10^{-2}$
80	$-4.531908936878510 \cdot 10^{-1}$	$-2.143962390514023 \cdot 10^{-1}$	$2.257260992626814 \cdot 10^{-2}$
160	$-4.531908942561719 \cdot 10^{-1}$	$-2.143962390521815 \cdot 10^{-1}$	$2.257260992583984 \cdot 10^{-2}$
320	$-4.531908942563441 \cdot 10^{-1}$	$-2.143962390523505 \cdot 10^{-1}$	$2.257260992574010 \cdot 10^{-2}$
N	$\alpha^- = 0.1, \alpha^+ = 0.5$		
40	$-4.973797626336336 \cdot 10^{-1}$	$-2.493921527942218 \cdot 10^{-1}$	$-2.421291139374552 \cdot 10^{-3}$
80	$-4.973803204933291 \cdot 10^{-1}$	$-2.493921527835682 \cdot 10^{-1}$	$-2.421291075123571 \cdot 10^{-3}$
160	$-4.973803207792765 \cdot 10^{-1}$	$-2.493921527836697 \cdot 10^{-1}$	$-2.421291075038974 \cdot 10^{-3}$
320	$-4.973803207792820 \cdot 10^{-1}$	$-2.493921527836825 \cdot 10^{-1}$	$-2.421291075023438 \cdot 10^{-3}$
N	$\alpha^- = 0.5, \alpha^+ = 0.5$		
40	$-4.929960887507939 \cdot 10^{-1}$	$-2.457806486412775 \cdot 10^{-1}$	0
80	$-4.929969170859144 \cdot 10^{-1}$	$-2.457806487260477 \cdot 10^{-1}$	0
160	$-4.929969175106339 \cdot 10^{-1}$	$-2.457806487262743 \cdot 10^{-1}$	0
320	$-4.929969175106543 \cdot 10^{-1}$	$-2.457806487263101 \cdot 10^{-1}$	0
N	$\alpha^- = 0.9, \alpha^+ = 0.5$		
40	$-4.534062814454845 \cdot 10^{-1}$	$-2.157171478841731 \cdot 10^{-1}$	$2.015572595767706 \cdot 10^{-2}$
80	$-4.534073845792502 \cdot 10^{-1}$	$-2.157171489697080 \cdot 10^{-1}$	$2.015572528443494 \cdot 10^{-2}$
160	$-4.534073851449353 \cdot 10^{-1}$	$-2.157171489704385 \cdot 10^{-1}$	$2.015572528409092 \cdot 10^{-2}$
320	$-4.534073851451054 \cdot 10^{-1}$	$-2.157171489705985 \cdot 10^{-1}$	$2.015572528400665 \cdot 10^{-2}$
N	$\alpha^- = 0.1, \alpha^+ = 0.9$		
40	$-4.974858789916249 \cdot 10^{-1}$	$-2.595414592543473 \cdot 10^{-1}$	$-2.257261066335325 \cdot 10^{-2}$
80	$-4.974864142551398 \cdot 10^{-1}$	$-2.595414589039385 \cdot 10^{-1}$	$-2.257260992626814 \cdot 10^{-2}$
160	$-4.974864145295048 \cdot 10^{-1}$	$-2.595414589038611 \cdot 10^{-1}$	$-2.257260992583984 \cdot 10^{-2}$
320	$-4.974864145295096 \cdot 10^{-1}$	$-2.595414589038307 \cdot 10^{-1}$	$-2.257260992574010 \cdot 10^{-2}$
N	$\alpha^- = 0.5, \alpha^+ = 0.9$		
40	$-4.932784265823357 \cdot 10^{-1}$	$-2.560285997995272 \cdot 10^{-1}$	$-2.015572595767706 \cdot 10^{-2}$
80	$-4.932792215166352 \cdot 10^{-1}$	$-2.560285995385778 \cdot 10^{-1}$	$-2.015572528443494 \cdot 10^{-2}$
160	$-4.932792219242289 \cdot 10^{-1}$	$-2.560285995386204 \cdot 10^{-1}$	$-2.015572528409092 \cdot 10^{-2}$
320	$-4.932792219242472 \cdot 10^{-1}$	$-2.560285995386118 \cdot 10^{-1}$	$-2.015572528400665 \cdot 10^{-2}$
N	$\alpha^- = 0.9, \alpha^+ = 0.9$		
40	$-4.552117604120091 \cdot 10^{-1}$	$-2.267329398398684 \cdot 10^{-1}$	0
80	$-4.552128207420271 \cdot 10^{-1}$	$-2.267329405296475 \cdot 10^{-1}$	0
160	$-4.552128212857627 \cdot 10^{-1}$	$-2.267329405301690 \cdot 10^{-1}$	0
320	$-4.552128212859188 \cdot 10^{-1}$	$-2.267329405302786 \cdot 10^{-1}$	0

TABLE 15: The values of the approximated velocity $u^N(y)$ of the Couette flow at $y = 0.25$ and 0.5, for the Knudsen number $k = 0.003$ and $40 \leq N \leq 320$ and $\alpha^{\pm} = 0, 0.1, 0.5, 0.9$

y	0.25	0.5
N	$\alpha^- = 0.1$, $\alpha^+ = 0$	
40	$2.486430998951956 \cdot 10^{-1}$	$4.978923621936468 \cdot 10^{-1}$
80	$2.486430999076636 \cdot 10^{-1}$	$4.978928607999532 \cdot 10^{-1}$
160	$2.486430999077841 \cdot 10^{-1}$	$4.978928610555076 \cdot 10^{-1}$
320	$2.486430999078009 \cdot 10^{-1}$	$4.978928610555117 \cdot 10^{-1}$
N	$\alpha^- = 0.5$, $\alpha^+ = 0$	
40	$2.498610780272724 \cdot 10^{-1}$	$4.979025749897046 \cdot 10^{-1}$
80	$2.498610780073449 \cdot 10^{-1}$	$4.979030711796869 \cdot 10^{-1}$
160	$2.498610780074223 \cdot 10^{-1}$	$4.979030714340027 \cdot 10^{-1}$
320	$2.498610780074311 \cdot 10^{-1}$	$4.979030714340067 \cdot 10^{-1}$
N	$\alpha^- = 0.9$, $\alpha^+ = 0$	
40	$2.599974756758559 \cdot 10^{-1}$	$4.979875690952791 \cdot 10^{-1}$
80	$2.599974753168704 \cdot 10^{-1}$	$4.979880451752697 \cdot 10^{-1}$
160	$2.599974753167697 \cdot 10^{-1}$	$4.979880454192784 \cdot 10^{-1}$
320	$2.599974753167355 \cdot 10^{-1}$	$4.979880454192818 \cdot 10^{-1}$
N	$\alpha^- = 0.1$, $\alpha^+ = 0.1$	
40	$2.481726581713780 \cdot 10^{-1}$	$4.973670121734446 \cdot 10^{-1}$
80	$2.481726581931904 \cdot 10^{-1}$	$4.973675727481073 \cdot 10^{-1}$
160	$2.481726581933352 \cdot 10^{-1}$	$4.973675730354466 \cdot 10^{-1}$
320	$2.481726581933559 \cdot 10^{-1}$	$4.973675730354522 \cdot 10^{-1}$
N	$\alpha^- = 0.5$, $\alpha^+ = 0.1$	
40	$2.493921527942218 \cdot 10^{-1}$	$4.973797626336336 \cdot 10^{-1}$
80	$2.493921527835682 \cdot 10^{-1}$	$4.973803204933291 \cdot 10^{-1}$
160	$2.493921527836697 \cdot 10^{-1}$	$4.973803207792765 \cdot 10^{-1}$
320	$2.493921527836825 \cdot 10^{-1}$	$4.973803207792820 \cdot 10^{-1}$
N	$\alpha^- = 0.9$, $\alpha^+ = 0.1$	
40	$2.595414592543473 \cdot 10^{-1}$	$4.974858789916249 \cdot 10^{-1}$
80	$2.595414589039386 \cdot 10^{-1}$	$4.974864142551398 \cdot 10^{-1}$
160	$2.595414589038611 \cdot 10^{-1}$	$4.974864145295048 \cdot 10^{-1}$
320	$2.595414589038307 \cdot 10^{-1}$	$4.974864145295096 \cdot 10^{-1}$
N	$\alpha^- = 0.1$, $\alpha^+ = 0.5$	
40	$2.445495705154727 \cdot 10^{-1}$	$4.929621717342966 \cdot 10^{-1}$
80	$2.445495706333211 \cdot 10^{-1}$	$4.929630040815979 \cdot 10^{-1}$
160	$2.445495706335918 \cdot 10^{-1}$	$4.929630045083754 \cdot 10^{-1}$
320	$2.445495706336356 \cdot 10^{-1}$	$4.929630045083960 \cdot 10^{-1}$
N	$\alpha^- = 0.5$, $\alpha^+ = 0.5$	
40	$2.457806486412775 \cdot 10^{-1}$	$4.929960887507939 \cdot 10^{-1}$
80	$2.457806487260477 \cdot 10^{-1}$	$4.929969170859144 \cdot 10^{-1}$
160	$2.457806487262743 \cdot 10^{-1}$	$4.929969175106339 \cdot 10^{-1}$
320	$2.457806487263101 \cdot 10^{-1}$	$4.929969175106543 \cdot 10^{-1}$
N	$\alpha^- = 0.9$, $\alpha^+ = 0.5$	
40	$2.560285997995272 \cdot 10^{-1}$	$4.932784265823357 \cdot 10^{-1}$
80	$2.560285995385778 \cdot 10^{-1}$	$4.932792215166352 \cdot 10^{-1}$
160	$2.560285995386204 \cdot 10^{-1}$	$4.932792219242289 \cdot 10^{-1}$
320	$2.560285995386118 \cdot 10^{-1}$	$4.932792219242472 \cdot 10^{-1}$
N	$\alpha^- = 0.1$, $\alpha^+ = 0.9$	
40	$2.143962379276408 \cdot 10^{-1}$	$4.531897854229757 \cdot 10^{-1}$
80	$2.143962390514023 \cdot 10^{-1}$	$4.531908936878510 \cdot 10^{-1}$
160	$2.143962390521815 \cdot 10^{-1}$	$4.531908942561719 \cdot 10^{-1}$
320	$2.143962390523505 \cdot 10^{-1}$	$4.531908942563441 \cdot 10^{-1}$
N	$\alpha^- = 0.5$, $\alpha^+ = 0.9$	
40	$2.157171478841731 \cdot 10^{-1}$	$4.534062814454845 \cdot 10^{-1}$
80	$2.157171489697080 \cdot 10^{-1}$	$4.534073845792502 \cdot 10^{-1}$
160	$2.157171489704385 \cdot 10^{-1}$	$4.534073851449353 \cdot 10^{-1}$
320	$2.157171489705985 \cdot 10^{-1}$	$4.534073851451054 \cdot 10^{-1}$
N	$\alpha^- = 0.9$, $\alpha^+ = 0.9$	
40	$2.267329398398684 \cdot 10^{-1}$	$4.552117604120091 \cdot 10^{-1}$
80	$2.267329405296475 \cdot 10^{-1}$	$4.552128207420271 \cdot 10^{-1}$
160	$2.267329405301690 \cdot 10^{-1}$	$4.552128212857627 \cdot 10^{-1}$
320	$2.267329405302786 \cdot 10^{-1}$	$4.552128212859188 \cdot 10^{-1}$

TABLE 16: The values of the approximated velocity $u^N(y)$ of the Couette flow at $y = -0.5, -0.25$ and 0, for the Knudsen number $k = 0.3$ and $40 \leq N \leq 320$ and $\alpha^{\pm} = 0, 0.1, 0.5, 0.9$

y	-0.5	-0.25	0
N	$\alpha^- = 0.1,\ \alpha^+ = 0$		
40	$-3.403395737761162 \cdot 10^{-1}$	$-1.438796507326413 \cdot 10^{-1}$	$1.828445577046693 \cdot 10^{-2}$
80	$-3.403399142618361 \cdot 10^{-1}$	$-1.438796507327614 \cdot 10^{-1}$	$1.828445577043595 \cdot 10^{-2}$
160	$-3.403399144360987 \cdot 10^{-1}$	$-1.438796507327614 \cdot 10^{-1}$	$1.828445577043594 \cdot 10^{-2}$
320	$-3.403399144360988 \cdot 10^{-1}$	$-1.438796507327614 \cdot 10^{-1}$	$1.828445577043595 \cdot 10^{-2}$
N	$\alpha^- = 0.5,\ \alpha^+ = 0$		
40	$-1.688916247974614 \cdot 10^{-1}$	$-2.460582575751259 \cdot 10^{-3}$	$1.256026835278990 \cdot 10^{-1}$
80	$-1.688920170784959 \cdot 10^{-1}$	$-2.460582576118213 \cdot 10^{-3}$	$1.256026835276786 \cdot 10^{-1}$
160	$-1.688920172792688 \cdot 10^{-1}$	$-2.460582576118222 \cdot 10^{-3}$	$1.256026835276786 \cdot 10^{-1}$
320	$-1.688920172792689 \cdot 10^{-1}$	$-2.460582576118223 \cdot 10^{-3}$	$1.256026835276786 \cdot 10^{-1}$
N	$\alpha^- = 0.9,\ \alpha^+ = 0$		
40	$2.687193265588022 \cdot 10^{-1}$	$3.298540473557721 \cdot 10^{-1}$	$3.737556991235644 \cdot 10^{-1}$
80	$2.687191444111723 \cdot 10^{-1}$	$3.298540473553485 \cdot 10^{-1}$	$3.737556991232718 \cdot 10^{-1}$
160	$2.687191443179471 \cdot 10^{-1}$	$3.298540473553485 \cdot 10^{-1}$	$3.737556991232718 \cdot 10^{-1}$
320	$2.687191443179471 \cdot 10^{-1}$	$3.298540473553485 \cdot 10^{-1}$	$3.737556991232718 \cdot 10^{-1}$
N	$\alpha^- = 0.1,\ \alpha^+ = 0.1$		
40	$-3.460745244874303 \cdot 10^{-1}$	$-1.565901938908892 \cdot 10^{-1}$	0
80	$-3.460748527430044 \cdot 10^{-1}$	$-1.565901938909850 \cdot 10^{-1}$	0
160	$-3.460748529110076 \cdot 10^{-1}$	$-1.565901938909850 \cdot 10^{-1}$	0
320	$-3.460748529110077 \cdot 10^{-1}$	$-1.565901938909850 \cdot 10^{-1}$	0
N	$\alpha^- = 0.5,\ \alpha^+ = 0.1$		
40	$-1.781782994066064 \cdot 10^{-1}$	$-1.635734327977227 \cdot 10^{-2}$	$1.083110471487726 \cdot 10^{-1}$
80	$-1.781786806852322 \cdot 10^{-1}$	$-1.635734328011383 \cdot 10^{-2}$	$1.083110471485781 \cdot 10^{-1}$
160	$-1.781786808803740 \cdot 10^{-1}$	$-1.635734328011383 \cdot 10^{-2}$	$1.083110471485781 \cdot 10^{-1}$
320	$-1.781786808803741 \cdot 10^{-1}$	$-1.635734328011384 \cdot 10^{-2}$	$1.083110471485781 \cdot 10^{-1}$
N	$\alpha^- = 0.9,\ \alpha^+ = 0.1$		
40	$2.613410772114594 \cdot 10^{-1}$	$3.219070317818373 \cdot 10^{-1}$	$3.654546221144794 \cdot 10^{-1}$
80	$2.613408968120973 \cdot 10^{-1}$	$3.219070317814132 \cdot 10^{-1}$	$3.654546221141851 \cdot 10^{-1}$
160	$2.613408967197669 \cdot 10^{-1}$	$3.219070317814132 \cdot 10^{-1}$	$3.654546221141851 \cdot 10^{-1}$
320	$2.613408967197669 \cdot 10^{-1}$	$3.219070317814132 \cdot 10^{-1}$	$3.654546221141851 \cdot 10^{-1}$
N	$\alpha^- = 0.1,\ \alpha^+ = 0.5$		
40	$-3.797478901675806 \cdot 10^{-1}$	$-2.314544470159641 \cdot 10^{-1}$	$-1.083110471487726 \cdot 10^{-1}$
80	$-3.797481466125853 \cdot 10^{-1}$	$-2.314544470159075 \cdot 10^{-1}$	$-1.083110471485781 \cdot 10^{-1}$
160	$-3.797481467438154 \cdot 10^{-1}$	$-2.314544470159075 \cdot 10^{-1}$	$-1.083110471485781 \cdot 10^{-1}$
320	$-3.797481467438155 \cdot 10^{-1}$	$-2.314544470159075 \cdot 10^{-1}$	$-1.083110471485781 \cdot 10^{-1}$
N	$\alpha^- = 0.5,\ \alpha^+ = 0.5$		
40	$-2.359373435896947 \cdot 10^{-1}$	$-1.029628108979324 \cdot 10^{-1}$	0
80	$-2.359376564381444 \cdot 10^{-1}$	$-1.029628108980881 \cdot 10^{-1}$	0
160	$-2.359376565982631 \cdot 10^{-1}$	$-1.029628108980881 \cdot 10^{-1}$	0
320	$-2.359376565982631 \cdot 10^{-1}$	$-1.029628108980881 \cdot 10^{-1}$	0
N	$\alpha^- = 0.9,\ \alpha^+ = 0.5$		
40	$2.083008351580724 \cdot 10^{-1}$	$2.647169500005161 \cdot 10^{-1}$	$3.054908788361871 \cdot 10^{-1}$
80	$2.083006673265707 \cdot 10^{-1}$	$2.647169500001255 \cdot 10^{-1}$	$3.054908788359191 \cdot 10^{-1}$
160	$2.083006672406727 \cdot 10^{-1}$	$2.647169500001254 \cdot 10^{-1}$	$3.054908788359191 \cdot 10^{-1}$
320	$2.083006672406726 \cdot 10^{-1}$	$2.647169500001254 \cdot 10^{-1}$	$3.054908788359191 \cdot 10^{-1}$
N	$\alpha^- = 0.1,\ \alpha^+ = 0.9$		
40	$-4.588119504461960 \cdot 10^{-1}$	$-4.079251865117673 \cdot 10^{-1}$	$-3.654546221144794 \cdot 10^{-1}$
80	$-4.588120382821635 \cdot 10^{-1}$	$-4.079251865115932 \cdot 10^{-1}$	$-3.654546221141850 \cdot 10^{-1}$
160	$-4.588120383271186 \cdot 10^{-1}$	$-4.079251865115932 \cdot 10^{-1}$	$-3.654546221141851 \cdot 10^{-1}$
320	$-4.588120383271186 \cdot 10^{-1}$	$-4.079251865115932 \cdot 10^{-1}$	$-3.654546221141851 \cdot 10^{-1}$
N	$\alpha^- = 0.5,\ \alpha^+ = 0.9$		
40	$-3.974628278221813 \cdot 10^{-1}$	$-3.457472849566265 \cdot 10^{-1}$	$-3.054908788361871 \cdot 10^{-1}$
80	$-3.974629493030403 \cdot 10^{-1}$	$-3.457472849564759 \cdot 10^{-1}$	$-3.054908788359191 \cdot 10^{-1}$
160	$-3.974629493652154 \cdot 10^{-1}$	$-3.457472849564759 \cdot 10^{-1}$	$-3.054908788359191 \cdot 10^{-1}$
320	$-3.974629493652154 \cdot 10^{-1}$	$-3.457472849564759 \cdot 10^{-1}$	$-3.054908788359191 \cdot 10^{-1}$
N	$\alpha^- = 0.9,\ \alpha^+ = 0.9$		
40	$-6.052122943999570 \cdot 10^{-2}$	$-2.547081487435013 \cdot 10^{-2}$	0
80	$-6.052133357410923 \cdot 10^{-2}$	$-2.547081487443600 \cdot 10^{-2}$	0
160	$-6.052133362740629 \cdot 10^{-2}$	$-2.547081487443600 \cdot 10^{-2}$	0
320	$-6.052133362740632 \cdot 10^{-2}$	$-2.547081487443600 \cdot 10^{-2}$	0

TABLE 17: The values of the approximated velocity $u^N(y)$ of the Couette flow at $y = 0.25$ and 0.5, for the Knudsen number $k = 0.3$ and $40 \leq N \leq 320$ and $\alpha^{\pm} = 0, 0.1, 0.5, 0.9$

y	0.25	0.5
N	$\alpha^- = 0.1,\ \alpha^+ = 0$	
40	$1.799605066181221 \cdot 10^{-1}$	$3.721600156384742 \cdot 10^{-1}$
80	$1.799605066181782 \cdot 10^{-1}$	$3.721603185573492 \cdot 10^{-1}$
160	$1.799605066181782 \cdot 10^{-1}$	$3.721603187123847 \cdot 10^{-1}$
320	$1.799605066181782 \cdot 10^{-1}$	$3.721603187123848 \cdot 10^{-1}$
N	$\alpha^- = 0.5,\ \alpha^+ = 0$	
40	$2.517194363565842 \cdot 10^{-1}$	$4.009339692328798 \cdot 10^{-1}$
80	$2.517194363564994 \cdot 10^{-1}$	$4.009342039713626 \cdot 10^{-1}$
160	$2.517194363564994 \cdot 10^{-1}$	$4.009342040915031 \cdot 10^{-1}$
320	$2.517194363564994 \cdot 10^{-1}$	$4.009342040915031 \cdot 10^{-1}$
N	$\alpha^- = 0.9,\ \alpha^+ = 0$	
40	$4.164435956764891 \cdot 10^{-1}$	$4.666989925154014 \cdot 10^{-1}$
80	$4.164435956763170 \cdot 10^{-1}$	$4.666990714225932 \cdot 10^{-1}$
160	$4.164435956763170 \cdot 10^{-1}$	$4.666990714629784 \cdot 10^{-1}$
320	$4.164435956763170 \cdot 10^{-1}$	$4.666990714629784 \cdot 10^{-1}$
N	$\alpha^- = 0.1,\ \alpha^+ = 0.1$	
40	$1.565901938908892 \cdot 10^{-1}$	$3.460745244874303 \cdot 10^{-1}$
80	$1.565901938909850 \cdot 10^{-1}$	$3.460748527430044 \cdot 10^{-1}$
160	$1.565901938909850 \cdot 10^{-1}$	$3.460748529110076 \cdot 10^{-1}$
320	$1.565901938909850 \cdot 10^{-1}$	$3.460748529110077 \cdot 10^{-1}$
N	$\alpha^- = 0.5,\ \alpha^+ = 0.1$	
40	$2.314544470159641 \cdot 10^{-1}$	$3.797478901675806 \cdot 10^{-1}$
80	$2.314544470159075 \cdot 10^{-1}$	$3.797481466125653 \cdot 10^{-1}$
160	$2.314544470159075 \cdot 10^{-1}$	$3.797481467438155 \cdot 10^{-1}$
320	$2.314544470159075 \cdot 10^{-1}$	$3.797481467438155 \cdot 10^{-1}$
N	$\alpha^- = 0.9,\ \alpha^+ = 0.1$	
40	$4.079251865117673 \cdot 10^{-1}$	$4.588119504461960 \cdot 10^{-1}$
80	$4.079251865115932 \cdot 10^{-1}$	$4.588120382821635 \cdot 10^{-1}$
160	$4.079251865115932 \cdot 10^{-1}$	$4.588120383271186 \cdot 10^{-1}$
320	$4.079251865115932 \cdot 10^{-1}$	$4.588120383271186 \cdot 10^{-1}$
N	$\alpha^- = 0.1,\ \alpha^+ = 0.5$	
40	$1.635734327977227 \cdot 10^{-2}$	$1.781782994066064 \cdot 10^{-1}$
80	$1.635734328011383 \cdot 10^{-2}$	$1.781786806853222 \cdot 10^{-1}$
160	$1.635734328011384 \cdot 10^{-2}$	$1.781786808803740 \cdot 10^{-1}$
320	$1.635734328011384 \cdot 10^{-2}$	$1.781786808803741 \cdot 10^{-1}$
N	$\alpha^- = 0.5,\ \alpha^+ = 0.5$	
40	$1.029628108979324 \cdot 10^{-1}$	$2.359373435896947 \cdot 10^{-1}$
80	$1.029628108980881 \cdot 10^{-1}$	$2.359376564381444 \cdot 10^{-1}$
160	$1.029628108980881 \cdot 10^{-1}$	$2.359376565982631 \cdot 10^{-1}$
320	$1.029628108980881 \cdot 10^{-1}$	$2.359376565982631 \cdot 10^{-1}$
N	$\alpha^- = 0.9,\ \alpha^+ = 0.5$	
40	$3.457472849566265 \cdot 10^{-1}$	$3.974628278221813 \cdot 10^{-1}$
80	$3.457472849564759 \cdot 10^{-1}$	$3.974629493030403 \cdot 10^{-1}$
160	$3.457472849564759 \cdot 10^{-1}$	$3.974629493652154 \cdot 10^{-1}$
320	$3.457472849564759 \cdot 10^{-1}$	$3.974629493652154 \cdot 10^{-1}$
N	$\alpha^- = 0.1,\ \alpha^+ = 0.9$	
40	$-3.219070317818373 \cdot 10^{-1}$	$-2.613410772114594 \cdot 10^{-1}$
80	$-3.219070317814132 \cdot 10^{-1}$	$-2.613408968120973 \cdot 10^{-1}$
160	$-3.219070317814132 \cdot 10^{-1}$	$-2.613408967197669 \cdot 10^{-1}$
320	$-3.219070317814132 \cdot 10^{-1}$	$-2.613408967197669 \cdot 10^{-1}$
N	$\alpha^- = 0.5,\ \alpha^+ = 0.9$	
40	$-2.647169500005161 \cdot 10^{-1}$	$-2.083008351580724 \cdot 10^{-1}$
80	$-2.647169500001255 \cdot 10^{-1}$	$-2.083006673265707 \cdot 10^{-1}$
160	$-2.647169500001254 \cdot 10^{-1}$	$-2.083006672406727 \cdot 10^{-1}$
320	$-2.647169500001254 \cdot 10^{-1}$	$-2.083006672406726 \cdot 10^{-1}$
N	$\alpha^- = 0.9,\ \alpha^+ = 0.9$	
40	$2.547081487435013 \cdot 10^{-2}$	$6.052122943999570 \cdot 10^{-2}$
80	$2.547081487443600 \cdot 10^{-2}$	$6.052133357410923 \cdot 10^{-2}$
160	$2.547081487443600 \cdot 10^{-2}$	$6.052133362740629 \cdot 10^{-2}$
320	$2.547081487443600 \cdot 10^{-2}$	$6.052133362740632 \cdot 10^{-2}$

TABLE 18: The values of the approximated velocity $u^N(y)$ of the Couette flow at $y = -0.5, -0.25$ and 0, for the Knudsen number $k = 1$ and $40 \leq N \leq 320$ and $\alpha^{\pm} = 0, 0.1, 0.5, 0.9$

y	-0.5	-0.25	0
N	$\alpha^- = 0.1, \alpha^+ = 0$		
40	$-2.109264974895379 \cdot 10^{-1}$	$-7.657954878285799 \cdot 10^{-2}$	$3.045502957107436 \cdot 10^{-2}$
80	$-2.109266824327677 \cdot 10^{-1}$	$-7.657954878287711 \cdot 10^{-2}$	$3.045502957106962 \cdot 10^{-2}$
160	$-2.109266825274213 \cdot 10^{-1}$	$-7.657954878287711 \cdot 10^{-2}$	$3.045502957106962 \cdot 10^{-2}$
320	$-2.109266825274214 \cdot 10^{-1}$	$-7.657954878287711 \cdot 10^{-2}$	$3.045502957106962 \cdot 10^{-2}$
N	$\alpha^- = 0.5, \alpha^+ = 0$		
40	$7.373121237020718 \cdot 10^{-2}$	$1.087164245203674 \cdot 10^{-1}$	$1.835790423113157 \cdot 10^{-1}$
80	$7.372940900209559 \cdot 10^{-2}$	$1.087164245203247 \cdot 10^{-1}$	$1.835790423112905 \cdot 10^{-1}$
160	$7.372940807913324 \cdot 10^{-2}$	$1.087164245203246 \cdot 10^{-1}$	$1.835790423112905 \cdot 10^{-1}$
320	$7.372940807913279 \cdot 10^{-2}$	$1.087164245203247 \cdot 10^{-1}$	$1.835790423112905 \cdot 10^{-1}$
N	$\alpha^- = 0.9, \alpha^+ = 0$		
40	$3.705543113321463 \cdot 10^{-1}$	$3.993551453888850 \cdot 10^{-1}$	$4.191975979772947 \cdot 10^{-1}$
80	$3.705542494476108 \cdot 10^{-1}$	$3.993551453888577 \cdot 10^{-1}$	$4.191975979772760 \cdot 10^{-1}$
160	$3.705542494159383 \cdot 10^{-1}$	$3.993551453888577 \cdot 10^{-1}$	$4.191975979772760 \cdot 10^{-1}$
320	$3.705542494159383 \cdot 10^{-1}$	$3.993551453888577 \cdot 10^{-1}$	$4.191975979772760 \cdot 10^{-1}$
N	$\alpha^- = 0.1, \alpha^+ = 0.1$		
40	$-2.279354772021872 \cdot 10^{-1}$	$-1.012535691998093 \cdot 10^{-1}$	0
80	$-2.279356512634220 \cdot 10^{-1}$	$-1.012535691998240 \cdot 10^{-1}$	0
160	$-2.279356513525062 \cdot 10^{-1}$	$-1.012535691998240 \cdot 10^{-1}$	0
320	$-2.279356513525063 \cdot 10^{-1}$	$-1.012535691998240 \cdot 10^{-1}$	0
N	$\alpha^- = 0.5, \alpha^+ = 0.1$		
40	$-1.289959652255936 \cdot 10^{-2}$	$8.451562408585686 \cdot 10^{-2}$	$1.567048378339302 \cdot 10^{-1}$
80	$-1.289976965378952 \cdot 10^{-2}$	$8.451562408581767 \cdot 10^{-2}$	$1.567048378339083 \cdot 10^{-1}$
160	$-1.289976974239795 \cdot 10^{-2}$	$8.451562408581767 \cdot 10^{-2}$	$1.567048378339083 \cdot 10^{-1}$
320	$-1.289976974239799 \cdot 10^{-2}$	$8.451562408581767 \cdot 10^{-2}$	$1.567048378339083 \cdot 10^{-1}$
N	$\alpha^- = 0.9, \alpha^+ = 0.1$		
40	$3.615238657001369 \cdot 10^{-1}$	$3.900484622997055 \cdot 10^{-1}$	$4.097590705974012 \cdot 10^{-1}$
80	$3.615238044575424 \cdot 10^{-1}$	$3.900484622996779 \cdot 10^{-1}$	$4.097590705973822 \cdot 10^{-1}$
160	$3.615238044261984 \cdot 10^{-1}$	$3.900484622996779 \cdot 10^{-1}$	$4.097590705973822 \cdot 10^{-1}$
320	$3.615238044261984 \cdot 10^{-1}$	$3.900484622996779 \cdot 10^{-1}$	$4.097590705973822 \cdot 10^{-1}$
N	$\alpha^- = 0.1, \alpha^+ = 0.5$		
40	$-3.143654349720722 \cdot 10^{-1}$	$-2.272511955128323 \cdot 10^{-1}$	$-1.567048378339302 \cdot 10^{-1}$
80	$-3.143655537372018 \cdot 10^{-1}$	$-2.272511955128258 \cdot 10^{-1}$	$-1.567048378339083 \cdot 10^{-1}$
160	$-3.143655537979856 \cdot 10^{-1}$	$-2.272511955128258 \cdot 10^{-1}$	$-1.567048378339083 \cdot 10^{-1}$
320	$-3.143655537979856 \cdot 10^{-1}$	$-2.272511955128258 \cdot 10^{-1}$	$-1.567048378339083 \cdot 10^{-1}$
N	$\alpha^- = 0.5, \alpha^+ = 0.5$		
40	$-1.301734542462826 \cdot 10^{-1}$	$-5.582382954301948 \cdot 10^{-2}$	0
80	$-1.301735856945808 \cdot 10^{-1}$	$-5.582382954303522 \cdot 10^{-2}$	0
160	$-1.301735857618557 \cdot 10^{-1}$	$-5.582382954303522 \cdot 10^{-2}$	0
320	$-1.301735857618558 \cdot 10^{-1}$	$-5.582382954303522 \cdot 10^{-2}$	0
N	$\alpha^- = 0.9, \alpha^+ = 0.5$		
40	$2.958528843957777 \cdot 10^{-1}$	$3.222920158549017 \cdot 10^{-1}$	$3.407911563618258 \cdot 10^{-1}$
80	$2.958528278214937 \cdot 10^{-1}$	$3.222920158548758 \cdot 10^{-1}$	$3.407911563618080 \cdot 10^{-1}$
160	$2.958528277925390 \cdot 10^{-1}$	$3.222920158548758 \cdot 10^{-1}$	$3.407911563618080 \cdot 10^{-1}$
320	$2.958528277925389 \cdot 10^{-1}$	$3.222920158548758 \cdot 10^{-1}$	$3.407911563618080 \cdot 10^{-1}$
N	$\alpha^- = 0.1, \alpha^+ = 0.9$		
40	$-4.515215605392093 \cdot 10^{-1}$	$-4.285850175828079 \cdot 10^{-1}$	$-4.097590705974012 \cdot 10^{-1}$
80	$-4.515215915546983 \cdot 10^{-1}$	$-4.285850175827960 \cdot 10^{-1}$	$-4.097590705973822 \cdot 10^{-1}$
160	$-4.515215915705720 \cdot 10^{-1}$	$-4.285850175827960 \cdot 10^{-1}$	$-4.097590705973822 \cdot 10^{-1}$
320	$-4.515215915705720 \cdot 10^{-1}$	$-4.285850175827960 \cdot 10^{-1}$	$-4.097590705973822 \cdot 10^{-1}$
N	$\alpha^- = 0.5, \alpha^+ = 0.9$		
40	$-3.825992818743259 \cdot 10^{-1}$	$-3.588626354470207 \cdot 10^{-1}$	$-3.407911563618258 \cdot 10^{-1}$
80	$-3.825993236023198 \cdot 10^{-1}$	$-3.588626354470103 \cdot 10^{-1}$	$-3.407911563618080 \cdot 10^{-1}$
160	$-3.825993236236761 \cdot 10^{-1}$	$-3.588626354470103 \cdot 10^{-1}$	$-3.407911563618080 \cdot 10^{-1}$
320	$-3.825993236236761 \cdot 10^{-1}$	$-3.588626354470103 \cdot 10^{-1}$	$-3.407911563618080 \cdot 10^{-1}$
N	$\alpha^- = 0.9, \alpha^+ = 0.9$		
40	$-2.696231867151717 \cdot 10^{-2}$	$-1.118826068834401 \cdot 10^{-2}$	0
80	$-2.696235229803405 \cdot 10^{-2}$	$-1.118826068834936 \cdot 10^{-2}$	0
160	$-2.696235231524411 \cdot 10^{-2}$	$-1.118826068834936 \cdot 10^{-2}$	0
320	$-2.696235231524412 \cdot 10^{-2}$	$-1.118826068834936 \cdot 10^{-2}$	0

TABLE 19: The values of the approximated velocity $u^N(y)$ of the Couette flow at $y = 0.25$ and 0.5, for the Knudsen number $k = 1$ and $40 \leq N \leq 320$ and $\alpha^{\pm} = 0, 0.1, 0.5, 0.9$

y	0.25	0.5
N	$\alpha^- = 0.1$, $\alpha^+ = 0$	
40	$1.368731713732195 \cdot 10^{-1}$	$2.673902362028769 \cdot 10^{-1}$
80	$1.368731713732286 \cdot 10^{-1}$	$2.673904015572797 \cdot 10^{-1}$
160	$1.368731713732286 \cdot 10^{-1}$	$2.673904016419077 \cdot 10^{-1}$
320	$1.368731713732286 \cdot 10^{-1}$	$2.673904016419078 \cdot 10^{-1}$
N	$\alpha^- = 0.5$, $\alpha^+ = 0$	
40	$2.563219462178745 \cdot 10^{-1}$	$3.443876933492997 \cdot 10^{-1}$
80	$2.563219462178645 \cdot 10^{-1}$	$3.443878039688068 \cdot 10^{-1}$
160	$2.563219462178645 \cdot 10^{-1}$	$3.443878040254216 \cdot 10^{-1}$
320	$2.563219462178645 \cdot 10^{-1}$	$3.443878040254217 \cdot 10^{-1}$
N	$\alpha^- = 0.9$, $\alpha^+ = 0$	
40	$4.380451963883620 \cdot 10^{-1}$	$4.605631577708625 \cdot 10^{-1}$
80	$4.380451963883503 \cdot 10^{-1}$	$4.605631858051690 \cdot 10^{-1}$
160	$4.380451963883503 \cdot 10^{-1}$	$4.605631858195169 \cdot 10^{-1}$
320	$4.380451963883503 \cdot 10^{-1}$	$4.605631858195169 \cdot 10^{-1}$
N	$\alpha^- = 0.1$, $\alpha^+ = 0.1$	
40	$1.012535691998093 \cdot 10^{-1}$	$2.279354772021872 \cdot 10^{-1}$
80	$1.012535691998240 \cdot 10^{-1}$	$2.279356512634220 \cdot 10^{-1}$
160	$1.012535691998240 \cdot 10^{-1}$	$2.279356513525062 \cdot 10^{-1}$
320	$1.012535691998240 \cdot 10^{-1}$	$2.279356513525063 \cdot 10^{-1}$
N	$\alpha^- = 0.5$, $\alpha^+ = 0.1$	
40	$2.272511955128323 \cdot 10^{-1}$	$3.143654349720722 \cdot 10^{-1}$
80	$2.272511955128258 \cdot 10^{-1}$	$3.143655537372018 \cdot 10^{-1}$
160	$2.272511955128258 \cdot 10^{-1}$	$3.143655537979856 \cdot 10^{-1}$
320	$2.272511955128258 \cdot 10^{-1}$	$3.143655537979856 \cdot 10^{-1}$
N	$\alpha^- = 0.9$, $\alpha^+ = 0.1$	
40	$4.285850175828079 \cdot 10^{-1}$	$4.515215605392093 \cdot 10^{-1}$
80	$4.285850175827960 \cdot 10^{-1}$	$4.515215915546983 \cdot 10^{-1}$
160	$4.285850175827960 \cdot 10^{-1}$	$4.515215915705720 \cdot 10^{-1}$
320	$4.285850175827960 \cdot 10^{-1}$	$4.515215915705720 \cdot 10^{-1}$
N	$\alpha^- = 0.1$, $\alpha^+ = 0.5$	
40	$-8.451562408585686 \cdot 10^{-2}$	$1.289959652255936 \cdot 10^{-2}$
80	$-8.451562408581767 \cdot 10^{-2}$	$1.289976965378952 \cdot 10^{-2}$
160	$-8.451562408581767 \cdot 10^{-2}$	$1.289976974239795 \cdot 10^{-2}$
320	$-8.451562408581767 \cdot 10^{-2}$	$1.289976974239799 \cdot 10^{-2}$
N	$\alpha^- = 0.5$, $\alpha^+ = 0.5$	
40	$5.582382954301946 \cdot 10^{-2}$	$1.301734542462826 \cdot 10^{-1}$
80	$5.582382954303522 \cdot 10^{-1}$	$1.301735856945806 \cdot 10^{-1}$
160	$5.582382954303522 \cdot 10^{-1}$	$1.301735857618557 \cdot 10^{-1}$
320	$5.582382954303522 \cdot 10^{-2}$	$1.301735857618558 \cdot 10^{-1}$
N	$\alpha^- = 0.9$, $\alpha^+ = 0.5$	
40	$3.588626354470207 \cdot 10^{-1}$	$3.825992818743259 \cdot 10^{-1}$
80	$3.588626354470103 \cdot 10^{-1}$	$3.825993236023198 \cdot 10^{-1}$
160	$3.588626354470103 \cdot 10^{-1}$	$3.825993236236761 \cdot 10^{-1}$
320	$3.588626354470103 \cdot 10^{-1}$	$3.825993236236761 \cdot 10^{-1}$
N	$\alpha^- = 0.1$, $\alpha^+ = 0.9$	
40	$-3.900484622997055 \cdot 10^{-1}$	$-3.615238657001369 \cdot 10^{-1}$
80	$-3.900484622996779 \cdot 10^{-1}$	$-3.615238044575424 \cdot 10^{-1}$
160	$-3.900484622996779 \cdot 10^{-1}$	$-3.615238044261984 \cdot 10^{-1}$
320	$-3.900484622996779 \cdot 10^{-1}$	$-3.615238044261984 \cdot 10^{-1}$
N	$\alpha^- = 0.5$, $\alpha^+ = 0.9$	
40	$-3.222920158549017 \cdot 10^{-1}$	$-2.958528843957777 \cdot 10^{-1}$
80	$-3.222920158548758 \cdot 10^{-1}$	$-2.958528278214937 \cdot 10^{-1}$
160	$-3.222920158548758 \cdot 10^{-1}$	$-2.958528277925390 \cdot 10^{-1}$
320	$-3.222920158548758 \cdot 10^{-1}$	$-2.958528277925389 \cdot 10^{-1}$
N	$\alpha^- = 0.9$, $\alpha^+ = 0.9$	
40	$1.118826068834401 \cdot 10^{-2}$	$2.696231867151717 \cdot 10^{-2}$
80	$1.118826068834936 \cdot 10^{-2}$	$2.696235229803405 \cdot 10^{-2}$
160	$1.118826068834936 \cdot 10^{-2}$	$2.696235231524411 \cdot 10^{-2}$
320	$1.118826068834936 \cdot 10^{-2}$	$2.696235231524412 \cdot 10^{-2}$

TABLE 20: The values of the approximated velocity $u^N(y)$ of the Couette flow at $y = -0.5, -0.25$ and 0, for the Knudsen number $k = 2$ and $40 \leq N \leq 320$ and $\alpha^{\pm} = 0, 0.1, 0.5, 0.9$

y	-0.5	-0.25	0
N	$\alpha^- = 0.1$, $\alpha^+ = 0$		
40	$-1.394003828510785 \cdot 10^{-1}$	$-4.191643274346711 \cdot 10^{-2}$	$3.625033272939019 \cdot 10^{-2}$
80	$-1.394004982036027 \cdot 10^{-1}$	$-4.191643274347313 \cdot 10^{-2}$	$3.625033272938870 \cdot 10^{-2}$
160	$-1.394004982626397 \cdot 10^{-1}$	$-4.191643274347313 \cdot 10^{-2}$	$3.625033272938870 \cdot 10^{-2}$
320	$-1.394004982626398 \cdot 10^{-1}$	$-4.191643274347313 \cdot 10^{-2}$	$3.625033272938870 \cdot 10^{-2}$
N	$\alpha^- = 0.5$, $\alpha^+ = 0$		
40	$8.494005301864806 \cdot 10^{-2}$	$1.543115856264126 \cdot 10^{-1}$	$2.061726546203782 \cdot 10^{-1}$
80	$8.493994906486309 \cdot 10^{-2}$	$1.543115856264008 \cdot 10^{-1}$	$2.061726546203713 \cdot 10^{-1}$
160	$8.493994901165987 \cdot 10^{-2}$	$1.543115856264008 \cdot 10^{-1}$	$2.061726546203713 \cdot 10^{-1}$
320	$8.493994901165984 \cdot 10^{-2}$	$1.543115856264008 \cdot 10^{-1}$	$2.061726546203713 \cdot 10^{-1}$
N	$\alpha^- = 0.9$, $\alpha^+ = 0$		
40	$4.008174269276555 \cdot 10^{-1}$	$4.188377296898878 \cdot 10^{-1}$	$4.314891395368673 \cdot 10^{-1}$
80	$4.008173949095708 \cdot 10^{-1}$	$4.188377296898816 \cdot 10^{-1}$	$4.314891395368630 \cdot 10^{-1}$
160	$4.008173948931840 \cdot 10^{-1}$	$4.188377296898816 \cdot 10^{-1}$	$4.314891395368630 \cdot 10^{-1}$
320	$4.008173948931840 \cdot 10^{-1}$	$4.188377296898816 \cdot 10^{-1}$	$4.314891395368630 \cdot 10^{-1}$
N	$\alpha^- = 0.1$, $\alpha^+ = 0.1$		
40	$-1.642936690036072 \cdot 10^{-1}$	$-7.327182523944650 \cdot 10^{-2}$	0
80	$-1.642937763929955 \cdot 10^{-1}$	$-7.327182523945102 \cdot 10^{-2}$	0
160	$-1.642937764479570 \cdot 10^{-1}$	$-7.327182523945102 \cdot 10^{-2}$	0
320	$-1.642937764479570 \cdot 10^{-1}$	$-7.327182523945102 \cdot 10^{-2}$	0
N	$\alpha^- = 0.5$, $\alpha^+ = 0.1$		
40	$5.903736107799532 \cdot 10^{-2}$	$1.254526366694325 \cdot 10^{-1}$	$1.752887502545996 \cdot 10^{-1}$
80	$5.903726172755933 \cdot 10^{-2}$	$1.254526366694217 \cdot 10^{-1}$	$1.752887502545936 \cdot 10^{-1}$
160	$5.903726167671208 \cdot 10^{-2}$	$1.254526366694217 \cdot 10^{-1}$	$1.752887502545936 \cdot 10^{-1}$
320	$5.903726167671206 \cdot 10^{-2}$	$1.254526366694217 \cdot 10^{-1}$	$1.752887502545936 \cdot 10^{-1}$
N	$\alpha^- = 0.9$, $\alpha^+ = 0.1$		
40	$3.913352987694977 \cdot 10^{-1}$	$4.091830308226884 \cdot 10^{-1}$	$4.217551802447860 \cdot 10^{-1}$
80	$3.913352670884397 \cdot 10^{-1}$	$4.091830308226821 \cdot 10^{-1}$	$4.217551802447817 \cdot 10^{-1}$
160	$3.913352670722254 \cdot 10^{-1}$	$4.091830308226821 \cdot 10^{-1}$	$4.217551802447817 \cdot 10^{-1}$
320	$3.913352670722254 \cdot 10^{-1}$	$4.091830308226821 \cdot 10^{-1}$	$4.217551802447817 \cdot 10^{-1}$
N	$\alpha^- = 0.1$, $\alpha^+ = 0.5$		
40	$-2.833582713729014 \cdot 10^{-1}$	$-2.239069631785943 \cdot 10^{-1}$	$-1.752887502545996 \cdot 10^{-1}$
80	$-2.833583406746069 \cdot 10^{-1}$	$-2.239069631785925 \cdot 10^{-1}$	$-1.752887502545936 \cdot 10^{-1}$
160	$-2.833583407100753 \cdot 10^{-1}$	$-2.239069631785925 \cdot 10^{-1}$	$-1.752887502545936 \cdot 10^{-1}$
320	$-2.833583407100753 \cdot 10^{-1}$	$-2.239069631785925 \cdot 10^{-1}$	$-1.752887502545936 \cdot 10^{-1}$
N	$\alpha^- = 0.5$, $\alpha^+ = 0.5$		
40	$-8.707704655545018 \cdot 10^{-2}$	$-3.765776759652863 \cdot 10^{-2}$	0
80	$-8.707711993887009 \cdot 10^{-2}$	$-3.765776759653277 \cdot 10^{-2}$	0
160	$-8.707711997642750 \cdot 10^{-2}$	$-3.765776759653277 \cdot 10^{-2}$	0
320	$-8.707711997642751 \cdot 10^{-2}$	$-3.765776759653277 \cdot 10^{-2}$	0
N	$\alpha^- = 0.9$, $\alpha^+ = 0.5$		
40	$3.220262259712840 \cdot 10^{-1}$	$3.385541512409283 \cdot 10^{-1}$	$3.503617615868520 \cdot 10^{-1}$
80	$3.220261967537037 \cdot 10^{-1}$	$3.385541512409225 \cdot 10^{-1}$	$3.503617615868480 \cdot 10^{-1}$
160	$3.220261967387503 \cdot 10^{-1}$	$3.385541512409225 \cdot 10^{-1}$	$3.503617615868480 \cdot 10^{-1}$
320	$3.220261967387502 \cdot 10^{-1}$	$3.385541512409225 \cdot 10^{-1}$	$3.503617615868480 \cdot 10^{-1}$
N	$\alpha^- = 0.1$, $\alpha^+ = 0.9$		
40	$-4.481398298947552 \cdot 10^{-1}$	$-4.337290180855282 \cdot 10^{-1}$	$-4.217551802447860 \cdot 10^{-1}$
80	$-4.481398464843468 \cdot 10^{-1}$	$-4.337290180855255 \cdot 10^{-1}$	$-4.217551802447817 \cdot 10^{-1}$
160	$-4.481398464928373 \cdot 10^{-1}$	$-4.337290180855255 \cdot 10^{-1}$	$-4.217551802447817 \cdot 10^{-1}$
320	$-4.481398464928373 \cdot 10^{-1}$	$-4.337290180855255 \cdot 10^{-1}$	$-4.217551802447817 \cdot 10^{-1}$
N	$\alpha^- = 0.5$, $\alpha^+ = 0.9$		
40	$-3.767502664963592 \cdot 10^{-1}$	$-3.618795400913077 \cdot 10^{-1}$	$-3.503617615868520 \cdot 10^{-1}$
80	$-3.767502883999263 \cdot 10^{-1}$	$-3.618795400913055 \cdot 10^{-1}$	$-3.503617615868480 \cdot 10^{-1}$
160	$-3.767502884111365 \cdot 10^{-1}$	$-3.618795400913055 \cdot 10^{-1}$	$-3.503617615868480 \cdot 10^{-1}$
320	$-3.767502884111365 \cdot 10^{-1}$	$-3.618795400913055 \cdot 10^{-1}$	$-3.503617615868480 \cdot 10^{-1}$
N	$\alpha^- = 0.9$, $\alpha^+ = 0.9$		
40	$-1.684283451332681 \cdot 10^{-2}$	$-7.082404920082913 \cdot 10^{-3}$	0
80	$-1.684285168635734 \cdot 10^{-2}$	$-7.082404920084131 \cdot 10^{-3}$	0
160	$-1.684285169514645 \cdot 10^{-2}$	$-7.082404920084131 \cdot 10^{-3}$	0
320	$-1.684285169514646 \cdot 10^{-2}$	$-7.082404920084131 \cdot 10^{-3}$	0

TABLE 21: The values of the approximated velocity $u^N(y)$ of the Couette flow at $y = 0.25$ and 0.5, for the Knudsen number $k = 2$ and $40 \leq N \leq 320$ and $\alpha^{\pm} = 0, 0.1, 0.5, 0.9$

y	0.25	0.5
N	$\alpha^- = 0.1$, $\alpha^+ = 0$	
40	$1.139258975475742 \cdot 10^{-1}$	$2.086172285191984 \cdot 10^{-1}$
80	$1.139258975475771 \cdot 10^{-1}$	$2.086173320866516 \cdot 10^{-1}$
160	$1.139258975475771 \cdot 10^{-1}$	$2.086173321396570 \cdot 10^{-1}$
320	$1.139258975475771 \cdot 10^{-1}$	$2.086173321396570 \cdot 10^{-1}$
N	$\alpha^- = 0.5$, $\alpha^+ = 0$	
40	$2.564547428032803 \cdot 10^{-1}$	$3.167985524171794 \cdot 10^{-1}$
80	$2.564547428032775 \cdot 10^{-1}$	$3.167986175332673 \cdot 10^{-1}$
160	$2.564547428032775 \cdot 10^{-1}$	$3.167986175665934 \cdot 10^{-1}$
320	$2.564547428032775 \cdot 10^{-1}$	$3.167986175665935 \cdot 10^{-1}$
N	$\alpha^- = 0.9$, $\alpha^+ = 0$	
40	$4.434679463954785 \cdot 10^{-1}$	$4.576209267966367 \cdot 10^{-1}$
80	$4.434679463954758 \cdot 10^{-1}$	$4.576209418596134 \cdot 10^{-1}$
160	$4.434679463954758 \cdot 10^{-1}$	$4.576209418673226 \cdot 10^{-1}$
320	$4.434679463954758 \cdot 10^{-1}$	$4.576209418673226 \cdot 10^{-1}$
N	$\alpha^- = 0.1$, $\alpha^+ = 0.1$	
40	$7.327182523944650 \cdot 10^{-2}$	$1.642936690036072 \cdot 10^{-1}$
80	$7.327182523945102 \cdot 10^{-2}$	$1.642937763929955 \cdot 10^{-1}$
160	$7.327182523945102 \cdot 10^{-2}$	$1.642937764479570 \cdot 10^{-1}$
320	$7.327182523945102 \cdot 10^{-2}$	$1.642937764479570 \cdot 10^{-1}$
N	$\alpha^- = 0.5$, $\alpha^+ = 0.1$	
40	$2.239069631785943 \cdot 10^{-1}$	$2.833582713729014 \cdot 10^{-1}$
80	$2.239069631785925 \cdot 10^{-1}$	$2.833583406746069 \cdot 10^{-1}$
160	$2.239069631785925 \cdot 10^{-1}$	$2.833583407100753 \cdot 10^{-1}$
320	$2.239069631785925 \cdot 10^{-1}$	$2.833583407100753 \cdot 10^{-1}$
N	$\alpha^- = 0.9$, $\alpha^+ = 0.1$	
40	$4.337290180855282 \cdot 10^{-1}$	$4.481398298947552 \cdot 10^{-1}$
80	$4.337290180855255 \cdot 10^{-1}$	$4.481398464843468 \cdot 10^{-1}$
160	$4.337290180855255 \cdot 10^{-1}$	$4.481398464928373 \cdot 10^{-1}$
320	$4.337290180855255 \cdot 10^{-1}$	$4.481398464928373 \cdot 10^{-1}$
N	$\alpha^- = 0.1$, $\alpha^+ = 0.5$	
40	$-1.254526366694325 \cdot 10^{-1}$	$-5.903736107799532 \cdot 10^{-2}$
80	$-1.254526366694217 \cdot 10^{-1}$	$-5.903726172755933 \cdot 10^{-2}$
160	$-1.254526366694217 \cdot 10^{-1}$	$-5.903726167671208 \cdot 10^{-2}$
320	$-1.254526366694217 \cdot 10^{-1}$	$-5.903726167671206 \cdot 10^{-2}$
N	$\alpha^- = 0.5$, $\alpha^+ = 0.5$	
40	$3.765776759652863 \cdot 10^{-2}$	$8.707704655545018 \cdot 10^{-2}$
80	$3.765776759653277 \cdot 10^{-2}$	$8.707711993887009 \cdot 10^{-2}$
160	$3.765776759653277 \cdot 10^{-2}$	$8.707711997642750 \cdot 10^{-2}$
320	$3.765776759653277 \cdot 10^{-2}$	$8.707711997642751 \cdot 10^{-2}$
N	$\alpha^- = 0.9$, $\alpha^+ = 0.5$	
40	$3.618795400913077 \cdot 10^{-1}$	$3.767502664963592 \cdot 10^{-1}$
80	$3.618795400913055 \cdot 10^{-1}$	$3.767502883999263 \cdot 10^{-1}$
160	$3.618795400913055 \cdot 10^{-1}$	$3.767502884111365 \cdot 10^{-1}$
320	$3.618795400913055 \cdot 10^{-1}$	$3.767502884111365 \cdot 10^{-1}$
N	$\alpha^- = 0.1$, $\alpha^+ = 0.9$	
40	$-4.091830308226884 \cdot 10^{-1}$	$-3.913352987694977 \cdot 10^{-1}$
80	$-4.091830308226821 \cdot 10^{-1}$	$-3.913352670884397 \cdot 10^{-1}$
160	$-4.091830308226821 \cdot 10^{-1}$	$-3.913352670722254 \cdot 10^{-1}$
320	$-4.091830308226821 \cdot 10^{-1}$	$-3.913352670722254 \cdot 10^{-1}$
N	$\alpha^- = 0.5$, $\alpha^+ = 0.9$	
40	$-3.385541512409283 \cdot 10^{-1}$	$-3.220262259712840 \cdot 10^{-1}$
80	$-3.385541512409225 \cdot 10^{-1}$	$-3.220261967537037 \cdot 10^{-1}$
160	$-3.385541512409225 \cdot 10^{-1}$	$-3.220261967387503 \cdot 10^{-1}$
320	$-3.385541512409225 \cdot 10^{-1}$	$-3.220261967387503 \cdot 10^{-1}$
N	$\alpha^- = 0.9$, $\alpha^+ = 0.9$	
40	$7.082404920082913 \cdot 10^{-3}$	$1.684283451332681 \cdot 10^{-2}$
80	$7.082404920084131 \cdot 10^{-3}$	$1.684285168635734 \cdot 10^{-2}$
160	$7.082404920084131 \cdot 10^{-3}$	$1.684285169514645 \cdot 10^{-2}$
320	$7.082404920084131 \cdot 10^{-3}$	$1.684285169514646 \cdot 10^{-2}$

TABLE 22: The values of the approximated velocity $u^N(y)$ of the Couette flow at $y = -0.5, -0.25$ and 0, for the Knudsen number $k = 10$ and $40 \leq N \leq 320$ and $\alpha^{\pm} = 0, 0.1, 0.5, 0.9$

y	-0.5	-0.25	0
N	$\alpha^- = 0.1,\ \alpha^+ = 0$		
40	$-2.307846758713362 \cdot 10^{-2}$	$1.381792659172284 \cdot 10^{-2}$	$4.477578877814241 \cdot 10^{-2}$
80	$-2.307849809980413 \cdot 10^{-1}$	$1.381792659172251 \cdot 10^{-2}$	$4.477578877814232 \cdot 10^{-2}$
160	$-2.307849811542036 \cdot 10^{-2}$	$1.381792659172251 \cdot 10^{-2}$	$4.477578877814232 \cdot 10^{-2}$
320	$-2.307849811542036 \cdot 10^{-2}$	$1.381792659172251 \cdot 10^{-2}$	$4.477578877814232 \cdot 10^{-2}$
N	$\alpha^- = 0.5,\ \alpha^+ = 0$		
40	$1.917830999176494 \cdot 10^{-1}$	$2.157147388637924 \cdot 10^{-1}$	$2.347520100315204 \cdot 10^{-1}$
80	$1.917830753292282 \cdot 10^{-1}$	$2.157147388637918 \cdot 10^{-1}$	$2.347520100315201 \cdot 10^{-1}$
160	$1.917830753166440 \cdot 10^{-1}$	$2.157147388637918 \cdot 10^{-1}$	$2.347520100315201 \cdot 10^{-1}$
320	$1.917830753166440 \cdot 10^{-1}$	$2.157147388637918 \cdot 10^{-1}$	$2.347520100315201 \cdot 10^{-1}$
N	$\alpha^- = 0.9,\ \alpha^+ = 0$		
40	$4.344510312922155 \cdot 10^{-1}$	$4.400019188557676 \cdot 10^{-1}$	$4.442172496079084 \cdot 10^{-1}$
80	$4.34451024649477 \cdot 10^{-1}$	$4.40001918855767 \cdot 10^{-1}$	$4.44217249607908 \cdot 10^{-1}$
160	$4.344510246460774 \cdot 10^{-1}$	$4.400019188557673 \cdot 10^{-1}$	$4.442172496079082 \cdot 10^{-1}$
320	$4.344510246460774 \cdot 10^{-1}$	$4.400019188557673 \cdot 10^{-1}$	$4.442172496079082 \cdot 10^{-1}$
N	$\alpha^- = 0.1,\ \alpha^+ = 0.1$		
40	$-6.263380978830734 \cdot 10^{-2}$	$-2.863650655786129 \cdot 10^{-2}$	0
80	$-6.263383777029075 \cdot 10^{-2}$	$-2.863650655786152 \cdot 10^{-2}$	0
160	$-6.263383778461179 \cdot 10^{-2}$	$-2.863650655786152 \cdot 10^{-2}$	0
320	$-6.263383778461179 \cdot 10^{-2}$	$-2.863650655786152 \cdot 10^{-2}$	0
N	$\alpha^- = 0.5,\ \alpha^+ = 0.1$		
40	$1.574261632163222 \cdot 10^{-1}$	$1.802252331390138 \cdot 10^{-1}$	$1.984259276238300 \cdot 10^{-1}$
80	$1.574261398490683 \cdot 10^{-1}$	$1.802252331390133 \cdot 10^{-1}$	$1.984259276238297 \cdot 10^{-1}$
160	$1.574261398371090 \cdot 10^{-1}$	$1.802252331390133 \cdot 10^{-1}$	$1.984259276238297 \cdot 10^{-1}$
320	$1.574261398371090 \cdot 10^{-1}$	$1.802252331390133 \cdot 10^{-1}$	$1.984259276238297 \cdot 10^{-1}$
N	$\alpha^- = 0.9,\ \alpha^+ = 0.1$		
40	$4.243819669629124 \cdot 10^{-1}$	$4.298788967370492 \cdot 10^{-1}$	$4.340659342253555 \cdot 10^{-1}$
80	$4.243819603917520 \cdot 10^{-1}$	$4.298788967370490 \cdot 10^{-1}$	$4.340659342253554 \cdot 10^{-1}$
160	$4.243819603883889 \cdot 10^{-1}$	$4.298788967370490 \cdot 10^{-1}$	$4.340659342253554 \cdot 10^{-1}$
320	$4.243819603883889 \cdot 10^{-1}$	$4.298788967370490 \cdot 10^{-1}$	$4.340659342253554 \cdot 10^{-1}$
N	$\alpha^- = 0.1,\ \alpha^+ = 0.5$		
40	$-2.370782167962822 \cdot 10^{-1}$	$-2.162449194807811 \cdot 10^{-1}$	$-1.984259276238300 \cdot 10^{-1}$
80	$-2.370782336175935 \cdot 10^{-1}$	$-2.162449194807810 \cdot 10^{-1}$	$-1.984259276238297 \cdot 10^{-1}$
160	$-2.370782336262026 \cdot 10^{-1}$	$-2.162449194807810 \cdot 10^{-1}$	$-1.984259276238297 \cdot 10^{-1}$
320	$-2.370782336262026 \cdot 10^{-1}$	$-2.162449194807810 \cdot 10^{-1}$	$-1.984259276238297 \cdot 10^{-1}$
N	$\alpha^- = 0.5,\ \alpha^+ = 0.5$		
40	$-2.982209393487885 \cdot 10^{-2}$	$-1.334563392411286 \cdot 10^{-2}$	0
80	$-2.982211064666643 \cdot 10^{-2}$	$-1.334563392411304 \cdot 10^{-2}$	0
160	$-2.982211065521943 \cdot 10^{-2}$	$-1.334563392411304 \cdot 10^{-2}$	0
320	$-2.982211065521944 \cdot 10^{-2}$	$-1.334563392411304 \cdot 10^{-2}$	0
N	$\alpha^- = 0.9,\ \alpha^+ = 0.5$		
40	$3.507918129996729 \cdot 10^{-1}$	$3.558743710057917 \cdot 10^{-1}$	$3.597953393526013 \cdot 10^{-1}$
80	$3.507918069516432 \cdot 10^{-1}$	$3.558743710057915 \cdot 10^{-1}$	$3.597953393526011 \cdot 10^{-1}$
160	$3.507918069485479 \cdot 10^{-1}$	$3.558743710057914 \cdot 10^{-1}$	$3.597953393526011 \cdot 10^{-1}$
320	$3.507918069485479 \cdot 10^{-1}$	$3.558743710057915 \cdot 10^{-1}$	$3.597953393526011 \cdot 10^{-1}$
N	$\alpha^- = 0.1,\ \alpha^+ = 0.9$		
40	$-4.427131781027587 \cdot 10^{-1}$	$-4.380844928136334 \cdot 10^{-1}$	$-4.340659342253555 \cdot 10^{-1}$
80	$-4.427131817678769 \cdot 10^{-1}$	$-4.380844928136333 \cdot 10^{-1}$	$-4.340659342253554 \cdot 10^{-1}$
160	$-4.427131817697527 \cdot 10^{-1}$	$-4.380844928136333 \cdot 10^{-1}$	$-4.340659342253554 \cdot 10^{-1}$
320	$-4.427131817697527 \cdot 10^{-1}$	$-4.380844928136333 \cdot 10^{-1}$	$-4.340659342253554 \cdot 10^{-1}$
N	$\alpha^- = 0.5,\ \alpha^+ = 0.9$		
40	$-3.683043165137232 \cdot 10^{-1}$	$-3.636352143540133 \cdot 10^{-1}$	$-3.597953393526013 \cdot 10^{-1}$
80	$-3.683043211946540 \cdot 10^{-1}$	$-3.636352143540132 \cdot 10^{-1}$	$-3.597953393526011 \cdot 10^{-1}$
160	$-3.683043211970496 \cdot 10^{-1}$	$-3.636352143540132 \cdot 10^{-1}$	$-3.597953393526011 \cdot 10^{-1}$
320	$-3.683043211970496 \cdot 10^{-1}$	$-3.636352143540132 \cdot 10^{-1}$	$-3.597953393526011 \cdot 10^{-1}$
N	$\alpha^- = 0.9,\ \alpha^+ = 0.9$		
40	$-5.295971983368881 \cdot 10^{-3}$	$-2.324767111939705 \cdot 10^{-3}$	0
80	$-5.295975500074703 \cdot 10^{-3}$	$-2.324767111939750 \cdot 10^{-3}$	0
160	$-5.295975501874536 \cdot 10^{-3}$	$-2.324767111939750 \cdot 10^{-3}$	0
320	$-5.295975501874537 \cdot 10^{-3}$	$-2.324767111939750 \cdot 10^{-3}$	0

TABLE 23: The values of the approximated velocity $u^N(y)$ of the Couette flow at $y = 0.25$ and 0.5, for the Knudsen number $k = 10$ and $40 \leq N \leq 320$ and $\alpha^{\pm} = 0, 0.1, 0.5, 0.9$

y	0.25	0.5
N	$\alpha^- = 0.1,\ \alpha^+ = 0$	
40	$7.556323781567342 \cdot 10^{-2}$	$1.115827488680976 \cdot 10^{-1}$
80	$7.556323781567356 \cdot 10^{-2}$	$1.115827764795537 \cdot 10^{-1}$
160	$7.556323781567356 \cdot 10^{-2}$	$1.115827764936851 \cdot 10^{-1}$
320	$7.556323781567356 \cdot 10^{-2}$	$1.115827764936851 \cdot 10^{-1}$
N	$\alpha^- = 0.5,\ \alpha^+ = 0$	
40	$2.532904113064432 \cdot 10^{-1}$	$2.746501971917829 \cdot 10^{-1}$
80	$2.532904113064430 \cdot 10^{-1}$	$2.746502132112466 \cdot 10^{-1}$
160	$2.532904113064430 \cdot 10^{-1}$	$2.746502132194453 \cdot 10^{-1}$
320	$2.532904113064430 \cdot 10^{-1}$	$2.746502132194453 \cdot 10^{-1}$
N	$\alpha^- = 0.9,\ \alpha^+ = 0$	
40	$4.482428205580523 \cdot 10^{-1}$	$4.528135812333202 \cdot 10^{-1}$
80	$4.48242820558052 \cdot 10^{-1}$	$4.52813584587666 \cdot 10^{-1}$
160	$4.482428205580522 \cdot 10^{-1}$	$4.528135845893825 \cdot 10^{-1}$
320	$4.482428205580522 \cdot 10^{-1}$	$4.528135845893825 \cdot 10^{-1}$
N	$\alpha^- = 0.1,\ \alpha^+ = 0.1$	
40	$2.863650655786129 \cdot 10^{-2}$	$6.263380978830734 \cdot 10^{-2}$
80	$2.863650655786152 \cdot 10^{-2}$	$6.263383777029075 \cdot 10^{-2}$
160	$2.863650655786152 \cdot 10^{-2}$	$6.263383778461179 \cdot 10^{-2}$
320	$2.863650655786152 \cdot 10^{-2}$	$6.263383778461179 \cdot 10^{-2}$
N	$\alpha^- = 0.5,\ \alpha^+ = 0.1$	
40	$2.162449194807811 \cdot 10^{-1}$	$2.370782167962822 \cdot 10^{-1}$
80	$2.162449194807810 \cdot 10^{-1}$	$2.370782336175935 \cdot 10^{-1}$
160	$2.162449194807810 \cdot 10^{-1}$	$2.370782336262026 \cdot 10^{-1}$
320	$2.162449194807810 \cdot 10^{-1}$	$2.370782336262026 \cdot 10^{-1}$
N	$\alpha^- = 0.9,\ \alpha^+ = 0.1$	
40	$4.380844928136334 \cdot 10^{-1}$	$4.427131781027587 \cdot 10^{-1}$
80	$4.380844928136333 \cdot 10^{-1}$	$4.427131817678769 \cdot 10^{-1}$
160	$4.380844928136333 \cdot 10^{-1}$	$4.427131817697527 \cdot 10^{-1}$
320	$4.380844928136333 \cdot 10^{-1}$	$4.427131817697527 \cdot 10^{-1}$
N	$\alpha^- = 0.1,\ \alpha^+ = 0.5$	
40	$-1.802252331390138 \cdot 10^{-1}$	$-1.574261632163222 \cdot 10^{-1}$
80	$-1.802252331390133 \cdot 10^{-1}$	$-1.574261398490683 \cdot 10^{-1}$
160	$-1.802252331390133 \cdot 10^{-1}$	$-1.574261398371090 \cdot 10^{-1}$
320	$-1.802252331390133 \cdot 10^{-1}$	$-1.574261398371090 \cdot 10^{-1}$
N	$\alpha^- = 0.5,\ \alpha^+ = 0.5$	
40	$1.334563392411286 \cdot 10^{-2}$	$2.982209393487685 \cdot 10^{-2}$
80	$1.334563392411304 \cdot 10^{-2}$	$2.982211064666643 \cdot 10^{-2}$
160	$1.334563392411304 \cdot 10^{-2}$	$2.982211065521943 \cdot 10^{-2}$
320	$1.334563392411304 \cdot 10^{-2}$	$2.982211065521944 \cdot 10^{-2}$
N	$\alpha^- = 0.9,\ \alpha^+ = 0.5$	
40	$3.636352143540133 \cdot 10^{-1}$	$3.683043165137232 \cdot 10^{-1}$
80	$3.636352143540132 \cdot 10^{-1}$	$3.683043211946540 \cdot 10^{-1}$
160	$3.636352143540132 \cdot 10^{-1}$	$3.683043211970496 \cdot 10^{-1}$
320	$3.636352143540132 \cdot 10^{-1}$	$3.683043211970496 \cdot 10^{-1}$
N	$\alpha^- = 0.1,\ \alpha^+ = 0.9$	
40	$-4.298788967370492 \cdot 10^{-1}$	$-4.243819669629124 \cdot 10^{-1}$
80	$-4.298788967370490 \cdot 10^{-1}$	$-4.243819603917520 \cdot 10^{-1}$
160	$-4.298788967370490 \cdot 10^{-1}$	$-4.243819603883889 \cdot 10^{-1}$
320	$-4.298788967370490 \cdot 10^{-1}$	$-4.243819603883889 \cdot 10^{-1}$
N	$\alpha^- = 0.5,\ \alpha^+ = 0.9$	
40	$-3.558743710057917 \cdot 10^{-1}$	$-3.507918129996729 \cdot 10^{-1}$
80	$-3.558743710057915 \cdot 10^{-1}$	$-3.507918069516433 \cdot 10^{-1}$
160	$-3.558743710057915 \cdot 10^{-1}$	$-3.507918069485479 \cdot 10^{-1}$
320	$-3.558743710057915 \cdot 10^{-1}$	$-3.507918069485479 \cdot 10^{-1}$
N	$\alpha^- = 0.9,\ \alpha^+ = 0.9$	
40	$2.324767111939705 \cdot 10^{-3}$	$5.295971983368881 \cdot 10^{-3}$
80	$2.324767111939750 \cdot 10^{-3}$	$5.295975500074703 \cdot 10^{-3}$
160	$2.324767111939750 \cdot 10^{-3}$	$5.295975501874536 \cdot 10^{-3}$
320	$2.324767111939750 \cdot 10^{-3}$	$5.295975501874537 \cdot 10^{-3}$

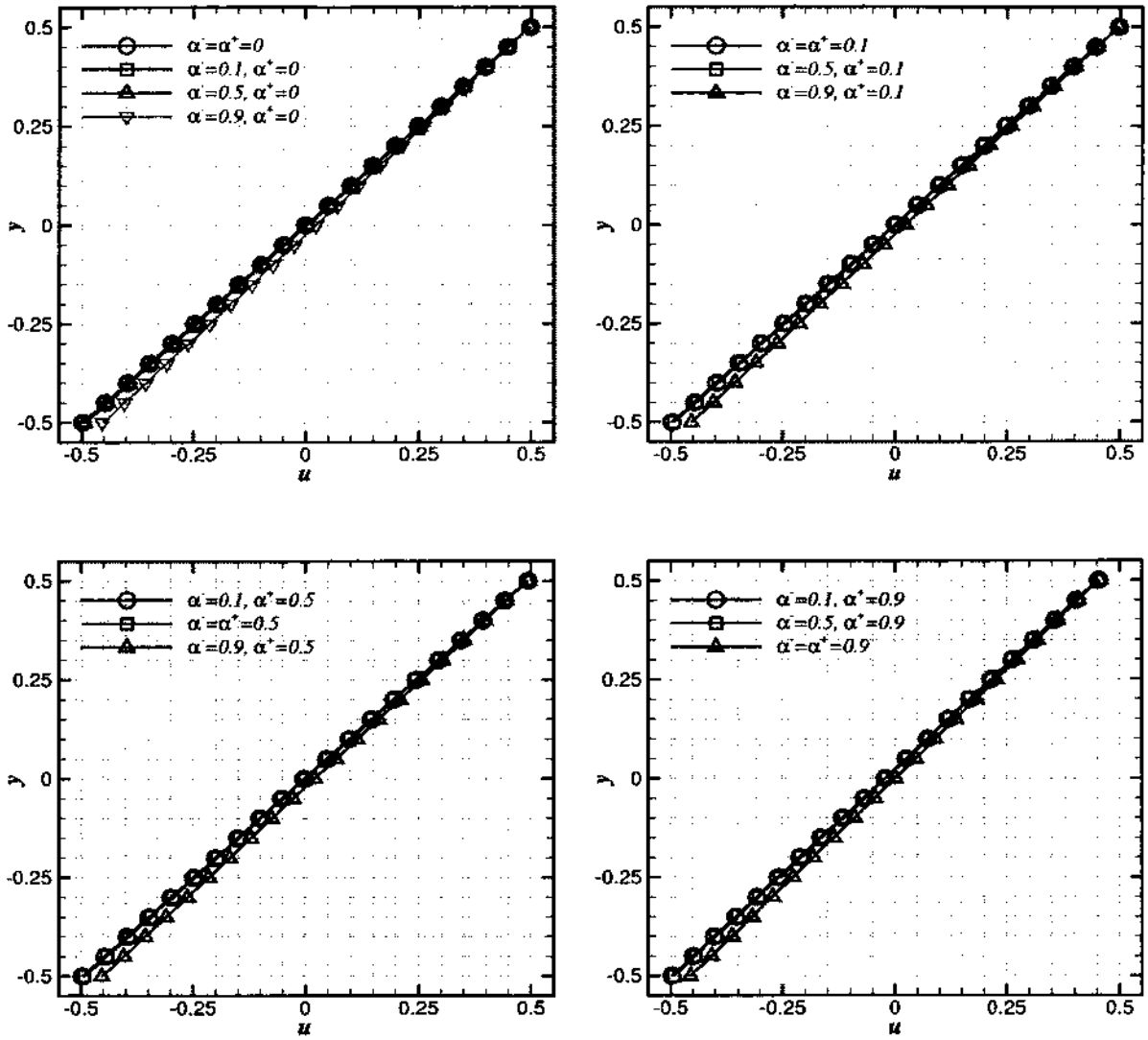

FIG. 3: The velocity profiles of the Couette flow problem for $k = 0.003$. Top row, from left to right: $\alpha^+ = 0$, $\alpha^- = 0$, 0.1, 0.5, 0.9 and $\alpha^+ = 0.1$, $\alpha^- = 0.1$, 0.5, 0.9. Bottom row, from left to right: $\alpha^+ = 0.5$, $\alpha^- = 0.1$, 0.5, 0.9 and $\alpha^+ = 0.9$, $\alpha^- = 0.1$, 0.5, 0.9.

3.3 SOLVING THE INTEGRAL EQUATION FOR THE POISEUILLE FLOW PROBLEM WITH CHUNK BASED COLLOCATION METHOD

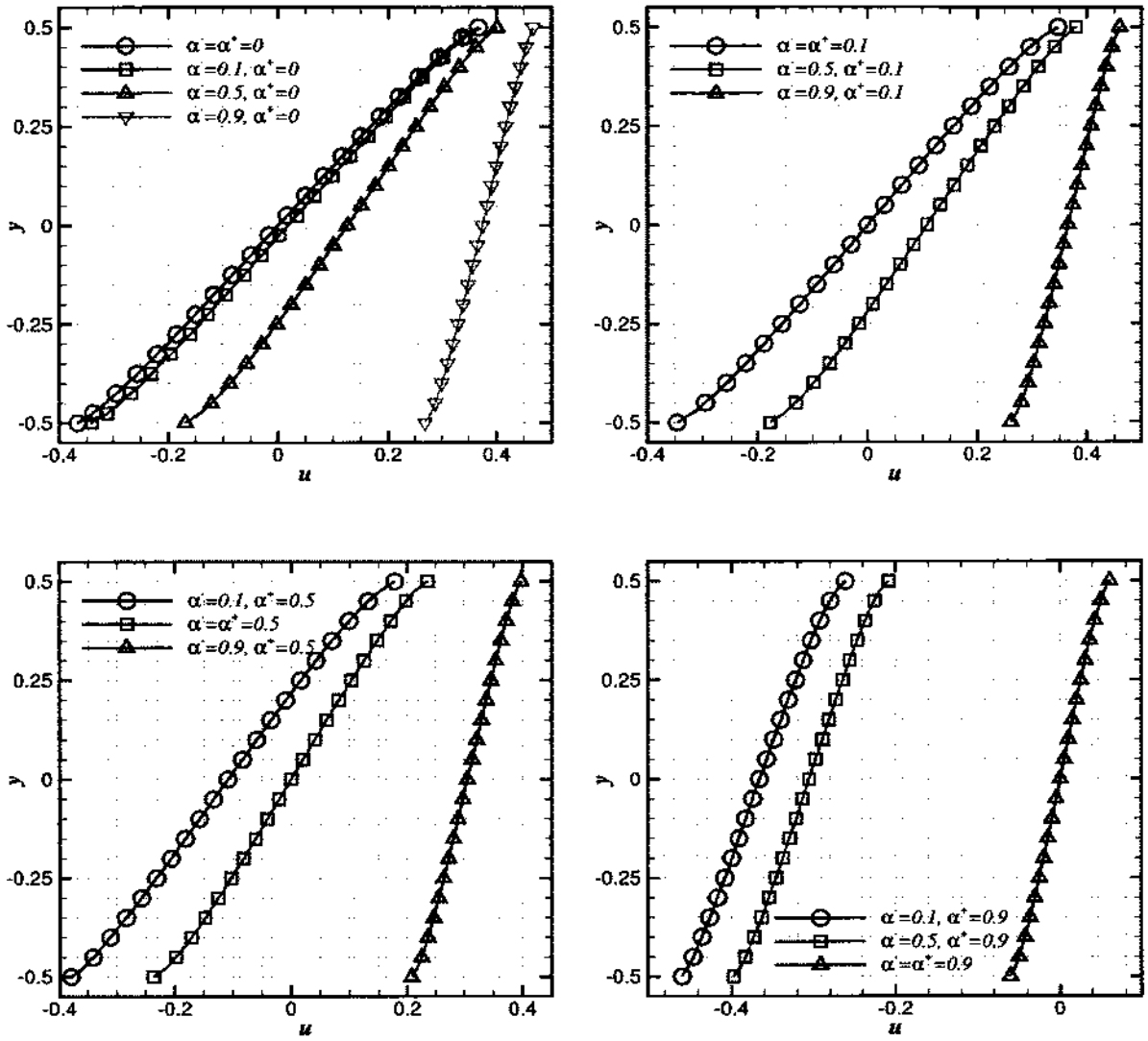

FIG. 4: The velocity profiles of the Couette flow problem for $k = 0.3$. Top row, from left to right: $\alpha^+ = 0$, $\alpha^- = 0$, 0.1, 0.5, 0.9 and $\alpha^+ = 0.1$, $\alpha^- = 0.1$, 0.5, 0.9. Bottom row, from left to right: $\alpha^+ = 0.5$, $\alpha^- = 0.1$, 0.5, 0.9 and $\alpha^+ = 0.9$, $\alpha^- = 0.1$, 0.5, 0.9.

In this section, we give a byproduct of the solutions to the Couette flow problem, the solutions to the Poiseuille flow problem. Comparing equation (66) of the Poiseuille flow problem with the equation (104) of the steady Couette flow problem, we see the only difference is the RHS term. Hence, the process of solving for the Poiseuille flow problem is identical to that of solving for the Couette flow problem

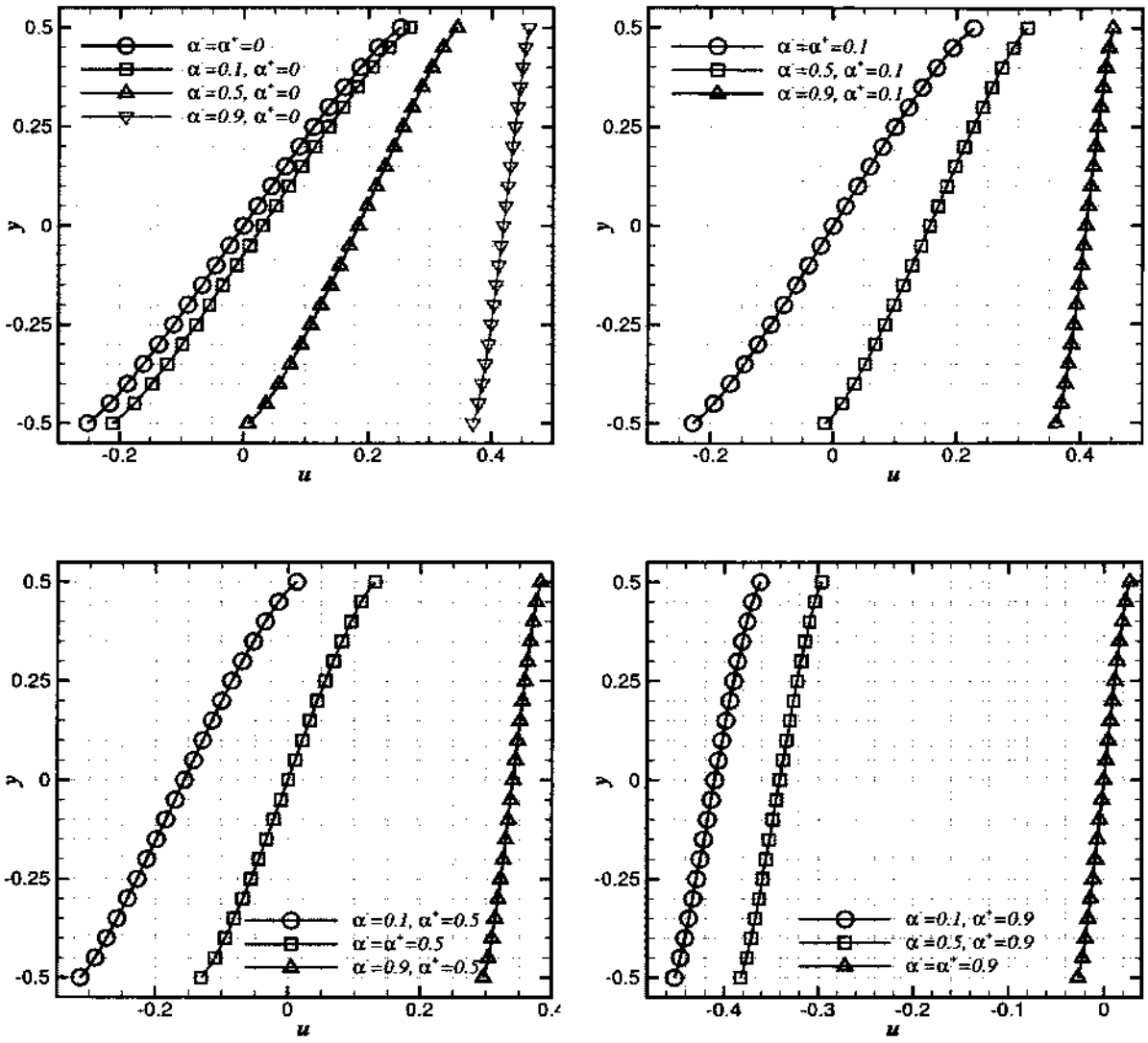

FIG. 5: The velocity profiles of the Couette flow problem for $k = 1.0$. Top row, from left to right: $\alpha^+ = 0$, $\alpha^- = 0$, 0.1, 0.5, 0.9 and $\alpha^+ = 0.1$, $\alpha^- = 0.1$, 0.5, 0.9. Bottom row, from left to right: $\alpha^+ = 0.5$, $\alpha^- = 0.1$, 0.5, 0.9 and $\alpha^+ = 0.9$, $\alpha^- = 0.1$, 0.5, 0.9.

except that in the linear system equation (103), the elements in $\boldsymbol{F}$ are uniformly $\pi^{1/2}$. Hence it suffices that we only illustrate the result of our computation when $M = 10$ and $N = 320$.

Figure 9-13 show the velocity profiles of the Poiseuille flow problem for $k =$ 0.003, 0.3, 1.0, 2.0, 10.0 with various accommodation ratios at the upper and lower

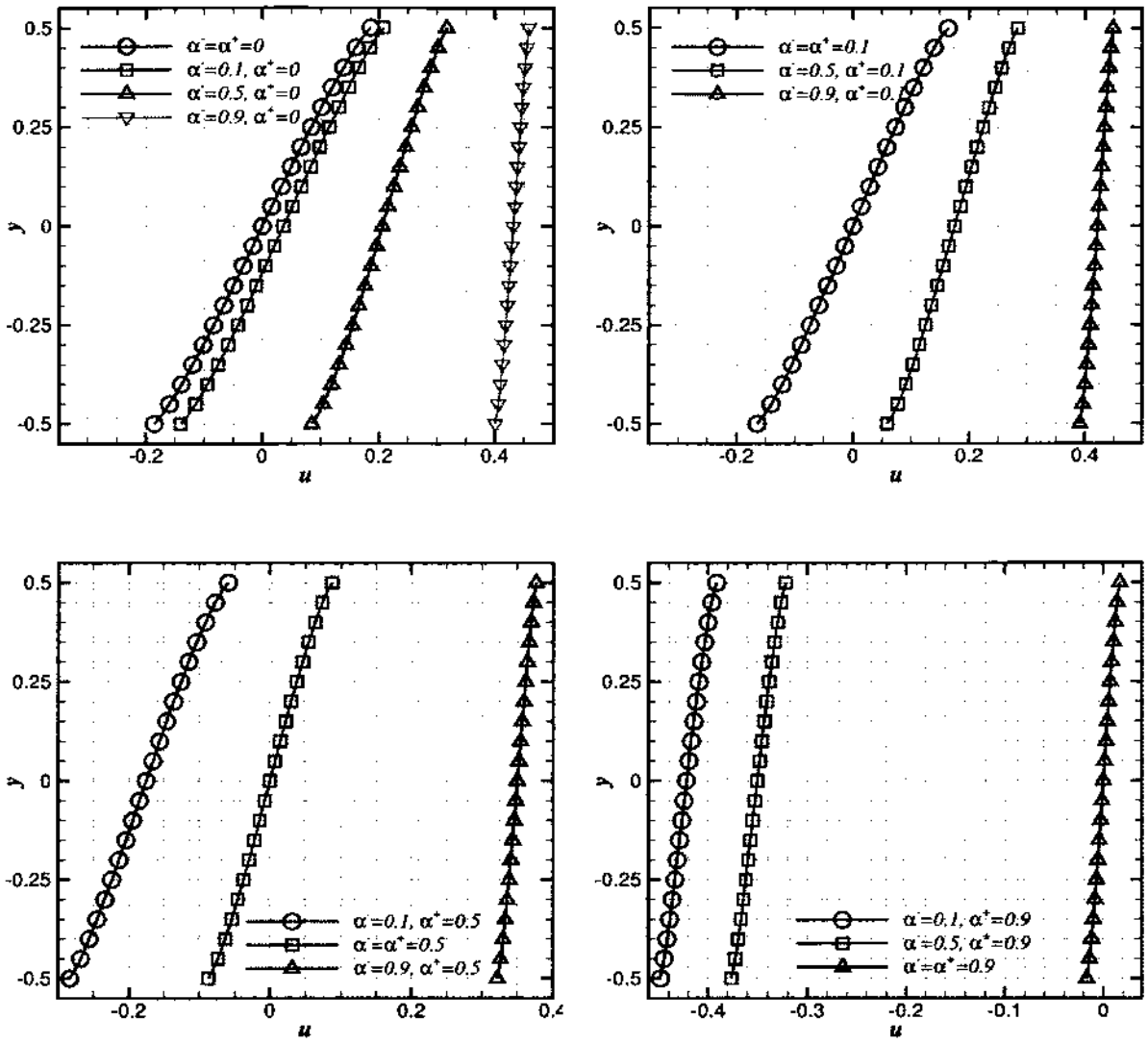

FIG. 6: The velocity profiles of the Couette flow problem for $k = 2.0$. Top row, from left to right: $\alpha^+ = 0$, $\alpha^- = 0$, 0.1, 0.5, 0.9 and $\alpha^+ = 0.1$, $\alpha^- = 0.1$, 0.5, 0.9. Bottom row, from left to right: $\alpha^+ = 0.5$, $\alpha^- = 0.1$, 0.5, 0.9 and $\alpha^+ = 0.9$, $\alpha^- = 0.1$, 0.5, 0.9.

walls. Figure 14-18 show the comparisons of a high precision velocity solution with a quadratic profile. In the comparisons, we choose the cases of k = 0.003, 0.3, 1.0, 2.0, 10.0 and equal accommodation ratios at the upper and lower walls. The quadratic profiles are computed such that the slip velocity and total mass flow rate are identified with those of the corresponding high precision solution. In

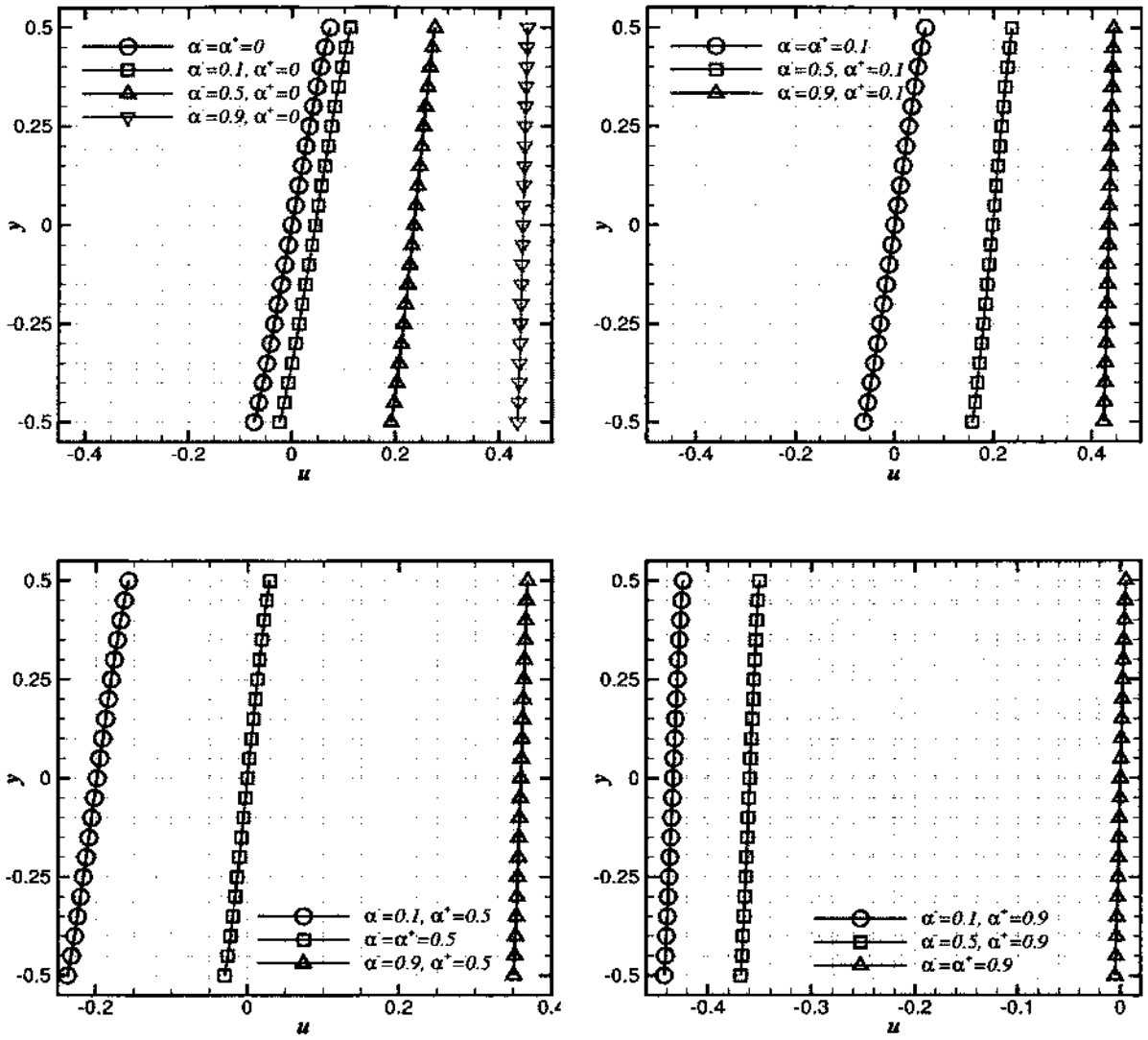

FIG. 7: The velocity profiles of the Couette flow problem for $k = 10.0$. Top row, from left to right: $\alpha^+ = 0$, $\alpha^- = 0$, 0.1, 0.5, 0.9 and $\alpha^+ = 0.1$, $\alpha^- = 0.1$, 0.5, 0.9. Bottom row, from left to right: $\alpha^+ = 0.5$, $\alpha^- = 0.1$, 0.5, 0.9 and $\alpha^+ = 0.9$, $\alpha^- = 0.1$, 0.5, 0.9.

Figure 14 the high precision profiles are hardly distinguishable from the corresponding quadratic profiles. However, Figure 15-18 manifest obvious differences between the high precision solutions and the quadratic profiles. Hence, the quadratic solution of Poiseuille flow is only valid in near continuous flow when k is sufficiently close to 0.

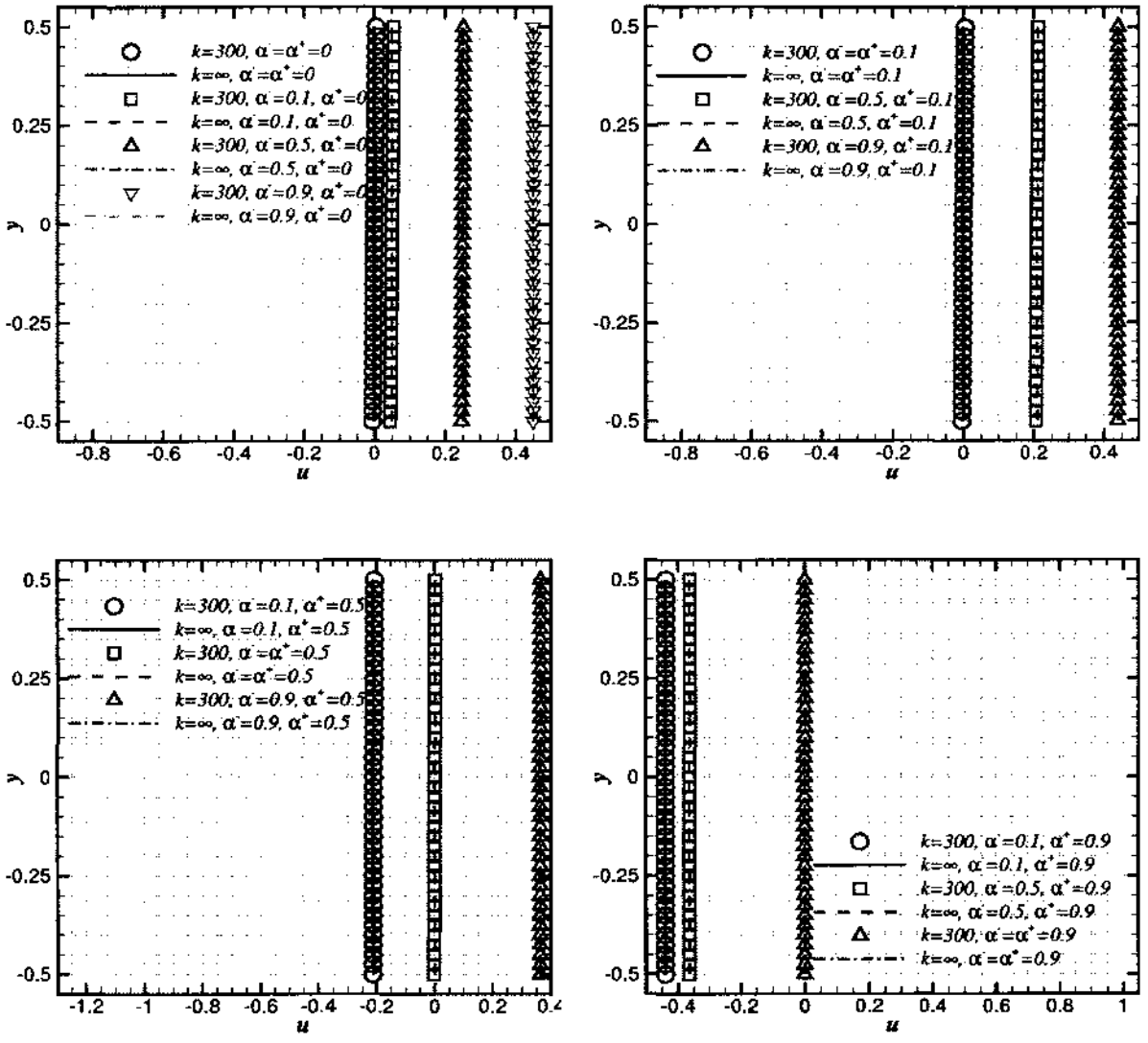

FIG. 8: The velocity profiles of the Couette flow problem for $k = 300.0$ and free molecular flow. Top row, from left to right: $\alpha^+ = 0$, $\alpha^- = 0$, 0.1, 0.5, 0.9 and $\alpha^+ = 0.1$, $\alpha^- = 0.1$, 0.5, 0.9. Bottom row, from left to right: $\alpha^+ = 0.5$, $\alpha^- = 0.1$, 0.5, 0.9 and $\alpha^+ = 0.9$, $\alpha^- = 0.1$, 0.5, 0.9.

We also computed the shear stress T_{xy}, the upper and lower half channel mass flow rates $Q^{\pm}$ for the Poiseuille flows from equation (71), equation (107) and

TABLE 24: The dependence of the stress T_{xy} on the Knudsen number k and various accommodation ratios $\alpha^{\pm}$ for the Couette flow problem

α^+	0.0	0.1	0.5	0.9
α^-	$k = 0.003$			
0.1	$-1.489979691463144 \cdot 10^{-3}$	$-1.489043399389355 \cdot 10^{-3}$	$-1.481832584402827 \cdot 10^{-3}$	$-1.421820207755527 \cdot 10^{-3}$
0.5	$-1.482759827467247 \cdot 10^{-3}$	$-1.481832584402827 \cdot 10^{-3}$	$-1.474691270778127 \cdot 10^{-3}$	$-1.415244326513074 \cdot 10^{-3}$
0.9	$-1.422673845622606 \cdot 10^{-3}$	$-1.421820207755527 \cdot 10^{-3}$	$-1.415244326513074 \cdot 10^{-3}$	$-1.360404449783136 \cdot 10^{-3}$
α^-	$k = 0.3$			
0.1	$-8.992833904468987 \cdot 10^{-2}$	$-8.666444972988237 \cdot 10^{-2}$	$-6.759707858916663 \cdot 10^{-2}$	$-2.311408070206627 \cdot 10^{-2}$
0.5	$-6.956172509857737 \cdot 10^{-2}$	$-6.759707858916663 \cdot 10^{-2}$	$-5.541877997358581 \cdot 10^{-2}$	$-2.150044078421201 \cdot 10^{-2}$
0.9	$-2.333895677099649 \cdot 10^{-2}$	$-2.311408070206627 \cdot 10^{-2}$	$-2.150044078421201 \cdot 10^{-2}$	$-1.333813635834104 \cdot 10^{-2}$
α^-	$k = 1.0$			
0.1	$-1.584929600446099 \cdot 10^{-1}$	$-1.488704157308196 \cdot 10^{-1}$	$-1.007386051173426 \cdot 10^{-1}$	$-2.607635444470014 \cdot 10^{-2}$
0.5	$-1.050297657081390 \cdot 10^{-1}$	$-1.007386051173426 \cdot 10^{-1}$	$-7.617694825897675 \cdot 10^{-2}$	$-2.407237158046933 \cdot 10^{-2}$
0.9	$-2.635370285166484 \cdot 10^{-2}$	$-2.607635444470014 \cdot 10^{-2}$	$-2.407237158046933 \cdot 10^{-2}$	$-1.429651925848904 \cdot 10^{-2}$
α^-	$k = 2.0$			
0.1	$-1.922235658380698 \cdot 10^{-1}$	$-1.784436264364144 \cdot 10^{-1}$	$-1.137914613870899 \cdot 10^{-1}$	$-2.689406198024603 \cdot 10^{-2}$
0.5	$-1.192157333370045 \cdot 10^{-1}$	$-1.137914613870899 \cdot 10^{-1}$	$-8.357896315183509 \cdot 10^{-2}$	$-2.478119212980463 \cdot 10^{-2}$
0.9	$-2.718528121847265 \cdot 10^{-2}$	$-2.689406198024603 \cdot 10^{-2}$	$-2.478119212980463 \cdot 10^{-2}$	$-1.454867257171203 \cdot 10^{-2}$
α^-	$k = 10.0$			
0.1	$-2.367266827911574 \cdot 10^{-1}$	$-2.164788680562340 \cdot 10^{-1}$	$-1.286081730379985 \cdot 10^{-1}$	$-2.766990972009083 \cdot 10^{-2}$
0.5	$-1.354844126934459 \cdot 10^{-1}$	$-1.286081730379985 \cdot 10^{-1}$	$-9.149188224129712 \cdot 10^{-2}$	$-2.544964951340495 \cdot 10^{-2}$
0.9	$-2.797513050216179 \cdot 10^{-2}$	$-2.766990972009083 \cdot 10^{-2}$	$-2.544964951340495 \cdot 10^{-2}$	$-1.478088309686578 \cdot 10^{-2}$

TABLE 25: The dependence of the upper half channel mass flow rate Q^+ on the Knudsen number k and various accommodation ratios $\alpha^{\pm}$ for the Couette flow problem

α^+	0.0	0.1	0.5	0.9
α^-	$k = 0.003$			
0.1	$1.243236389918302 \cdot 10^{-1}$	$1.240888404082707 \cdot 10^{-1}$	$1.222780057856699 \cdot 10^{-1}$	$1.072021430586492 \cdot 10^{-1}$
0.5	$1.249326179189773 \cdot 10^{-1}$	$1.246983765107177 \cdot 10^{-1}$	$1.228935293117802 \cdot 10^{-1}$	$1.078625794090409 \cdot 10^{-1}$
0.9	$1.300007323295986 \cdot 10^{-1}$	$1.297729364188381 \cdot 10^{-1}$	$1.280173755218030 \cdot 10^{-1}$	$1.133703200004656 \cdot 10^{-3}$
α^-	$k = 0.3$			
0.1	$9.166968229567601 \cdot 10^{-2}$	$8.011634556950527 \cdot 10^{-2}$	$1.023241549406719 \cdot 10^{-2}$	$-1.600165272644038 \cdot 10^{-1}$
0.5	$1.271241624501532 \cdot 10^{-1}$	$1.171059069625410 \cdot 10^{-1}$	$5.312841827165381 \cdot 10^{-2}$	$-1.315021516837137 \cdot 10^{-1}$
0.9	$2.086309979401282 \cdot 10^{-1}$	$2.044188650972435 \cdot 10^{-1}$	$1.734974975972017 \cdot 10^{-1}$	$1.325656464182656 \cdot 10^{-2}$
α^-	$k = 1.0$			
0.1	$6.989968333631282 \cdot 10^{-2}$	$5.217363145254992 \cdot 10^{-2}$	$-4.071775299089517 \cdot 10^{-2}$	$-1.944860324298967 \cdot 10^{-1}$
0.5	$1.290746275480407 \cdot 10^{-1}$	$1.146172398291713 \cdot 10^{-1}$	$2.903001102159472 \cdot 10^{-2}$	$-1.606653555110294 \cdot 10^{-1}$
0.9	$2.192367922526527 \cdot 10^{-1}$	$2.145338552444451 \cdot 10^{-1}$	$1.797686317720526 \cdot 10^{-1}$	$5.868897905952011 \cdot 10^{-3}$
α^-	$k = 2.0$			
0.1	$5.802298169360082 \cdot 10^{-2}$	$3.774449083500993 \cdot 10^{-2}$	$-6.168514247231815 \cdot 10^{-2}$	$-2.042595897746842 \cdot 10^{-1}$
0.5	$1.288417887590505 \cdot 10^{-1}$	$1.126180413689672 \cdot 10^{-1}$	$1.955826706637816 \cdot 10^{-2}$	$-1.689828445753342 \cdot 10^{-1}$
0.9	$2.218635649883712 \cdot 10^{-1}$	$2.170108108374072 \cdot 10^{-1}$	$1.811445651243179 \cdot 10^{-1}$	$3.706235409410164 \cdot 10^{-3}$
α^-	$k = 10.0$			
0.1	$3.811724861616665 \cdot 10^{-2}$	$1.466324171139570 \cdot 10^{-2}$	$-8.981435554118011 \cdot 10^{-2}$	$-2.148541440947941 \cdot 10^{-1}$
0.5	$1.268223507303812 \cdot 10^{-1}$	$1.083127424402046 \cdot 10^{-1}$	$6.873159034620266 \cdot 10^{-3}$	$-1.778622891623948 \cdot 10^{-1}$
0.9	$2.241547608641367 \cdot 10^{-1}$	$2.190798757563043 \cdot 10^{-1}$	$1.818698005956585 \cdot 10^{-1}$	$1.203549098759847 \cdot 10^{-3}$

equation (108), respectively. The integrals in the equations are computed piecewisely over each subinterval E_j by using a shifted and scaled 10^{th} order Gauss-Legendre quadrature. Table 27-29 give the value of $T_{xy} - y/2$, Q^- and Q^+ for $k = 0.003$, 0.3, 1.0, 2.0, 10.0 and various values of accommodation ratios $\alpha^{\pm}$, respectively.

TABLE 26: The dependence of the lower half channel mass flow rate Q^- on the Knudsen number k and various accommodation ratios $\alpha^\pm$ for the Couette flow problem

α^+	0.0	0.1	0.5	0.9
α^-	$k = 0.003$			
0.1	$-1.240094689025684 \cdot 10^{-1}$	$-1.240886404082707 \cdot 10^{-1}$	$-1.246983765107177 \cdot 10^{-1}$	$-1.297729364188381 \cdot 10^{-1}$
0.5	$-1.221980849264881 \cdot 10^{-1}$	$-1.222780057856699 \cdot 10^{-1}$	$-1.228935293117802 \cdot 10^{-1}$	$-1.280173755218030 \cdot 10^{-1}$
0.9	$-1.071164095338633 \cdot 10^{-1}$	$-1.072021430586492 \cdot 10^{-1}$	$-1.078625794090409 \cdot 10^{-1}$	$-1.133703200004656 \cdot 10^{-3}$
α^-	$k = 0.3$			
0.1	$-7.384311742472288 \cdot 10^{-2}$	$-8.011634556950527 \cdot 10^{-2}$	$-1.171059069625410 \cdot 10^{-1}$	$-2.044188650972435 \cdot 10^{-1}$
0.5	$-3.354842023752215 \cdot 10^{-3}$	$-1.023241549406719 \cdot 10^{-2}$	$-5.312841827165381 \cdot 10^{-2}$	$-1.734974975972017 \cdot 10^{-1}$
0.9	$1.639769346462065 \cdot 10^{-1}$	$1.600165272644038 \cdot 10^{-1}$	$1.315021516837137 \cdot 10^{-1}$	$-1.325656464182656 \cdot 10^{-2}$
α^-	$k = 1.0$			
0.1	$-3.995732959211067 \cdot 10^{-2}$	$-5.217363145254992 \cdot 10^{-2}$	$-1.146172398291713 \cdot 10^{-1}$	$-2.145338552444451 \cdot 10^{-1}$
0.5	$5.273733742737116 \cdot 10^{-2}$	$4.071775299089517 \cdot 10^{-2}$	$-2.903001102159472 \cdot 10^{-2}$	$-1.797686317720526 \cdot 10^{-1}$
0.9	$1.991294832457538 \cdot 10^{-1}$	$1.944860324298967 \cdot 10^{-1}$	$1.606653565110294 \cdot 10^{-1}$	$-5.868897905952011 \cdot 10^{-3}$
α^-	$k = 2.0$			
0.1	$-2.216952705090054 \cdot 10^{-2}$	$-3.774449083500993 \cdot 10^{-2}$	$-1.126180413689672 \cdot 10^{-1}$	$-2.170108108374072 \cdot 10^{-1}$
0.5	$7.605302093923219 \cdot 10^{-2}$	$6.168514247231815 \cdot 10^{-2}$	$-1.955826706637816 \cdot 10^{-2}$	$-1.811445651243179 \cdot 10^{-1}$
0.9	$2.090803623785145 \cdot 10^{-1}$	$2.042595897746842 \cdot 10^{-1}$	$1.689828445753342 \cdot 10^{-1}$	$-3.706235409410164 \cdot 10^{-3}$
α^-	$k = 10.0$			
0.1	$6.525145576124438 \cdot 10^{-3}$	$-1.466324171139570 \cdot 10^{-2}$	$-1.083127424402046 \cdot 10^{-1}$	$-2.190798757563043 \cdot 10^{-1}$
0.5	$1.075389477860743 \cdot 10^{-1}$	$8.981435554118011 \cdot 10^{-2}$	$-6.873159034620266 \cdot 10^{-3}$	$-1.818698005956585 \cdot 10^{-1}$
0.9	$2.199137901425876 \cdot 10^{-1}$	$2.148541440947941 \cdot 10^{-1}$	$1.778622891623948 \cdot 10^{-1}$	$-1.203549098759847 \cdot 10^{-3}$

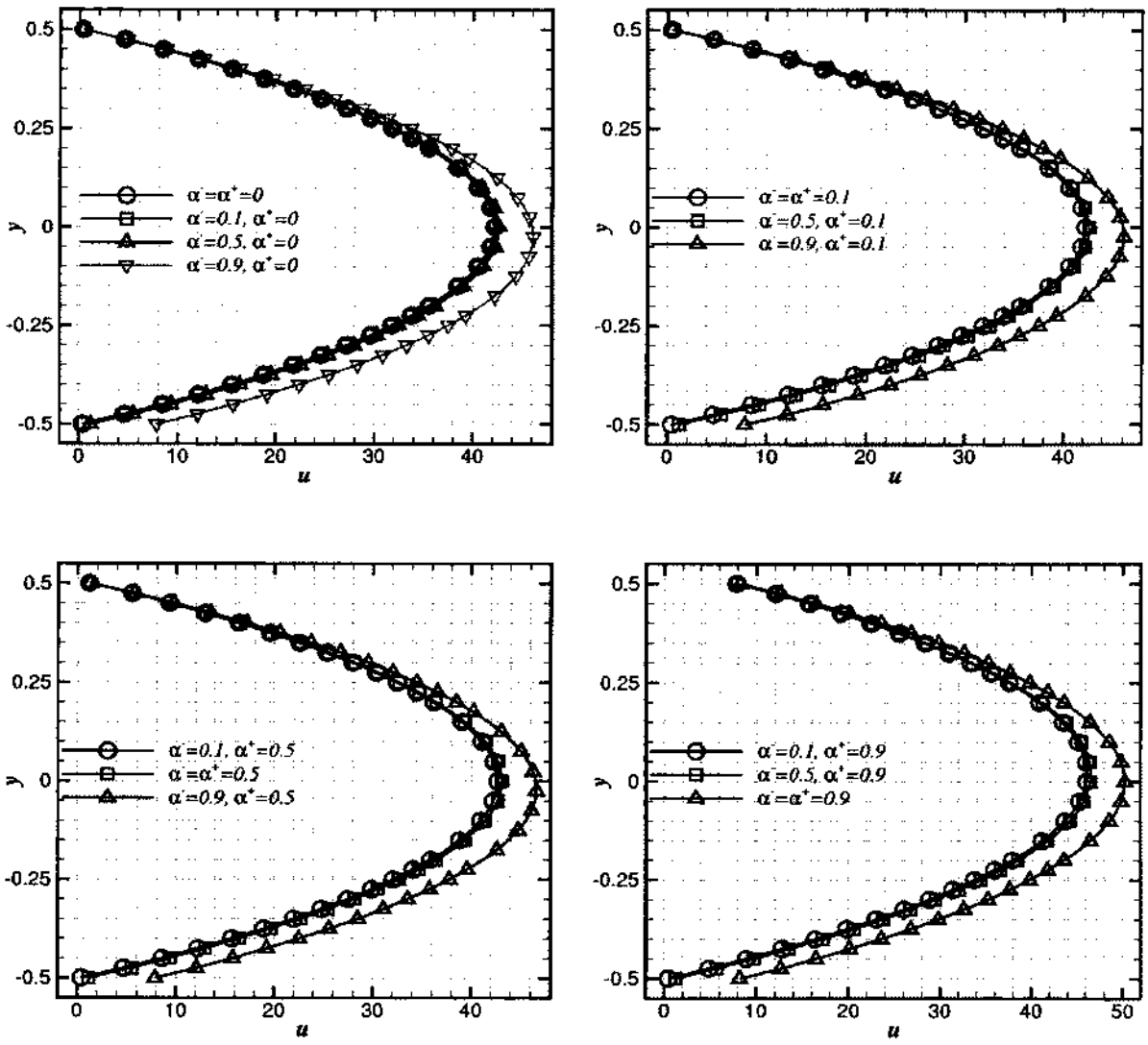

FIG. 9: The velocity profiles of the Poiseuille flow problem for $k = 0.003$. Top row, from left to right: $\alpha^+ = 0$, $\alpha^- = 0$, 0.1, 0.5, 0.9 and $\alpha^+ = 0.1$, $\alpha^- = 0.1$, 0.5, 0.9. Bottom row, from left to right: $\alpha^+ = 0.5$, $\alpha^- = 0.1$, 0.5, 0.9 and $\alpha^+ = 0.9$, $\alpha^- = 0.1$, 0.5, 0.9.

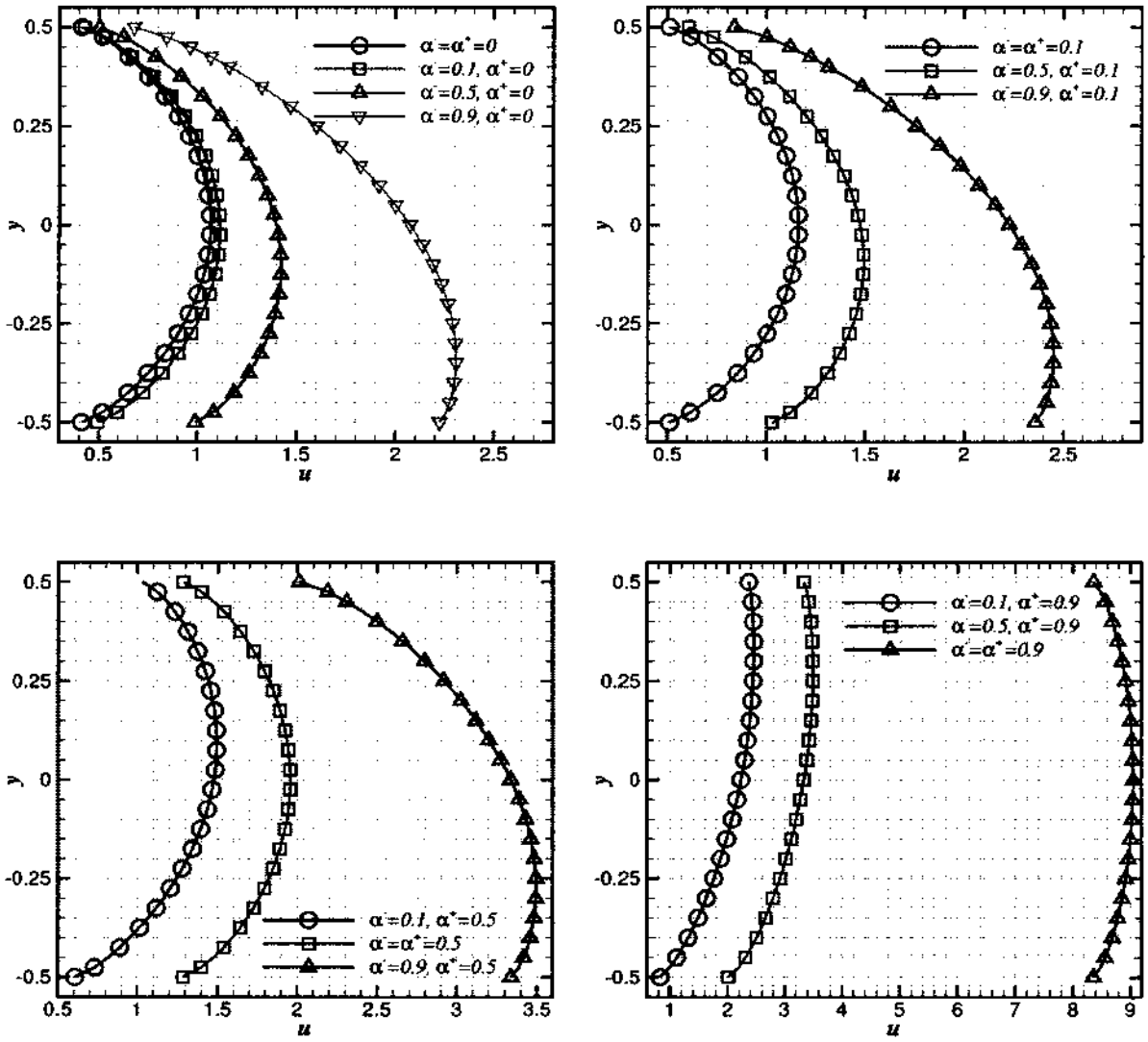

FIG. 10: The velocity profiles of the Poiseuille flow problem for $k = 0.3$. Top row, from left to right: $\alpha^+ = 0$, $\alpha^- = 0$, 0.1, 0.5, 0.9 and $\alpha^+ = 0.1$, $\alpha^- = 0.1$, 0.5, 0.9. Bottom row, from left to right: $\alpha^+ = 0.5$, $\alpha^- = 0.1$, 0.5, 0.9 and $\alpha^+ = 0.9$, $\alpha^- = 0.1$, 0.5, 0.9.

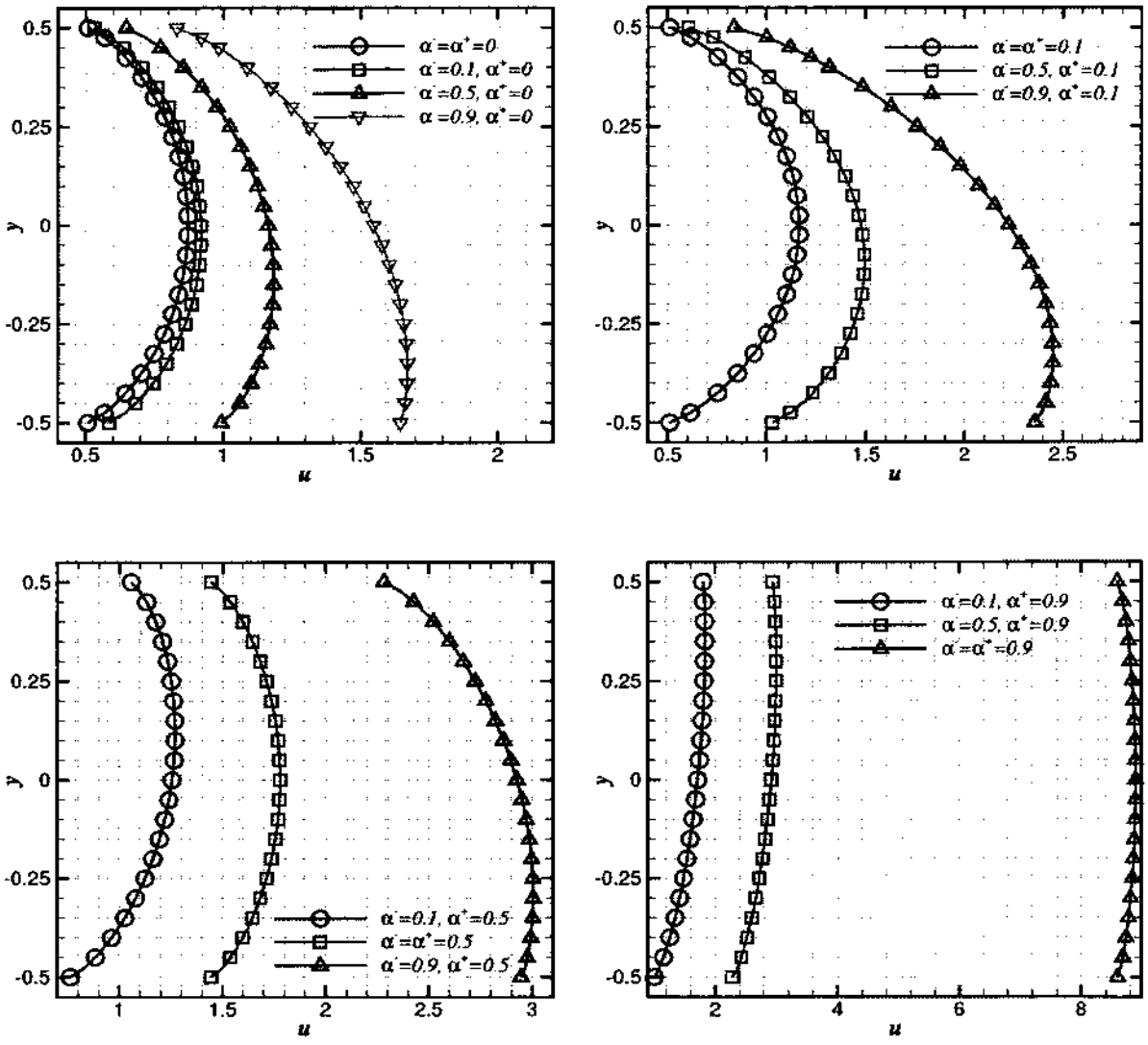

FIG. 11: The velocity profiles of the Poiseuille flow problem for $k = 1.0$. Top row, from left to right: $\alpha^+ = 0$, $\alpha^- = 0$, 0.1, 0.5, 0.9 and $\alpha^+ = 0.1$, $\alpha^- = 0.1$, 0.5, 0.9. Bottom row, from left to right: $\alpha^+ = 0.5$, $\alpha^- = 0.1$, 0.5, 0.9 and $\alpha^+ = 0.9$, $\alpha^- = 0.1$, 0.5, 0.9.

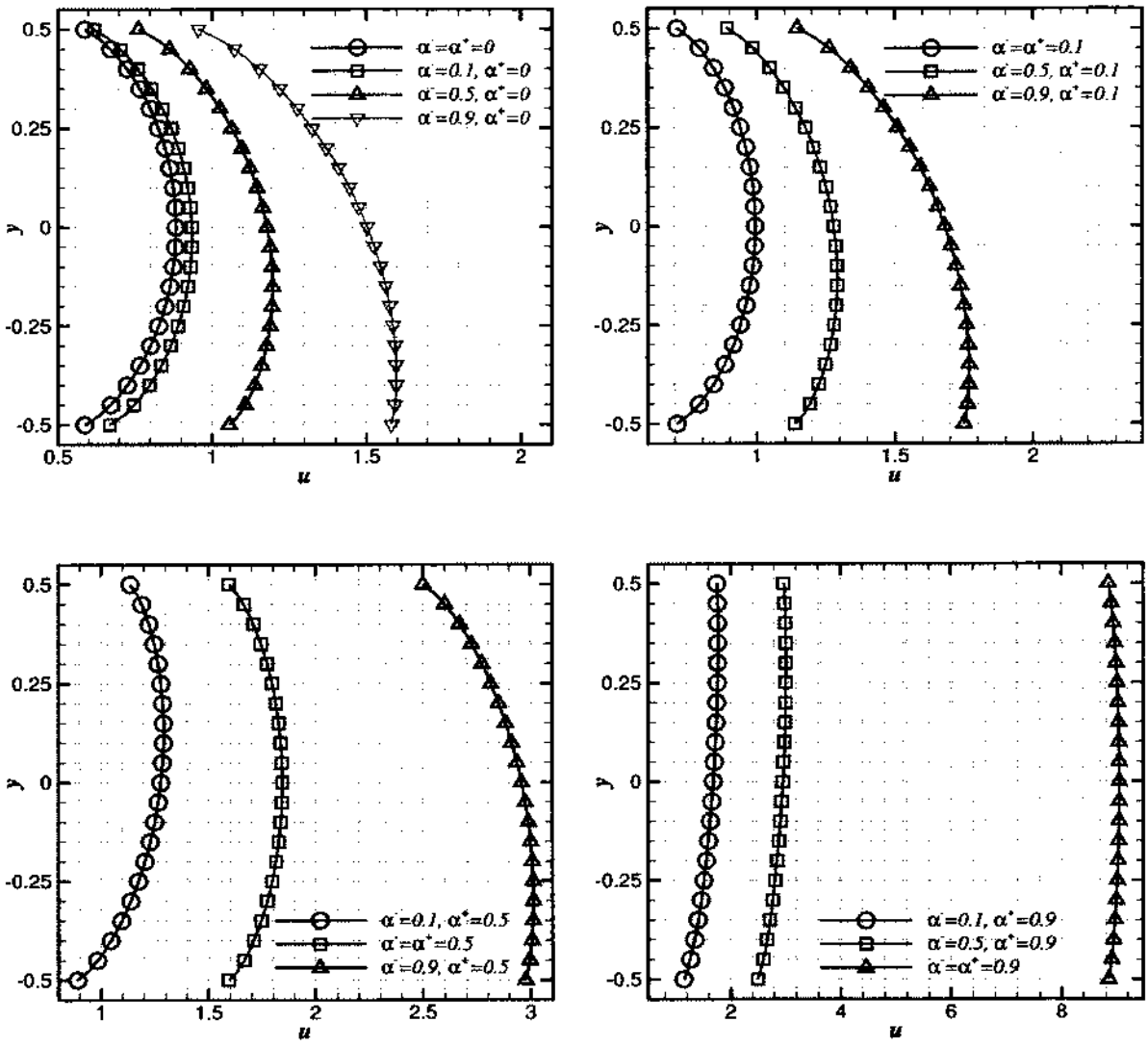

FIG. 12: The velocity profiles of the Poiseuille flow problem for $k = 2.0$. Top row, from left to right: $\alpha^+ = 0$, $\alpha^- = 0$, 0.1, 0.5, 0.9 and $\alpha^+ = 0.1$, $\alpha^- = 0.1$, 0.5, 0.9. Bottom row, from left to right: $\alpha^+ = 0.5$, $\alpha^- = 0.1$, 0.5, 0.9 and $\alpha^+ = 0.9$, $\alpha^- = 0.1$, 0.5, 0.9.

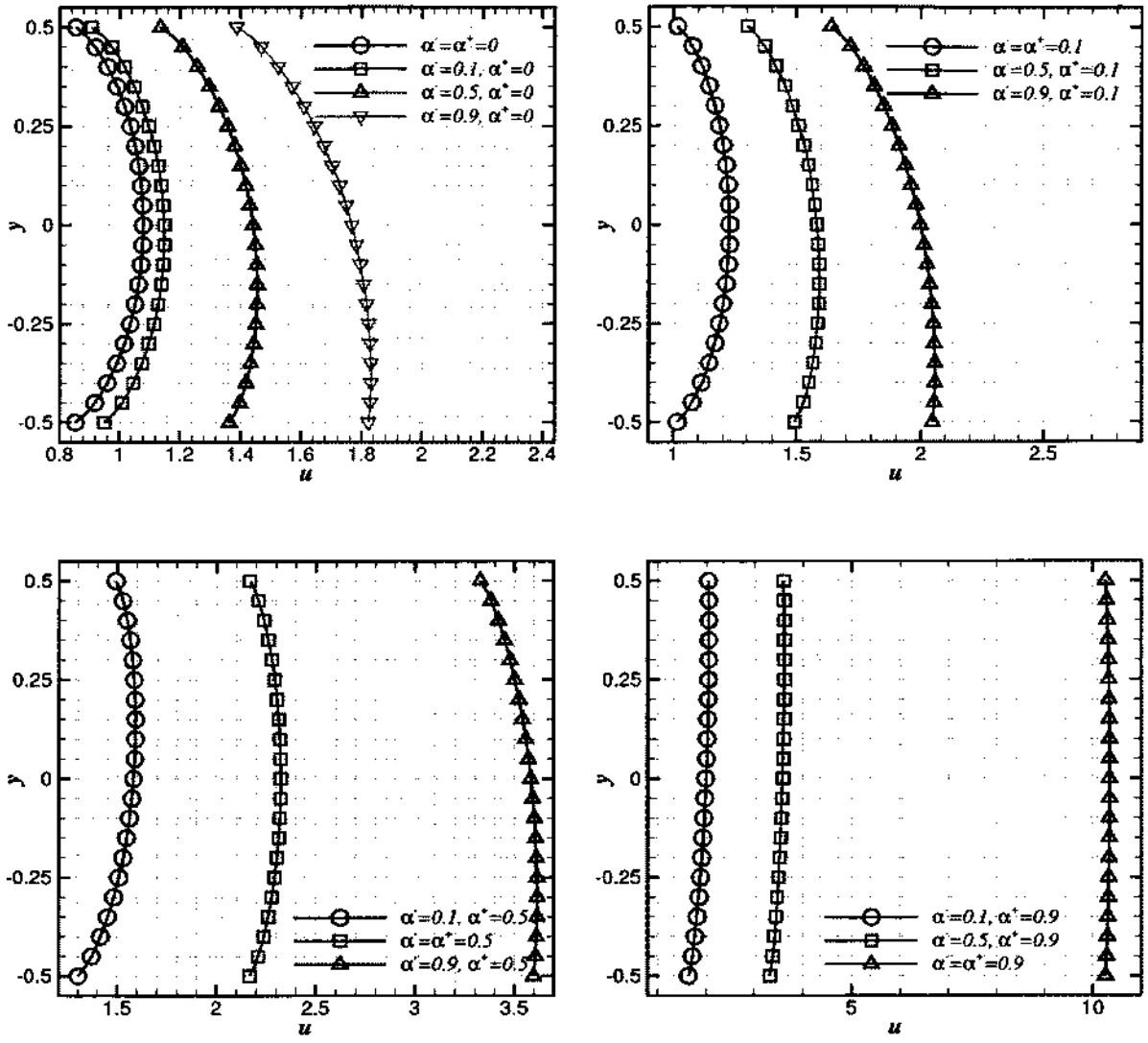

FIG. 13: The velocity profiles of the Poiseuille flow problem for $k = 10.0$. Top row, from left to right: $\alpha^+ = 0$, $\alpha^- = 0$, 0.1, 0.5, 0.9 and $\alpha^+ = 0.1$, $\alpha^- = 0.1$, 0.5, 0.9. Bottom row, from left to right: $\alpha^+ = 0.5$, $\alpha^- = 0.1$, 0.5, 0.9 and $\alpha^+ = 0.9$, $\alpha^- = 0.1$, 0.5, 0.9.

3.4 SOLVING THE INTEGRAL EQUATION FOR THE KRAMERS PROBLEM WITH CHUNK BASED COLLOCATION METHOD

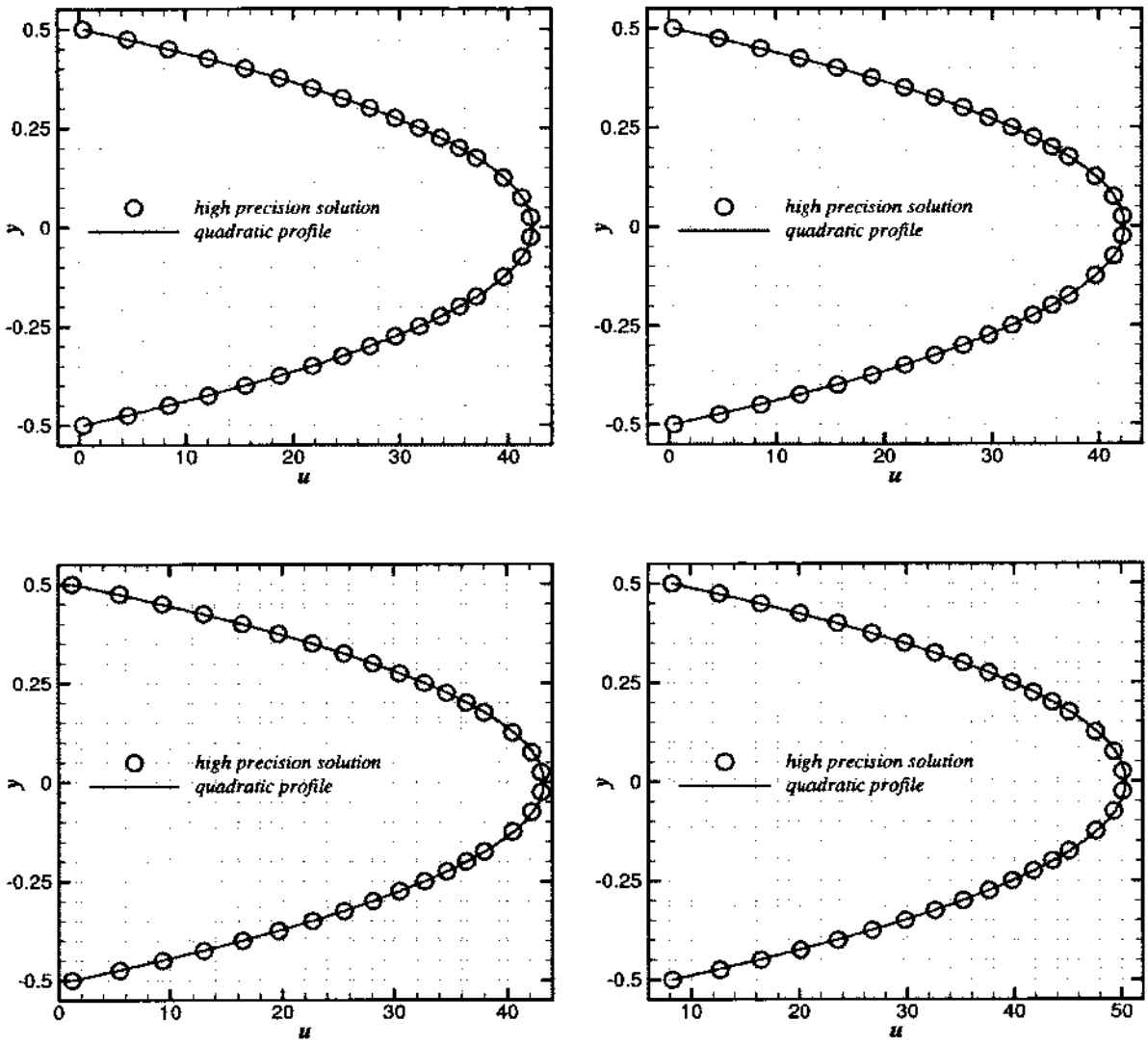

FIG. 14: Comparisons of Poiseuille flow velocities for $k = 0.003$: high precision solution v.s. quadratic profile. Top row, from left to right: $\alpha^+ = \alpha^- = 0$ and $\alpha^+ = \alpha^- = 0.1$. Bottom row, from left to right: $\alpha^+ = \alpha^- = 0.5$ and $\alpha^+ = \alpha^- = 0.9$.

In this section, we solve Kramers problem with the combined diffusive and specular reflection boundary condition and Knudsen number k with chunk based collocation method. Recall equation (47) for Kramers problem, one needs a transform to convert the integral interval $[0, \infty)$ to a finite interval *i.e.*, $[0, 1]$. The transform should be delicately chosen in order to mitigate the fast decaying property of the

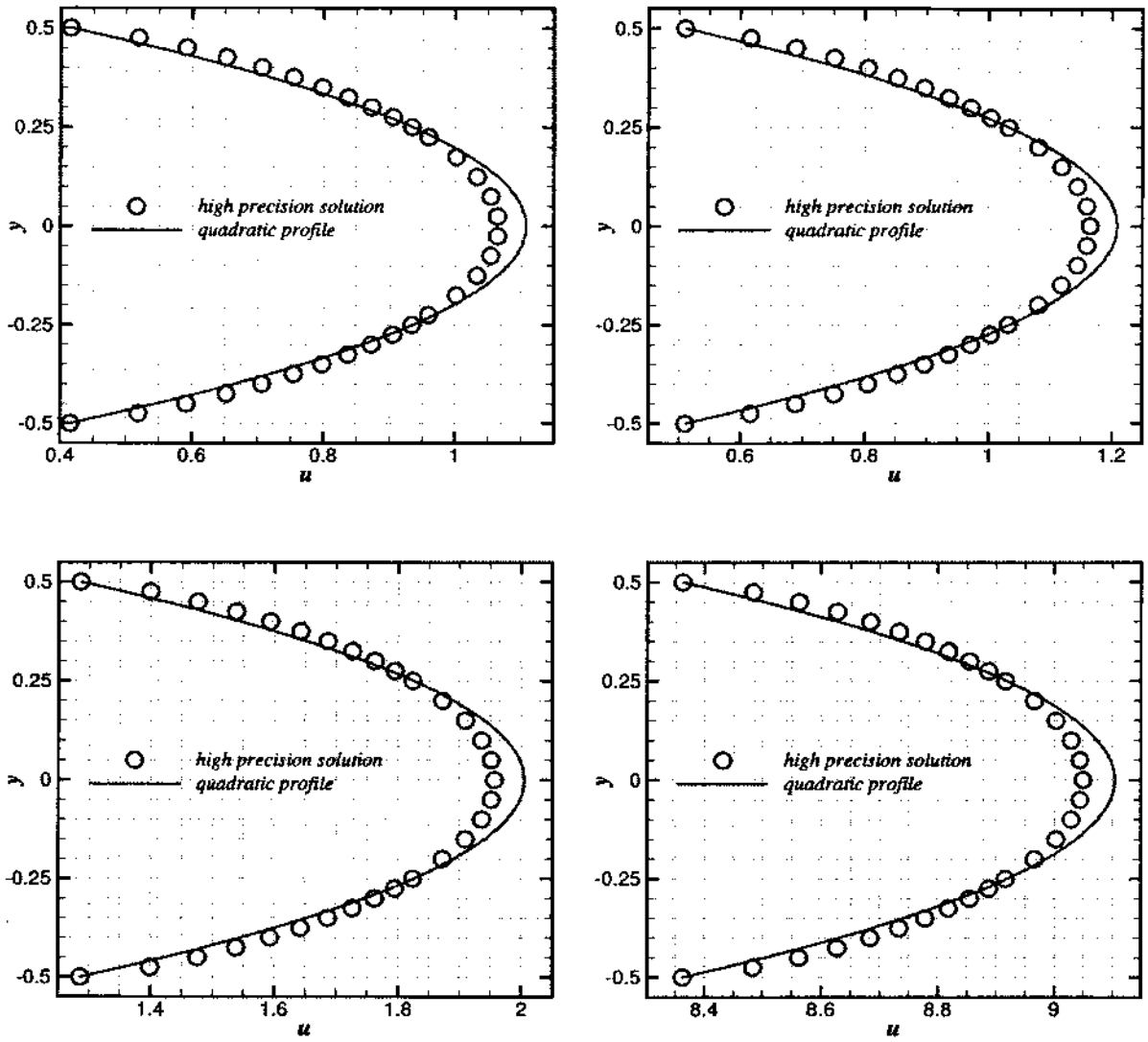

FIG. 15: Comparisons of Poiseuille flow velocities for $k = 0.3$: high precision solution v.s. quadratic profile. Top row, from left to right: $\alpha^+ = \alpha^- = 0$ and $\alpha^+ = \alpha^- = 0.1$. Bottom row, from left to right: $\alpha^+ = \alpha^- = 0.5$ and $\alpha^+ = \alpha^- = 0.9$.

RHS function $(1 + \alpha)I_1(y)$. Since when $y \to \infty$, $I_{-1}(y) \sim \frac{\sqrt{\pi y}}{3} e^{-2(y/2)^{2/3}}$, we use the inverse function of $e^{-2(y/2)^{2/3}}$, namely $y = \varphi(x) = 2(-\ln x/3)^{2/3}$ as the transform

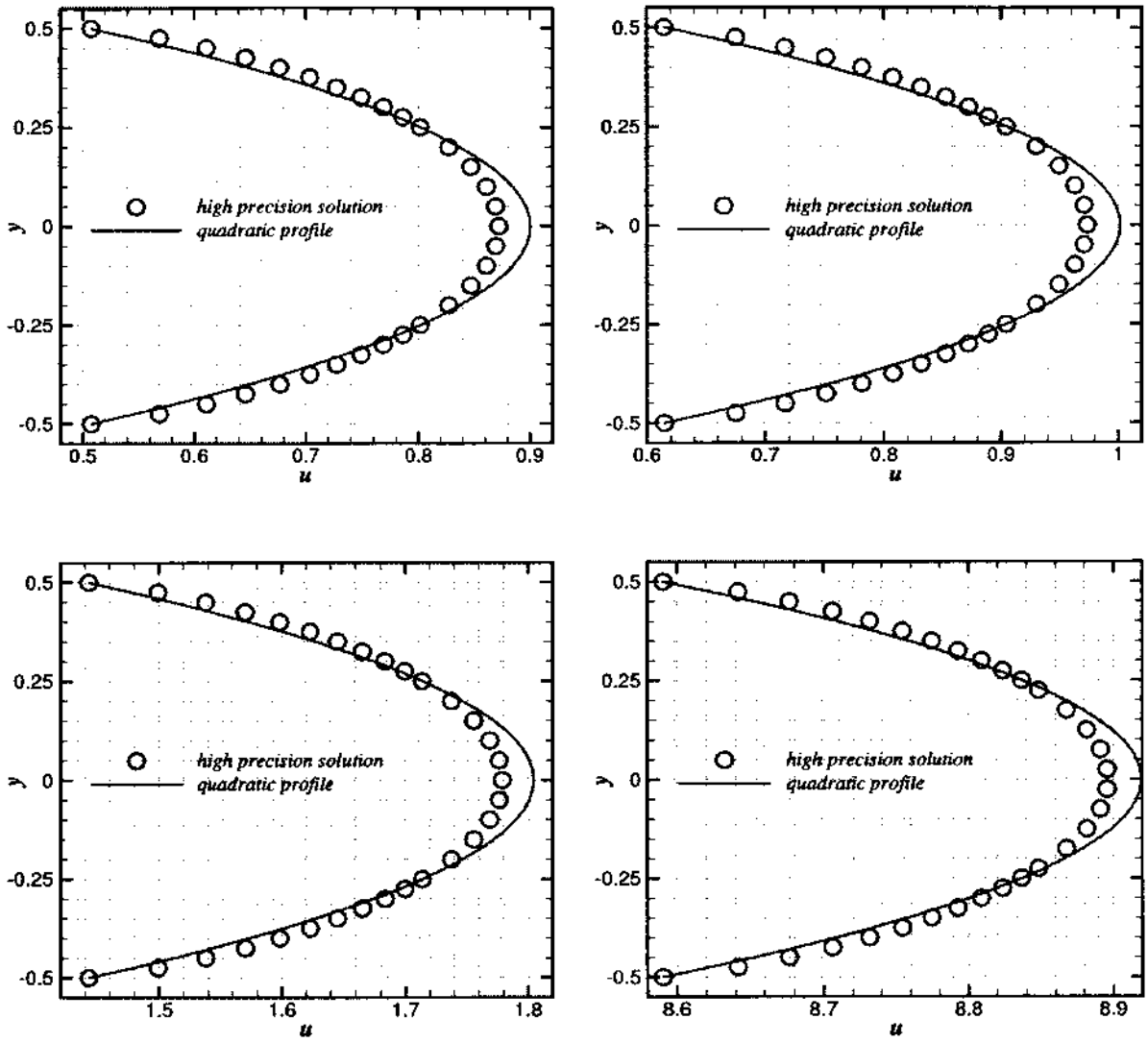

FIG. 16: Comparisons of Poiseuille flow velocities for $k = 1.0$: high precision solution v.s. quadratic profile. Top row, from left to right: $\alpha^+ = \alpha^- = 0$ and $\alpha^+ = \alpha^- = 0.1$. Bottom row, from left to right: $\alpha^+ = \alpha^- = 0.5$ and $\alpha^+ = \alpha^- = 0.9$.

function. Hence equation (47) is converted to equation (109),

$$\tilde{q}(x) - \pi^{-1/2} \int_0^1 [I_{-1}(|\varphi(x)-\varphi(t)|)+\alpha I_{-1}(\varphi(x)+\varphi(t))]\tilde{q}(t)\varphi'(t)\,\mathrm{d}t = \pi^{-1/2}(1+\alpha)I_1(\varphi(x)), \tag{109}$$

where $\tilde{q}(x) = q(y)$.

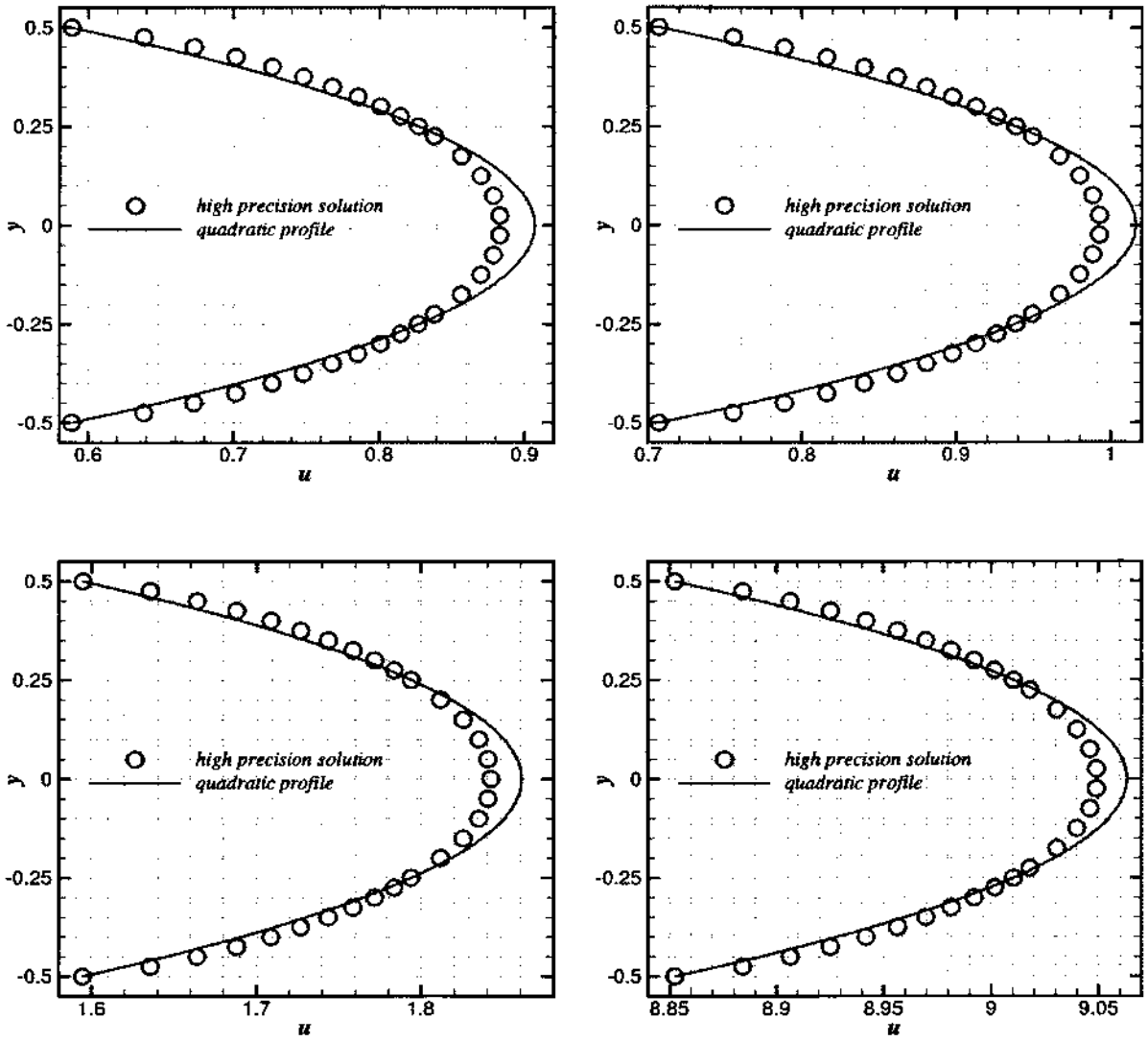

FIG. 17: Comparisons of Poiseuille flow velocities for $k = 2.0$: high precision solution v.s. quadratic profile. Top row, from left to right: $\alpha^+ = \alpha^- = 0$ and $\alpha^+ = \alpha^- = 0.1$. Bottom row, from left to right: $\alpha^+ = \alpha^- = 0.5$ and $\alpha^+ = \alpha^- = 0.9$.

The interval $[0, 1]$ is decomposed into N disjoint subintervals $\cup_{j=1}^{N} E_j$ and $\tilde{q}(x)$ is approximated by piece-wise $(M-1)^{th}$ order expansion of scaled and shifted Gause-Legendre polynomials,

$$\tilde{q}^N(x) = \sum_{j=1}^{N} \tilde{q}_j^N(x),\ x \in [0, 1], \tag{110}$$

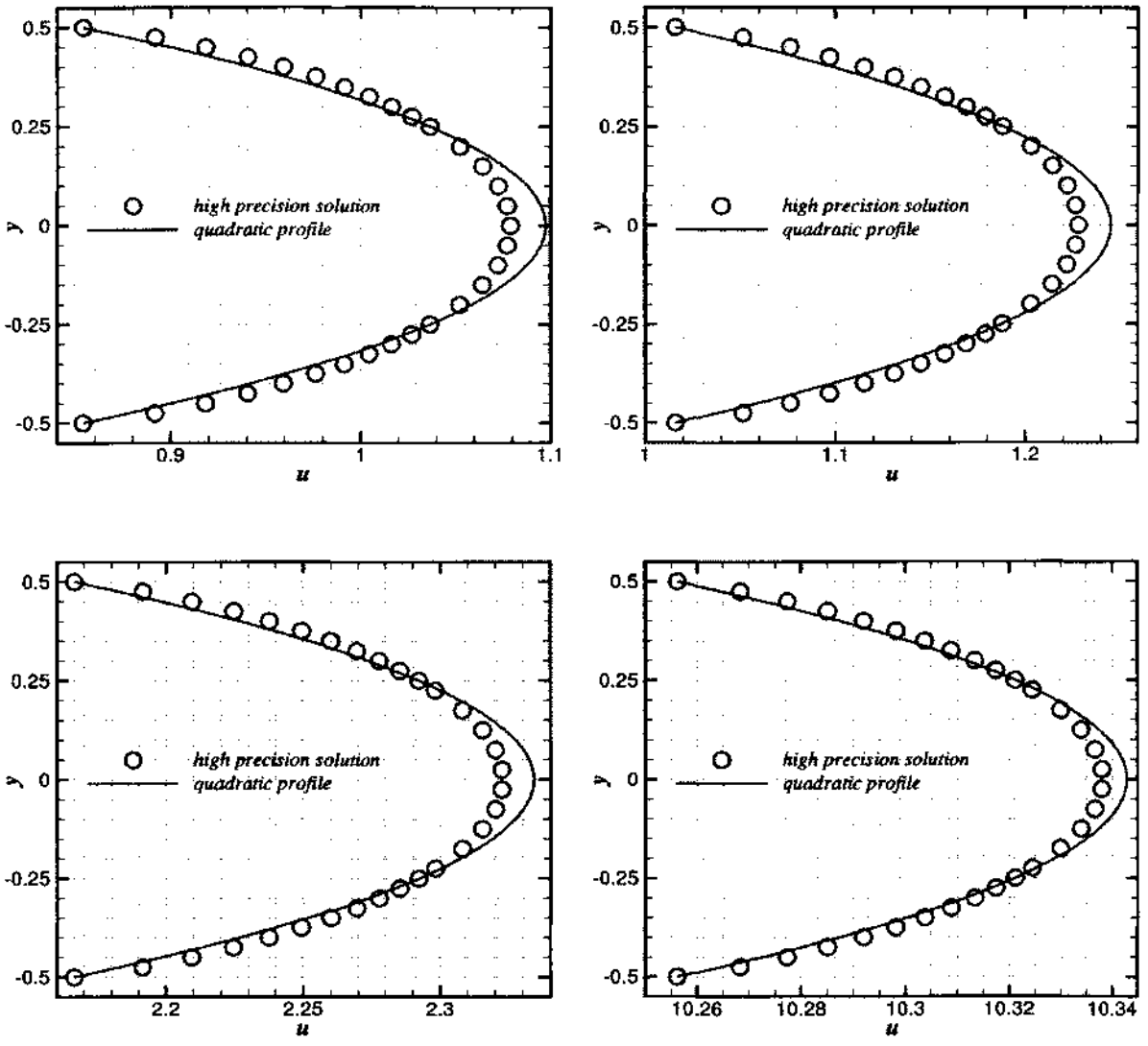

FIG. 18: Comparisons of Poiseuille flow velocities for $k = 10.0$: high precision solution v.s. quadratic profile. Top row, from left to right: $\alpha^+ = \alpha^- = 0$ and $\alpha^+ = \alpha^- = 0.1$. Bottom row, from left to right: $\alpha^+ = \alpha^- = 0.5$ and $\alpha^+ = \alpha^- = 0.9$.

where

$$\tilde{q}_j^N(x) = \begin{cases} \sum_{m=1}^{M} c_{j,m} L_{j,m-1}(x),\ x \in E_j, \\ 0,\ x \notin E_j. \end{cases}$$

Let $\{x_m\}_{m=1}^M$ be the set of M^{th} order Gauss-Legendre abscissas and let $\{x_{j,m}\}_{m=1}^M$ be the set of M^{th} order scaled and shifted Gauss-Legendre abscissas on the subinterval

TABLE 27: The dependence of the channel center stress $T_{xy} - y/2$ on the Knudsen number k and various accommodation ratios $\alpha^{\pm}$ for the Poiseuille flow problem

α^+	0.0	0.1	0.5	0.9
α^-	$k = 0.003$			
0.1	$1.570858305888211 \cdot 10^{-4}$	0	$-1.210191417554551 \cdot 10^{-3}$	$-1.128545314534777 \cdot 10^{-2}$
0.5	$1.367273337213620 \cdot 10^{-3}$	$1.210191417554551 \cdot 10^{-3}$	0	$-1.007744847754483 \cdot 10^{-2}$
0.9	$1.144221864747623 \cdot 10^{-2}$	$1.128545314534777 \cdot 10^{-2}$	$1.007744847754483 \cdot 10^{-2}$	0
α^-	$k = 0.3$			
0.1	$8.913282435524290 \cdot 10^{-3}$	0	$-5.343674573452724 \cdot 10^{-2}$	$-1.822176961818260 \cdot 10^{-1}$
0.5	$6.188466021353581 \cdot 10^{-2}$	$5.343674573452724 \cdot 10^{-2}$	0	$-1.524998246413054 \cdot 10^{-1}$
0.9	$1.863039662941896 \cdot 10^{-1}$	$1.822176961818260 \cdot 10^{-1}$	$1.524998246413054 \cdot 10^{-1}$	0
α^-	$k = 1.0$			
0.1	$1.497117687210425 \cdot 10^{-2}$	0	$-7.766749641004987 \cdot 10^{-2}$	$-2.045099438372151 \cdot 10^{-1}$
0.5	$9.090598248772540 \cdot 10^{-2}$	$7.766749641004987 \cdot 10^{-2}$	0	$-1.702169936415773 \cdot 10^{-1}$
0.9	$2.091831377492486 \cdot 10^{-1}$	$2.045099438372151 \cdot 10^{-1}$	$1.702169936415773 \cdot 10^{-1}$	0
α^-	$k = 2.0$			
0.1	$1.792672732135084 \cdot 10^{-2}$	0	$-8.715159192064605 \cdot 10^{-2}$	$-2.106352003060539 \cdot 10^{-1}$
0.5	$1.024474048491454 \cdot 10^{-1}$	$8.715159192064605 \cdot 10^{-2}$	0	$-1.750637048498325 \cdot 10^{-1}$
0.9	$2.154719636834514 \cdot 10^{-1}$	$2.106352003060539 \cdot 10^{-1}$	$1.750637048498325 \cdot 10^{-1}$	0
α^-	$k = 10.0$			
0.1	$2.232119709614557 \cdot 10^{-2}$	0	$-9.906354899069245 \cdot 10^{-2}$	$-2.169670099255494 \cdot 10^{-1}$
0.5	$1.171806492582279 \cdot 10^{-1}$	$9.906354899069245 \cdot 10^{-2}$	0	$-1.798660448790268 \cdot 10^{-1}$
0.9	$2.220342755033624 \cdot 10^{-1}$	$2.169670099255494 \cdot 10^{-1}$	$1.798660448790268 \cdot 10^{-1}$	0

TABLE 28: The dependence of the upper half channel mass flow rate Q^+ on the Knudsen number k and various accommodation ratios $\alpha^{\pm}$ for the Poiseuille flow problem

α^+	0.0	0.1	0.5	0.9
α^-	$k = 0.003$			
0.1	$1.415698073489974 \cdot 10^{1}$	$1.419640790968141 \cdot 10^{1}$	$1.450028862362330 \cdot 10^{1}$	$1.703132286312486 \cdot 10^{1}$
0.5	$1.425905726845356 \cdot 10^{1}$	$1.429873994836680 \cdot 10^{1}$	$1.460459734436412 \cdot 10^{1}$	$1.715264655566804 \cdot 10^{1}$
0.9	$1.510885573967081 \cdot 10^{1}$	$1.515068953083646 \cdot 10^{1}$	$1.547319196813729 \cdot 10^{1}$	$1.816475627121494 \cdot 10^{1}$
α^-	$k = 0.3$			
0.1	$4.542655080790500 \cdot 10^{-1}$	$4.879776642605176 \cdot 10^{-1}$	$6.930230164322536 \cdot 10^{-1}$	$1.195897456796713 \cdot 10^{0}$
0.5	$5.480008958421860 \cdot 10^{-1}$	$5.931487678267830 \cdot 10^{-1}$	$8.826884699702297 \cdot 10^{-1}$	$1.722412055255644 \cdot 10^{0}$
0.9	$7.690177507335172 \cdot 10^{-1}$	$8.475332807902532 \cdot 10^{-1}$	$1.425426859599006 \cdot 10^{0}$	$4.428483578655410 \cdot 10^{0}$
α^-	$k = 1.0$			
0.1	$4.028021573906146 \cdot 10^{-1}$	$4.363202236976626 \cdot 10^{-1}$	$6.114747583495295 \cdot 10^{-1}$	$9.003515239637751 \cdot 10^{-1}$
0.5	$4.950840254433967 \cdot 10^{-1}$	$5.456452033232609 \cdot 10^{-1}$	$8.420545502837424 \cdot 10^{-1}$	$1.490878709120579 \cdot 10^{0}$
0.9	$7.246972723179124 \cdot 10^{-1}$	$2.145338552444451 \cdot 10^{-1}$	$1.345916167851299 \cdot 10^{0}$	$4.404883852485195 \cdot 10^{0}$
α^-	$k = 2.0$			
0.1	$4.211251040540518 \cdot 10^{-1}$	$4.565236539643114 \cdot 10^{-1}$	$6.287615048525338 \cdot 10^{-1}$	$8.730946193991625 \cdot 10^{-1}$
0.5	$5.187489001847155 \cdot 10^{-1}$	$5.743447972211195 \cdot 10^{-1}$	$8.860927219236485 \cdot 10^{-1}$	$1.498322956716600 \cdot 10^{0}$
0.9	$6.497419809122507 \cdot 10^{-1}$	$7.411121909707257 \cdot 10^{-1}$	$1.394761757766220 \cdot 10^{0}$	$4.496487172523202 \cdot 10^{0}$
α^-	$k = 10.0$			
0.1	$5.387360417634455 \cdot 10^{-1}$	$5.844765785528613 \cdot 10^{-1}$	$7.855351002448069 \cdot 10^{-1}$	$1.021313796947412 \cdot 10^{0}$
0.5	$6.686788834560907 \cdot 10^{-1}$	$7.443513717380217 \cdot 10^{-1}$	$1.139101559821288 \cdot 10^{0}$	$1.804010254788733 \cdot 10^{0}$
0.9	$8.124500795815605 \cdot 10^{-1}$	$9.325310276077970 \cdot 10^{-1}$	$1.743869486891740 \cdot 10^{0}$	$5.156986493808719 \cdot 10^{0}$

E_j. We denote $\tilde{\boldsymbol{q}}_j$ as an M-tupple column with entry $\tilde{q}_{j,m} = \tilde{q}_j^N(x_{j,m})$. We substitute equation (110) into equation (109) and use the linear relation $\boldsymbol{c}_j = P\tilde{\boldsymbol{q}}_j$ from Appendix C to obtain

$$\tilde{q}_i^N(x) - \frac{1}{\pi^{1/2}} \sum_{j=1}^{N} \boldsymbol{\Psi}_j^T(x) P \boldsymbol{u}_j = \frac{1+\alpha}{\pi^{1/2}} I_1(\varphi(x)), \tag{111}$$

TABLE 29: The dependence of the lower half channel mass flow rate Q^- on the Knudsen number k and various accommodation ratios $\alpha^{\pm}$ for the Poiseuille flow problem

α^+	0.0	0.1	0.5	0.9
α^-	$k = 0.003$			
0.1	$1.418312495868741 \cdot 10^{1}$	$1.419640790968141 \cdot 10^{1}$	$1.429873994836680 \cdot 10^{1}$	$1.515068953083646 \cdot 10^{1}$
0.5	$1.448674943151412 \cdot 10^{1}$	$1.450028862362330 \cdot 10^{1}$	$1.460459734436412 \cdot 10^{1}$	$1.547319196813729 \cdot 10^{1}$
0.9	$1.701557841271955 \cdot 10^{1}$	$1.703132286312486 \cdot 10^{1}$	$1.715264655566804 \cdot 10^{1}$	$1.816475627121494 \cdot 10^{1}$
α^-	$k = 0.3$			
0.1	$4.704873284996498 \cdot 10^{-1}$	$4.879776642605176 \cdot 10^{-1}$	$5.931487678267830 \cdot 10^{-1}$	$8.475332807902532 \cdot 10^{-1}$
0.5	$6.631067951487771 \cdot 10^{-1}$	$6.930230164322536 \cdot 10^{-1}$	$8.826884699702297 \cdot 10^{-1}$	$1.425426859599006 \cdot 10^{0}$
0.9	$1.123606376793833 \cdot 10^{0}$	$1.195897456796713 \cdot 10^{0}$	$1.722412055255644 \cdot 10^{0}$	$4.428483578655410 \cdot 10^{0}$
α^-	$k = 1.0$			
0.1	$4.152903271008151 \cdot 10^{-1}$	$4.363202236976626 \cdot 10^{-1}$	$5.456452033232609 \cdot 10^{-1}$	$7.246972723179124 \cdot 10^{-1}$
0.5	$5.720838052499721 \cdot 10^{-1}$	$6.114747583495295 \cdot 10^{-1}$	$8.420545502837424 \cdot 10^{-1}$	$1.345916167851299 \cdot 10^{0}$
0.9	$8.194826323438264 \cdot 10^{-1}$	$9.003515239637751 \cdot 10^{-1}$	$1.490878709120579 \cdot 10^{0}$	$4.404883852485195 \cdot 10^{0}$
α^-	$k = 2.0$			
0.1	$4.322703263390911 \cdot 10^{-1}$	$4.565236539643114 \cdot 10^{-1}$	$5.743447972211195 \cdot 10^{-1}$	$7.411121909707257 \cdot 10^{-1}$
0.5	$5.830836851821827 \cdot 10^{-1}$	$6.287615048525338 \cdot 10^{-1}$	$8.860927219236485 \cdot 10^{-1}$	$1.394761757766220 \cdot 10^{0}$
0.9	$7.864392600185172 \cdot 10^{-1}$	$8.730946193991625 \cdot 10^{-1}$	$1.498322956716600 \cdot 10^{0}$	$4.496487172523202 \cdot 10^{0}$
α^-	$k = 10.0$			
0.1	$5.481932770626116 \cdot 10^{-1}$	$5.844765765528613 \cdot 10^{-1}$	$7.443513717380217 \cdot 10^{-1}$	$9.325310276077970 \cdot 10^{-1}$
0.5	$7.184631788495736 \cdot 10^{-1}$	$7.855351002448069 \cdot 10^{-1}$	$1.139101559821288 \cdot 10^{0}$	$1.743869486891740 \cdot 10^{0}$
0.9	$9.070412634603708 \cdot 10^{-1}$	$1.021313796947412 \cdot 10^{0}$	$1.804010254788733 \cdot 10^{0}$	$5.156986493808719 \cdot 10^{0}$

where $\Psi_j^T(x)$ is an M-tuple column vector with entry

$$\Psi_{j,m} = \int_{E_j} [I_{-1}(|\varphi(x)-\varphi(t)|)+\alpha I_{-1}(\varphi(x)+\varphi(t))]\varphi'(t)L_{j,m-1}(t)\,\mathrm{d}t,\ m = 1, 2, \cdots, M.$$

We substitute $x_{i,n}$ for x with $n = 1, 2, \cdots, M$ in equation (111), respectively, to obtain a linear system of M equations for $\tilde{\boldsymbol{q}}_i$,

$$\tilde{\boldsymbol{q}}_i - \frac{1}{\pi^{1/2}} \sum_{j=1}^{N} \boldsymbol{\Psi}_{j,i}^T P \tilde{\boldsymbol{q}}_j = \frac{1+\alpha}{\pi^{1/2}} \boldsymbol{F}_i, \tag{112}$$

where we denote the $M \times M$ matrix $\boldsymbol{\Psi}_{j,i}$ by

$$\boldsymbol{\Psi}_{j,i} = (\boldsymbol{\Psi}_j(x_{i,1})\, \boldsymbol{\Psi}_j(x_{i,2}) \cdots \boldsymbol{\Psi}_j(x_{i,M})).$$

and denote the M-tupple column vector $\boldsymbol{F}_i$ by

$$\boldsymbol{F}_i = (I_1(\varphi(x_{i,1}))\, I_1(\varphi(x_{i,2})) \cdots I_1(\varphi(x_{i,M})))^T.$$

By using the same decomposition as Equation (100), Equation (112) is rewritten in:

$$A\tilde{\boldsymbol{q}} = \boldsymbol{F}, \tag{113}$$

where

$$A = \begin{pmatrix} \boldsymbol{\Phi}_{1,1}P & \boldsymbol{\Phi}_{1,2}P & \cdots & \boldsymbol{\Phi}_{1,N}P \\ \boldsymbol{\Phi}_{2,1}P & \boldsymbol{\Phi}_{2,2}P & \cdots & \boldsymbol{\Phi}_{2,N}P \\ \cdots & \cdots & \cdots & \cdots \\ \boldsymbol{\Phi}_{N,1}P & \boldsymbol{\Phi}_{N,2}P & \cdots & \boldsymbol{\Phi}_{N,N}P \end{pmatrix},$$

$$\tilde{\boldsymbol{q}} = (\tilde{\boldsymbol{q}}_1^T\, \tilde{\boldsymbol{q}}_2^T \cdots \tilde{\boldsymbol{q}}_N^T)^T$$

and

$$\boldsymbol{F} = (1+\alpha)(\boldsymbol{F}_1^T\, \boldsymbol{F}_2^T \cdots \boldsymbol{F}_N^T)^T.$$

In the Kramers problem, the m^{th} row and n^{th} column entry of $\Phi_{i,j}$ reads

$$\begin{aligned}
&\mathrm{ent}_{mn}\, \Phi_{i,j} \\
&= \begin{cases}
(-1)^n[I_0(\varphi(x_{j-1}) - \varphi(x_{i,m})) + \alpha I_0(\varphi(x_{i,m}) + \varphi(x_{j-1}))] \\
+[I_0(\varphi(x_j) - \varphi(x_{i,m})) + \alpha I_0(\varphi(x_{i,m}) + \varphi(x_j))] \\
-\int_{-1}^{1}[I_0(\varphi(x_{j,t}) - \varphi(x_{i,m})) + \alpha I_0(\varphi(x_{i,m}) + \varphi(x_{j,t}))]L'_{n-1}(t)\,\mathrm{d}t, & j < i, \\
\\
(-1)^n I_0(\varphi(x_{i-1}) - \varphi(x_{i,m})) - I_0(\varphi(x_{i,m}) - \varphi(x_i)) \\
+\alpha[(-1)^n I_0(\varphi(x_{i,m}) + \varphi(x_{i-1})) + I_0(\varphi(x_{i,m}) + \varphi(x_i))] \\
-\int_{-1}^{x_m}[I_0(\varphi(x_{i,t}) - \varphi(x_{i,m})) + \alpha I_0(\varphi(x_{i,m}) + \varphi(x_{i,t}))]L'_{n-1}(t)\,\mathrm{d}t \\
+\int_{x_m}^{1}[I_0(\varphi(x_{i,m}) - \varphi(x_{i,t})) - \alpha I_0(\varphi(x_{i,m}) + \varphi(x_{i,t}))]L'_{n-1}(t)\,\mathrm{d}t, & j = i, \\
\\
-[I_0(\varphi(x_{i,m}) - \varphi(x_j)) - \alpha I_0(\varphi(x_{i,m}) + \varphi(x_j))] \\
+(-1)^{n+1}[I_0(\varphi(x_{i,m}) - \varphi(x_{j-1})) - \alpha I_0(\varphi(x_{i,m}) + \varphi(x_{j-1}))] \\
+\int_{-1}^{1}[I_0(\varphi(x_{i,m}) - \varphi(x_{j,t})) - \alpha I_0(\varphi(x_{i,m}) + \varphi(x_{j,t}))]L'_{n-1}(t)\,\mathrm{d}t, & j > i,
\end{cases}
\end{aligned} \tag{114}$$

where $x_{j,t} = x_{j-1} + \frac{(t+1)(x_j - x_{j-1})}{2}$.

We use the same subdivision of the interval as we did in the Couette flow problem and translate the subintervals from $[-1/2, 1/2]$ to $[0,1]$. Numerically, we choose $N = 320$ and $M = 10$ and solve equation (113) for $\tilde{\boldsymbol{q}}$ with various values of accommodation ratio α. Then, we use the transform $\varphi(x) = 2(-\ln x/3)^{2/3}$ to map $\tilde{\boldsymbol{q}}$ on the interval $x \in [0,1]$ to corresponding $\boldsymbol{q}$ on the interval $y \in [0,\infty)$. We also compute the shear stress by the formula below derived from equation (49),

$$T_{xy} = \pi^{-1/2}(1-\alpha)\int_0^1 (\varphi(t) + \tilde{q}(t))I_0(\varphi(t))\varphi'(t)\,\mathrm{d}t,$$

where the integral is evaluated piece-wise by a 10^{th} order scaled and shifted Gauss-Legendre quadrature on each subinterval E_j. Cercignani [4] defines $q(\infty)$ as the slip coefficient of the Kramers problem, which can be considered as the macroscopic slip velocity in contrast with the (microscopic) slip velocity $q(0)$ at the boundary. By using the fast decay proper of $q(y)$, we use $q(10^7)$ to approximate $q(\infty)$. We tabulate the accommodation ratio α dependence of the slip velocity $q(0)$, the approximated

TABLE 30: The accommodation ratio α dependence of the slip velocity $q(0)$, the approximated slip coefficient $q(10^7)$ and the shear stress T_{xy}

α	$q(0)$	$q(10^7)$	T_{xy}
0.0	$7.071067811865468 \cdot 10^{-1}$	$1.016191418323346 \cdot 10^{0}$	$-5.230964573859846 \cdot 10^{-1}$
0.001	$7.086820767105562 \cdot 10^{-1}$	$1.018105271637540 \cdot 10^{0}$	$-5.233552791792914 \cdot 10^{-1}$
0.01	$7.230190811074491 \cdot 10^{-1}$	$1.035492188939355 \cdot 10^{0}$	$-5.256880038420038 \cdot 10^{-1}$
0.1	$8.839366725938867 \cdot 10^{-1}$	$1.227197911287705 \cdot 10^{0}$	$-5.493480811866413 \cdot 10^{-1}$
0.2	$1.109556489218961 \cdot 10^{0}$	$1.487654338703426 \cdot 10^{0}$	$-5.763610881893807 \cdot 10^{-1}$
0.3	$1.405054175925948 \cdot 10^{0}$	$1.818667048076728 \cdot 10^{0}$	$-6.041587684357618 \cdot 10^{-1}$
0.4	$1.805584301989019 \cdot 10^{0}$	$2.255409689068308 \cdot 10^{0}$	$-6.327652866198790 \cdot 10^{-1}$
0.5	$2.374435133397930 \cdot 10^{0}$	$2.861190317159085 \cdot 10^{0}$	$-6.622057227152184 \cdot 10^{-1}$
0.6	$3.238196345027700 \cdot 10^{0}$	$3.762619138936156 \cdot 10^{0}$	$-6.925061148782125 \cdot 10^{-1}$
0.7	$4.692262201783895 \cdot 10^{0}$	$5.255111728226256 \cdot 10^{0}$	$-7.236935047786326 \cdot 10^{-1}$
0.8	$7.622844354596162 \cdot 10^{0}$	$8.224901859074006 \cdot 10^{0}$	$-7.557959855183786 \cdot 10^{-1}$
0.9	$1.646106156479885 \cdot 10^{1}$	$1.710313126923792 \cdot 10^{1}$	$-7.888427523126342 \cdot 10^{-1}$

slip coefficient $q(10^7)$ and the shear stress T_{xy} in Table 30. In the case of completely diffusive boundary condition at the wall, *i.e.*, $\alpha = 0$, both the microscopic and the macroscopic slip velocities are studied analytically or with high precision by researchers. Cercignani [5] (in equation (29)) gives an analytical solution of the microscopic slip velocity $q(0) = \sqrt{2}/2$. The difference between this analytical solution and our numerical solution is less than 10^{-15}. Loyalka [6] gives a high precision solution of the macroscopic slip velocity $q(\infty) = 1.016191418323352759\cdots$. The difference between this high precision solution and our numerical approximation is less than 10^{-14}. Hence, our solutions are reliable and of high precision. The shear stress has high linear dependence on the accomodation ratio. Figure 19 shows the shear stress versus the accommodation ratio and linear mean square fitting of the shear stress. To depict the structure of velocity profile in the near boundary Knudsen lay, Cercignani [4] defines the function of velocity defect by $I(y) = 2\pi^{1/2}[q(\infty) - q(y)]$. Figure 20 shows the velocity defect of the Kramer flow problem for α ranging from 0 to 0.9.

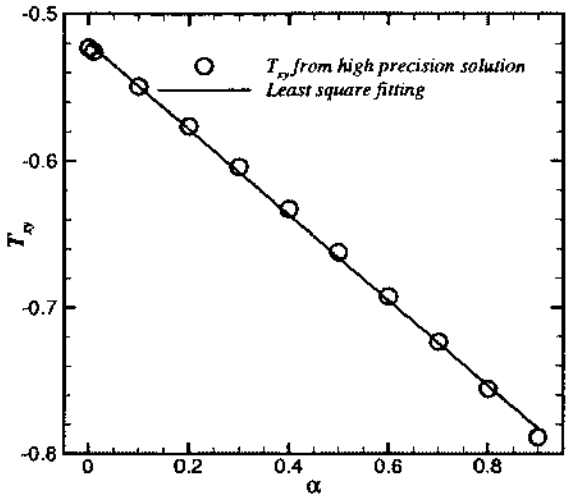

FIG. 19: Shear stress versus the accommodation ratio $\alpha = 0, 0.001, 0.01, 0.1, 0.2, 0.3, 0.4, 0.5, 0.6, 0.7, 0.8, 0.9$.

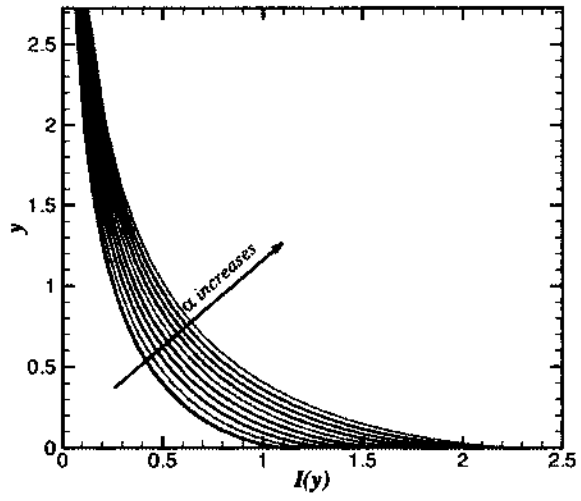

FIG. 20: The velocity defect of the Kramer flow problem for $\alpha = 0, 0.1, 0.2, 0.3, 0.4, 0.5, 0.6, 0.7, 0.8, 0.9$ with $y \in [0, 2.72703]$.

CHAPTER 4

ANALYSIS OF THE COUETTE FLOW

In this chapter, we approximate the velocity profiles with different Knudsen numbers by fitting various model functions. We start from Gross *et al*'s linear approximation to the velocity profile with purely diffusive boundary condition for arbitrary Knudsen number [8]. By substituting the linear approximation into the integral equation, we obtain an approximation to the velocity in terms of Abramowitz functions. Adjusting the coefficients of the Abramowitz functions by using least square fitting, we obtain very accurate velocity profiles of the rarefied Couette flows with different Knudsen numbers, which is optimal in the sense of L_2 norm. Since the approximations to the velocity in terms of the Abramowitz functions is still not very convenient to use, we further approximate the velocities with odd degree polynomials by using least square fitting. As to use which degree polynomial should be used as the pattern function, we apply the variational method to show that the cubic approximation to the velocity is a good choice. Besides the velocity profile, we discuss the boundary information, such as the velocity defect, the microscopic slip velocity and the macroscopic slip velocity at the boundary. We analyze the microscopic slip velocity, the macroscopic slip velocity and the half channel mass flow rate as functions of the Knudsen number by using the asymptotic behaviors of the Abramowitz functions of order $-1, 0, 1$ and 2. As a result, we obtain very accurate relationships between the microscopic slip velocity and the Knudsen number, the macroscopic slip velocity and the Knudsen number, as well as, the half channel mass flow rate and the Knudsen number. At the end of this section, we construct the effective viscosity of the rarefied Couette flow by using one of the cubic approximations to the velocity. We reproduce this cubic approximation to the velocity by using the two relaxation time lattice Boltzmann equation (TRT-LBE) with the effective viscosity and Dirichlet boundary condition. This shows the rarefied Couette flow can be characterized by a Navier-Stoke like equation with appropriate stress tensor.

4.1 FIRST APPROXIMATION OF VELOCITY

In this section, we construct an approximation to the velocity profile of the Couette flow problem with purely diffusive walls. Our approximation captures the leading order singularity of the velocity profile at the boundaries. First we explore the features of the velocity. It is obvious that, at finite Knudsen number k, the boundary velocity does not equal the wall velocity, *i.e.*, there is a microscopic slip velocity u_s. It has been proven the boundary velocity derivative $u'(\pm 1/2)$ is infinite. In the framework of hydrodynamic equation, the velocity of Couette flow is a straight line. Figure 21 shows the Knudsen number dependence of the velocity $u(y)$ computed by the chunk based collocation method with $N = 320$. The velocities are compared with each corresponding straight line $u_1^*(y) = u'(0)y$ for various values of Knudsen number k. The staight lines are solutions to the Navier-Stokes equation for various values of k with slip velocities. The figure shows that in the bulk flow region, the velocity $u(y)$ is close to the hydrodynamic solution $u_1^*(y)$; however, near the boundary, the nonlinear property of $u(y)$ makes it off the straight line. To measure the kinetic component of the velocity, we compute the nonlinear component of the normalized velocity $u(y)/u(1/2)$,

$$u_{NL} = \frac{u(y)}{u(1/2)} - 2y. \tag{115}$$

Figure 21 shows the nonlinear component of $u(y)/u(1/2)$ increases as k increases. On balance, there exists a singular nonlinear Knudsen layer near the walls. The high precision solutions of the Couette flow problem enable us to gain some insights concerning the Knudsen layer by using relatively simpler approximations. The simplest approximation for the velocity of Couette flow problem is the linear approximation by Gross *et al.* [8]. Noticing the discontinuity of the distribution function in phase space at the boundaries, they construct two half range polynimial distribution functions as trial functions. They compute full range moments by using the trial polynomials and set up moment equations by integrating the integrodifferential equation for Couette flow over the phase space. They solve the moment equation along with the boundary conditions for the coefficients of the trial polynomials. Then, they obtain the velocity function by integrating over the phase space. The first approximation to the velocity is:

$$\tilde{u}_0(y) = \frac{y}{1 + k\sqrt{\pi/2}}. \tag{116}$$

By substituting equation (116) into the integral term of equation (72), we obtain an approximate solution to the velocity which captures the nonlinearity and the

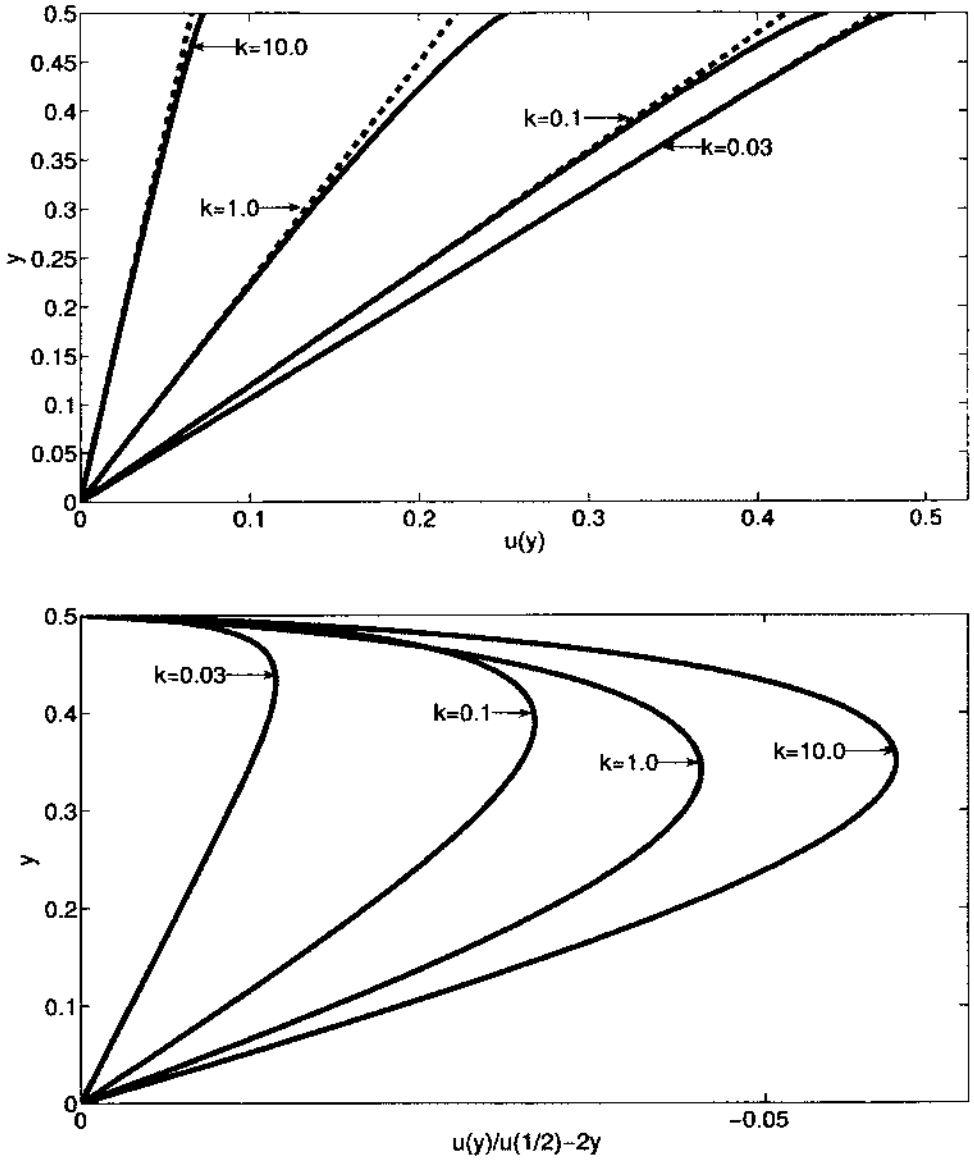

FIG. 21: The Knudsen number dependence of velocity $u(y)$. Top: The solid and dashed lines corresponds to the numerical solution $u^N(y)$ with $N = 320$ and $u_1^* = u'(0)y$, *i.e.*, the straight line tangent to $u(y)$ at $y = 0$. Bottom: The normalized nonlinear component of the velocity, u_{NL} defined by Equation (115), $u(y)/u(1/2)$.

singularity of the Knudsen layer near the boundary:

$$\tilde{u}(y) = \frac{k}{1 + k\sqrt{\pi/2}} \left[\frac{y}{k} + \frac{F_0(y,k)}{2\sqrt{2}} - \frac{F_1(y,k)}{\sqrt{\pi}} \right]. \tag{117}$$

Near the wall at $y = +1/2, \delta = (1/2-y) \ll 1$, both $I_n((1/2+y)/k) = I_n((1-\delta)/k) \approx I_n(1/k)$ and $I_n((1/2-y)/k) = I_n(\delta/k)$ can be approximated by their leading order expansions [1] given in Appendix A. Hence, equation (117) becomes:

$$\begin{aligned}\tilde{u}(y) &\approx a_0 \left\{ (\delta/k) + \frac{(\delta/k)\ln(\delta/k)}{\sqrt{2}} + \frac{1}{k} + \left[\frac{\sqrt{\pi}}{2\sqrt{2}} - \frac{1}{\sqrt{\pi}} - \frac{I_0(1/k)}{\sqrt{2}} + \frac{2I_1(1/k)}{\sqrt{\pi}} \right] \right\} \\ &= a_0(\delta/k)\left(1 + \frac{\ln(\delta/k)}{\sqrt{2}}\right) + \tilde{u}(1/2) \end{aligned} \tag{118}$$

where

$$\begin{aligned}\tilde{u}(1/2) &= a_0 \left[\frac{1}{k} + \frac{2F_1(0,k)}{\sqrt{\pi}} - \frac{F_0(0,k)}{\sqrt{2}} \right] \\ &= a_0 \left[\frac{1}{k} + \frac{\sqrt{\pi}}{2\sqrt{2}} - \frac{1}{\sqrt{\pi}} - \frac{I_0(1/k)}{\sqrt{2}} + \frac{2I_1(1/k)}{\sqrt{\pi}} \right]\end{aligned}$$

and

$$a_0 = \frac{k}{2 + k\sqrt{2\pi}}.$$

Equation (118) shows the leading order singularity of the velocity at the boundary $y = \pm 1/2$ is $(\delta/k)\ln(\delta/k)$ with $\delta = 1/2 \mp y$. When $y \to \pm 1/2, u'(y) \sim \ln(\delta/k)$, thus $u'(y)$ blows up at the boundaries $y = \pm 1/2$ for $k \neq 0$. While the approximated solution $\tilde{u}(y)$ conserves the singularity of the velocity, it does not approximate it well quantitatively. For instance, $\tilde{u}(1/2) \neq u(1/2)$ and $\tilde{u}'(0) \neq u'(0)$.

We can improve the approximation of the velocity based on $\tilde{u}(y)$ by assuming the approximation of $u(y)$ has the following form:

$$\tilde{u}_1(y) = A(k) + B(k)F_0(y,k) + C(k)F_1(y,k), \tag{119}$$

where $A(k), B(k)$ and $C(k)$ are functions of k alone and are fully determined by the following constrains on $\tilde{u}_1(y,k)$:

$$\begin{aligned}\tilde{u}_1(1/2) &= u(1/2), \\ \tilde{u}_1'(0) &= u'(0), \\ \int_0^{1/2} \tilde{u}_1(y)\,\mathrm{d}y &= Q,\end{aligned}$$

where $u(1/2), u'(0)$ and Q are obtained by using the accurate solution $u^N(y)$ with

TABLE 31: Coefficients of the approximation $\tilde{u}(y) = Ay + BF_0(y,k) + CF_1(y,k)$

k	A	B	C
0.003	$9.939398011037547 \cdot 10^{-1}$	$4.203888321649420 \cdot 10^{-4}$	$1.098149648651225 \cdot 10^{-3}$
0.01	$9.800810019019697 \cdot 10^{-1}$	$1.381929614714690 \cdot 10^{-3}$	$3.609153178711989 \cdot 10^{-3}$
0.03	$9.425419498579877 \cdot 10^{-1}$	$4.117989399334418 \cdot 10^{-3}$	$1.017084072395429 \cdot 10^{-2}$
0.1	$8.329356170017682 \cdot 10^{-1}$	$1.958836369520414 \cdot 10^{-2}$	$1.480875860779301 \cdot 10^{-2}$
0.3	$6.379645268711726 \cdot 10^{-1}$	$6.031742674360471 \cdot 10^{-2}$	$-9.010953908070029 \cdot 10^{-3}$
1.0	$3.827430174542746 \cdot 10^{-1}$	$1.289092270309213 \cdot 10^{-1}$	$-9.736027778683470 \cdot 10^{-2}$
2.0	$2.644689510083537 \cdot 10^{-1}$	$1.695879157944917 \cdot 10^{-1}$	$-1.888905977706435 \cdot 10^{-1}$
3.0	$2.100280076555217 \cdot 10^{-1}$	$1.909461676316779 \cdot 10^{-1}$	$-2.566629932617473 \cdot 10^{-1}$
5.0	$1.554441376291299 \cdot 10^{-1}$	$2.141141551745609 \cdot 10^{-1}$	$-3.566589264444766 \cdot 10^{-1}$
7.0	$1.267321809253623 \cdot 10^{-1}$	$2.269031187313728 \cdot 10^{-1}$	$-4.302171682790011 \cdot 10^{-1}$
10.0	$1.015072463335740 \cdot 10^{-1}$	$2.383573140063627 \cdot 10^{-1}$	$-5.141844415188976 \cdot 10^{-1}$

TABLE 32: L2 error of the approximation $\tilde{u}_1(y) = Ay + BF_0(y,k) + CF_1(y,k)$ and the shear stress T_{xy} obtained from $\tilde{u}_1(y)$

k	$\|\delta\tilde{u}_1\|_2$	T_{xy}
0.003	$4.119601276915541 \cdot 10^{-5}$	$-1.490909701655703 \cdot 10^{-3} \pm 5.4872 \cdot 10^{-15}$
0.01	$2.871350474093244 \cdot 10^{-5}$	$-4.900405009089867 \cdot 10^{-3} \pm 2.0275 \cdot 10^{-14}$
0.03	$2.827978188662598 \cdot 10^{-4}$	$-1.413793251056168 \cdot 10^{-2} \pm 5.6901 \cdot 10^{-9}$
0.1	$6.854709346659341 \cdot 10^{-4}$	$-4.155030609974823 \cdot 10^{-2} \pm 2.0460 \cdot 10^{-6}$
0.3	$4.829075597474416 \cdot 10^{-4}$	$-9.344448147076767 \cdot 10^{-2} \pm 5.6934 \cdot 10^{-6}$
1.0	$2.075774717255118 \cdot 10^{-4}$	$-1.694619104626556 \cdot 10^{-1} \pm 2.3569 \cdot 10^{-6}$
2.0	$1.102324807418621 \cdot 10^{-4}$	$-2.083321401486735 \cdot 10^{-1} \pm 8.0488 \cdot 10^{-7}$
3.0	$7.337088550969131 \cdot 10^{-5}$	$-2.266437144577648 \cdot 10^{-1} \pm 3.7549 \cdot 10^{-7}$
5.0	$4.269904069281610 \cdot 10^{-5}$	$-2.446632605710038 \cdot 10^{-1} \pm 1.2894 \cdot 10^{-7}$
7.0	$2.950323276648715 \cdot 10^{-5}$	$-2.536943515313993 \cdot 10^{-1} \pm 6.0449 \cdot 10^{-8}$
10.0	$1.977231898835104 \cdot 10^{-5}$	$-2.611624596132240 \cdot 10^{-1} \pm 2.6077 \cdot 10^{-8}$

$N = 320$. Specifically, the equation for A, B and C are:

$$A + \frac{2}{k} I_{-1}\left(\frac{1}{2k}\right) B + \frac{2}{k} I_0\left(\frac{1}{2k}\right) C = u'(0),$$

$$\frac{1}{2}A + \left[\frac{\sqrt{\pi}}{2} - I_0\left(\frac{1}{k}\right)\right] B + \left[\frac{1}{2} - I_1\left(\frac{1}{k}\right)\right] C = u(1/2),$$

$$\frac{1}{8}A + k\left[\frac{1}{2} + I_1\left(\frac{1}{k}\right) - 2I_1\left(\frac{1}{2k}\right)\right] B + k\left[\frac{\sqrt{\pi}}{4} + I_2\left(\frac{1}{k}\right) - 2I_2\left(\frac{1}{2k}\right)\right] C = Q.$$

The numerical solutions of $A(k), B(k)$ and $C(k)$ are given in Table 31. The solutions of $A(k), B(k)$ and $C(k)$ are smoothly dependent on k. To measure the accuracy and quality of the approximate solution $\tilde{u}_1(y)$, we compute the global L_2 error of $\tilde{u}_1(y)$ and shear stress T_{xy} obtained form $\tilde{u}_1(y)$. The results are tabulated in Table 32. The half channel mass flow rate Q is used as one of the constraints to determine $\tilde{u}_1(y)$ and Q, computed from the approximate solution $\tilde{u}_1(y)$, is identical to Q computed with $u^N(y)$ in Table 13. The L_2 global error never exceeds $7 \cdot 10^{-4}$ and the error in the stress T_{xy} obtained from $\tilde{u}_1(y)$ are in the fifth digit or smaller. Hence, the solution $\tilde{u}_1(y)$ is a highly effective approximation in terms of the stated measurements.

However, to construct the Maxwell type slip velocity boundary condition, which

can be used in the framework of Navier-Stokes equations [9]-[15], we cannot allow a boundary singularity in the velocity $u(y)$, since these boundary conditions include derivatives of $u(y)$ at the boundary. To accommodate the Maxwell type slip velocity boundary condition, we need to consider other approximations of $u(y)$ in the following section.

4.2 VARIATIONAL APPROACH TO COUETTE FLOW

In this section, we discuss the variational approach to the Couette flow problem, which leads us to odd degree polynomial approximations to the velocity $u(y)$. The approxiamtions possess correct symmetry of the flow but without the boundary singularities and thus can be used to construct Maxwell slip boundary conditions. As a preparation, we define an integral operator A associated with equation (72) by

$$A\varphi(y) = \frac{1}{\pi^{1/2}k}\int_{-1/2}^{1/2} I_{-1}\left(\frac{|y-s|}{k}\right)\varphi(s)\,\mathrm{d}s \tag{120}$$

Then, a simple calculation shows that A is self-adjoint and equation (72) can be rewritten as:

$$u - Au = \pi^{-1/2}F_0(\cdot,k)/2. \tag{121}$$

Since $\pi^{-1/2}G_0(y,k) < 1$, one also has

$$\begin{aligned}\|A\|_2^2 &= \int_{-1/2}^{1/2}\left[\frac{1}{\pi^{1/2}k}\int_{-1/2}^{1/2} I_{-1}\left(\frac{|y-s|}{k}\right)\mathrm{d}s\right]^2\mathrm{d}y \\ &= \int_{-1/2}^{1/2}[1-\pi^{1/2}G_0(y,k)]^2\,\mathrm{d}y < 1.\end{aligned}$$

We define the functional $J(u)$ as

$$J(u) = \int_{-1/2}^{1/2} u(y)[u(y) - Au(y) - \pi^{-1/2}F_0(y,k)]\,\mathrm{d}y, \tag{122}$$

Then, if u is the solution to equation (121), we have

$$\begin{aligned}J(u+\delta u) &= -\frac{1}{2\pi^{1/2}}\int_{-1/2}^{1/2} u(y)F_0(y,k)\,\mathrm{d}y + \int_{-1/2}^{1/2}[\delta u(y) - A\delta u(y)]\delta u(y)\,\mathrm{d}y \\ &\geq -\frac{1}{2\pi^{1/2}}\int_{-1/2}^{1/2} u(y)F_0(y,k)\,\mathrm{d}y + (1-\|A\|_2)\int_{-1/2}^{1/2}[\delta u(y)]^2\,\mathrm{d}y,\end{aligned}$$

where $\|A\|_2$ is the L_2 operator norm of A, which results in

$$\min J(u) = -\frac{1}{2\pi^{1/2}}\int_{-1/2}^{1/2} u(y)F_0(y,k)\,\mathrm{d}y.$$

Hence solving equation (121) is equivalent to minimizing the functional $J(u)$. Considering that $u(y)$ is an odd function, Cercignani [7] uses a linear function $u_1(y) = a_1 y$ and a cubic function $u_3(y) = a_1 y + a_2 y^3$ as trial functions, respectively, to minimize the functional by determining the coefficients. The results in his paper have a few typos. We repeat Cercignani's process to correct the typos in u_1 and u_3 and derive a fifth power approximation $u_5(y) = a_1 y + a_2 y^3 + a_3 y^5$ to the velocity.

For u_1, we have

$$J(u_1) = a_1^2 C_{11} + 2a_1 b_1, \tag{123}$$

where C_{11} and b_1 are scalars:

$$C_{11} = -\frac{k(-1+4k^2)}{4\pi^{1/2}} + \frac{k}{2\pi^{1/2}} I_1(1/k) + \frac{2k^2}{\pi^{1/2}} I_2(1/k) + \frac{2k^3}{\pi^{1/2}} I_3(1/k)$$

and

$$b_1 = \frac{k^2}{4} - \frac{k}{4\pi^{1/2}} - \frac{k}{2\pi^{1/2}} I_1(1/k) - \frac{k^2}{\pi^{1/2}} I_2(1/k).$$

When $a_1 = -b_1/C_{11}$, $J(u_1)$ takes its minimum $\min J(u_1) = -b_1^2/C_{11}$.

For u_3, we have

$$J(u_3) = \boldsymbol{a}^T C \boldsymbol{a} + 2\boldsymbol{a}^T \boldsymbol{b}, \tag{124}$$

where $\boldsymbol{a} = [a_1\, a_2]^T$, C is a 2×2 matrix and $\boldsymbol{b}$ is a 2-tuple column vector (with C_{11} and b_1 defined in equation (123)):

$$\begin{aligned}
C_{12} = C_{21} = &-\frac{k(-1+2\pi^{1/2}k - 12k^2 + 192k^4)}{16\pi^{1/2}} \\
&+ \frac{k}{8\pi^{1/2}} I_1(1/k) + \frac{k^2}{\pi^{1/2}} I_2(1/k) + \frac{9k^3}{2\pi^{1/2}} I_3(1/k) + \frac{12k^4}{\pi^{1/2}} I_4(1/k) + \frac{12k^5}{\pi^{1/2}} I_5(1/k), \\
C_{22} = &-\frac{k(-5+12\pi^{1/2}k - 60k^2 + 69120k^6)}{320\pi^{1/2}} \\
&+ \frac{k}{32\pi^{1/2}} I_1(1/k) + \frac{3k^2}{8\pi^{1/2}} I_2(1/k) + \frac{21k^3}{8\pi^{1/2}} I_3(1/k) + \frac{12k^4}{\pi^{1/2}} I_4(1/k) + \frac{36k^5}{\pi^{1/2}} I_5(1/k) \\
&+ \frac{72k^6}{\pi^{1/2}} I_6(1/k) + \frac{72k^7}{\pi^{1/2}} I_7(1/k)
\end{aligned}$$

and

$$\begin{aligned}
b_2 = &\frac{k(-1+3\pi^{1/2}k - 24k^2 + 36\pi^{1/2}k^3)}{16\pi^{1/2}} \\
&- \frac{k}{8\pi^{1/2}} I_1(1/k) - \frac{3k^2}{4\pi^{1/2}} I_2(1/k) - \frac{3k^3}{\pi^{1/2}} I_3(1/k) - \frac{6k^4}{\pi^{1/2}} I_4(1/k).
\end{aligned}$$

When $\boldsymbol{a} = -C^{-1}\boldsymbol{b}$, $J(u_3)$ takes its minimum $\min J(u_3) = -\boldsymbol{b}^T C \boldsymbol{b}$.

For u_5, we have

$$J(u_5) = \boldsymbol{a}^T C \boldsymbol{a} + 2\boldsymbol{a}^T \boldsymbol{b}, \tag{125}$$

where $\boldsymbol{a} = [a_1\, a_2\, a_3]^T$, C is a 3×3 matrix and $\boldsymbol{b}$ is a 3-tuple column vector (with $C_{11}, C_{12}, C_{21}, C_{22}, b_1$ and b_2 defined in equation (124)):

$$
\begin{aligned}
C_{13} = C_{31} = & -\frac{k(-1 + 4\pi^{1/2}k - 60k^2 + 240\pi^{1/2}k^3 - 1920k^4 + 46080k^6)}{64\pi^{1/2}} \\
& + \frac{k}{32\pi^{1/2}} I_1(1/k) + \frac{3k^2}{8\pi^{1/2}} I_2(1/k) + \frac{25k^3}{8\pi^{1/2}} I_3(1/k) + \frac{20k^4}{\pi^{1/2}} I_4(1/k) + \frac{90k^5}{\pi^{1/2}} I_5(1/k) \\
& + \frac{240k^6}{\pi^{1/2}} I_6(1/k) + \frac{240k^7}{\pi^{1/2}} I_7(1/k), \\
C_{23} = C_{32} = & -\frac{k(-7 + 26\pi^{1/2}k - 308k^2 + 1008\pi^{1/2}k^3 - 6720k^4 + 30965760k^8)}{1792\pi^{1/2}} \\
& + \frac{k}{128\pi^{1/2}} I_1(1/k) + \frac{k^2}{8\pi^{1/2}} I_2(1/k) + \frac{41k^3}{32\pi^{1/2}} I_3(1/k) + \frac{39k^4}{4\pi^{1/2}} I_4(1/k) \\
& + \frac{225k^5}{4\pi^{1/2}} I_5(1/k) + \frac{240k^6}{\pi^{1/2}} I_6(1/k) + \frac{720k^7}{\pi^{1/2}} I_7(1/k) + \frac{1440k^8}{\pi^{1/2}} I_8(1/k) \\
& + \frac{1440k^9}{\pi^{1/2}} I_9(1/k), \\
C_{33} = & -\frac{k(-63 + 280\pi^{1/2}k - 3780k^2 + 12960\pi^{1/2}k^3 - 80640k^4 + 111476736000k^{10})}{64512\pi^{1/2}} \\
& + \frac{k}{512\pi^{1/2}} I_1(1/k) + \frac{5k^2}{128\pi^{1/2}} I_2(1/k) + \frac{65k^3}{128\pi^{1/2}} I_3(1/k) + \frac{5k^4}{\pi^{1/2}} I_4(1/k) \\
& + \frac{155k^5}{4\pi^{1/2}} I_5(1/k) + \frac{240k^6}{\pi^{1/2}} I_6(1/k) + \frac{1200k^7}{\pi^{1/2}} I_7(1/k) + \frac{4800k^8}{\pi^{1/2}} I_8(1/k) \\
& + \frac{14400k^9}{\pi^{1/2}} I_9(1/k) + \frac{28800k^{10}}{\pi^{1/2}} I_{10}(1/k) + \frac{28800k^{11}}{\pi^{1/2}} I_{11}(1/k)
\end{aligned}
$$

and

$$
\begin{aligned}
b_3 = & \frac{k(-1 + 5\pi^{1/2}k - 80k^2 + 360\pi^{1/2}k^3 - 3840k^4 + 7200\pi^{1/2}k^5)}{64\pi^{1/2}} \\
& - \frac{k}{32\pi^{1/2}} I_1(1/k) - \frac{5k^2}{16\pi^{1/2}} I_2(1/k) - \frac{5k^3}{2\pi^{1/2}} I_3(1/k) - \frac{15k^4}{\pi^{1/2}} I_4(1/k) - \frac{60k^5}{\pi^{1/2}} I_5(1/k) \\
& - \frac{120k^6}{\pi^{1/2}} I_6(1/k).
\end{aligned}
$$

When $\boldsymbol{a} = -\boldsymbol{C}^{-1}\boldsymbol{b}$, $J(u_5)$ takes its minimum $\min J(u_5) = -\boldsymbol{b}^T\boldsymbol{C}\boldsymbol{b}$.

Numerically, we compute the coefficient $\boldsymbol{a}$ for $u_i(y)(i = 1, 3, 5)$ with various values of Knudsen number k. Table 33 shows the dependence of $u'(0)$ (from the chunk based collocation method with $N = 320$) on the Knudsen number k. It also shows the values of the coefficients of the approximating polynomials with different Knudsen numbers. From Table 33, we see the data in Column 3, 4, 6 are comparable to the corresponding data in Column 2 with maximal error of 5.9%, 1.9% and 1.6%, respectively. Hence, $u_5(y)$ approximates the channel center velocity derivative better

TABLE 33: The Knudsen number k dependence of the channel center velocity derivative $u'(0)$ from the chunk based collocation method with $N = 320$ and the Knudsen number k dependence of the coefficient $\boldsymbol{a}$ of the approximating polynomials $u_i(y)(i = 1, 3, 5)$

k	$u'(0)$	a_1 in u_1	a_1 in u_3	a_2 in u_3	a_1 in u_5	a_2 in u_5	a_3 in u_5
0.003	0.9939398	0.9947184	0.9929339	0.0072139	0.9952324	−.0238571	0.0880272
0.01	0.9800810	0.9826685	0.9769576	0.0236446	0.9835892	−.0687376	0.2683308
0.03	0.9425456	0.9502473	0.9349869	0.0672586	0.9488144	−.1391455	0.6329034
0.1	0.8352858	0.8568842	0.8227120	0.1753863	0.8424347	−.1540480	1.0970568
0.3	0.6635301	0.6950267	0.6510242	0.2625771	0.6695625	−.0687077	1.1575623
1.0	0.4442285	0.4704244	0.4359153	0.2225343	0.4479078	0.0017742	0.7873837
2.0	0.3274746	0.3465408	0.3218842	0.1617227	0.3322778	−.0309175	0.6902592
3.0	0.2672070	0.2821909	0.2629650	0.1268029	0.2630458	0.1253016	0.0053853
5.0	0.2016944	0.2122520	0.1988081	0.0890557	0.1988323	0.0886461	0.0013898
7.0	0.1652086	0.1733971	0.1630107	0.0689292	0.1630107	0.0689294	−.0000006
10.0	0.1321956	0.1383468	0.1305844	0.0515863	0.1305787	0.0516244	−.0000037

TABLE 34: The Knudsen number k dependence of the shear stress T_{xy} from the chunk based collocation method(CBCM) and from the variational method(VM) for $u_i(y)(i = 1, 3, 5)$

k	CBCM	VM u_1	VM u_3	VM u_5
0.003	$-1.490917181735522 \cdot 10^{-3}$	$-1.490987948149614 \cdot 10^{-3}$	$-1.490984161701514 \cdot 10^{-3}$	$-1.490977924605591 \cdot 10^{-3}$
0.01	$-4.900405672137432 \cdot 10^{-3}$	$-4.901230187447619 \cdot 10^{-3}$	$-4.901103937520052 \cdot 10^{-3}$	$-4.900933966942994 \cdot 10^{-3}$
0.03	$-1.413798608606268 \cdot 10^{-2}$	$-1.414434693381853 \cdot 10^{-2}$	$-1.414185590198566 \cdot 10^{-2}$	$-1.413988260192384 \cdot 10^{-2}$
0.1	$-4.155607783123266 \cdot 10^{-2}$	$-4.159365541027001 \cdot 10^{-2}$	$-4.156541993764190 \cdot 10^{-2}$	$-4.155844050094137 \cdot 10^{-2}$
0.3	$-9.344983511406519 \cdot 10^{-2}$	$-9.350441887110406 \cdot 10^{-2}$	$-9.345537977623374 \cdot 10^{-2}$	$-9.345078104108148 \cdot 10^{-2}$
1.0	$-1.694625753368526 \cdot 10^{-1}$	$-1.694785574186922 \cdot 10^{-1}$	$-1.694635061100609 \cdot 10^{-1}$	$-1.694627042080296 \cdot 10^{-1}$
2.0	$-2.083322536749430 \cdot 10^{-1}$	$-2.083367793068504 \cdot 10^{-1}$	$-2.083324741941339 \cdot 10^{-1}$	$-2.083322248627858 \cdot 10^{-1}$
3.0	$-2.266437497658104 \cdot 10^{-1}$	$-2.266456482855672 \cdot 10^{-1}$	$-2.266438356055570 \cdot 10^{-1}$	$-2.266438346139731 \cdot 10^{-1}$
5.0	$-2.446632678455999 \cdot 10^{-1}$	$-2.446638401551333 \cdot 10^{-1}$	$-2.446632919270730 \cdot 10^{-1}$	$-2.446632919604103 \cdot 10^{-1}$
7.0	$-2.536943539674481 \cdot 10^{-1}$	$-2.536946007822580 \cdot 10^{-1}$	$-2.536943639841660 \cdot 10^{-1}$	$-2.536943639841249 \cdot 10^{-1}$
10.0	$-2.611624603488406 \cdot 10^{-1}$	$-2.611625580141201 \cdot 10^{-1}$	$-2.611624643551445 \cdot 10^{-1}$	$-2.611624642878188 \cdot 10^{-1}$

than $u_1(y)$ and slight better than $u_3(y)$. Since both $u_3(y)$ and $u_5(y)$ can depict the nonlinear feature of the Couette flow velocity profile, it's necessary to ask the question: Which model should we use to describe the Couette flow velocity effectively and efficiently? To answer this question, we turn to another point of view. Recalling equation (34), with purely diffusive upper and lower walls, *i.e.*, $\alpha^- = \alpha^+ = 0$, the shear stress, $T_{xy}(u)$, can be rewritten in terms of $\min J(u)$, namely,

$$T_{xy}(u) = -\frac{1}{4\pi^{1/2}} - \frac{I_1(1/k)}{2\pi^{1/2}} - \frac{\min J(u)}{k}. \tag{126}$$

We compute the shear stress from equation (126) for $u_i(y)(i = 1, 3, 5)$ with various values of the Knudsen number k. Table 34 shows a comparison of the shear stress from the chunk based collocation method with $N = 320$ and the shear stress from the variational method with $u_i(y)(i = 1, 3, 5)$ for various Knudsen numbers. From Table 34, we see the maximal error of the shear stress computed from the variational method by using $u_1(y)$, $u_3(y)$ and $u_5(y)$ are $9.0 \cdot 10^{-4}$, $2.7 \cdot 10^{-4}$ and $1.3 \cdot 10^{-4}$,

respectively. Although, the error of $u_5(y)$ is one half of the error of $u_3(y)$, the latter error is quite small. Considering efficiency, it is more appropriate to use a cubic curve to approximate the velocity profile.

4.3 CUBIC APPROXIMATION TO COUETTE FLOW

In this section, we reconsider the cubic approximation to the Couette flow problem with purely diffusive walls. Although we can obtain the cubic approximation $u_3(y)$ to the velocity $u(y)$ of the Couette flow problem, it is complicated in k and it is not the optimal approximation in L_2. However, we can improve the cubic approximation by the following cubic function:

$$\tilde{u}_2(y) = u'(0)y + ay^3, \ |y| \leq h_0 \leq 1/2, \tag{127}$$

where $u'(0)$ is computed with $u^N(y)$ given in Table 10 and a is the only parameter dependent on k in equation (127). We compute a by the least-square fitting of $\tilde{u}_2(y)$ to $u(y)$ and by using different flow domain sizes $|y| \leq h_0, h_0 = 0.1$, 0.25, 0.4 and 0.5. The results are tabulated in Table 35. The coefficient a in equation (127) measures the strength of the nonlinear component of the velocity $u(y)$. It should be noted from Table 35 that the maximum of a occurs at $k = 1.0$. However, if $u(y)$ is normalized by $u(1/2)$, then we see the term $a/u(1/2)$ increases monotonically with k as shown in Figure 21. For almost all cases of k, a increases monotonically as the domain size in which $\tilde{u}_2(y)$ is used to appproximate $u(y)$ increases. For all values of $k \in [0.003, 10.0]$, the velocity $u(y)$ is well approximated by $\tilde{u}_2(y)$ in the flow domain about the channel center. The L_2 global error of $\tilde{u}_2(y)$ in the domain $|y| \leq 0.1$ never exceeds $5 \cdot 10^{-6}$. Other quantities like the boundary value $\tilde{u}_2(1/2)$, the half channel mass flow rate Q and the shear stress T_{xy} can be use to measure the accuracy of $\tilde{u}_2(y)$ in approximating $u(y)$. The values of $\tilde{u}_2(1/2), Q$ and T_{xy} computed from $\tilde{u}_2(y)$ are given in Table 36 and Table 37. Comparing $\tilde{u}_2(1/2)$ in Table 36 and with the data of Table 10, we see the errors of $\tilde{u}_2(1/2)$ are less than 3%. Comparing the data of Q and T_{xy} of Table 37 computed by using $\tilde{u}_2(y)$ with the data of Table 13, we see the errors of Q are less that 1% and the errors of T_{xy} are less than 0.5%. Thus, for pratical purposes and in terms of the above measurements, $\tilde{u}_2(y)$ is an adequate approximation for $u(y)$.

If the boundary value $u(1/2)$ is the quantity of primary concern, we can use the following approximation of the velocity u_y:

$$\tilde{u}_3(y) = u'(0)y + 4[2u(1/2) - u'(0)]y^3, \ |y| \leq 1/2. \tag{128}$$

TABLE 35: The coefficient a of the cubic term in $\tilde{u}_2(y) = u'(0)y + ay^3$ and L_2 global error of $\tilde{u}_2(y)$.

k	a	$\|\delta\tilde{u}_2\|_2$
	$0 \le y \le 0.1$	
0.003	$5.099593062063754 \cdot 10^{-8}$	$1.387416890726450 \cdot 10^{-10}$
0.01	$3.343744310958851 \cdot 10^{-6}$	$3.018312188907554 \cdot 10^{-11}$
0.03	$5.281661481222335 \cdot 10^{-4}$	$8.615577123508974 \cdot 10^{-8}$
0.1	$3.221450332360452 \cdot 10^{-2}$	$1.724997898197065 \cdot 10^{-6}$
1.0	$1.087385972974718 \cdot 10^{-1}$	$4.631343201891701 \cdot 10^{-6}$
2.0	$8.404038575996586 \cdot 10^{-2}$	$4.469282519835852 \cdot 10^{-6}$
3.0	$6.752579776310266 \cdot 10^{-2}$	$4.247256374952163 \cdot 10^{-6}$
5.0	$4.852427628554858 \cdot 10^{-2}$	$3.903912283246445 \cdot 10^{-6}$
7.0	$3.799335117677678 \cdot 10^{-2}$	$3.663665126306314 \cdot 10^{-6}$
10.0	$2.876474290181471 \cdot 10^{-2}$	$3.410930773482218 \cdot 10^{-6}$
	$0 \le y \le 0.25$	
0.003	$6.910398731314538 \cdot 10^{-9}$	$1.644013286614898 \cdot 10^{-10}$
0.01	$2.281723886791297 \cdot 10^{-7}$	$4.460931942661247 \cdot 10^{-9}$
0.03	$9.362491604139115 \cdot 10^{-6}$	$6.026274060272408 \cdot 10^{-7}$
0.1	$3.801461067150716 \cdot 10^{-4}$	$8.586732529157279 \cdot 10^{-5}$
1.0	$1.166555192399757 \cdot 10^{-1}$	$2.128157496862178 \cdot 10^{-4}$
2.0	$8.965402727287951 \cdot 10^{-2}$	$2.042116189364138 \cdot 10^{-4}$
3.0	$7.187268534084894 \cdot 10^{-2}$	$1.936725914101620 \cdot 10^{-4}$
5.0	$5.153603790568363 \cdot 10^{-2}$	$1.777257280703251 \cdot 10^{-4}$
7.0	$4.030682982958223 \cdot 10^{-2}$	$1.666780655119464 \cdot 10^{-4}$
10.0	$3.048715410738038 \cdot 10^{-2}$	$1.551114351650349 \cdot 10^{-4}$
	$0 \le y \le 0.4$	
0.003	$3.461904416529674 \cdot 10^{-9}$	$1.567671040975640 \cdot 10^{-10}$
0.01	$1.856312338363668 \cdot 10^{-5}$	$1.782432352486531 \cdot 10^{-6}$
0.03	$3.299567364766678 \cdot 10^{-3}$	$1.450084228468318 \cdot 10^{-4}$
0.1	$5.579151702265811 \cdot 10^{-2}$	$1.013531724190039 \cdot 10^{-3}$
1.0	$1.375949468072168 \cdot 10^{-1}$	$2.084057222480417 \cdot 10^{-3}$
2.0	$1.043359531536905 \cdot 10^{-1}$	$1.972366748527839 \cdot 10^{-3}$
3.0	$8.318922556028895 \cdot 10^{-2}$	$1.861238739383532 \cdot 10^{-3}$
5.0	$5.934281798850302 \cdot 10^{-2}$	$1.701043912144287 \cdot 10^{-3}$
7.0	$4.629066041789258 \cdot 10^{-2}$	$1.592616799844646 \cdot 10^{-3}$
10.0	$3.493410766837902 \cdot 10^{-2}$	$1.480376752127701 \cdot 10^{-3}$
	$0 \le y \le 0.45$	
0.003	$1.019246570609792 \cdot 10^{-7}$	$2.467123049928927 \cdot 10^{-8}$
0.01	$1.451549152540907 \cdot 10^{-4}$	$2.144411513469176 \cdot 10^{-5}$
0.03	$6.572911061238614 \cdot 10^{-3}$	$4.940184918247531 \cdot 10^{-4}$
0.1	$6.996991026752306 \cdot 10^{-2}$	$2.361733077307577 \cdot 10^{-3}$
1.0	$1.517910790377233 \cdot 10^{-1}$	$4.327565380978811 \cdot 10^{-3}$
2.0	$1.141552197717352 \cdot 10^{-1}$	$4.058963119981552 \cdot 10^{-3}$
3.0	$9.071566848876420 \cdot 10^{-2}$	$3.817658857583769 \cdot 10^{-3}$
5.0	$6.450797155323322 \cdot 10^{-2}$	$3.479542775938702 \cdot 10^{-3}$
7.0	$5.023949416869138 \cdot 10^{-2}$	$3.253945303818349 \cdot 10^{-3}$
10.0	$3.786238847877981 \cdot 10^{-2}$	$3.022084185455364 \cdot 10^{-3}$
	$0 \le y \le 0.5$	
0.003	$1.004492580134579 \cdot 10^{-3}$	$4.148750667025172 \cdot 10^{-4}$
0.01	$4.397838806966825 \cdot 10^{-3}$	$1.346080444053811 \cdot 10^{-3}$
0.03	$2.219498738086498 \cdot 10^{-2}$	$3.746758468324083 \cdot 10^{-3}$
0.1	$1.055162854697281 \cdot 10^{-1}$	$8.374694271083522 \cdot 10^{-3}$
1.0	$1.801024605942818 \cdot 10^{-1}$	$1.163865625409967 \cdot 10^{-2}$
2.0	$1.333459015123582 \cdot 10^{-1}$	$1.067311848993107 \cdot 10^{-2}$
3.0	$1.053062819728655 \cdot 10^{-1}$	$9.954121683657420 \cdot 10^{-3}$
5.0	$7.444629837254586 \cdot 10^{-2}$	$9.006831059797778 \cdot 10^{-3}$
7.0	$5.780969662306304 \cdot 10^{-2}$	$8.395321211779156 \cdot 10^{-3}$
10.0	$4.345906835580813 \cdot 10^{-2}$	$7.777547893488955 \cdot 10^{-3}$

There is no fitting parameter in the above approximation of $u(y)$, because $\tilde{u}_3(1/2) = u(1/2)$ and $\tilde{u}_3'(0) = u'(0)$ and both $u(1/2)$ and $u'(k)$ are provided by the accrate solution given by Table 10. We compute the L_2 global error, the half channel mass flow rate Q and the shear stress T_{xy} by using the approximate solution $\tilde{u}_3(y)$. The results are tabulated in Table 38 and Table 39. The L_2 global errors of $\tilde{u}_3(y)$ are larger

TABLE 36: The Knudsen number k dependence of $\tilde{u}_2(1/2)$.

k	$\tilde{u}_2(1/2)$
0.003	$4.97095462124394\,1 \cdot 10^{-1} \pm 0.1599\%$
0.01	$4.90590230804875\,6 \cdot 10^{-1} \pm 0.5029\%$
0.03	$4.74047173334958\,3 \cdot 10^{-1} \pm 1.2414\%$
0.1	$4.30832418507282\,7 \cdot 10^{-1} \pm 2.3553\%$
0.3	$3.56386880373190\,6 \cdot 10^{-1} \pm 2.9481\%$
1.0	$2.44627042447598\,2 \cdot 10^{-1} \pm 2.8723\%$
2.0	$1.80405526157724\,6 \cdot 10^{-1} \pm 2.6132\%$
3.0	$1.46766788216714\,3 \cdot 10^{-1} \pm 2.4340\%$
5.0	$1.10153003205453\,5 \cdot 10^{-1} \pm 2.2037\%$
7.0	$8.98305294756862\,2 \cdot 10^{-2} \pm 2.0567\%$
10.0	$7.15301730703245\,4 \cdot 10^{-2} \pm 1.9088\%$

TABLE 37: The Knudsen number k dependence of the half channel flow rate Q and the shear stress T_{xy} computed from $\tilde{u}_2(y) = u'(0)y + ay^3$.

k	Q	T_{xy}
0.003	$1.24258170334533\,9 \cdot 10^{-1} \pm 0.0110\%$	$-1.49090982370148\,1 \cdot 10^{-3} \pm 1.2153 \cdot 10^{-10}$
0.01	$1.22578841469860\,0 \cdot 10^{-1} \pm 0.0374\%$	$-4.90042479930558\,0 \cdot 10^{-3} \pm 1.9790 \cdot 10^{-8}$
0.03	$1.18170771683341\,2 \cdot 10^{-1} \pm 0.1322\%$	$-1.41404825652145\,3 \cdot 10^{-2} \pm 2.4966 \cdot 10^{-6}$
0.1	$1.06059412666356\,2 \cdot 10^{-1} \pm 0.3373\%$	$-4.16534345223410\,6 \cdot 10^{-2} \pm 9.7357 \cdot 10^{-5}$
0.3	$8.60189898608953\,3 \cdot 10^{-2} \pm 0.4882\%$	$-9.37054451861021\,2 \cdot 10^{-2} \pm 2.5561 \cdot 10^{-4}$
1.0	$5.83426596651139\,0 \cdot 10^{-2} \pm 0.5092\%$	$-1.69607006850974\,3 \cdot 10^{-1} \pm 1.4443 \cdot 10^{-4}$
2.0	$4.30178518283005\,7 \cdot 10^{-2} \pm 0.4700\%$	$-2.08397760227147\,5 \cdot 10^{-1} \pm 6.5507 \cdot 10^{-5}$
3.0	$3.50462863983525\,6 \cdot 10^{-2} \pm 0.4393\%$	$-2.26680987589562\,3 \cdot 10^{-1} \pm 3.7238 \cdot 10^{-5}$
5.0	$2.64901740082170\,7 \cdot 10^{-2} \pm 0.8365\%$	$-2.44680154514857\,6 \cdot 10^{-1} \pm 1.6887 \cdot 10^{-5}$
7.0	$2.64901740082170\,7 \cdot 10^{-2} \pm 0.8365\%$	$-2.53704013305639\,0 \cdot 10^{-1} \pm 9.6593 \cdot 10^{-6}$
10.0	$1.72034953245216\,3 \cdot 10^{-2} \pm 0.3442\%$	$-2.61167668438158\,2 \cdot 10^{-1} \pm 5.2081 \cdot 10^{-6}$

than those of $\tilde{u}_2(y)$ given by equation (127) by a factor no more than 3; the errors in Q and T_{xy} are also larger than those of $\tilde{u}_2(y)$, although they remain relatively small. The errors in Q and T_{xy} are bounded by 2.4% and 0.7%, respectively. Comparing the cubic approximations $\tilde{u}_3(y)$ in the variational method, $\tilde{u}_2(y)$ by fitting and $\tilde{u}_3(y)$ to the velocity $u(y)$, we see $\tilde{u}_2(y)$ is the best choice of the three to be used for practical purposes, for instance, as a model for the velocity at the walls.

TABLE 38: The Knudsen number k dependence of the L_2 error of the approximate solution $\tilde{u}_3(y) = u'(0)y + 4[2u(1/2) - u'(0)]y^3$.

k	$\|\delta\tilde{u}_3\|_2$
0.003	$1.14696493217453\,6 \cdot 10^{-3}$
0.01	$3.63476775973766\,8 \cdot 10^{-3}$
0.03	$9.21306459931187\,4 \cdot 10^{-3}$
0.1	$1.83506853391897\,7 \cdot 10^{-2}$
0.3	$2.38220176032253\,6 \cdot 10^{-2}$
1.0	$2.35957365520383\,4 \cdot 10^{-2}$
2.0	$2.14643636378344\,0 \cdot 10^{-2}$
3.0	$1.99532333853680\,9 \cdot 10^{-2}$
5.0	$1.80000786413817\,0 \cdot 10^{-2}$
7.0	$1.67532944559497\,1 \cdot 10^{-2}$
10.0	$1.55015577207858\,6 \cdot 10^{-2}$

TABLE 39: The Knudsen number k dependence of the half channel mass flow rate Q and the shear stress T_{xy} computed from the approximate solution $\tilde{u}_3(y) = u'(0)y + 4[2u(1/2) - u'(0)]y^3$.

k	Q	T_{xy}
0.003	$1.243576794787881 \cdot 10^{-1} \pm 0.0910\%$	$-1.490910597484586 \cdot 10^{-3} \pm 8.953113235597027 \cdot 10^{-10}$
0.01	$1.228887852159983 \cdot 10^{-1} \pm 0.2903\%$	$-4.900514063030057 \cdot 10^{-3} \pm 1.090533615572334 \cdot 10^{-7}$
0.03	$1.189098335236083 \cdot 10^{-1} \pm 0.7585\%$	$-1.414617804249189 \cdot 10^{-2} \pm 8.192027317418041 \cdot 10^{-6}$
0.1	$1.073584404744730 \cdot 10^{-1} \pm 1.5663\%$	$-4.183060986138169 \cdot 10^{-2} \pm 2.745320357895181 \cdot 10^{-4}$
0.3	$8.737220100800198 \cdot 10^{-2} \pm 2.0690\%$	$-9.425838992151225 \cdot 10^{-2} \pm 8.085548079423271 \cdot 10^{-4}$
1.0	$5.924694685784809 \cdot 10^{-2} \pm 2.0670\%$	$-1.699706480158879 \cdot 10^{-1} \pm 5.080726790643864 \cdot 10^{-4}$
2.0	$4.362294848033766 \cdot 10^{-2} \pm 1.6833\%$	$-2.085717852369104 \cdot 10^{-1} \pm 2.395315619725946 \cdot 10^{-4}$
3.0	$3.550396843366418 \cdot 10^{-2} \pm 1.7510\%$	$-2.267821881356465 \cdot 10^{-1} \pm 1.384383698378733 \cdot 10^{-4}$
5.0	$2.668530049229303 \cdot 10^{-2} \pm 1.5793\%$	$-2.447270513741618 \cdot 10^{-1} \pm 6.378352856226122 \cdot 10^{-5}$
7.0	$2.179015169162721 \cdot 10^{-2} \pm 1.4694\%$	$-2.537311316853772 \cdot 10^{-1} \pm 3.677771792920392 \cdot 10^{-5}$
10.0	$1.737748781489167 \cdot 10^{-2} \pm 1.3590\%$	$-2.611824247306578 \cdot 10^{-1} \pm 1.996438181728344 \cdot 10^{-5}$

4.4 THE VELOCITY DEFECT, SLIP VELOCITY AND THE HALF CHANNEL MASS FLOW RATE

In this section, we discuss the velocity defect and slip velocity and the half channel mass flow rate of the Couette flow problem with purely diffusive walls. The linear velocity $u_1^*(y) = u'(0)y$ is the hydrodynamic component of the velocity $u(y)$. Thus, the kinetic component of the velocity $u(y)$ can be characterized by the velocity defect, defined as:

$$u_{\rm d} = \frac{\sqrt{2\pi}}{u(1/2)}[u(y) - u'(0)y]. \tag{129}$$

The velocity defect shows the structure of Knudsen layer in the velocity profile $u(y)$. For Kramers problem which has only one wall, the flow domain is a semi-plane with $y \geq 0$. The velocity defect is a function of y/k. For the Couette flow, the velocity defect $u_{\rm d}$ is not a function of only y/k, but a function of both y/k and k.

The microscopic slip velocity $u_{\rm s}$ and the macroscopic slip velocity $U_{\rm s}$ are defined by:

$$u_{\rm s} = U_{\rm w} - u(1/2) = 1/2 - u(1/2), \tag{130}$$

$$U_{\rm s} = U_{\rm w} - u'(0)/2 = [1 - u'(0)]/2, \tag{131}$$

where $U_{\rm w} = 1/2$ is the normalized velocity of the wall at $y = 1/2$. The velocity at the wall and the velocity derivative at the channel center are $u(1/2)$ and $u'(0)$, respectively, obtained by the high precision solution of equation (72). It is noted that the difference between $u_{\rm s}$ and $U_{\rm s}$ is due to the nonlinearity in $u(y)$.

Figure 22 shows the profiles of velocity defect $u_{\rm d}(y)$ and the velocity defect $u_{\rm d}(y)$ normalized by its maximum value at the boundary $u_{\rm d}(1/2)$ for $k = 0.03$, 0.1, 1.0 and 10.0. The velocity defect shows a non-monotonic dependence on k: it increases

rapidly to its maximal value at $k \approx 1$, then decreases slightly and slowly as k enlarges, as seen in Figure 22. The reason for this non-monotonic k dependence of $u_d(y)$ can be explained as follows. From Figure 21 we see that the microscopic slip velocity $u_s(y)$ increases along with k, hence the magnitude of the velocity $u(y)$ decreases. On the other hand, the kinetic component of the velocity, *i.e.*, $u(y) - u'(0)y$ increases with k. Hence, the nonlinearity in the velocity $u(y)$ increases while its magnitude $u(1/2)$ decreases as k increases. Therefore, the non-montonic k dependence of the velocity defect $u_d(y)$ is due to the competition between the increasing nonlinearity and the decreasing magnitude of $u(1/2)$, which is characterized by the quantity $1 - \frac{u'(0)}{2u(1/2)}$. However, the non-monotonic k dependence of the velocity defect $u_d(y)$ can be removed when it is normalized by its maximum $u_d(1/2)$. From Figure 22 we see $u_d(y)/u_d(1/2)$ increase monotonically with k.

The microscopic slip velocity u_s can be directly extracted from the high precision solutions of $u(y)$. To gain some insights concerning the k dependence of u_s, we can use the approximate solutions to $u(y)$. To capture the singular behavior of $u(y)$, we can use $\tilde{u}_1(y)$ from equation (119) given in terms of Abramowitz functions I_0 and I_1. Similarly, u_s can be approximated in terms of I_0 and I_1 with the formula:

$$u_{s1} = \frac{k}{1 + 2A_2 k}\left[A_2 + A_0\left(I_0(1/k) - \frac{\sqrt{\pi}}{2}\right) + A_1\left(I_1(1/k) - \frac{1}{2}\right)\right], \tag{132}$$

where the coefficients A_0, A_1 and A_2 are obtained by the least square fitting of u_s with $0.003 \leq k \leq 10$. The data of $u_s = 1/2 - u(1/2)$ are extracted from the the data of $u(1/2)$ given in Table 10. The approximation in equation (132) has the correct asymptotic behaviors of u_s, *i.e.*, $u_s = 0$ at $k = 0$ and $u_s \to 1/2$ as $k \to \infty$.

Taking into account the asymptotic behaviors of I_0 and I_1 at 0 and ∞, we can use the simpler approximation for u_s:

$$u_{s2} = \frac{B_1 k + B_2 \ln(1 + k)}{1 + 2B_1 k}, \tag{133}$$

where the coefficients B_1 and B_2 are obtained by the least square fitting in the interval $0.003 \leq k \leq 0.3$. Surprisingly and usefully, u_{s2} in Equation (133) also yields a good approximation for the whole range of k.

If one needs an even simpler approximation for u_s which maintains the correct limits at $k = 0$, one can use the rational approximation:

$$u_{s3} = \frac{C_1 k}{1 + C_2 k}, \tag{134}$$

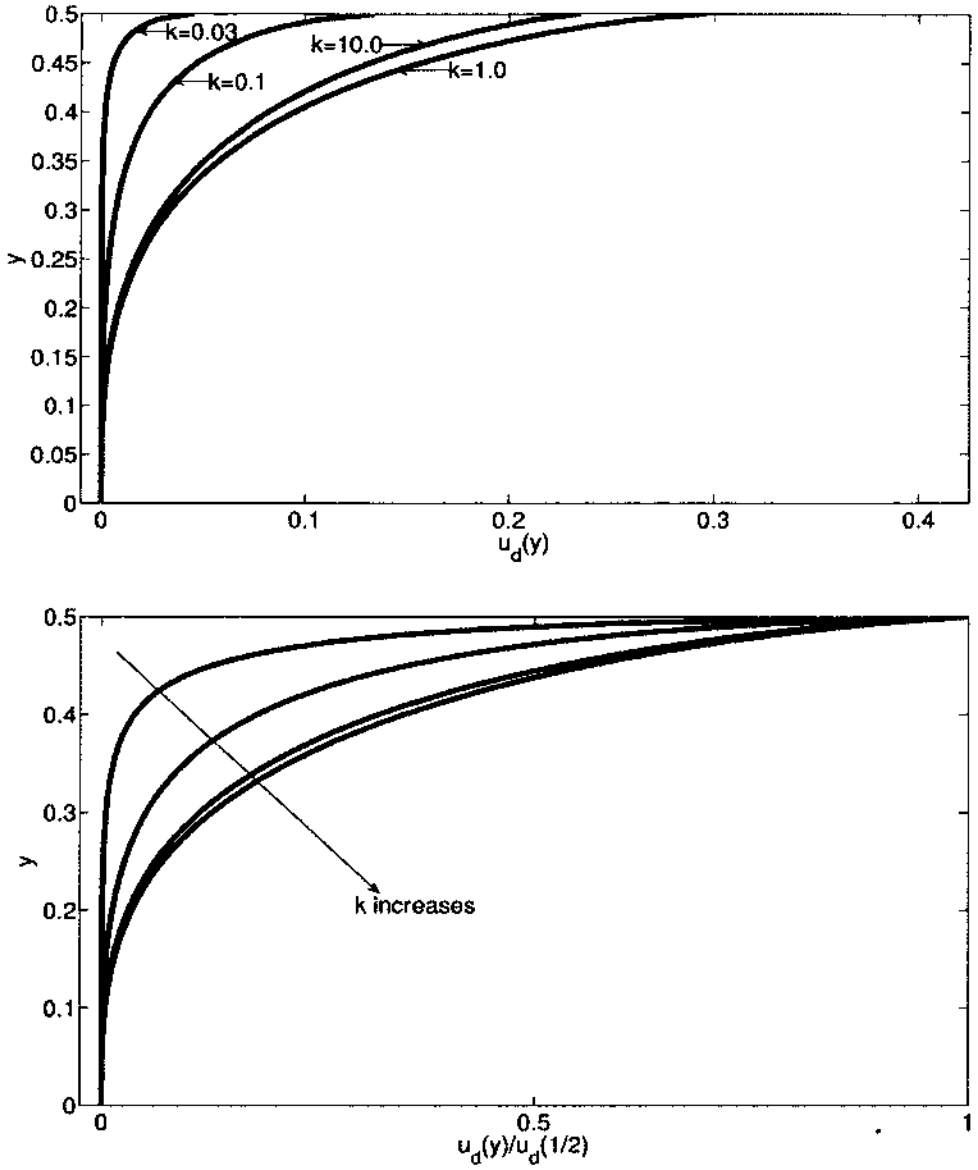

FIG. 22: The velocity defect $u_{\rm d}(y)$ (top) and the normalized velocity defect $u_{\rm d}(y)/u_{\rm d}(1/2)$ (bottom) for $k = 0.03$, 0.1, 1.0 and 10.0. The normalized velocity defect increases monotonically as k increases.

where the coefficients C_1 and C_2 are obtained by the least square fitting in the interval $0.003 \leq k \leq 0.3$. We can set $C_2 = 2C_1$ to satisfy the asymptotic limit of u_s at $k \to \infty$. However, this increases the L_2 error in the fitting range of k.

TABLE 40: The values of parameters in the models for the microscopic slip velocity u_s, the fitting range of k for the parameters and the L_2 error of the approximations in the corresponding fitting range of k.

Approximation	Coefficients	Range of k	$\|\delta u_s\|_2$
Eq.(132)	$A_0 = 0.4701623488541722$ $A_1 = -0.3569325916063242$ $A_2 = 0.930308894938529$5	$0.003 \leq k \leq 10.0$	$1.1205 \cdot 10^{-3}$
Eq.(133)	$B_1 = 1.279758697826314$ $B_2 = -0.5685759260098272$	$0.003 \leq k \leq 0.3$	$4.6599 \cdot 10^{-4}$
Eq.(134)	$C_1 = 0.7037931880441636$ $C_2 = 1.967040348835866$	$0.003 \leq k \leq 0.3$	$5.0112 \cdot 10^{-4}$
Eq.(134)	$C_1 = 0.6171898550504058$ $C_2 = 2C_1$	$0.003 \leq k \leq 0.3$	$3.4415 \cdot 10^{-2}$
Eq.(135)	$D_1 = 0.7049600580160285$ $D_2 = -1.320955381122892$ $D_3 = 1.488348609420158$	$0.003 \leq k \leq 0.3$	$9.4363 \cdot 10^{-5}$

Finally, we can use the following cubic polynomial to approximate u_2 of $k < 1$:

$$u_{s4} = D_1 k + D_2 k^2 + D_3 k^3, \tag{135}$$

where the coefficients D_1, D_2 and D_3 are obtained by the least square fitting for $0.003 \leq k \leq 0.3$. The values of the coefficients in approximations u_{s1}, u_{s2}, u_{s3} and u_{s4}, given by equations (132)-(135) in the range of k in which the coefficients are obtained are tabulated in Table 40 along with respective L_2 errors. Figure 23 illustrates the k dependence of the microscopic slip velocity u_s along with the approximations of u_s given by equations (132)-(135). The approximation of equation (132) matches u_s very well, the asymptotic values of u_s in both $k = 0$ and $k \to \infty$ are captured and the L_2 global error is $1.1205 \cdot 10^{-3}$ in the range of $0.003 \leq k \leq 10.0$. Although the coefficients B_1 and B_2 in equation (133) are obtained in the interval $0.003 \leq k \leq 0.3$, the approximation of equation (133) is indistinguishable from that of equation (132). The approximations of equations (134)-(135) are only valid for small values of k, *i.e.*, $0.003 \leq k \leq 0.3$. The L_2 errors of these approximations on the inteval $0.003 \leq k \leq 0.3$ are $5.0112 \cdot 10^{-4}$ and $9.4363 \cdot 10^{-5}$, respectively. It is noted that though the approximation of equation (134) with $C_2 = 2C_1$ has correct asymptotic limits at both $k = 0$ and $k \to \infty$, the case with $C_2 \neq C_1$ actually fits u_s better in the same interval. When we consider the slip velocity models which can be used as boundary conditions in the Navier-Stokes equations, the macroscopic slip velocity U_s is used [12]-[16]. The approximations for U_s can be directly derived from those for the velocity, for instance, $\tilde{u}_1(y)$ of Equation (119), which is written in terms of Abramowitz functions I_0 and I_1. We can approximate U_s in terms of I_{-1} and I_0

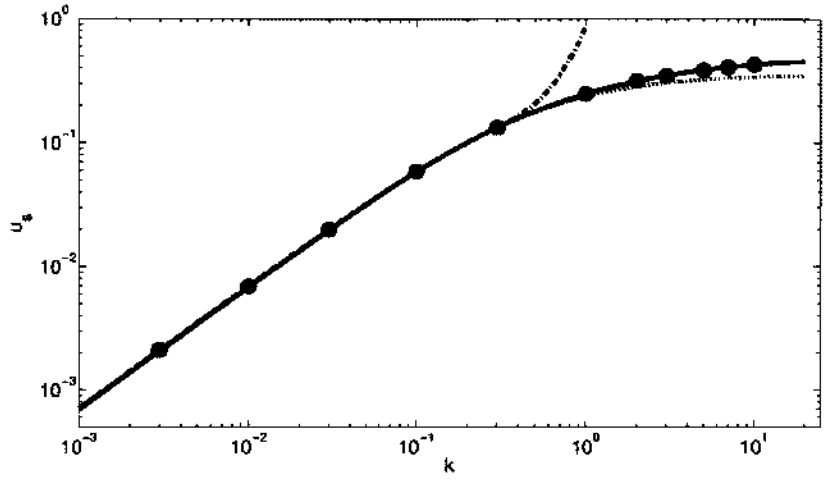

FIG. 23: The k dependence of the slip velocity u_s. The circles are obtained from the high precision solution of the integral equation (72) given in Table 10. The solid, dash, dot and dash-dot lines are the approximations of u_s by equations (132)-(134) with $C_2 \neq C_1$ and equation (135), respectively. The lines of equations (132)-(133) overlap each other.

by using the derivative of $\tilde{u}_1(y)$ and derive the following formula:

$$U_{s1} = \frac{1}{2}\left[1 - \frac{1 + 2\hat{A}_1 I_{-1}(1/2k) + 2\hat{A}_2 I_0(1/2k)}{1 + \hat{A}_3 k}\right], \tag{136}$$

where the coefficients $\hat{A}_1$, $\hat{A}_2$ and $\hat{A}_3$ are obtained by the least square fitting of U_s with $0.003 \leq k \leq 10.0$. The data of $U_s = [1 - u'(0)]/2$ are extracted from the data of $u'(0)$ given in the Table 10. The above approximation of U_s includes the correct asymptotic behavior of U_s, *i.e.*, $U_s = 0$ at $k = 0$ and $U_s \to 1/2$ as $k \to \infty$.
Utilizing the asymptotic behavior of I_{-1} and I_0 at 0 and ∞, we can get rid of the Abramowitz functions in the approximation of U_s to derive:

$$U_{s2} = \frac{1}{2}\left\{1 - \frac{(t_1\hat{B}_1 + t_2\hat{B}_2)\exp\left[-3\,(4k)^{-2/3}\right] + 1 + k}{(k\hat{B}_3 + 1)(1 + k)}\right\} \tag{137}$$

where

$$t_1 = \sqrt{\pi/3}(4k)^{1/3} + k\ln(1 + 2k) - 3\gamma k/2,$$
$$t_2 = \sqrt{\pi/3} + \sqrt{\pi}k/2,$$

TABLE 41: The values of parameters in the models for the macroscopic slip velocity U_s, the fitting range of k for the parameters and the L_2 error of the approximations in the corresponding fitting range of k.

Approximation	Coefficients	Range of k	$\|\delta U_s\|_2$
Eq.(136)	$A_1 = 0.4366767230964805$	$0.003 \leq k \leq 10.0$	$6.6859 \cdot 10^{-3}$
	$A_2 = -0.2665031912984401$		
	$A_3 = 1.831497775849215$		
Eq.(137)	$\hat{B}_1 = 0.8876382348909353$	$0.003 \leq k \leq 10.0$	$2.8859 \cdot 10^{-3}$
	$\hat{B}_2 = 0.4524044608543894$		
	$\hat{B}_3 = 2.086076009043359$		
Eq.(138)	$\hat{C}_1 = 1.020794919617355$	$0.003 \leq k \leq 0.3$	$1.9980 \cdot 10^{-4}$
	$\hat{C}_2 = -2.191441518439700$		
	$\hat{C}_3 = 2.193562264423130$		

where $\gamma = 0.57721566490153286060\cdots$ is the Euler constant. The coefficients $\hat{B}_1$, $\hat{B}_2$ and $\hat{B}_3$ are obtained by the least square fitting in the interval $0.003 \leq k \leq 10.0$. It is noted that equation (137) also matches the correct asymptotic behavior of U_s when $k \to 0$ and $k \to \infty$.

If one only considers small values of k, one can use the following cubic polynomial approximation of k:

$$U_{s3} = \hat{C}_1 k + \hat{C}_2 k^2 + \hat{C}_3 k^3, \tag{138}$$

where $\hat{C}_1$, $\hat{C}_2$ and $\hat{C}_3$ are obtained by the least square fitting for $0.003 \leq k \leq 0.3$. The values of the coefficients in the approximations U_{s1}, U_{s2} and U_{s3} given by equations (136)-(138), respectively, are tabulated in Table 41 along with the L_2 error of the approximations in the range of k in which the coefficients are obtained.

Figure24 shows k dependence of the macroscopic velocity U_s along with the approximations of U_s given by equations (136)-(138). The approximation of equation (136) matches the asymptotic value of U_s as both $k \to 0$ and $k \to \infty$ exactly and the L_2 global error is $6.6859 \cdot 10^{-3}$ in the range of $0.003 \leq k \leq 10.0$. The approximation of equation (137) is indistinguishable from that of equation (136) when $k \geq 0.3$. Surprisingly, the L_2 global error of the approximation from equation (137) in the range of $0.003 \leq k \leq 10.0$ is $2.8859 \cdot 10^{-3}$, which is even lower than that of approximation from equation (136). The approximation of equation (138) fits U_s with the L_2 error of $1.9880 \cdot 10^{-4}$ in the range of $0.003 \leq k \leq 0.3$ which manifests it is a very good approximation for small values of k.

The half channel mass flow rate Q is a measure of not only the effect due to the slip velocity u_s (or U_s), but also the structure of the Knudsen layer in the velocity profile $u(y)$ [9]. Based on the approximation of the velocity $\tilde{u}(y)$ given by equation (119),

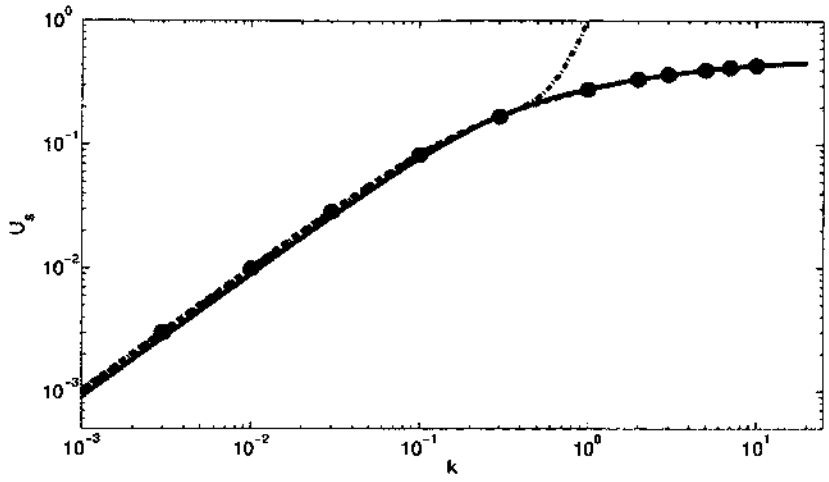

FIG. 24: The k dependence of the slip velocity U_s. The circles are obtained from the high precision solution of the integral equation (72) given in Table 10. The solid, dash and dash-dot lines are the approximations of u_s by equations (136)-(138), respectively. The lines of equations (136)-(137) overlap each other when $k \geq 0.3$.

we can approximate Q with the following formula:

$$Q_1 = \frac{k}{1+\bar{A}_3 k}\left[\frac{1}{8k} + \bar{A}_1 k\left(\frac{1}{2} + I_1(1/k) - 2I_1(1/2k)\right)\right.$$
$$\left. + \bar{A}_2 k\left(\frac{\sqrt{\pi}}{4} + I_2(1/k) - 2I_2(1/2k)\right)\right], \tag{139}$$

where the coefficients $\bar{A}_1$, $\bar{A}_2$ and $\bar{A}_3$ are obtained by the least square fitting on the range $0.003 \leq k \leq 10.0$. The approximation Q_1 of Q from equation (139) conserves its asymptotic behavior as $k \to 0$ and $k \to \infty$. By using the asymptotic behavior of the Abramowitz functions I_1 and I_2, one can approximate Q without using the Abramowitz functions but also conserve the asymptotic behavior of Q when $k \to 0$ and $k \to \infty$ by using the following formula:

$$Q_2 = \frac{1 + 8\bar{B}_1 \ln(1+k^2)}{8(1+\bar{B}_2 k)}, \tag{140}$$

where the coefficients $\bar{B}_1$ and $\bar{B}_2$ are obtained by the least square fitting on the range $0.003 \leq k \leq 10.0$. For small $k < 1$, we can use the following rational approximation:

$$Q_3 = \frac{1 + 8\bar{C}_1 k^2}{8(1+\bar{C}_2 k)}, \tag{141}$$

TABLE 42: The values of parameters in the models for the half channel mass flow rate Q, the fitting range of k for the parameters and the L_2 error of the approximations in the corresponding fitting range of k.

Approximation	Coefficients	Range of k	$\|\delta Q\|_2$
Eq.(139)	$A_1 = 0.4339896731456645$	$0.003 \leq k \leq 10.0$	$2.7451 \cdot 10^{-3}$
	$A_2 = -0.2037173094079779$		
	$A_3 = 1.916439270306587$		
Eq.(140)	$B_1 = 0.03771029254176309$	$0.003 \leq k \leq 10.0$	$9.6796 \cdot 10^{-3}$
	$B_2 = 1.665037574894380$		
Eq.(141)	$\bar{C}_1 = 0.1187836129667822$	$0.003 \leq k \leq 0.3$	$9.0564 \cdot 10^{-4}$
	$\bar{C}_2 = 1.949726554024494$		
Eq.(142)	$\bar{D}_1 = -0.2529994267391535$	$0.003 \leq k \leq 0.3$	$2.8209 \cdot 10^{-5}$
	$\bar{D}_2 = 0.6976773399315172$		
	$\bar{D}_3 = -0.9737045663563917$		

where the coefficients $\bar{C}_1$ and $\bar{C}_2$ are obtained by the least square fitting on the range $0.003 \leq k \leq 0.3$. We can also use a cubic polynomial to fit Q:

$$Q_4 = \frac{1}{8} + \bar{D}_1 k + \bar{D}_2 k^2 + \bar{D}_3 k^3, \tag{142}$$

where the coefficients $\bar{D}_1$, $\bar{D}_2$, $\bar{D}_3$ and $\bar{D}_4$ are obtained by the least square fitting on the range $0.003 \leq k \leq 0.3$. The values of the coefficients in the approximations of equations (139)-(142) are tabulated in Table 42 along with the L_2 error of the approximation in the range of k in which the coefficients are obtained.

Figure 25 illustrates the half channel mass flow rate Q normalized by its value at k, *i.e.*, $Q_0 = 1/8$ along with the approximations of Q given by equations (139)-(142), which are also normalized by Q_0. The approximation Q_1 of equation (139) in terms of Abramowitz functions I_1 and I_2 on the range $0.003 \leq k \leq 10.0$ has correct limits at $k = 0$ and $k = \infty$ and captures the values of Q in Table 13. It is noted that the simple formula Q_2 of equation (140) matches Q quite accurately with correct limits at $k = 0$ and $k = \infty$, as indicated by the small L_2 global error. We also see that the cubic polynomial approximation Q_4 is very accurate with L_2 error of $2.8209 \cdot 10^{-5}$ on the range $0.003 \leq k \leq 0.3$.

4.5 DIRICHLET BOUNDARY CONDITION, EFFECTIVE VISCOSITY AND VELOCITY REPRODUCING BY LATTICE BOLTZMANN EQUATION

The approximations of velocity and velocity slip enable us to reconsider the Couette flow problem in the Navier-Stokes equation framework for the whole range of the Knudsen number. That is one can specify the velocity slip and design the stress tensor of Navier-Stokes like equation of which the solution is an approximation to the

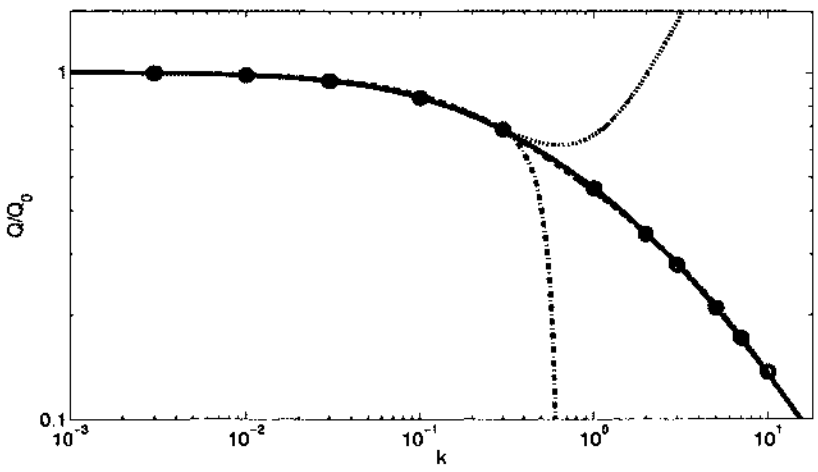

FIG. 25: The k dependence of the normalized half channel mass flow rate Q/Q_0. The circles are obtained from the high precision solution of the integral equation (72) given in Table 13. The solid, dash, dot and dash-dot lines are the approximations of Q/Q_0 by equations (139)-(142), respectively. The lines of equations (139)-(140) overlap each other.

velocity of the steady Couette flow problem. Actually, we have two types of Navier-Stokes models: one has constant kinematic shear viscosity with the macroscopic slip velocity U_s as its boundary condition; the other has coordinate y dependent kinematic shear viscosity, named effective viscosity, with the microscopic slip velocity u_s as its boundary condition. Both models, like what we have obtained from integral equation, have constant shear stress. However, the former produces linear velocity profile, thus can not capture the Knudsen layer. The latter model produces a nonlinear velocity profile, thus caputers the Knudsen layer. In this section, we set up the latter model by choosing a target velocity model of the steady Couette flow problem, specifying a proper Dirichlet boundary condition and finding the effective viscosity for the stress tensor in the Navier-Stokes equation. Then, we solve the Navier-Stokes equation by using lattice Boltzmann equation. As the result, the target velocity profile is reproduced.

For simplicity, we choose the approximation $\tilde{u}_3(y)$ of the velocity $u(y)$ from equation (128) as our target and use the approximated microscopic slip velocity u_{s2} given by equation (133) as the Dirichlet boundary condition. To dertermine the effetive

viscosity, we take a look at the Navier Stokes momentum equation:

$$\rho\frac{\mathrm{d}\boldsymbol{u}}{\mathrm{d}t} = -\boldsymbol{\nabla}p + \boldsymbol{\nabla}\cdot\{\rho\nu[\boldsymbol{\nabla}\boldsymbol{u} + \boldsymbol{\nabla}\boldsymbol{u}^T - (2\boldsymbol{\nabla}\cdot\boldsymbol{u}/D)I] + \rho\zeta(\boldsymbol{\nabla}\cdot\boldsymbol{u})I\}, \tag{143}$$

where I is the identity tensor and D is the dimension of the flow. For 2-D flow, the velocity $\boldsymbol{u} = (u, v)^T$, ρ and p are the density and static pressure, respective and ν and ζ are the kinematic shear viscosity and bulk viscosity, respectively. For steady planar Couette flow problem, $u = u(y), v \equiv 0$ and the density ρ and the static pressure p are constants. The kinematic viscoisties are independent of x. Consequently, one has $\frac{\mathrm{d}\boldsymbol{u}}{\mathrm{d}t} = 0, \boldsymbol{\nabla}p = 0, \boldsymbol{\nabla}(\rho\nu\boldsymbol{\nabla}\boldsymbol{u}^T) = 0$ and $\boldsymbol{\nabla}\cdot\boldsymbol{u} = 0$. Hence, equation (143) can be simplified as:

$$\nu\frac{\mathrm{d}u}{\mathrm{d}y} = C \tag{144}$$

where C is a constant to be determined.

To determine the effective viscosity ν, we need to follow three steps. First, we compute the value of ν at the channel center, *i.e.* $\nu(0)$, by using kinetic theory. Then, we determine the constant C in equation (144). Finally, we derive the ν profile by repeatedly using equation (144).

In kinetic theory, the mean free path λ of gas is related with kinemtic viscosity by the formula:

$$\lambda = \nu\sqrt{\frac{\pi}{2RT}}, \tag{145}$$

where $R = k_b/m$ is the Regnault constant and T is the temperature. Equation (145) is derived without boundary. Hence, we take the value of ν in equation (145) as the value at farthest position from the wall, *i.e.* $\nu(0)$. By using the definition of Knudsen number in terms of λ and the channel height d,

$$k = \frac{\sqrt{\pi}\lambda}{2d}, \tag{146}$$

we can write $\nu(0)$ in term of the Knudsen number k as

$$\nu(0) = \frac{2kd\sqrt{2RT}}{\pi}. \tag{147}$$

From equation (144) and equation (147), we have

$$C = \nu(0)u'(0) = \frac{2kd\sqrt{2RT}u'(0)}{\pi}.$$

Substituting $\tilde{u}_3(y)$ for $u(y)$ in equation (144), we can solve for ν as the formula:

$$\begin{aligned}\nu &= \frac{C}{u'(y)} \\ &= \frac{2kd\sqrt{2RT}u'(0)}{\pi[u'(0) + 12y^2(2u(1/2)/d^3 - u'(0)/d^2)]}.\end{aligned} \tag{148}$$

With the effective viscosity ν given by equation (148), the Navier-Stokes equation (143) can be solved with the wall boundary condition given by equation (133) and periodic boundary condition in the stream-wise direction to obtain a solution identical to $\tilde{u}_3(y)$. We will prove this assertion by reproducing the velocity profile using lattice Boltzmann method with the above mentioned boundary condition.

Lattice Boltzmann equation without external force is the following evolution equation of discrete distribution functions for moving particles:

$$f_i(\boldsymbol{x} + \boldsymbol{c}_i\delta_t, t + \delta_t) - f_i(\boldsymbol{x}, t) = \Omega_i(\boldsymbol{f}(\boldsymbol{x}, t)),\ i = 0, 1, \cdots, Q-1, \tag{149}$$

where $f_i(\boldsymbol{x}, t)$ is the distribution function associated with the particle at time t, moving from position $\boldsymbol{x}$ with velocity $\boldsymbol{c}_i$ and $\boldsymbol{f} = (f_0, f_1, \cdots, f_{Q-1})^T$. At time t all the particles within consideration are located on a structured lattice (normally a cartesian mesh grid) with a spacing $\delta_x = c\delta_t$. The set $\{\boldsymbol{c}_i\}$ is a symmetrical finite vector set called the discrete velocity set of the Lattice Boltzmann equation. The particle on a lattice grid $\boldsymbol{x}$ is only allowed to move with a velocity *i.e.*, $\boldsymbol{c}_i$, in the discrete velocity set. The choice of the discrete velocity set determines the macroscopic hydrodynamic equation to which the lattice Boltzmann equation recovers with Chapman Enskog expansion. In the current case, we use the classical D2Q9 velocity set below to make sure equation (149) recovers the Navier-Stokes equations with 2nd order precision in space-time,

$$\boldsymbol{c}_i = \begin{cases} (0,0)c, & i = 0, \\ (\pm 1, 0)c,\ (0, \pm 1)c, & i = 1, 2, 3, 4, \\ (\pm 1, \pm 1)c, & i = 5, 6, 7, 8. \end{cases} \tag{150}$$

where $c = \delta_x/\delta_t$ is the unit of velocity. Conventionally, we set $\delta_x = 1$ and $\delta_t = 1$, thus $c = 1$. The RHS of equation (149) is the discrete collision term whose specific form depends on the model we choose. To match the D2Q9 discrete velocity set, we use the multiple relaxation times (MRT) model and the discrete collision vector $\boldsymbol{\Omega}(\boldsymbol{f}) = (\Omega_0, \Omega_1, \cdots, \Omega_8)^T(\boldsymbol{f})$ reads:

$$\boldsymbol{\Omega}(\boldsymbol{f}) = -\boldsymbol{M}^{-1}\boldsymbol{S}(\boldsymbol{m} - \boldsymbol{m}^{eq}), \tag{151}$$

where the tranformation M mapping the distribution functions $\boldsymbol{f}$ to their moments $\boldsymbol{m}$ reads:

$$M = \begin{pmatrix} 1 & 1 & 1 & 1 & 1 & 1 & 1 & 1 & 1 \\ -4 & -1 & -1 & -1 & -1 & 2 & 2 & 2 & 2 \\ 4 & -2 & -2 & -2 & -2 & 1 & 1 & 1 & 1 \\ 0 & 1 & 0 & -1 & 0 & 1 & -1 & -1 & 1 \\ 0 & -2 & 0 & 2 & 0 & 1 & -1 & -1 & 1 \\ 0 & 0 & 1 & 0 & -1 & 1 & 1 & -1 & -1 \\ 0 & 0 & -2 & 0 & 2 & 1 & 1 & -1 & -1 \\ 0 & 1 & -1 & 1 & -1 & 0 & 0 & 0 & 0 \\ 0 & 0 & 0 & 0 & 0 & 1 & -1 & 1 & -1 \end{pmatrix}$$

and $S = \mathrm{diag}(0, s_e, s_\epsilon, 0, s_q, 0, s_q, s_\nu, s_\nu)$ is the diagonal matrix of relaxation ratios. Currently, we set $s_e = s_\epsilon = s_\nu$ and the MRT model given by equation (151) reduces to a two relaxation times (TRT) model, in which s_ν and s_q are the only two relaxation ratios to determine. The moments of the distribution function are:

$$\boldsymbol{m} = M\boldsymbol{f} = (\rho,\, e,\, \epsilon,\, j_x,\, q_x,\, j_y,\, q_y,\, p_{xx},\, p_{xy})^T.$$

The equilibrium distribution functions f_i^{eq} are given by

$$f_i^{eq} = w_i \rho \left[1 + \frac{\boldsymbol{c}_i \cdot \boldsymbol{u}}{c_s^2} + \frac{(\boldsymbol{c}_i \cdot \boldsymbol{u})^2}{2c_s^4} - \frac{|\boldsymbol{u}|^2}{2c_s^2} \right],$$

where $w_0 = 4/9, w_{1-4} = 1/9, w_{5-8} = 1/36$. For isothermal flow, the temperature T is a free variable. However, the speed of sound $c_s = \sqrt{RT}$ is not. We have $c_s = c/\sqrt{3} = \sqrt{3}/3$. Consequently, the equilibrium moments are:

$$\boldsymbol{m}^{eq} = M\boldsymbol{f}^{eq} = \rho(1,\, -2 + 3|\boldsymbol{u}|^2,\, 1 - 3|\boldsymbol{u}|^2,\, u,\, -u,\, v,\, -v,\, u^2 - v^2,\, uv)^T.$$

Among the nine moments, the density ρ and the momentum $\boldsymbol{j} = (j_x,\, j_y)^T$ are conserved quantities, which are unchanged in collision and are computed by:

$$\rho = \sum_{i=0}^{8} f_i,\; \boldsymbol{j} = \sum_{i=1}^{8} \boldsymbol{c}_i f_i = \rho \boldsymbol{u}. \tag{152}$$

The kinematic shear viscosity ν and bulk viscosity ζ are the same in TRT model and are related with the relaxation ratio s_ν by:

$$\nu = \zeta = \left(\frac{1}{s_\nu} - \frac{1}{2} \right) c_s^2 \delta_t = \frac{1}{3} \left(\frac{1}{s_\nu} - \frac{1}{2} \right). \tag{153}$$

Considering the symmetry of the Couette flow, we only simulate the flow by the lattice Boltzmann equation in the upper half channel. Starting from the channel center, we place N grid points ordered from 1 to N with spacing $\delta_x = d/(2N-1)$ along the direction of the channel height in the upper half channel. In the streamwise direction from the inlet to the outlet of the flow, we place M grid points ordered from 1 to M with the same spacing. We should note that the unit of length of the lattice Boltzmann simulation is different from that of the integral equation where $d = 1$. Here, since $\delta_x = 1$, in the lattice Boltzmann equation unit, the channel height d equals $2N-1$. The upper boundary of the channel is place at the position $y = N + 1/2$. For the rest of this section, we consider all quantities in the lattice Boltzmann equation unit, then by using equation (148) and equation (153), the relaxation ratio s_ν is computed by

$$\begin{aligned} s_\nu(j) &= \frac{2}{6\nu+1} \\ &= \frac{2\pi\{u'(0) + 12[2u(1/2) - u'(0)](j-1)^2/(2N-1)^2\}}{4\sqrt{6}(2N-1)ku'(0) + \pi\{u'(0) + 12[2u(1/2) - u'(0)](j-1)^2/(2N-1)^2\}}, \end{aligned} \tag{154}$$

where $j = 1, 2, \cdots, N$. In lattice Boltzmann simulation, the relaxation ratio $s_\nu(j)$ given by equation (154) guarantees that the recovered Navier-Stokes equation has correct kinematic shear viscosity ν given by equation (148). The relaxation ratio s_q does not affect any hydrodynamic parameter in the Navier-Stokes equation and can be regarded as a free parameter. In the simultion, we use the following relationship, equation (155), between the relaxation ratios s_q and s_ν [17] to compute $s_q(j)\,(j = 1, 2, \cdots, N)$

$$s_q = \frac{8(2 - s_\nu)}{8 - s_\nu}. \tag{155}$$

We use the bounce-back boundary given by equation (156) to implement the Dirichlet boundary condition for the upper boundary; the periodic boundary condition given by equation (157) and equation (158) for the left inlet and right outlet, respectively; and the asymmetric boundary condition given by equation (159) at the channel center,

$$\begin{cases} f_4(i,N) = f_2(i,N+1) \\ f_7(i,N) = f_5(i+1,N+1) - \rho(N)(1/2-u_s)U_w/3 \\ f_8(i,N) = f_6(i-1,N+1) + \rho(N)(1/2-u_s)U_w/3 \end{cases} \tag{156}$$

$$\begin{cases} f_1(1,j) = f_1(M+1,j) \\ f_5(1,j) = f_5(M+1,j) \\ f_8(1,j) = f_8(M+1,j) \end{cases} \tag{157}$$

$$\begin{cases} f_3(M,j) = f_3(0,j) \\ f_6(M,j) = f_6(0,j) \\ f_7(M,j) = f_7(0,j) \end{cases} \tag{158}$$

$$\begin{cases} f_2(i,1) = f_4(i,1) \\ f_5(i,1) = f_7(i,1) \\ f_6(i,1) = f_8(i,1) \end{cases} \tag{159}$$

$i = 1, 2, \cdots, M;\ j = 1, 2, \cdots, N,$

where U_w is the speed of the upper wall in LBE simulation, which can be given arbitrarily with the restriction of Mach number $2U_w/c_s < 0.1$. In the result, the macroscopic velocity $\boldsymbol{u}$ from equation (152) is normalized by $2U_w$.

Numerically, in the stream-wise direction, we fix the number of grids $M = 3$; in the span-wise direction, we vary the number of grids. We use $N = 1001, 2001, 4001$ and 8001, respective, for the cases of Knudsen number $k = 0.03, 0.1$ and 1.0 and use $N = 201, 401, 801$ and 1601, respective, for the case of $k = 10.0$. The L_∞ error and L_2 error of the lattice Boltzmann simulation produced velocity $\hat{u}_3(y)$ compared to the target velocity approximation $\tilde{u}_3$ for the cases of Knudsen number $k = 0.03, 0.1, 1.0, 10.0$ with different grid sizes are tabulated in Table 43, in which the rate of convergence for each case is also computed by using the L_2 error.

From Table 43, we see when the number of grids N is greater than 1000, the L_2 error of each simulation is at least less than 10^{-6}. The corresponding L_∞ error is more than one magnitude lesser. For the case $k = 10.0$, one does not need very dense mesh, when N is greater than 200, the L_2 error is roughly 10^{-6}. On balance, Table 43 shows that the lattice Boltzmann simulation with effective viscoisty is convergent and converges to the target function efficiently with the order of 1.5.

TABLE 43: The L_∞ error and L_2 error of the velocity $\hat{u}_3(y)$ from lattice Boltzmann equation compared to the target velocity $\tilde{u}_3(y)$ and the rate of convergence α of the lattice Boltzmann simulation computed from L_2 error.

k	N	$\|\delta\hat{u}_3\|_\infty$	$\|\delta\hat{u}_3\|_2$
0.03	1001	$7.0389182260655048 \cdot 10^{-9}$	$2.2217521798457231 \cdot 10^{-7}$
	2001	$1.7610521929611878 \cdot 10^{-9}$	$7.8575350220154914 \cdot 10^{-8}$
	4001	$4.4042952618263948 \cdot 10^{-10}$	$2.7770754042201867 \cdot 10^{-8}$
	8001	$1.1013140399640520 \cdot 10^{-10}$	$9.7748584184542483 \cdot 10^{-9}$
	α	1.5026	
0.1	1001	$1.9386528771203615 \cdot 10^{-8}$	$6.0873591823932551 \cdot 10^{-7}$
	2001	$4.8503176475200860 \cdot 10^{-9}$	$2.1530001558136440 \cdot 10^{-7}$
	4001	$1.2130292326162362 \cdot 10^{-9}$	$7.6130509309259764 \cdot 10^{-8}$
	8001	$3.0332875100569368 \cdot 10^{-10}$	$2.6907949996233101 \cdot 10^{-8}$
	α	1.5005	
1.0	1001	$2.0432891267851971 \cdot 10^{-8}$	$6.3731623644837895 \cdot 10^{-7}$
	2001	$5.1121781807772493 \cdot 10^{-9}$	$2.2540972820564877 \cdot 10^{-7}$
	4001	$1.2785059677611343 \cdot 10^{-9}$	$7.9709066183372552 \cdot 10^{-8}$
	8001	$3.1969360492212218 \cdot 10^{-10}$	$2.8183368703694177 \cdot 10^{-8}$
	α	1.5003	
10.0	201	$7.2312108870264957 \cdot 10^{-8}$	$1.0189967717959070 \cdot 10^{-5}$
	401	$1.8146651403760927 \cdot 10^{-8}$	$3.6094539972123638 \cdot 10^{-7}$
	801	$4.5452735603079830 \cdot 10^{-9}$	$1.2773312785518941 \cdot 10^{-7}$
	1601	$1.1373448016716026 \cdot 10^{-9}$	$4.5181613289800173 \cdot 10^{-8}$
	α	1.5018	

CHAPTER 5

MOLECULAR FLOW

In this chapter, we implement the MD simulation of the molecular Couette flow with Knudsen number ranging from 1.0 to 10.0 by using the open souce molecular dynamics simulation package LAMMPS [18]. The quality of the density profiles and the velocity profile from our MD simulation is much better than that of Barisik *et al*'s results [44, 45]. We model the density profiles and the velocity profiles by using the effective radial distribution functions, the solutions of the integral equation for the rarefied Couette flow and the density and velocity profiles from our MD simualtion. By using the modeled density and velocity functions, we construct the effective viscosity, which is in the stress tensor term of the Navier-Stokes equation. At last, we utilize the nonuniform mesh TRT-LBE simulations with 1D and 2D wall-gas interction, respectively, to reproduce the density profiles and the velocity profiles of the molecular Couette flow, in the Navier-Stokes equation framework.

5.1 THE 2D MOLECULAR DYNAMIC SIMULATION OF RAREFIED COUETTE FLOWS

In this section, we implement the molecular dynamic simulation for steady gaseous planar Couette flow of Argon with Knudsen number k ranging from 1.0 to 10.0 by using the open source molecular dynamics simulation package LAMMPS [18].
The units of the MD simulations are related to the Lennard-Jone's potential:

$$V_{LJ}(r) = 4k_bT_0\left[\left(\frac{\sigma}{r}\right)^{12} - \left(\frac{\sigma}{r}\right)^{6}\right] \tag{160}$$

The unit length is the zero inter-particle potential distance $\sigma = 0.3405$nm; the unit temperature is the characteristic temperature $T_0 = 119.8$K. The unit mass is the mass $m_0 = 6.63 \cdot 10^{-26}$kg of one simulated molecule. We set the Boltzmann constant $k_b = 1.3806 \cdot 10^{-23}$J/K to be unity. The unit time is $\tau = \sigma\sqrt{m_0/(k_bT_0)}$. The unit velocity is $v_0 = \sqrt{k_bT_0/m_0}$. Considering the structure of the molecule, the speed of sound is $c_s = \sqrt{\gamma k_bT/m_0}$, where the adiabatic index $\gamma = 5/3$ for monatomic molecules. In this case, it is Argon. In the current MD simulation, we set the Mach

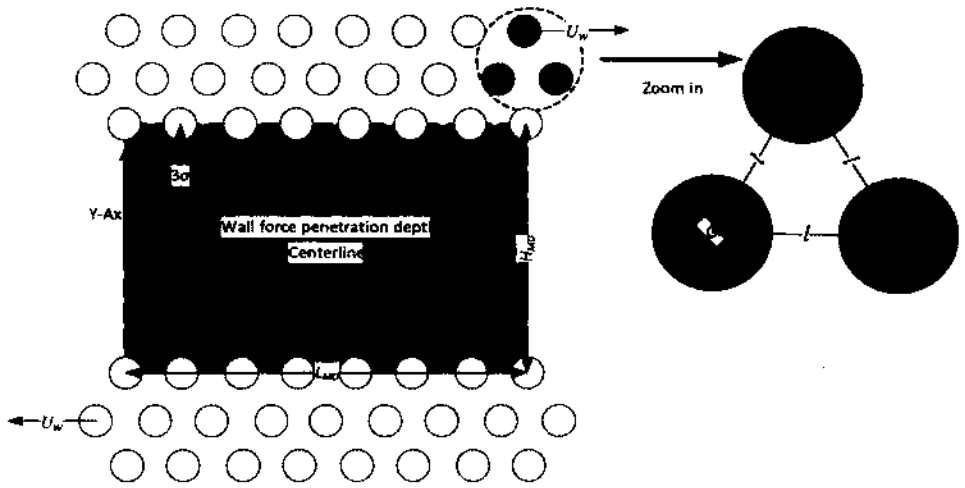

FIG. 26: The cross section of the MD simulation box for the planar gaseous Couette flow.

number $M = 0.6$ and the temperature $T = 298/119.8$. Then, the speed of the upper and lower moving walls in MD unit are $U_w^{\pm} = \pm\frac{Mc_s}{2v_0} = \pm\frac{M}{2}\sqrt{\frac{\gamma T}{T_0}} \approx \pm 0.610837$. Figure 26 shows a sketch of a cross section of the MD simulation box. As seen from Figure 26, the cross section has three zones, the upper and lower walls and the computational domain of the Argon gases confined between the walls. The walls are made of wall molecules. We adopt the (1,1,1) FCC lattice structure [44, 45] for the wall molecules. Specifically, each wall consists of three layers of wall molecules in a staggered lattice. As we zoom in, we see three adjacent wall molecules form an equilateral triangle with one molecule on each of its verteces and the wall lattice is an extension of the equilateral triangle. The length of the lattice of the walls, namely, the length of the edge of each equilateral triangle is $l = 0.3810/0.3405 \approx 1.1189$. The dimensions of the simulation box are the length of the wall denoted by L_{MD} in length, the height of the computational domain denoted by H_{MD} plus two times the wall thickness, *i.e.*, $\sqrt{3}l$ in height, and the width in the third dimension is perpendicular to the cross section shown in Figure 26. When simulating the Couette flow with different rarities, we use different channel lengths and heights and a fixed channel width to ensure the high quality of the MD simulation. Generally, we use longer and narrower channels for more rarefied flows; and use shorter and higher channels for less rarefied flows. We fix the width of the simulation box as $W = 1$. This is because LAMMPS is intrinsically in 3-D. To implement 2-D simulation, we technically zero

out the dimension in width by initially enforcing the width component of position coordinate of all molecules (both the wall molecules and the gas molecules) identically equal to 0.5 and setting the width component of velocity and force equal to 0 at each timestep for all molecules. In the simulation, we use a periodic boundary condition at the inlet and outlet of the channel, as well as at the lateral width direction. The forces applied to the wall molecules are also removed at each timestep, so that the walls move uniformly, the upper one along the stream wise direction, the lower one along the opposite stream wise direction. We set the cut-off distance of the intermolecular force equal to 3. We use Langevin thermostat for the wall molecules and the Nose-Hoover thermostat for the gas molecules. The start temperature and stop temperature of the Nose-Hoover thermostat are the same, equal to T, while the damping temperature is set to 0.1. Apart from the initialization, the gas molecule temperature is computed by using only the span-wise component of the gas molecules velocity. The simulation time step is 0.002, which is equivalent to 4.3116fs.

The number of gas molecules N in the simulation is determined by the Knudsen number k of the simulated system and the size of the simulation box. In 3D space, the mean free path of a monatomic hard spherical molecule is

$$\lambda = \frac{1}{\sqrt{2}\pi \emptyset^2 n}, \tag{161}$$

where $\emptyset$ is the diameter of the gas molecule (for Argon $\emptyset = 0.142/0.3405 \approx 0.4170$), n is the number density. With the width component of velocity and force being zero mentioned above, the calculation of the mean free path in equation (161) should be modified for the 2D cases by

$$\lambda = \frac{4}{\sqrt{2}(4\sqrt{3}+\pi)\emptyset^2 n}. \tag{162}$$

Recalling the definition equation (146) of Knudsen number k with $d = H_{MD}$, we can use equation (162) and the formula $n = N/(L_{MD}H_{MD}W)$ to obtain

$$k = \frac{\sqrt{2\pi}LW}{(4\sqrt{3}+\pi)\emptyset^2 N}.$$

Consequently, the number of gas molecules N is determined by

$$N = \frac{\sqrt{2\pi}L_{MD}W}{(4\sqrt{3}+\pi)\emptyset^2 k}. \tag{163}$$

We ran LAMMPS on a two-processor Intel Xeon E5-2660 2.2GHz 20 Core CPU with Knudsen number k ranging from 1.0 to 10.0 for $3 \cdot 10^8$ timesteps (approximately

TABLE 44: The length L_{MD} and height H_{MD} of the computational domain, the number N of gas molecules in the MD simulations and simulating time ($6 \cdot 10^8$ timesteps) in D/HH/MM/SS for Knudsen number $1.0 \leq k \leq 10.0$

k	L_{MD}	H_{MD}	N	simulating time
1.0	1560l	130l	2498	1/12/40/12
2.0	1560l	65l	1249	1/10/33/26
3.0	1560l	130l/3	833	1/09/54/05
4.0	1560l	65l/2	625	1/13/19/13
5.0	3120l	26l	999	2/14/24/01
6.0	3120l	65l/3	833	2/21/30/51
7.0	3120l	130l/7	714	2/13/55/35
8.0	4680l	65l/4	937	4/05/38/44
9.0	4680l	130l/9	833	4/05/23/16
10.0	4680l	13l	750	3/18/35/42

1.2935ms) to ensure the equilibrium state has arrived and then continue running another $3 \cdot 10^8$ timesteps for statistical averaging over one dimensional strips of bins with bin size equals 0.2. The length L_{MD} and height H_{MD} of the computational domain, the corresponding number of gas molecules N in the MD simulations and the simulating time ($6 \cdot 10^8$ timesteps) for various Knudsen numbers are tabulated in Table 44. From Table 44 we see, in order to obtain qualitative velocity and density data, the computational cost is quite high.

In order to obtain dimensionless velocity and density, we set up the y-axis in the spanwise direction pointing to the upper wall with the origin in the channel center. We also use the following renormalization after the statistical averaging for the MD data. The spanwise coordinate is normalized by the height of the computational domain H_{MD} so that the channel height is normalized to be 1 and $-1/2 \leq y \leq 1/2$. The macroscopic velocity is normalized by $2U_w$. The density is nomalized by the arithmetic mean of the number density. Figure 27-31 shows the velocity and density profiles of the MD simulations for various Knudsen numbers, in which the velocity profile is compared with corresponding high precision velocity from integral equation with purely diffusive walls.

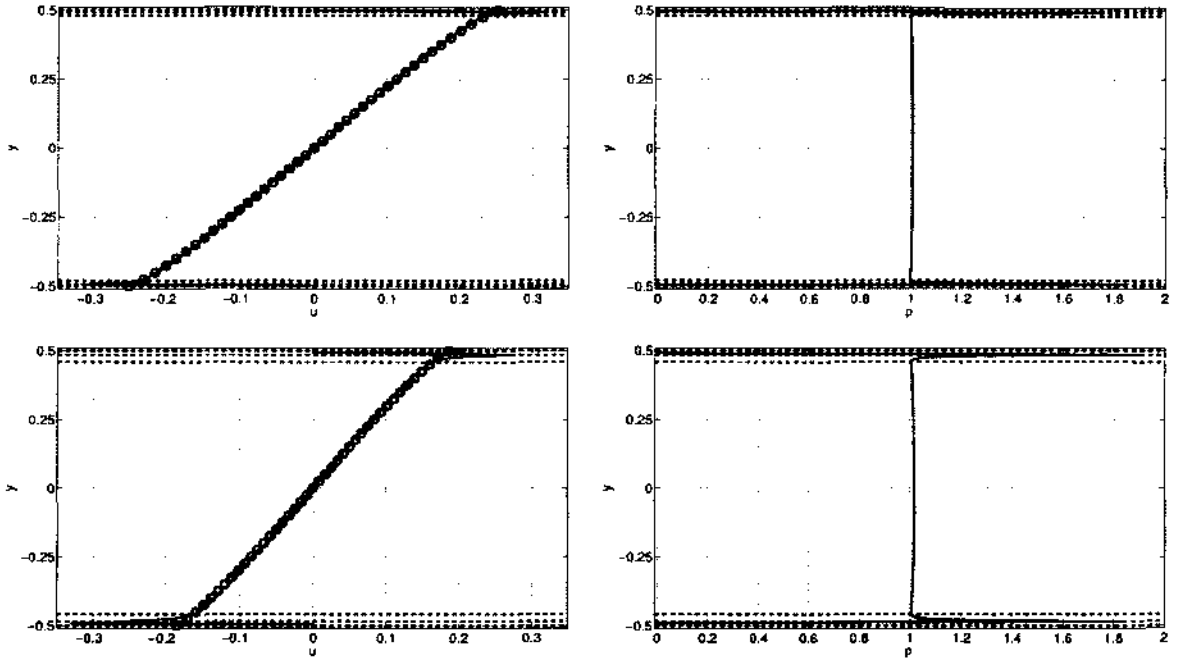

FIG. 27: The velocity profile (red solid line in the left figures) and density profile (red solid line in the right figures) of MD simulation with Knudsen number $k = 1.0$ and 2.0. The blue dash circle line in the left figures are the correponding high precision solution of velocity from equation (72). From the top row to the bottom row the corresponding value of k increases. The three dashed lines from the top to the bottom on the top of each figure represent the position of centers of the inner most wall molecules, the position of $\sqrt[6]{2}\sigma$ distance from the first dashed line and the position of 3σ distance from the first dashed line, respectively. The three dashed lines on the bottom of each figure are located similarly.

In all the figures, we draw two pairs of parallel dashed baselines, three on the top and three on the bottom. Take the three top baselines for example: the first line is the position of the center of the inner most top wall molecules, namely, the line through the centers of top wall molecules that are aligned closest to the gas molecules, the second and the third lines are the lines in the channel that are $\sqrt[6]{2}\sigma$ and 3σ away from the first line, respectively. The three bottom baselines are drawn similarly with respect to bottom wall. Hence, the region outside the first line is wall, without any gas molecule. The second line is approximately the turning point of repulsive and attractive wall-gas interaction, that is the region between the first and second lines could be regarded as the repulsive wall force region, while the region

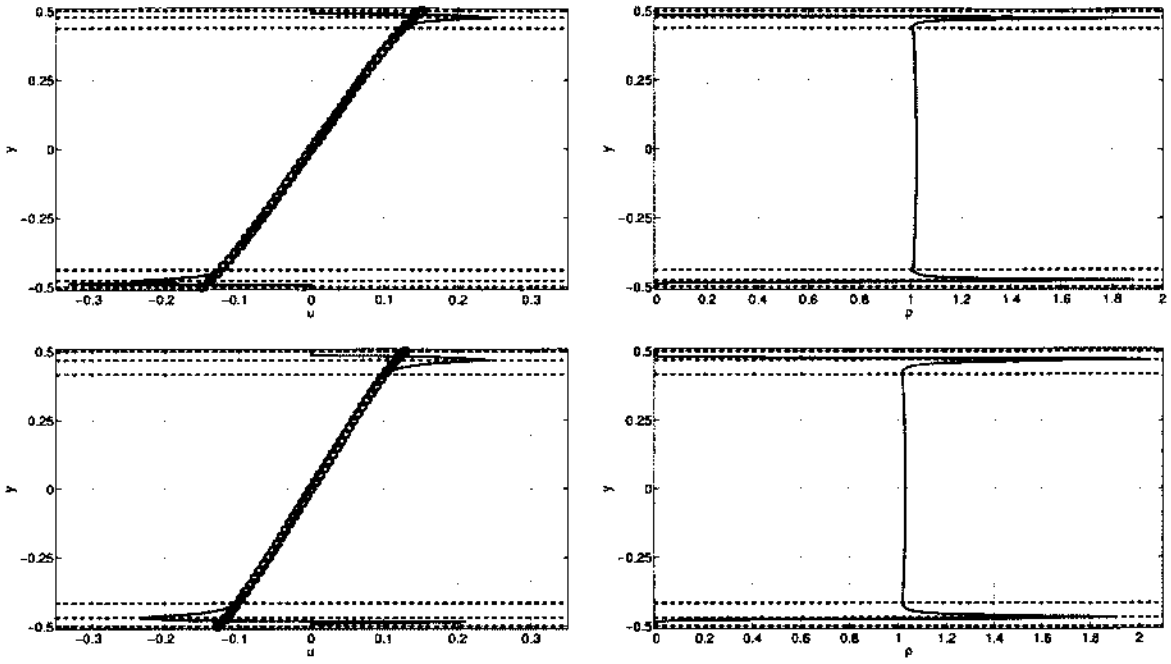

FIG. 28: The velocity profile (red solid line in the left figures) and density profile (red solid line in the right figures) of MD simulation with Knudsen number $k = 3.0$ and 4.0. The blue dash circle line in the left figures are the correponding high precision solution of velocity from equation (72). From the top row to the bottom row the corresponding value of k increases. The three dashed lines from the top to the bottom on the top of each figure represent the position of centers of the inner most wall molecules, the position of $\sqrt[6]{2}\sigma$ distance from the first dashed line and the position of 3σ distance from the first dashed line, respectively. The three dashed lines on the bottom of each figure are located similarly.

between the second and the third lines could be regarded as the attractive wall force region. The third line is approximately the wall force cutoff position. The region between the pair of the third lines of the top and the bottom walls is regarded free from wall force effect. Hence, from Figure 27-31 we see in the region without wall-gas interaction, the velocity from MD simulation matches the velocity from the integral equation with diffusive walls and the density in this region is almost a constant. In the attractive force region, the both the velocity and the density are increasing as the position approaches to the wall. The peak of density and velocity are reached near the second line. In the repulsive force region, the density drops abruptly as the position approaches further to the wall; the velocity drops to 0 near the wall,

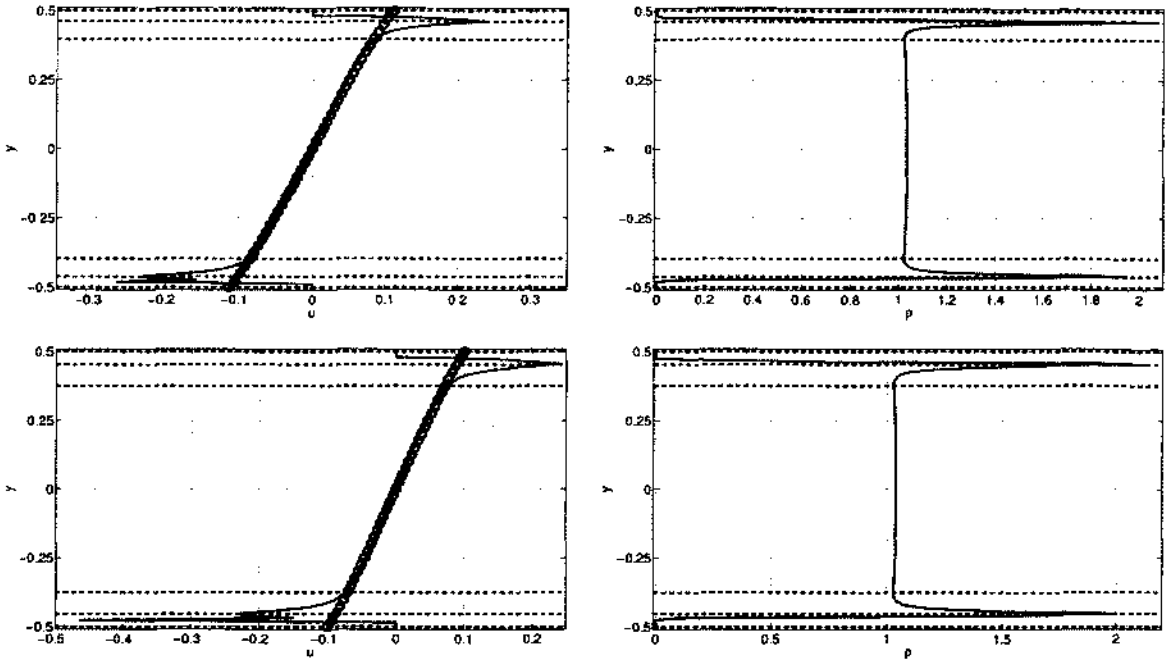

FIG. 29: The velocity profile (red solid line in the left figures) and density profile (red solid line in the right figures) of MD simulation with Knudsen number $k = 5.0$, and 6.0. The blue dash circle line in the left figures are the correponding high precision solution of velocity from equation (72). From the top row to the bottom row the corresponding value of k increases. The three dashed lines from the top to the bottom on the top of each figure represent the position of centers of the inner most wall molecules, the position of $\sqrt[6]{2}\sigma$ distance from the first dashed line and the position of 3σ distance from the first dashed line, respectively. The three dashed lines on the bottom of each figure are located similarly.

however, it shows a seemly random fluctuation of stronger or weaker intensity in the repulsive force region, even with statistical averaging over $3 \cdot 10^8$ timesteps.

5.2 MODELING THE MACROSCOPIC RESULTS OF THE 2D MOLECULAR DYNAMIC SIMULATION

In this section, we model the density profile and the velocity profile of the MD simulation for the rarefied gaseous planar Couette flow in a micro-scale channel by using smooth functions. The density and velocity models enable us to construct the stress tensor in the Navier-Stokes equation so that we can reproduce the MD simulation results by solving the Navier-Stokes equation.

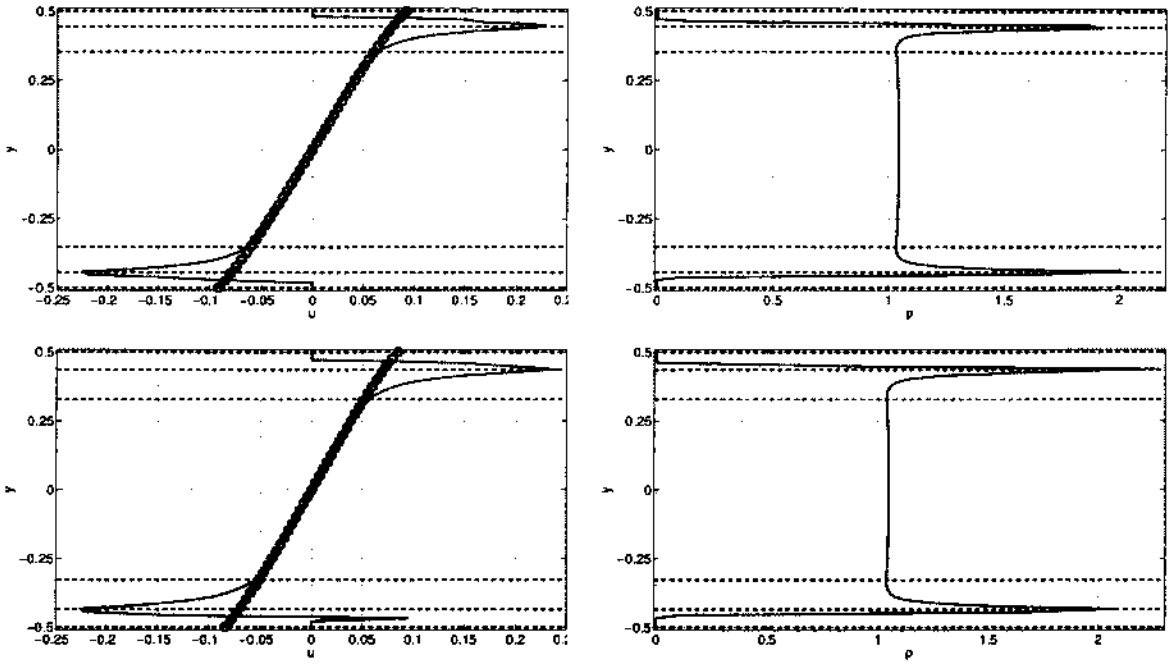

FIG. 30: The velocity profile (red solid line in the left figures) and density profile (red solid line in the right figures) of MD simulation with Knudsen number $k = 7.0$ and 8.0. The blue dash circle line in the left figures are the correponding high precision solution of velocity from equation (72). From the top row to the bottom row the corresponding value of k increases. The three dashed lines from the top to the bottom on the top of each figure represent the position of centers of the inner most wall molecules, the position of $\sqrt[6]{2}\sigma$ distance from the first dashed line and the position of 3σ distance from the first dashed line, respectively. The three dashed lines on the bottom of each figure are located similarly.

The form of the density function comes from the 2D steady Navier-Stokes equation with external force:

$$\rho(\boldsymbol{u}\cdot\boldsymbol{\nabla})\boldsymbol{u} = -\boldsymbol{\nabla}p + \boldsymbol{\nabla}\cdot\{\rho\nu[\boldsymbol{\nabla}\boldsymbol{u} + \boldsymbol{\nabla}\boldsymbol{u}^T - (\boldsymbol{\nabla}\cdot\boldsymbol{u})I] + \rho\zeta(\boldsymbol{\nabla}\cdot\boldsymbol{u})I\} + \rho\boldsymbol{a}, \quad (164)$$

where ρ is the density, $\boldsymbol{u} = (u, v)^T$ is the velocity, $p = k_b T\rho/m_0$ is the static pressure with k_b, T and m_0 being the Boltzmann constant, the ambient temperature and the mass of the gas molecule, respectively, ν is the kinematic shear viscosity, ζ is the kinematic bulk viscosity, I is the identity tensor, $\boldsymbol{a} = (a_x, a_y)^T$ is the acceleration applied to the flow.

In the micro-scale planar channel, we set up the coordinates system such that the

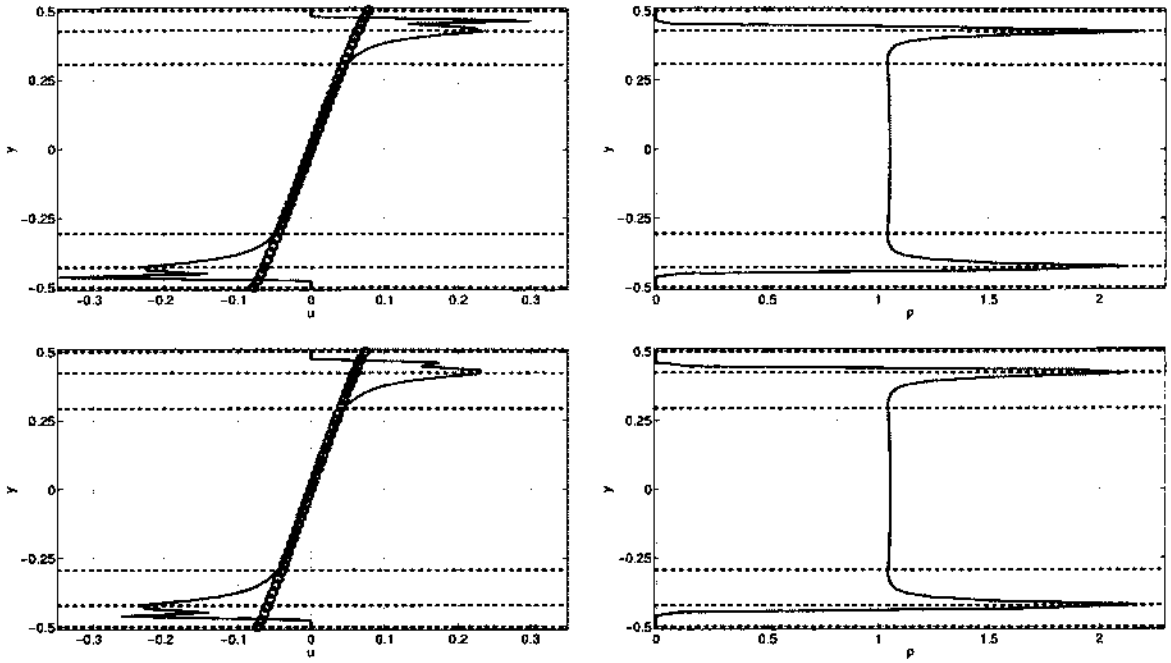

FIG. 31: The velocity profile (red solid line in the left figures) and density profile (red solid line in the right figures) of MD simulation with Knudsen number $k = 9.0$ and 10.0. The blue dash circle line in the left figures are the correponding high precision solution of velocity from equation (72). From the top row to the bottom row the corresponding value of k increases. The three dashed lines from the top to the bottom on the top of each figure represent the position of centers of the inner most wall molecules, the position of $\sqrt[6]{2}\sigma$ distance from the first dashed line and the position of 3σ distance from the first dashed line, respectively. The three dashed lines on the bottom of each figure are located similarly.

origin is located on the channel centerline, the x-axis points in the streamwise direction and the y-axis points to the upper wall. Due to symmetry, we only consider the upper half channel. We normalize the y coordinate by the height of the MD computational domain H_{MD}. So, $0 \leq y \leq 1/2$. If we ignore the lattice structure of the wall, the net wall-gas interaction in the streamwise direction is zero. With this simplification, the Couette flow problem is a one dimensional problem. Therefore, all the quantities are functions of y, *i.e.*, independent of x. Besides, we have $v = 0$

and $a_x = 0$. Denoting $\frac{\partial}{\partial y} = '$, equation (164) reduces to:

$$[(\ln u')' + (\ln \rho)']\nu + \nu', = 0$$
$$a_y - k_b T(\ln \rho)'/m_0. = 0$$

Solving these equations, we have

$$\rho \nu u' = P, \tag{165}$$
$$\rho = \rho_\infty e^{m_0 \int a_y \, dy/k_b T} := \rho_\infty g_{n,m,\rho}(1/2 - y), \tag{166}$$

where P is a constant, which can be estimated in the bulk region by using MD data. Equation (165) gives a relation of density, shear viscosity and velocity. Equation (166) is the model for the density profile and ρ_∞ is the density in the bulk region normalized by $g_{n,m,\rho}(1/2)$. Further, $g_{n,m,\rho}(r)$ is the effective radial distribution function with respect to ρ; $g_{n,m,\rho}(r)$ is defined as:

$$g_{n,m,\rho}(r) = \exp\left\{\frac{4T_0}{T}\left[\left(\frac{\sigma_\rho}{r}\right)^n - a_\rho\left(\frac{\sigma_\rho}{r}\right)^m\right]\right\}, \; r \in (0, 1/2]. \tag{167}$$

where r is the distance from the upper wall, T_0 is the characteristic temperature of the gas molecules, σ_ρ is the effective diameter with respect to density, a_ρ is a real number constant and n and m are natural number constants, representing the powers of the replusive and attractive parts, respectively.

The parameters σ_ρ and a_ρ in equation (167) can be determined by using the peak position (y_p, ρ_p) of the density profile and the bulk region density ρ_∞. Namely, we solve the equations:

$$\rho(y_p) = \rho_p,$$
$$\rho'(y_p) = 0.$$

The solutions are

$$\sigma_\rho = \left[\frac{Tm}{4T_0(n-m)} \ln \frac{\rho_p}{\rho_\infty}\right]^{1/n} (1/2 - y_p), \tag{168}$$
$$a_\rho = \frac{Tn}{4T_0(n-m)} \ln \frac{\rho_p}{\rho_\infty} \left[\frac{Tm}{4T_0(n-m)} \ln \frac{\rho_p}{\rho_\infty}\right]^{-m/n}. \tag{169}$$

To determine the integers n and m, the 10-4-3 potential for Lennard-Jones fluid confined between two walls [19] provides one option: $n = 10$ and $m = 4$. However, the shape of the density by using this parameter shows that the attractive part is slightly

stronger. We adjust the value of m by trying $m = 5$ and $m = 6$. By observation, we find $n = 10, m = 4$ is a good choice. Hence, the density ρ is approximated by $\rho_\infty g_{10,6,\rho}(1/2 - y)$.

Inspired by the density model, we use the multiplication of the cubic function $\tilde{u}_4(y) = c_1 y + c_3 y^3$ and the effective radial distribution function $g_{n,m,u}(r)$ with respect to velocity to model the velocity profile. The coefficients c_1 and c_3 of $\tilde{u}_4(y)$ are obtained by least square fitting of the high precision solution of equation (72) from the channel center to the wall-gas interaction cut-off position. The function $g_{n,m,u}(r)$ is defined as:

$$g_{n,m,u}(r) = \exp\left\{\frac{4T_0}{T}\left[\left(\frac{\sigma_u}{r}\right)^n - a_u\left(\frac{\sigma_u}{r}\right)^m\right]\right\}, \; r \in (0, 1/2], \tag{170}$$

where r is the distance from the upper wall, T_0 is the characteristic temperature of the gas molecules, σ_u is the effective diameter with respect to velocity, a_u is a real number constant and n and m are natural number constants.

We assume $u(y) = \tilde{u}_4(y) g_{n,m,u}(1/2 - y)$. The parameters σ_u and a_u in equation (170) can be solved from the following equations by using the peak position $(y_p,\ u_p)$ of the velocity profile

$$u(y_p) = u_p,$$
$$u'(y_p) = 0.$$

The solutions are

$$\sigma_u = t^{1/n}(1/2 - y_p) \tag{171}$$

$$a_u = \left[\frac{\tilde{u}_4'(y_p)}{\tilde{u}_4(y_p)}(1/2 - y_p) + n \ln \frac{u_p}{\tilde{u}_4(y_p)}\right] \frac{T}{4T_0(n-m)} t^{-m/n}, \tag{172}$$

where

$$t = \left[\frac{\tilde{u}_4'(y_p)}{\tilde{u}_4(y_p)}(1/2 - y_p) + m \ln \frac{u_p}{\tilde{u}_4(y_p)}\right] \frac{T}{4T_0(n-m)}.$$

The integers n and m in equation (171) and equation (172) are obtained by the trial and error method based on the shape of the velocity profile. We find $n = 10$ and $m = 3$ are appropriate parameters for the velocity profile. Hence, the velocity is approximated by $(c_1 y + c_3 y^3) g_{10,3,u}(1/2 - y)$.

The values of parameters ρ_∞, σ_ρ, a_ρ for density and c_1, c_3, σ_u, a_u for velocity are tabulated in Table 45 and Table 46, respectively, with Knudsen number $1.0 \leq k \leq 10.0$. It is seen from Table 45 and Table 46 that all the parameters except for a_u vary monotonically with respect to the Knudsen number k.

TABLE 45: The Knudsen number k dependence of the paramters ρ_∞, σ_ρ, a_ρ for the density

k	ρ_∞	σ_ρ	a_ρ
1.0	1.0096564587005836	$6.8407627443251443 \cdot 10^{-3}$	1.2953871593962714
2.0	1.0164970744305677	$1.3776006534918114 \cdot 10^{-2}$	1.3302408643885282
3.0	1.0232772236840917	$2.0742076609746234 \cdot 10^{-2}$	1.3511895646159018
4.0	1.0285774802244194	$2.7727047333082191 \cdot 10^{-2}$	1.3637736072422515
5.0	1.0342912357613776	$3.4711509337369724 \cdot 10^{-2}$	1.3728314219401070
6.0	1.0386670579971240	$4.1823206692981278 \cdot 10^{-2}$	1.3918182392070220
7.0	1.0446717255567732	$4.8440051285190314 \cdot 10^{-2}$	1.3536618715309610
8.0	1.0497800399203923	$5.6058410288833280 \cdot 10^{-2}$	1.4229595070760717
9.0	1.0527628193644460	$6.3001599052087159 \cdot 10^{-2}$	1.4179508120289994
10.0	1.0541739064985043	$6.9968807191129190 \cdot 10^{-2}$	1.4096028736928392

TABLE 46: The Knudsen number k dependence of the paramters c_1, c_3, σ_u, a_u for the velocity

k	c_1	c_3	σ_u	a_u
1.0	0.43812216481688304	$2.0211082971723135 \cdot 10^{-1}$	$5.6332382610516261 \cdot 10^{-3}$	0.54273693446520377
2.0	0.32326781196652482	$1.4874885692545189 \cdot 10^{-1}$	$1.1791421423819863 \cdot 10^{-2}$	0.74211999776645787
3.0	0.26398767665729778	$1.1716661913692647 \cdot 10^{-1}$	$1.8219742292206253 \cdot 10^{-2}$	0.91221339248279676
4.0	0.22704074302359056	$8.8150760043483239 \cdot 10^{-2}$	$2.4821095288668972 \cdot 10^{-2}$	1.0570034486742284
5.0	0.20019045640845781	$7.5324700184561597 \cdot 10^{-2}$	$3.1506698470106592 \cdot 10^{-2}$	1.1760093304065455
6.0	0.17996453068410015	$6.5831390877921267 \cdot 10^{-2}$	$3.8354683290036141 \cdot 10^{-2}$	1.2928626157142891
7.0	0.16439900002938146	$5.4565587898887651 \cdot 10^{-2}$	$4.5053688503986153 \cdot 10^{-2}$	1.3561386871393899
8.0	0.15145629967474097	$4.9157607387820421 \cdot 10^{-2}$	$5.2190362906552601 \cdot 10^{-2}$	1.4896826829548138
9.0	0.14070137778511336	$4.4745954387360301 \cdot 10^{-2}$	$5.9127305973404091 \cdot 10^{-2}$	1.5634507535912783
10.0	0.13159452442589459	$4.1075980350040363 \cdot 10^{-2}$	$6.6152314770343959 \cdot 10^{-2}$	1.6263501766694606

The velocity profiles and density profiles in Figure 27-31 should be theoretically anti-symmetric and symmetric about y-axis, respectly. However, due to statistical error, the anti-symmetry and symmetry are not shown in the figures. To tackle this issue, we modify the density $\rho_{MD}(y)$ and velocity $u_{MD}(y)$ from MD by $\tilde{\rho}_{MD}(y)$ and $\tilde{u}_{MD}(y)$, respectively

$$\tilde{\rho}_{MD}(y) = [\rho_{MD}(y) + \rho_{MD}(-y)]/2,$$
$$\tilde{u}_{MD}(y) = [u_{MD}(y) - u_{MD}(-y)]/2.$$

Figure 32-36 shows the comparison of the modeled velocity $(c_1 y + c_3 y^3) g_{10,3,u}(1/2 - y)$ with the modified MD velocity $\tilde{u}_{MD}(y)$ and the high precision solution of the integral equation (72); and the comparision of the modeled density $\rho_\infty g_{10,6,\rho}(1/2 - y)$ with the modified MD density $\tilde{\rho}_{MD}(y)$ for the Knudsen number ranging from 1.0 to 10.0.

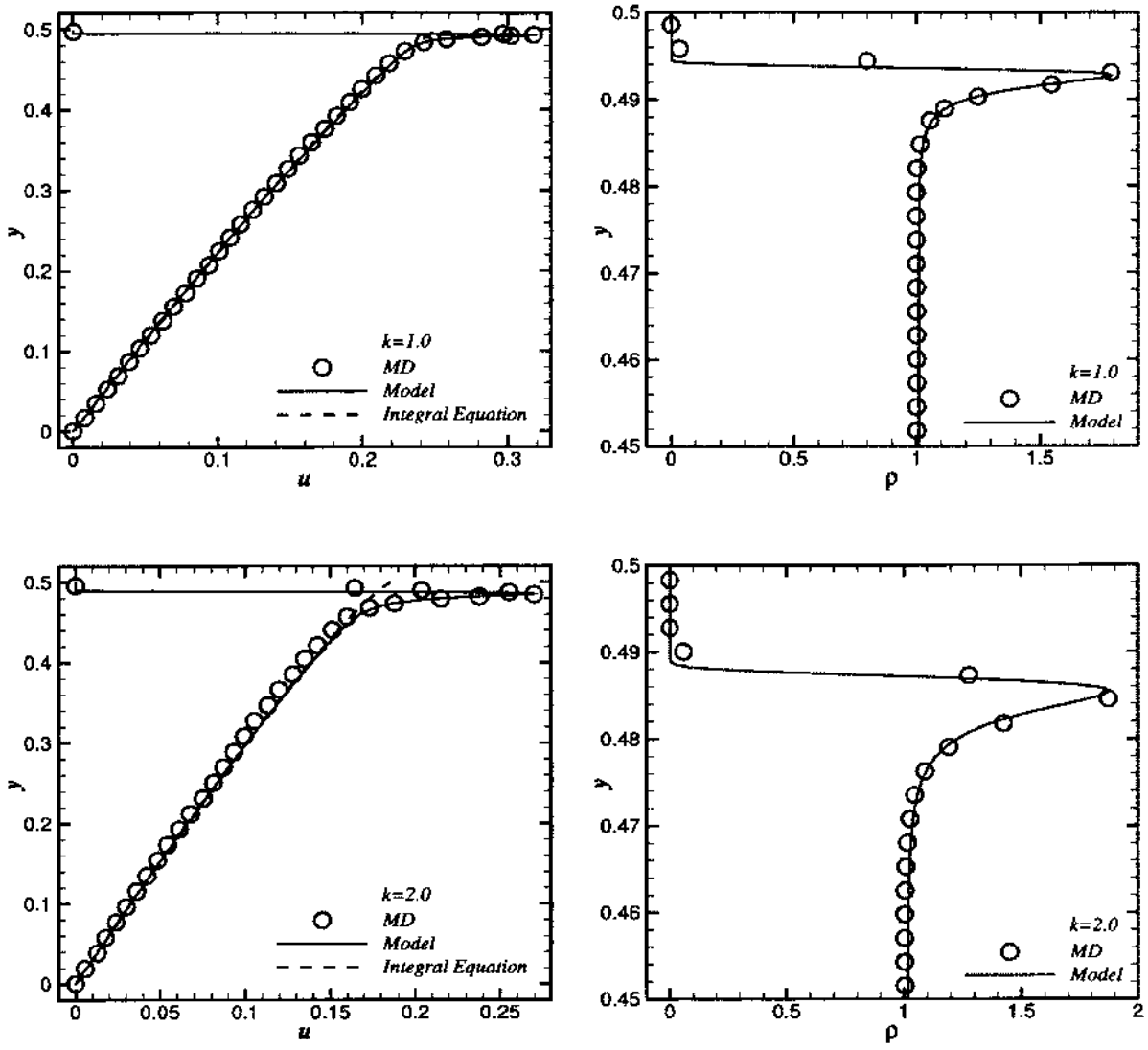

FIG. 32: Comparison of the velocity from the model $(c_1 y + c_3 y^3) g_{10,3,u}(1/2 - y)$, the modified MD data $\tilde{u}_{MD}(y)$ and the high precision solution of the integral equation (72) (left) and the comparison of the density from the model $\rho_\infty g_{10,6,\rho}(1/2 - y)$ and the modified MD data $\tilde{\rho}_{MD}(y)$ (right), with Knudsen number $k = 1.0$ and 2.0.

The velocity profile of the Couette flow in micro-scale channel should be approximated more accurately by the high precision solution of the integral equation in bulk flow region without the influence of wall-gas interaction; whereas in the near wall region, where the wall effect exits, the MD data is more accuate both for the velocity

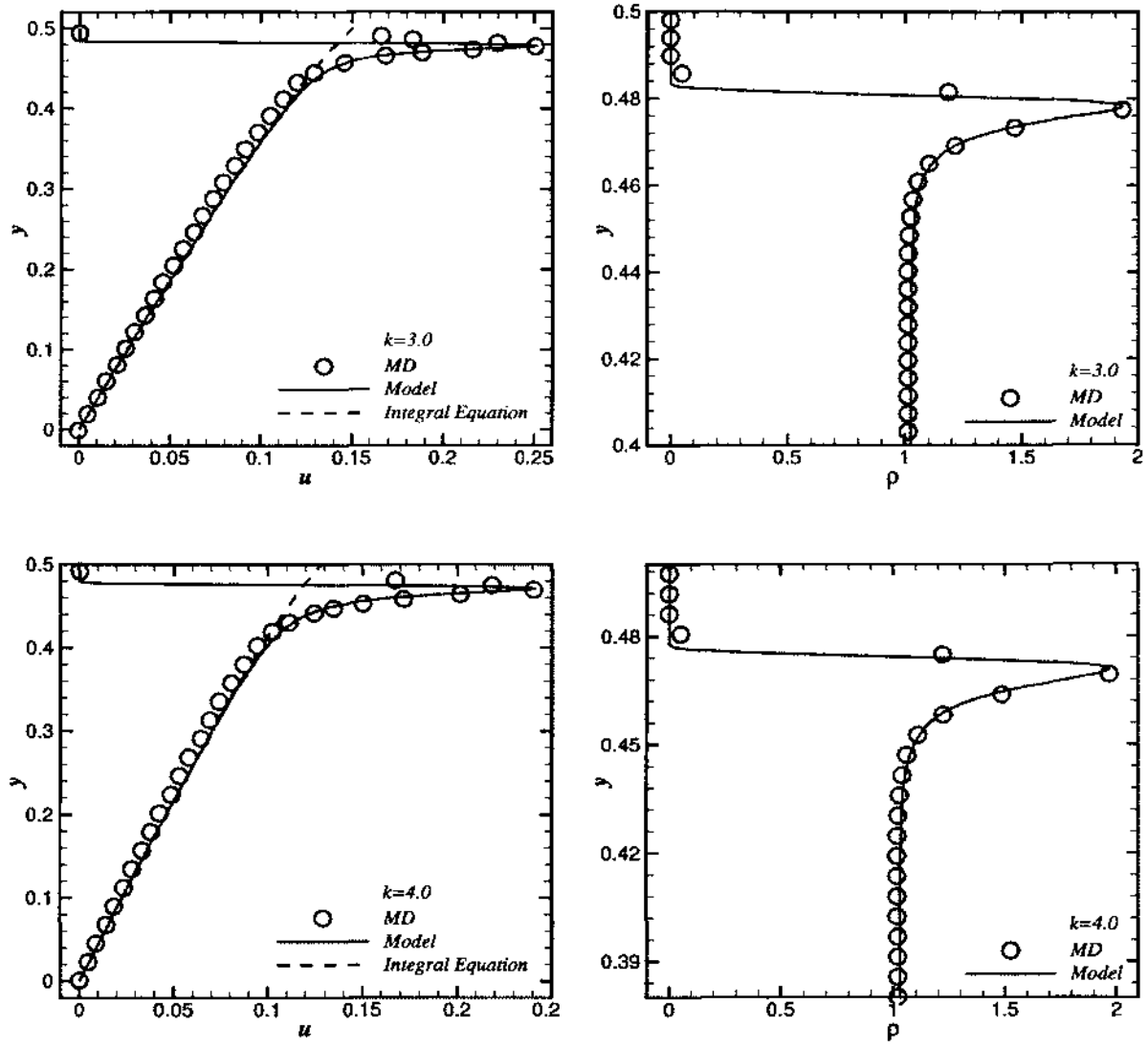

FIG. 33: Comparison of the velocity from the model $(c_1 y + c_3 y^3) g_{10,3,u}(1/2 - y)$, the modified MD data $\tilde{u}_{MD}(y)$ and the high precision solution of the integral equation (72) (left) and the comparison of the density from the model $\rho_\infty g_{10,6,\rho}(1/2 - y)$ and the modified MD data $\tilde{\rho}_{MD}(y)$ (right), with Knudsen number $k = 3.0$ and 4.0.

profile and density profile. From Figure 32-36, we see for velocity, that our model matches both the high precision solution of the integral equation and the modified MD velocity in correct region with smooth connection and for density, our model captures the modified MD density profile. On balance, our models only utilize the

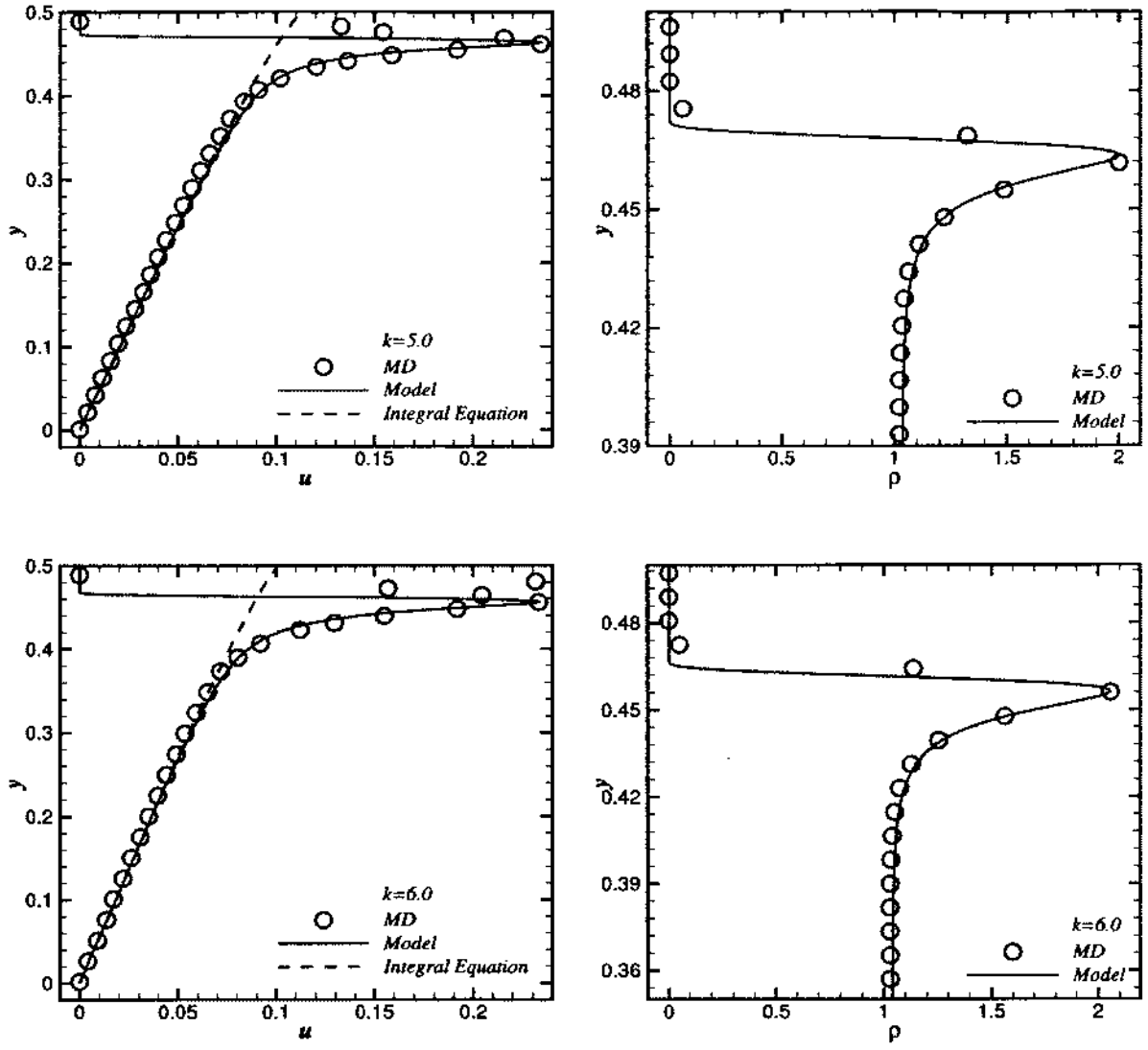

FIG. 34: Comparison of the velocity from the model $(c_1 y + c_3 y^3) g_{10,3,u}(1/2 - y)$, the modified MD data $\tilde{u}_{MD}(y)$ and the high precision solution of the integral equation (72) (left) and the comparison of the density from the model $\rho_\infty g_{10,6,\rho}(1/2 - y)$ and the modified MD data $\tilde{\rho}_{MD}(y)$ (right), with Knudsen number $k = 5.0$ and 6.0.

peak information of the MD data and an approximation of the solution to an integral equation but approximate the velocity and density effectively.

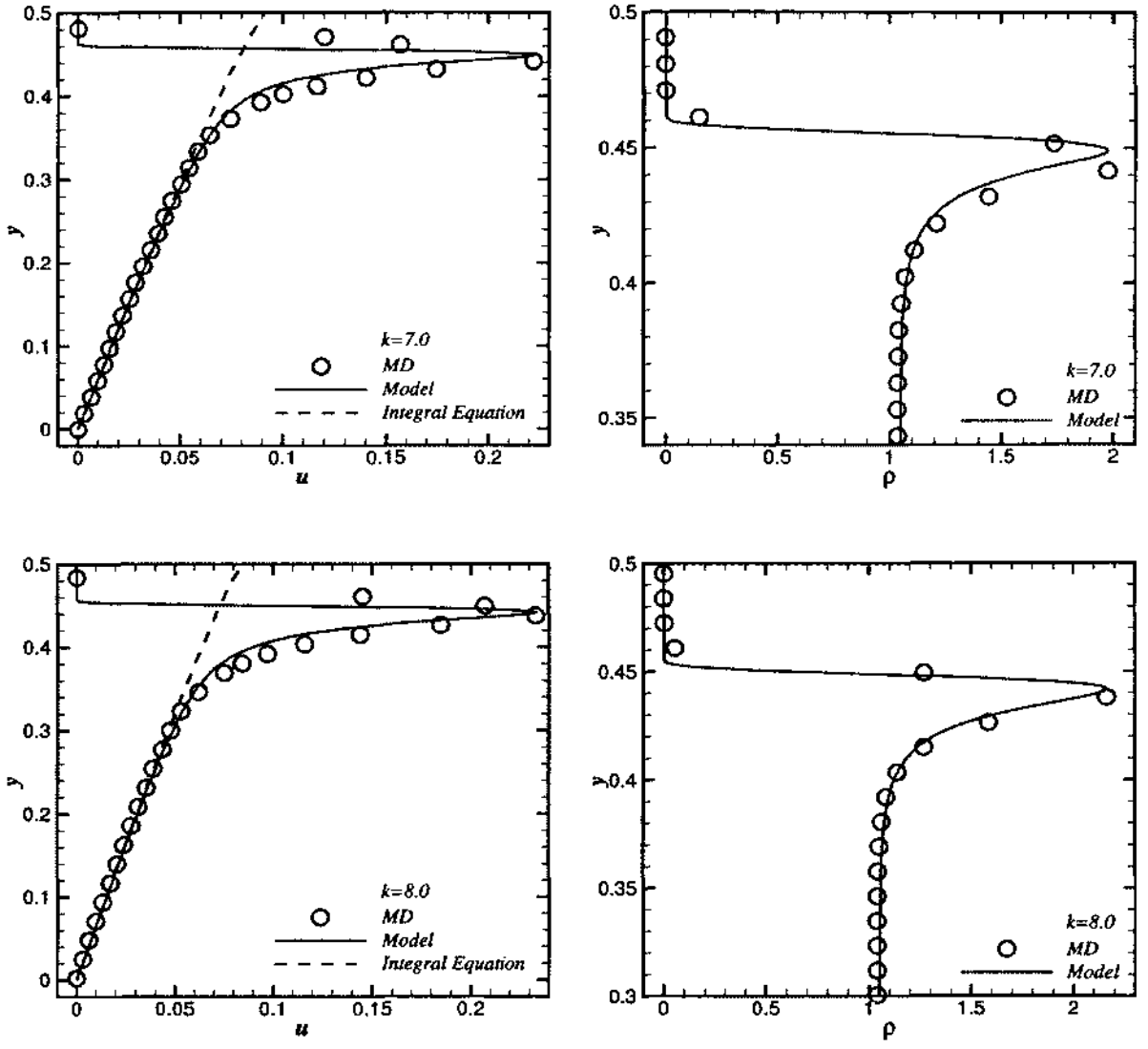

FIG. 35: Comparison of the velocity from the model $(c_1 y + c_3 y^3) g_{10,3,u}(1/2 - y)$, the modified MD data $\tilde{u}_{MD}(y)$ and the high precision solution of the integral equation (72) (left) and the comparison of the density from the model $\rho_\infty g_{10,6,\rho}(1/2 - y)$ and the modified MD data $\tilde{\rho}_{MD}(y)$ (right), with Knudsen number $k = 7.0$ and 8.0.

5.3 REPRODUCING MD DATA BY USING LATTICE BOLTZMANN EQUATION

In this section, we reproduce the velocity profile and density profile from MD simulation by using two relaxation time (TRT) lattice Boltzmann equation [48]. Since

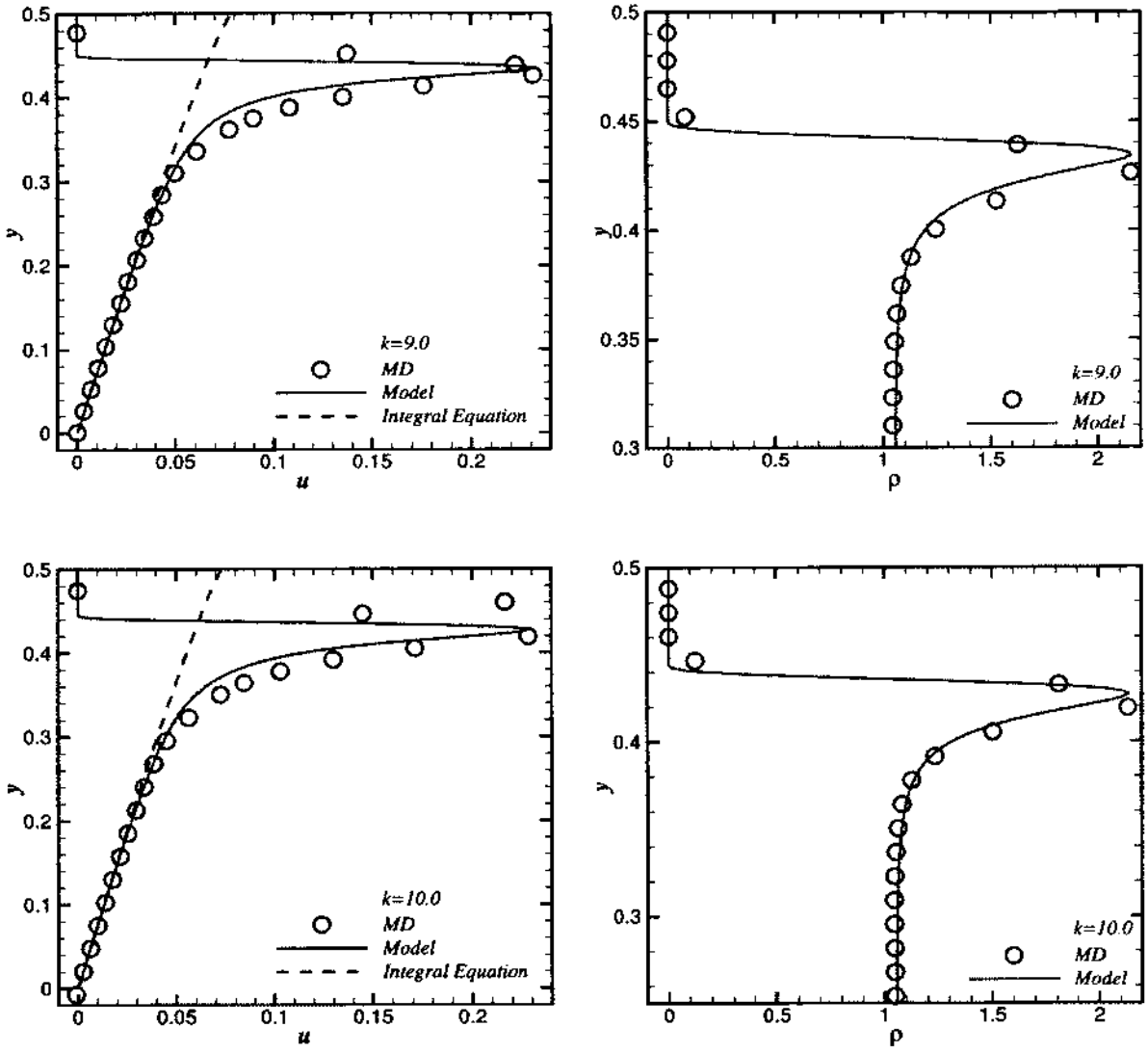

FIG. 36: Comparison of the velocity from the model $(c_1 y + c_3 y^3) g_{10,3,u}(1/2 - y)$, the modified MD data $\tilde{u}_{MD}(y)$ and the high precision solution of the integral equation (72) (left) and the comparison of the density from the model $\rho_\infty g_{10,6,\rho}(1/2 - y)$ and the modified MD data $\tilde{\rho}_{MD}(y)$ (right), with Knudsen number $k = 9.0$ and 10.0.

the MD data in the replusive force region suffer from statistical noise severely, thus are not reliable, we only reproduce the velocity and density functions in the attractive force region and the bulk flow region. Therefore, the repulsive wall force region forms a gap between the LBE compuational domain and the MD wall. We denote

the height of the gap by C_w and call it the inner cutoff distance. To simplify the problem, we first zero out the x-component of the wall force by averaging in the streamwise direction. Specifically, every gas molecular in the shaded region of Figure 37 is subject to the force field of the equivalent physical wall consisting of thirteen wall molecules: six on the first layer, five on the second and two on the third. Suppose we draw a red horizontal line segment in the shaded region with distance y from the channel center line. We denote by $a_{\text{net},y}(x,y)$ the y-component accelaration at coordinate (x,y), deduced by net Lennard-Jones force of the thirteen wall molecules, then the averaged 1D accelaration $a_y(y)$ can be presented as the following integral and the corresponding 256 points Gauss-Legendre quadrature ($\{x_i\}$ are the shifted and scaled abscissas; $\{w_i\}$ are the weights) numerically;

$$\begin{aligned} a_y(y) &= \frac{1}{|\overline{AB}|}\int_{\overline{AB}} a_{\text{net},y}(x,y)\,\mathrm{d}x \\ &\approx \sum_{i=1}^{256} a_{\text{net},y}(x_i,y)w_i. \end{aligned} \tag{173}$$

After this simplification, the net wall force at any point in the channel only has a y-component with its magnitude varying also along the y-axis. We use the bisection method to precisely calculate the zero wall force critical position where the repulsive wall force region switches to the attractive wall force region. This critical position should be the position where both the density profile and the velocity profile reach the peak, therefore is y_p. Hence, the LBE computational domain is a rectangle from 0 (channel center line) to y_p (peak position) in the spanwise direction and with the distance between two adjacent wall molecules l indented by a half LBE grid size on both sides in the streamwise direction. We first consider a uniform mesh for LBE. Fixing the number of grids M in the streamwise direction (from 1 on the left to M on the right) the LBE grid size is computed as $\delta_x = l/M$. Consequently, in the spanwise direction, we should put $y_p/\delta_x + 1$ grids (form 1 on the bottom to N on the top). To ensure N is an integer and the inner cutoff distance C_w is fixed, we slightly adjust the channel height by setting the number of grids in the spanwise direction as $N = [y_p/\delta_x] + 1$, namely we round $p/\delta_x + 1$ to its closest integer. Figure 38 shows a comparison between the MD configuration and the LBE computational domain, in which the channel height adjustment is subject to the restriction of integer number of LBE grids. The upper MD wall and the upper equivalent physical wall in LBE

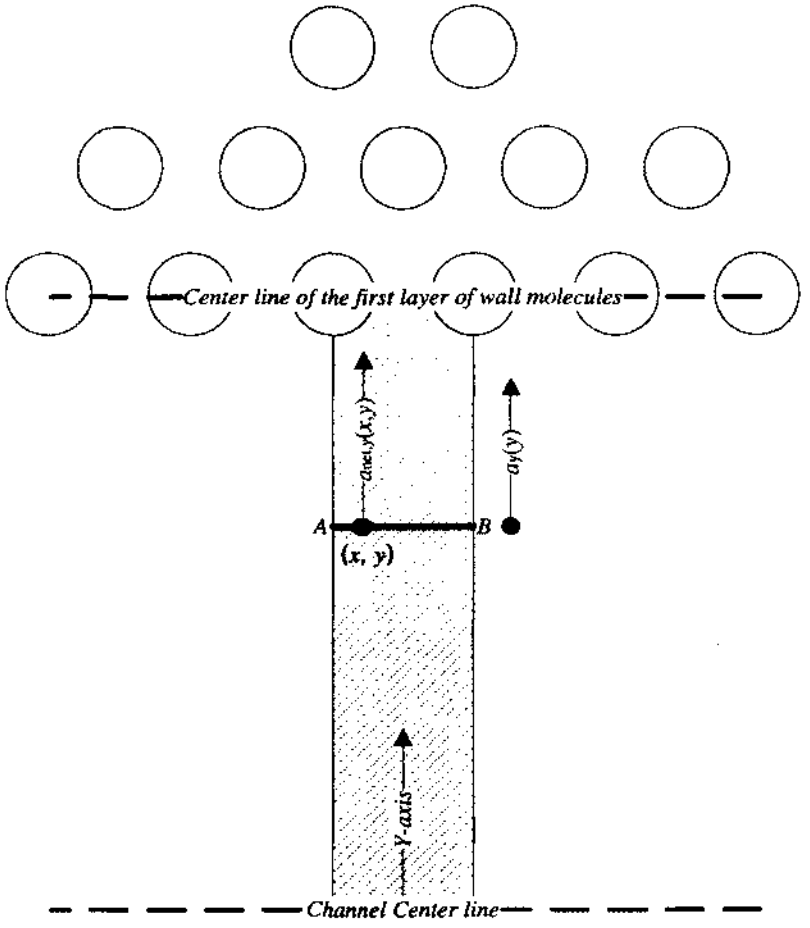

FIG. 37: Computation of the 1D acceleration by averaging.

which is located at $y_p + C_w$ overlap in the limit of $\delta_x \to 0$.

It should be noted that the 1D acceleration computed by $a_y(y)$ from equation (173) needs to be modified before we use it in LBE. This is because the 1D force from equation (173) only consider the wall force impact to the attractive force region. However, when the Knudsen number k is not very big, the collective impact of the bulk flow to the attractive force region cannot be neglected. We modified the force $a_y(y)$ by multiplying by a ratio r_V, *i.e.*, $\tilde{a}_y(y) = r_V a_y(y)$, where r_V is the quotient of a proper wall potential to the 1D acceleration $a_y(y)$ induced potential $V_1(y)$ when $y = y_p$. The proper wall potential is the formal potential $V_{10,6}(r)$ obtained from Equation (167) and defined by:

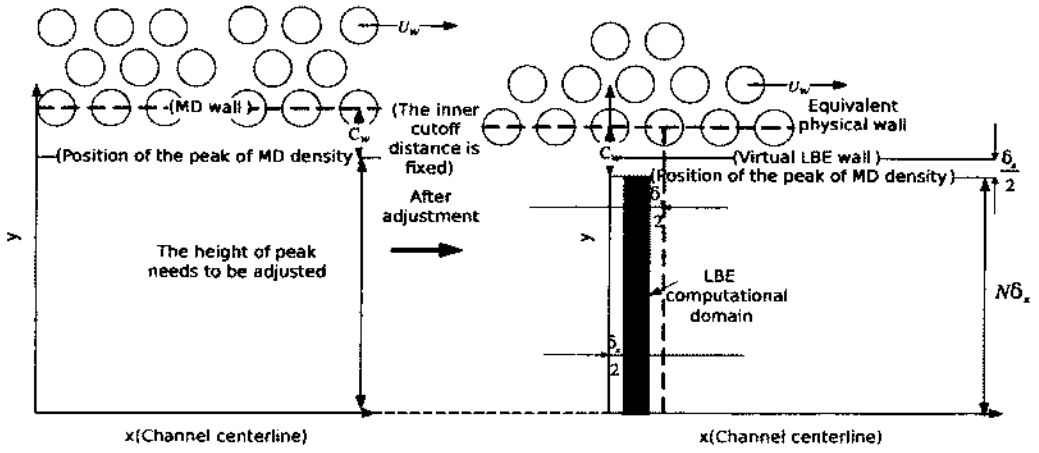

FIG. 38: The MD configuration and the LBE computational domain.

$$V_{10,6}(r) = \frac{4T_0}{T}\left[\left(\frac{\sigma_\rho}{r}\right)^{10} - a_\rho\left(\frac{\sigma_\rho}{r}\right)^4\right],\ r = \frac{1}{2}\left(1 - \frac{y}{y_p + C_w}\right),\ y \in [0, y_p], \quad (174)$$

where $T_0, T, \sigma_\rho, a_\rho$ have the same definition as in equation (167) and are listed in Table 46 for $1.0 \le k \le 10.0$. The potential $V_1(y)$ is defined by the following integral and evaluated numerically by using a 256 points in the Gauss-Legendre quadrature ($\{y_i\}$ are the shifted and scaled abscissas; $\{w_i\}$ are the weights),

$$\begin{aligned} V_1(y) &= -\int_{y_p + C_w - 3\sigma}^{y} a_y(s)\,\mathrm{d}s,\ y \in [y_p + C_w - 3\sigma, y_p] \\ &\approx -\sum_{i=1}^{256} a_y(y_i) w_i, \end{aligned} \quad (175)$$

where σ is the unit of length in MD simulation. Hence, the modified acceleration $\tilde{a}_y(y)$ is computed as

$$\tilde{a}_y(y) = a_y(y) V_{10,6}(C_w)/V_1(y_p),\ y \in [y_p + C_w - 3\sigma, y_p]. \quad (176)$$

In LBE simulation, the unit length is δ_x, $\tilde{a}_j$ is the counterpart of $\tilde{a}_y(y)$, defined by

$$\tilde{a}_j = a_y((j-1)\delta_x)\delta_x V_{10,6}(C_w)/V_1(y_p),\ j_0 \le j \le N, \quad (177)$$

where $j_0 = N - \lfloor (3\sigma - C_w)/\delta_x \rfloor - 1$.

We include the external wall-gas interaction into the MRT-LBE equation (149) in which the collision vector $\boldsymbol{\Omega}(\boldsymbol{f})$ is modified as

$$\boldsymbol{\Omega}(\boldsymbol{f}) = -M^{-1}[S(\boldsymbol{m} - \boldsymbol{m}^{eq}) - \delta_t(I - S/2)\hat{\boldsymbol{F}}], \quad (178)$$

where we use the Guo-Zheng-Shi force model $\hat{\boldsymbol{F}}$ for MRT-LBE [20] given by equation (179)

$$\hat{\boldsymbol{F}} = \rho[0,\ 6(\tilde{a}_x u + \tilde{a}_y v),\ -6(\tilde{a}_x u + \tilde{a}_y v),\ \tilde{a}_x,\ -\tilde{a}_x,\ \tilde{a}_y,\ -\tilde{a}_y,\ 2(\tilde{a}_x u - \tilde{a}_y v),\ \tilde{a}_x v + \tilde{a}_y u]^T. \tag{179}$$

Meanwhile the formula for $\boldsymbol{j}$ in equation (152) should be modified as

$$\boldsymbol{j} = \rho(\boldsymbol{u} - \delta_t \boldsymbol{a}/2). \tag{180}$$

In the case of 1D wall-gas interaction, Equation (179) and Equation (180) reduce to

$$\begin{aligned}
\hat{\boldsymbol{F}} &= \rho[0,\ 6\tilde{a}_j v,\ -6\tilde{a}_j v,\ 0,\ 0,\ \tilde{a}_j,\ -\tilde{a}_j,\ -2\tilde{a}_j v,\ \tilde{a}_j u]^T, \\
j_x &= \rho u, \\
j_y &= \rho(v - \delta_t \tilde{a}_j/2).
\end{aligned}$$

The relaxation ratios s_ν and s_q in LBE simulation are determined by equation (153) and equation (155), respectively. The shear viscosity $\nu(y)$ is computed from equation (165) and we have

$$\nu(y) = \frac{P}{\rho(y)u'(y)} = \frac{\rho(0)\nu(0)u'(0)}{\rho(y)u'(y)},$$

where $\rho(y)$ and $\rho(0)$ are computed with our density model $\rho_\infty g_{10,6,\rho}(1/2 - y)$, $\nu(0)$ is evaluated by equation (147) with $d = 2y_p$ and $u'(y)$ is computed by our velocity model $(c_1 y + c_3 y^3) g_{10,3,u}(1/2 - y)$. Without specifying the unit we use, $1/2$ in $g_{10,6,\rho}$ and $g_{10,3,u}$ should be replaced by $y_p + C_w$. Moveover, we find the position y_1 such that the line going through the point $(y_1, (c_1 y_1 + c_3 y_1^3) g_{10,3,u}(y_p + C_w - y_1))$ and the peak point (y_p, u_p) is tangent to the graph of the curve $(c_1 y + c_3 y^3) g_{10,3,u}(y_p + C_w - y)$ at $(y_1, (c_1 y_1 + c_3 y_1^3) g_{10,3,u}(y_p + C_w - y_1))$. We compute the slope of the line and denote it as $u'(y_1)$. In LBE simulation, we have

$$\nu_j = \begin{cases} \dfrac{4\sqrt{2/3}kc_1 y_p g_{10,6,\rho}(y_p + C_w) g_{10,3,u}(y_p + C_w)}{\pi g_{10,6,\rho}(y_p + C_w - y_j)[(c_1 y + c_3 y^3) g_{10,3,u}(y_p + C_w - y)]'_{y=y_j}}, & 1 \le j \le \lfloor y_1/\delta_x \rfloor + 1 \\ \dfrac{4\sqrt{2/3}kc_1 y_p g_{10,6,\rho}(y_p + C_w) g_{10,3,u}(y_p + C_w)}{\pi g_{10,6,\rho}(y_p + C_w - y_j) u'(y_1)}, & \lceil y_1/\delta_x \rceil + 1 \le j \le N \end{cases} \tag{181}$$

where $y_j = (j-1)\delta_x$.

It is noted that the wall-gas interaction only exerts in the attrative force region, where $y \in [y_p + C_w - 3\sigma, y_p]$. This region becomes attenuated as the Knudsen number k grows bigger. In order to resolve the wall force, one needs a very fine grid.

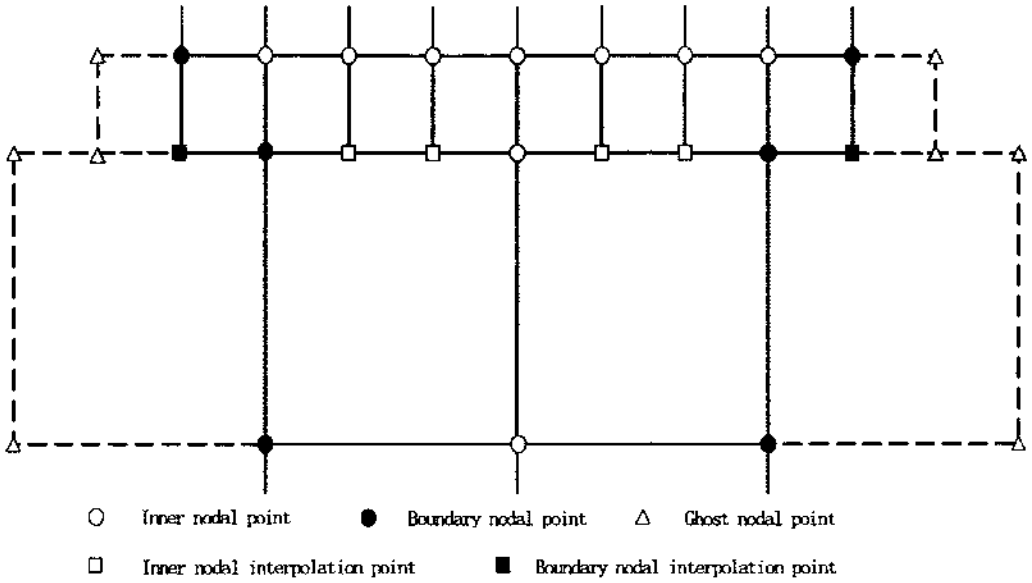

FIG. 39: The sketch of the interface of Tier 3 mesh with grid size of $9\delta_x$ and Tier 4 mesh with grid size of $27\delta_x$. The dash line grids are ghost grids.

However, the fine grid becomes ridiculously redundant in the much wider bulk flow region where no external force exits. Hence, we should consider a nonuniform mesh. For instance, we use four sets of uniform mesh with different mesh sizes to patch the LBE computational domain. Specifically, we use the finest mesh with grid size δ_x to cover the attractive force region (M grids in the stream-wise direction, named Tier 1 mesh), followed by three layers of secondary mesh with grid size $3\delta_x$ ($M/3$ grids in the stream-wise direction, named Tier 2 mesh) and then followed by three layers of tertiary mesh with grid size $9\delta_x$ ($M/9$ grids in the stream-wise direction, named Tier 3 mesh) and at last cover the rest of the region up to the channel center by the coarsest mesh with grid size $27\delta_x$ ($M/27$ grids in the stream-wise direction, named Tier 4 mesh).

On the four boundaries of the LBE computational domain, we use the bounce-back speculative reflection combined boundary condition given by equation (182), with β the fraction of bounce-back and $(1-\beta)$ the fraction of speculative reflection on the top; use periodic boundary condition on the left and right given by equation (157) and equation (158), where M is replaced by $M/3, M/9$ and $M/27$ in Tier 2, Tier 3 and Tier 4 mesh, respectively and use an antisymmetric boundary condition on the bottom given by equation (183)

$$\begin{cases} f_4(i,N) = f_2(i,N+1), \\ f_7(i,N) = \beta(f_5(i+1,N+1) - \rho(N)U_w/6) + (1-\beta)f_6(i-1,N+1), \\ f_8(i,N) = \beta(f_6(i-1,N+1) + \rho(N)U_w/6) + (1-\beta)f_5(i+1,N+1), \end{cases} \tag{182}$$

$1 \le i \le M,$

$$\begin{cases} f_2(i,1) = f_4(i,1), \\ f_5(i,1) = f_7(i,1), \\ f_6(i,1) = f_8(i,1), \end{cases} \tag{183}$$

$1 \le i \le M/27.$

Besides the four boundaries, we have inner boundaries of meshes with different size of grids. Figure 39 shows the sketch of the interface of Tier 3 and Tier 4 meshes. From Figure 39, we see at the interface layer between two meshes we have five different type of grid points: inner point, boundary point, ghost point, inner interpolation point and boundary interpolation point. The inner points are points where the fine mesh and coarse mesh overlap. After collision and streaming, f_2, f_5, f_6 are passed from the coarse mesh to the fine mesh and f_4, f_7, f_8 are passed from the fine mesh to the coarse mesh. More details of the information interchange between two meshes will be discussed later. The boundary points are almost the same as the inner points but are boundary points on the coarse mesh. Thus, on these points, after collision and streaming, we implement periodic boundary condition on the coarse mesh by using the information of corresponding ghost points and then interchange information betweent the coarse and fine grids. Ghost points are free from collision and streaming and are only used to store temporary information. The inner interpolation points are only grid points on the fine mesh, thus lack values of f_2, f_5, f_6. We impose the lacking value on these points by interpolation. After the distribution values on inner points and boundary points have been updated, the values of f_2, f_5 and f_6 on a inner interpolation point are computed by using corresponding values on its adjacent two inner points (or one inner point one boundary point) via linear interpolation. The boundary interpolation points are only grid points on the fine mesh and are also boundary points of the mesh. Thus, on these points, the order of implementation is collide, stream, implement periodic boundary condition and at last after the boundary points have been updated, compute f_2, f_5 and f_6 by using the corresponding values on the boundary points via linear interpolation.

We have discussed how to implement the evolution of patched meshes spatially. However, we need to consider the implementation temporally as well. Since the grid size of the coarser mesh is three times that of its adjacent finer mesh and the D2Q9 LBE velocity set given by Equation (150) is fixed, the timestep of the coarser mesh is also three times of that of its adjacent finer mesh, *i.e.*, $3\delta_t$ and δ_t, respectively. Hence, the evolution time between the two meshes are not completely matched. Consequently, not only the inner interpolation points and boundary interpolation points need spatial interpolation but all the finer grid points on the interface layer need temporal interpolation. For instance, both of the two meshes initiate and evolve at time t_0. Then, only the finer mesh evolves at time $t_0 + \delta_t$ and at time $t_0 + 2\delta_t$. At time $t_0 + 3\delta_t$, both meshes evolve again. We implement linear temporal interpolation of f_2, f_5, f_6 for a coarser grid on the interface lay at time $t_0 + \delta_t$ and $t_0 + 2\delta_t$, respectively, and then pass them to its overlaped finer grid at respective time.

On balance, the process of the nonuniform mesh LBE is as follows, in which f^i and g^i are multidimensional arrays for storing the distributions of Tier $i (i = 1, 2, 3, 4)$:

Step 1: Store macroscopic quantities, *i.e.*, the velocity and the density. Initialize f^1, f^2, f^3, f^4 by using the macroscopic quantities. Set $flag_1 = flag_2 = flag_3 = 0$ and $iter = 0$. Go to *Step* 2.

Step 2: If $iter = checkNum$, adjust f^1, f^2, f^3, f^4 in 0 direction to keep mass conservation, then compute macroscopic quatities and corresponding L_2 error with respect to the stored macroscopic quantities. Check if the stop criterion is satified. Stop if the criterion is satisfied, otherwise set $iter = 0$, update the stored macroscopic quantities and continue. If $iter < checkNum$, implement collision and streaming for f^1, f^2, f^3, f^4 and store the results in g^1, g^2, g^3, g^4. Go to *Step* 3.

Step 2′: If $iter = checkNum$, adjust g^1, g^2, g^3, g^4 in 0 direction to keep mass conservation, then compute macroscopic quatities and corresponding L_2 error with respect to the stored macroscopic quantities. Check if the stop criterion is satified. Stop if the criterion is satisfied, otherwise set $iter = 0$, update the stored macroscopic quantities and continue. If $iter < checkNum$, implement collision and streaming for g^1, g^2, g^3, g^4 and store the results in f^1, f^2, f^3, f^4. Go to *Step* 3′.

Step 3: Implement the top, left and right boundary condition for g^1. Then, implement inner boundary condition for missing distributions of g^1 at the interface between Tier 1 and Tier 2 meshes by using spacetime interpolation of f^2, g^2 on the inner points and boundary points of the interface. $flag_1 = flag_1 + 1$. If $flag_1 = 1$, go to *Step* 4, else, set $flag_1 = 0$, go to *Step* 5.

*Step*3′: Implement the top, left and right boundary condition for f^1. Then, implement inner boundary condition for missing distributions of f^1 at the interface between Tier 1 and Tier 2 meshes by using spacetime interpolation of f^2, g^2 on the inner points and boundary points of the interface. $flag_1 = flag_1 + 1$. If $flag_1 = 1$, go to *Step* 4′, else, set $flag_1 = 0$, go to *Step* 5′.

Step 4: Implement collision and streaming for g^1 and store the results in f^1. Go to *Step* 3′.

Step 4′: Implement collision and streaming for f^1 and store the results in g^1. Go to *Step* 3.

Step 5: Implement the left and right boundary condition for g^2. Then, receive the missing distributions of g^2 from g^1 at the interface between Tier 1 and Tier 2 meshes. After that, implement inner boundary condition for missing distributions of g^2 at the interface between Tier 2 and Tier 3 meshes by using spacetime interpolation of f^3, g^3 on the inner points and boundary points of the interface. $flag_2 = flag_2 + 1$. If $flag_2 = 1$, go to *Step* 6, else, set $flag_2 = 0$, go to *Step* 7.

Step 5′: Implement the left and right boundary condition for f^2. Then, receive the missing distributions of f^2 from f^1 at the interface between Tier 1 and Tier 2 meshes. After that, implement inner boundary condition for missing distributions of f^2 at the interface between Tier 2 and Tier 3 meshes by using spacetime interpolation of f^3, g^3 on the inner points and boundary points of the interface. $flag_2 = flag_2 + 1$. If $flag_2 = 1$, go to *Step* 6′, else, set $flag_2 = 0$, go to *Step* 7′.

Step 6: Implement collision and streaming for g^2 and store the results in f^2. Go to *Step* 5′.

Step 6′: Implement collision and streaming for f^2 and store the results in g^2. Go to *Step* 5.

Step 7: Implement the left and right boundary condition for g^3. Then, receive the missing distributions of g^3 from g^2 at the interface between Tier 2 and Tier 3 meshes. After that, implement inner boundary condition for missing distributions of g^3 at the interface between Tier 3 and Tier 4 meshes by using spacetime interpolation of f^4, g^4 on the inner points and boundary points of the interface. $flag_3 = flag_3 + 1$. If $flag_3 = 1$, go to *Step* 8, else, set $flag_3 = 0$, go to *Step* 9.

Step 7′: Implement the left and right boundary condition for f^3. Then, receive the missing distributions of f^3 from f^2 at the interface between Tier 2 and Tier 3 meshes. After that, implement inner boundary condition for missing distributions of f^2 at the interface between Tier 3 and Tier 4 meshes by using spacetime interpolation of f^4, g^4 on the inner points and boundary points of the interface. $flag_3 = flag_3 + 1$. If $flag_3 = 1$, go to *Step* 8′, else, set $flag_3 = 0$, go to *Step* 9′.

Step 8: Implement collision and streaming for g^3 and store the results in f^3. Go to *Step* 7′.

Step 8′: Implement collision and streaming for f^3 and store the results in g^3. Go to *Step* 7.

Step 9: Implement the left and right boundary condition for g^4. Then, receive the missing distributions of g^4 from g^3 at the interface between Tier 3 and Tier 4 meshes. After that, implement bottom boundary condition for g^4. $iter = iter + 1$. Go to *Step* 2′.

Step 9′: Implement the left and right boundary condition for f^4. Then, receive the missing distributions of f^4 from f^3 at the interface between Tier 3 and Tier 4 meshes. After that, implement bottom boundary condition for f^4. $iter = iter + 1$. Go to *Step* 2.

Since the timesteps in different patches of mesh are different, *i.e.*, $\delta_t, 3\delta_t, 9\delta_t$ and $27\delta_t$ on Tier 1, 2, 3 and Tier 4 mesh, respectively, we should use equation (153) very carefully to compute the relaxation ratio s_ν in different patches of mesh. We have

$$s_\nu(j) = \begin{cases} \frac{1}{3\nu_j/\delta_t + 1/2}, & j \text{ in Tier 1 mesh}, \\ \frac{1}{\nu_j/\delta_t + 1/2}, & j \text{ in Tier 2 mesh}, \\ \frac{1}{\nu_j/(3\delta_t) + 1/2}, & j \text{ in Tier 3 mesh}, \\ \frac{1}{\nu_j/(9\delta_t) + 1/2}, & j \text{ in Tier 4 mesh}, \end{cases} \tag{184}$$

TABLE 47: The Knudsen number k dependence of mesh sizes and the parameter β indicating the fraction of bounce back boundary condition in TRT-LBE simulation with 1D wall-gas interaction for the molecular Couette flow.

k	Tier 1	Tier 2	Tier 3	Tier 4	β
1.0	81 x 143	27 x 3	9 x 3	3 x 187	0.655
	162 x 286	54 x 6	18 x 6	6 x 374	
	324 x 572	108 x 12	36 x 12	12 x 748	
2.0	81 x 156	27 x 3	9 x 3	3 x 89	0.67
	162 x 312	54 x 6	18 x 6	6 x 178	
	324 x 624	108 x 12	36 x 12	12 x 356	
3.0	81 x 143	27 x 3	9 x 3	3 x 57	0.69
	162 x 286	54 x 6	18 x 6	6 x 114	
	324 x 572	108 x 12	36 x 12	12 x 228	
4.0	81 x 163	27 x 3	9 x 3	3 x 40	0.707
	162 x 326	54 x 6	18 x 6	6 x 80	
	324 x 652	108 x 12	36 x 12	12 x 160	
5.0	81 x 143	27 x 3	9 x 3	3 x 31	0.72
	162 x 286	54 x 6	18 x 6	6 x 62	
	324 x 572	108 x 12	36 x 12	12 x 124	
6.0	81 x 156	27 x 3	9 x 3	3 x 24	0.73
	162 x 312	54 x 6	18 x 6	6 x 48	
	324 x 624	108 x 12	36 x 12	12 x 96	
7.0	81 x 166	27 x 3	9 x 3	3 x 19	0.74
	162 x 332	54 x 6	18 x 6	6 x 38	
	324 x 664	108 x 12	36 x 12	12 x 76	
8.0	81 x 153	27 x 3	9 x 3	3 x 16	0.745
	162 x 306	54 x 6	18 x 6	6 x 32	
	324 x 612	108 x 12	36 x 12	12 x 64	
9.0	81 x 161	27 x 3	9 x 3	3 x 13	0.755
	162 x 322	54 x 6	18 x 6	6 x 26	
	324 x 644	108 x 12	36 x 12	12 x 52	
10.0	81 x 156	27 x 3	9 x 3	3 x 11	0.762
	162 x 312	54 x 6	18 x 6	6 x 22	
	324 x 624	108 x 12	36 x 12	12 x 44	

where ν_j is computed from equation (181).

Numerically, we implement the nonuniform mesh TRT-LBE to simulate the molecular Couette flow with Knudsen number $1.0 \leq k \leq 10.0$. The mesh sizes and the parameter β indicating the fraction of bounce back boundary condition are tabulated in Table 47. For each value of Knudsen number k, we implemented three TRT-LBE simulations, respectively, on three nonuniform meshes with basic, doubled and qudrupled mesh sizes, in order to show the grid convergence of our simulation.

Figure 40-44 show the comparison of the streamwise velocity profiles (left) and the comparison of the density profiles (right) for various Knudsen numbers: from the 1D wall-gas interaction TRT-LBE simulation with different nonuniform mesh given in Table 47, the MD simulation and the high precision solution of the integral equations for velocity.

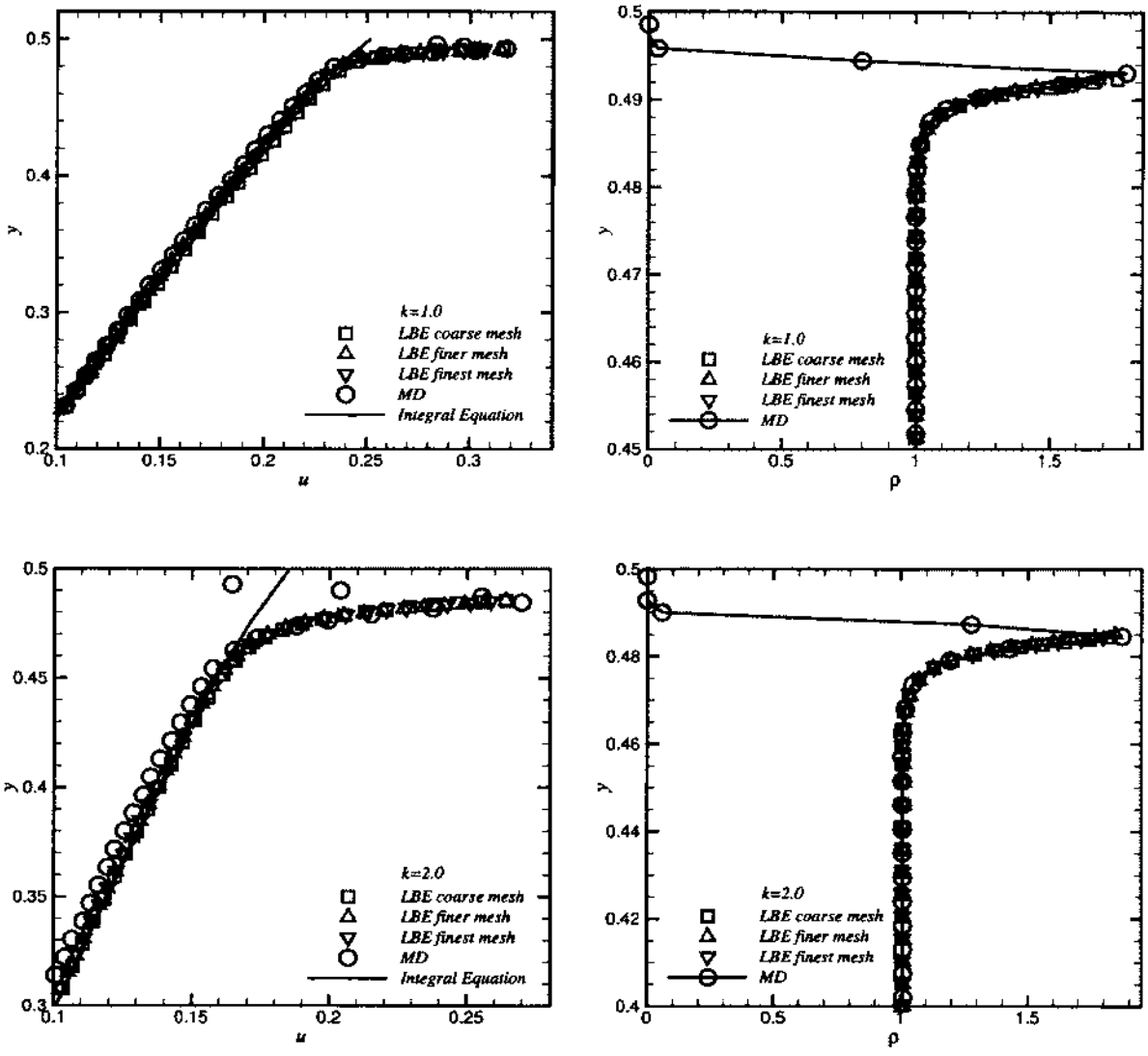

FIG. 40: Comparison of the streamwise velocity profiles (left) and the comparison of the density profiles (right) for Knudsen number $k = 1$ and 2: from the 1D wall-gas interaction TRT-LBE simulation with different nonuniform mesh given in Table 47, the MD simulation and the high precision solution of the integral equations for velocity.

From Figure 40-44, we see the 1D wall-gas interaction TRT-LBE simulations with three different meshes almost overlap. Hence, our LBE simulation is convergent. For all values of Knudsen number k that we have implemented simulations, the density profiles from LBE simulations match well with the corresponding MD simulation.

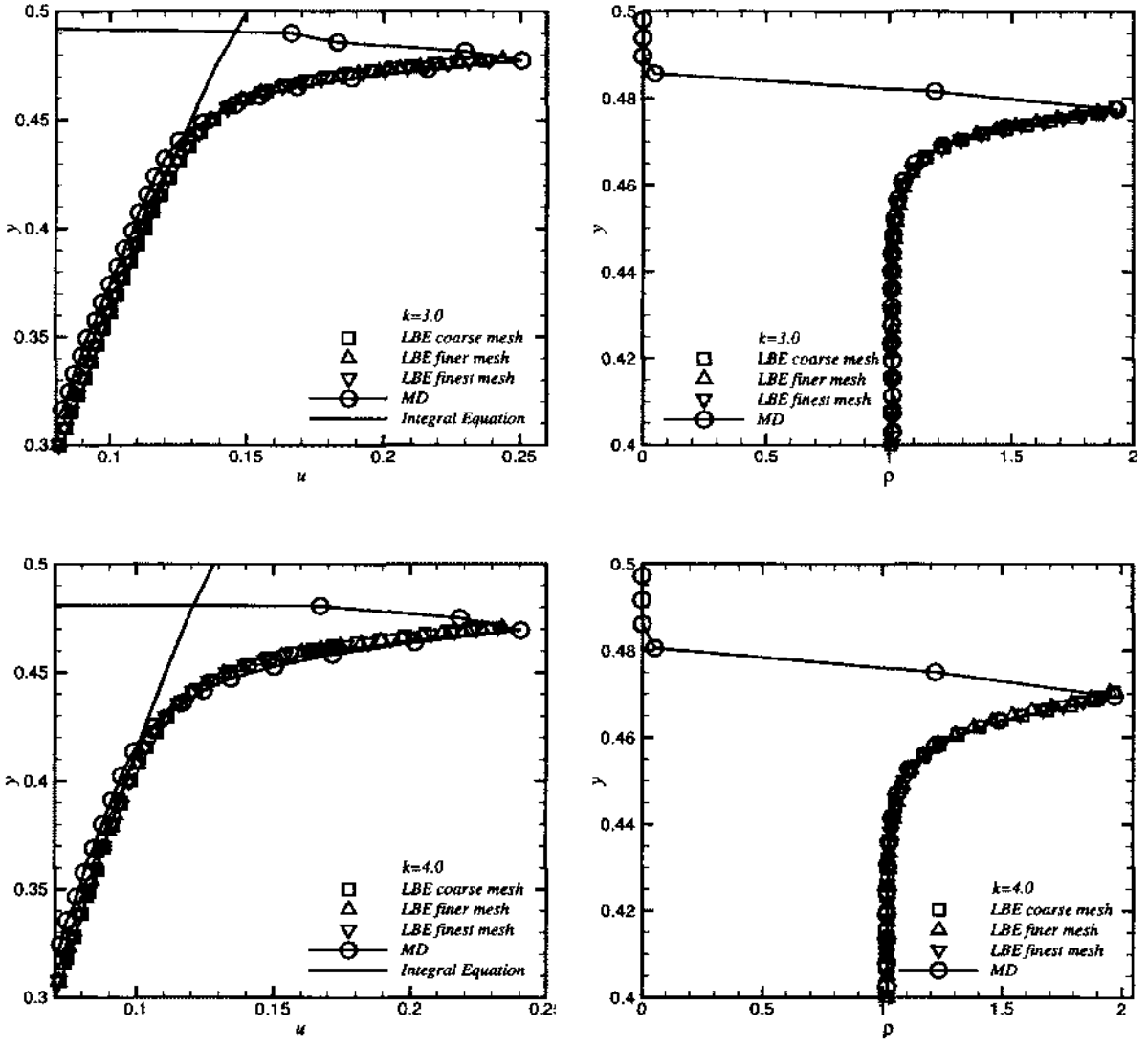

FIG. 41: Comparison of the streamwise velocity profiles (left) and the comparison of the density profiles (right) for Knudsen number $k = 3$ and 4: from the 1D wall-gas interaction TRT-LBE simulation with different nonuniform mesh given in Table 47, the MD simulation and the high precision solution of the integral equations for velocity.

The streamwise velocity profiles from LBE simulation also show very good agreement with that of the MD simulation in both the bulk flow region and the near wall region. However, when the Knudsen number $k \geq 7.0$, the streamwise velocity in the near wall region is a little off the velocity profile of the corresponding MD simulation.

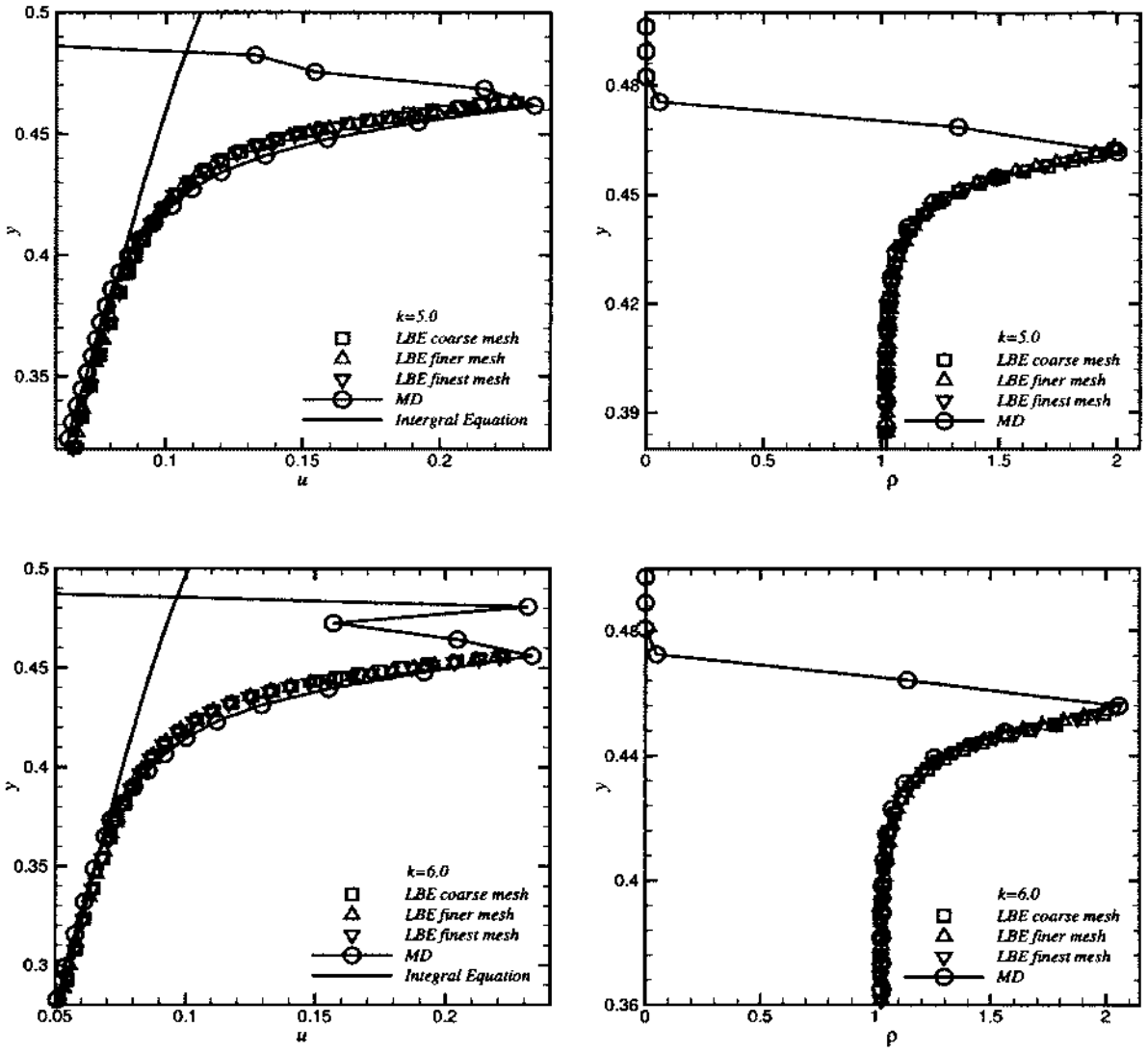

FIG. 42: Comparison of the streamwise velocity profiles (left) and the comparison of the density profiles (right) for Knudsen number $k = 5$ and 6: from the 1D wall-gas interaction TRT-LBE simulation with different nonuniform mesh given in Table 47, the MD simulation and the high precision solution of the integral equations for velocity.

This is in accordance with the fitting model of the velocity, which shows that a more accurate model for velocity is desirable in our future work.

A better near wall forcing model than the 1D wall-gas interaction is the 2D wall-gas interaction which also takes the stream-wise component of the wall-gas interaction

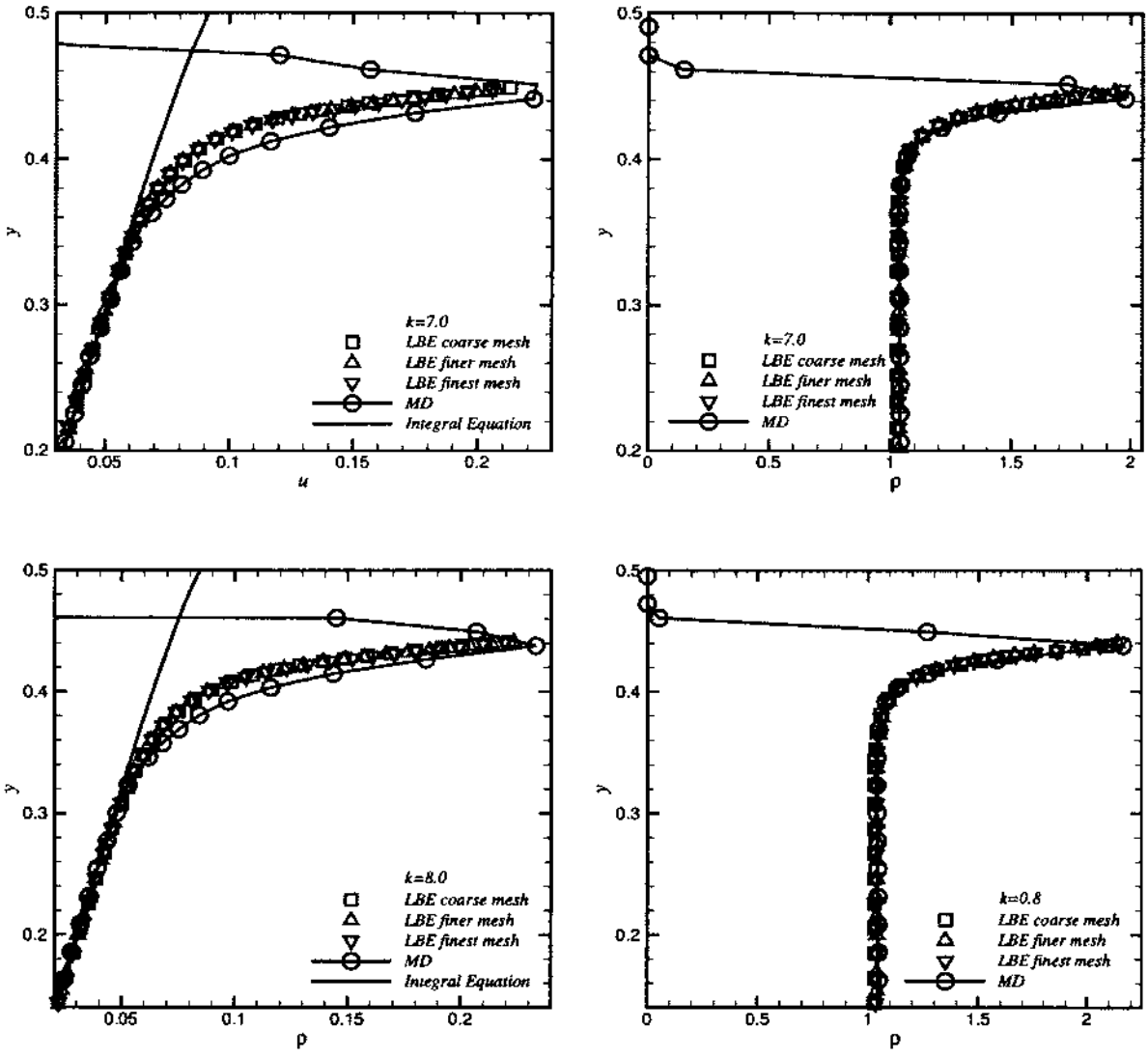

FIG. 43: Comparison of the streamwise velocity profiles (left) and the comparison of the density profiles (right) for Knudsen number $k = 7$ and 8: from the 1D wall-gas interaction TRT-LBE simulation with different nonuniform mesh given in Table 47, the MD simulation and the high precision solution of the integral equations for velocity.

into account. Since the wall molecules are moving in the streamwise direction, the wall-gas interaction is time dependent. However, we will not compute the wall force field at each and every time step, because such computation is highly time consuming. Our tack is that we choose an appropriate upper wall speed U_w such that after

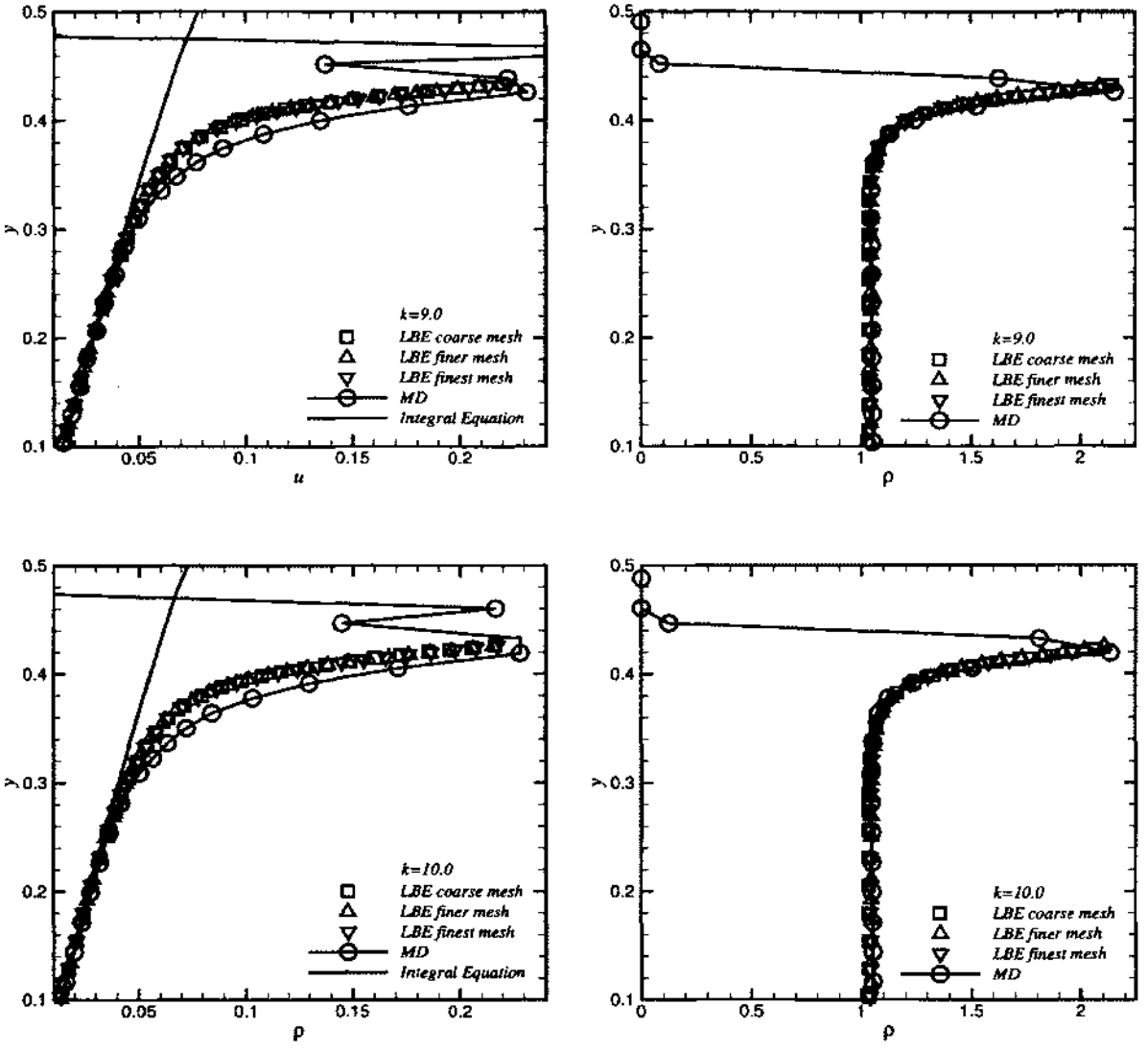

FIG. 44: Comparison of the streamwise velocity profiles (left) and the comparison of the density profiles (right) for Knudsen number $k = 9$ and 10: from the 1D wall-gas interaction TRT-LBE simulation with different nonuniform mesh given in Table 47, the MD simulation and the high precision solution of the integral equations for velocity.

N_t time steps every wall molecule has moved exactly one LBE grid length. By doing so, the wall motion is temporally periodical with period MN_t. Then, the 2D wall-gas interaction is also periodic with the same temporal period. The wall velocity U_w is

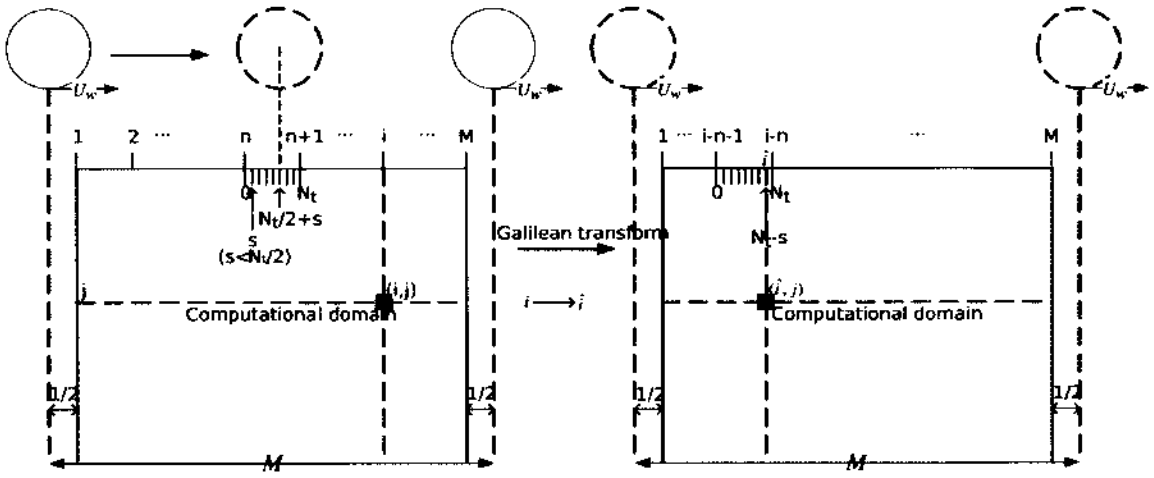

FIG. 45: The Galilean transform of a grid point in the LBE with 2D wall-gas interaction

computed as:

$$U_w = \frac{l}{MN_t\delta_t} = \frac{1}{N_t}.$$

Using the periodicity, it suffices that we just compute the wall force field MN_t times for different wall molecule positions. However, it is not necessary. We compute the 2D wall-gas interaction only once at initialization and store it for later use. We denote by $\boldsymbol{a}_{\rm net}(x,y)$ the accelaration at coordinate (x,y) deduced by net Lennard-Jones force of the thirteen molecules at $t=0$. Then, on grid point (i,j), $\boldsymbol{a}_{\rm net}(x,y)$ is modified as:

$$\tilde{\boldsymbol{a}}_{i,j} = \boldsymbol{a}_{\rm net}((i-1/2)\delta_x,(j-1)\delta_x)\delta_x V_{10,6}(C_w)/V_1(y_p),\ 1\le i\le M,\ j_0\le j\le N \quad (185)$$

where $j_0 = N - \lfloor (3\sigma - C_w)/\delta_x \rfloor - 1$.

By using the Galilean transform [49] (Page 6) and interpolation of $\tilde{\boldsymbol{a}}_{i,j}$, we are able to compute the 2D wall-gas interaction at any time step on each and every grid point. Figure 45 illustrates how we use the Galilean transform.

Assume that two adjacent wall molecules are initially ($t=0$) located at the position on the left side of Figure 45 and we have computed the wall force on every grid point at $t=0$. We explain the method we use to compute the wall force deduced accelaration applied on a grid point at time t, which is initially located at the grid (i,j) in the left side coordinate system at $t=0$. After $t = nN_t + s$ steps, as shown in

Figure 45, the left wall molecule has moved to the position of the dashed molecule. So, at time $t = nN_t + s$, we can translate the spatial coordinate to the right side of Figure 45, where the previous grid (i, j) becomes $(\hat{i}, j)$. We need to determine, in the right coordinate system, which two grid points are the closest left (i_l, j) and the closest right (i_r, j) neighbors of $(\hat{i}, j)$. Meanwhile, what is the ratio α of the distance from (i_l, j) to $(\hat{i}, j)$ to the distance from (i_l, j) to (i_r, j). The answers to these two questions are

$$i_r = \begin{cases} i - \hat{n} + M, & i \leq \hat{n}, \\ i - \hat{n}, & i > \hat{n}, \end{cases}$$

$$i_l = \begin{cases} i_r - 1, & i_r > 1, \\ M, & i_r = 1, \end{cases}$$

$$\alpha = \frac{s}{N_t},$$

where $\hat{n} \equiv n (\mathrm{mod}\, M)$ and $0 \leq \hat{n} < n$. Hence, the time dependent acceleration is computed as

$$\tilde{\boldsymbol{a}}_{i,j}(t) = (1 - \alpha)\tilde{\boldsymbol{a}}_{i_l,j} + \alpha\tilde{\boldsymbol{a}}_{i_r,j}.$$

Numerically, we implement the nonuniform mesh TRT-LBE with 2D wall-gas interaction to simulate the molecular Couette flow with Knudsen number $1.0 \leq k \leq 10.0$. We use the coarse meshes that are tabulated in Table 47. The parameter β indicating the fraction of bounce back boundary condition are the same as in the TRT-LBE simulation with 1D wall-gas interaction.

Figure 46-50 shows the comparison of the streamwise velocity profiles (left) and the comparison of the density profiles (right) for various Knudsen numbers: from the 2D wall-gas interaction TRT-LBE simulation at three positions (left $x = l/6$, center $x = l/2$ and right $x = 5l/6$) along x-axis, the MD simulation and the high precision solution of the integral equations for velocity.

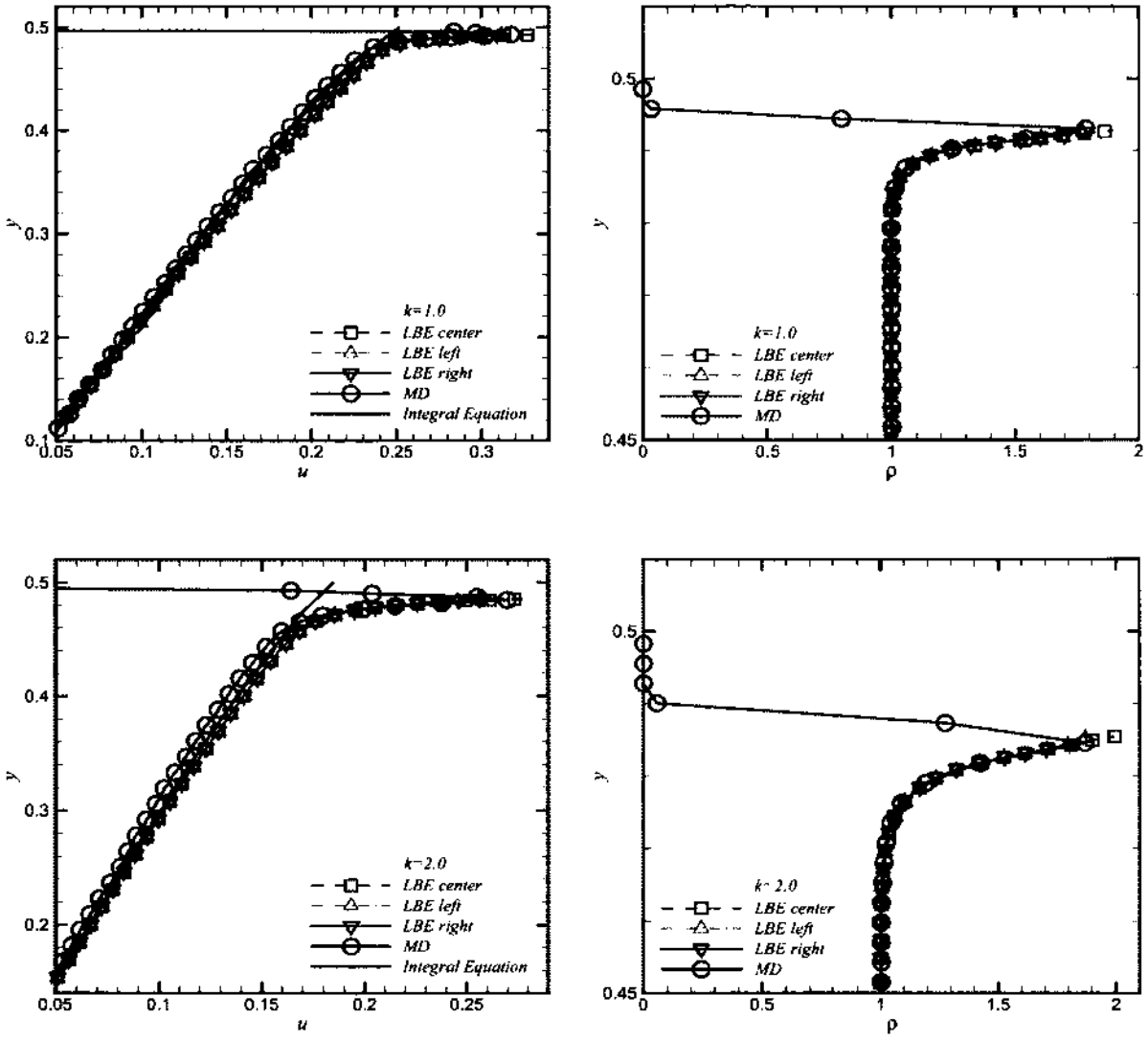

FIG. 46: Comparison of the streamwise velocity profiles (left) and the comparison of the density profiles (right) for Knudsen number $k = 1$ and 2: from the 2D wall-gas interaction TRT-LBE simulation at three positions (left $x = l/6$, center $x = l/2$ and right $x = 5l/6$) along x-axis, the MD simulation and the high precision solution of the integral equations for velocity.

From Figure 46-50, we see the 2D wall-gas interaction LBE-TRT simulations only have a slight difference to the corresponding 1D wall-gas interaction LBE-TRT simulations. Both the streamwise velocity profiles and the density profiles at $x = l/6$

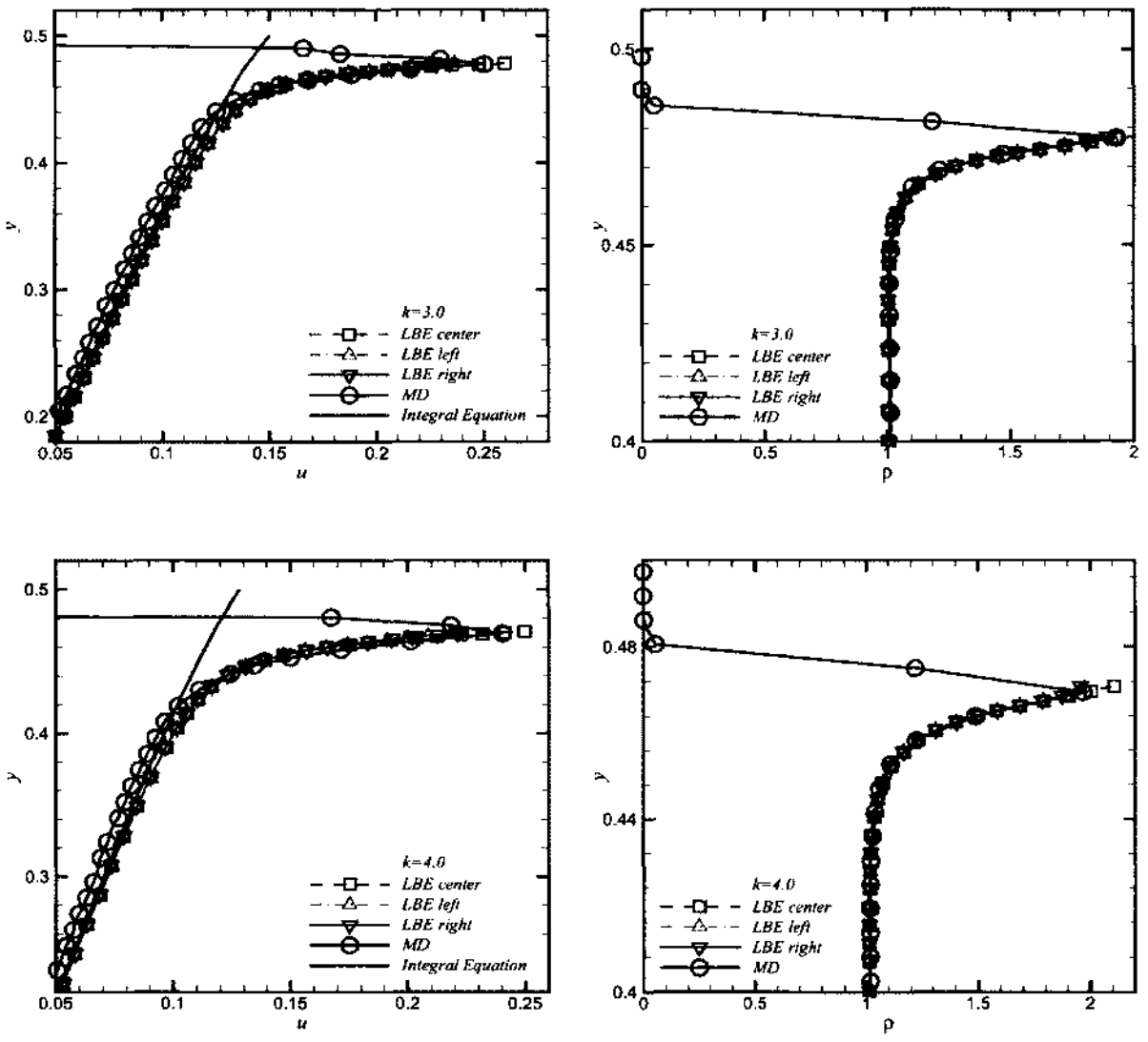

FIG. 47: Comparison of the streamwise velocity profiles (left) and the comparison of the density profiles (right) for Knudsen number $k = 3$ and 4: from the 2D wall-gas interaction TRT-LBE simulation at three positions (left $x = l/6$, center $x = l/2$ and right $x = 5l/6$) along x-axis, the MD simulation and the high precision solution of the integral equations for velocity.

(left) and $x = 5l/6$ (right) overlap and are lower than the corresponding MD peak values at the peak position. At $x = l/2$ (center), both the streamwise velocity profiles and the density profiles have an overshoot with respect to the MD peaks at the peak

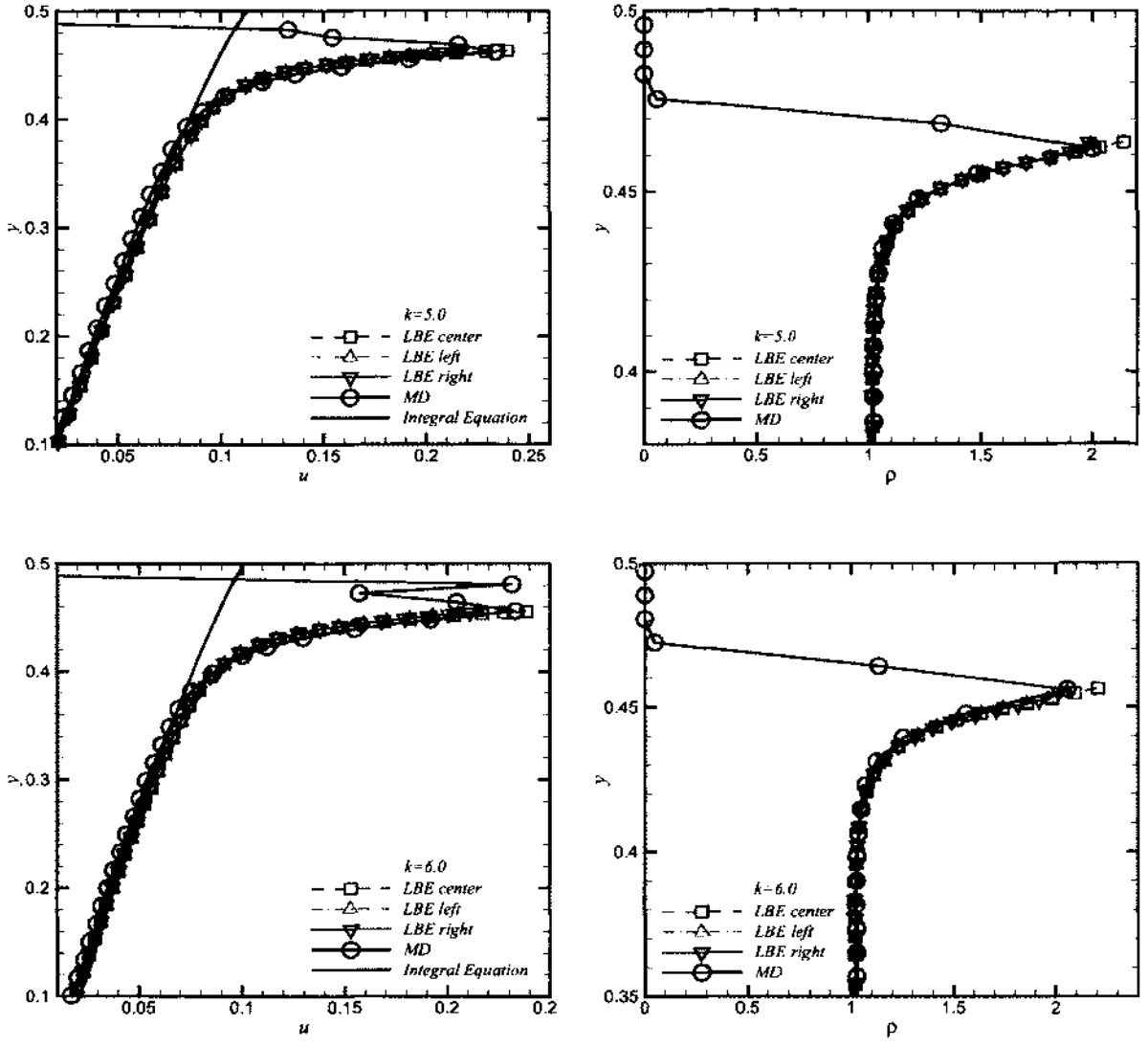

FIG. 48: Comparison of the streamwise velocity profiles (left) and the comparison of the density profiles (right) for Knudsen number $k = 5$ and 6: from the 2D wall-gas interaction TRT-LBE simulation at three positions (left $x = l/6$, center $x = l/2$ and right $x = 5l/6$) along x-axis, the MD simulation and the high precision solution of the integral equations for velocity.

position.

It should be mentioned that we use the same machine to run our codes for TRT-LBE

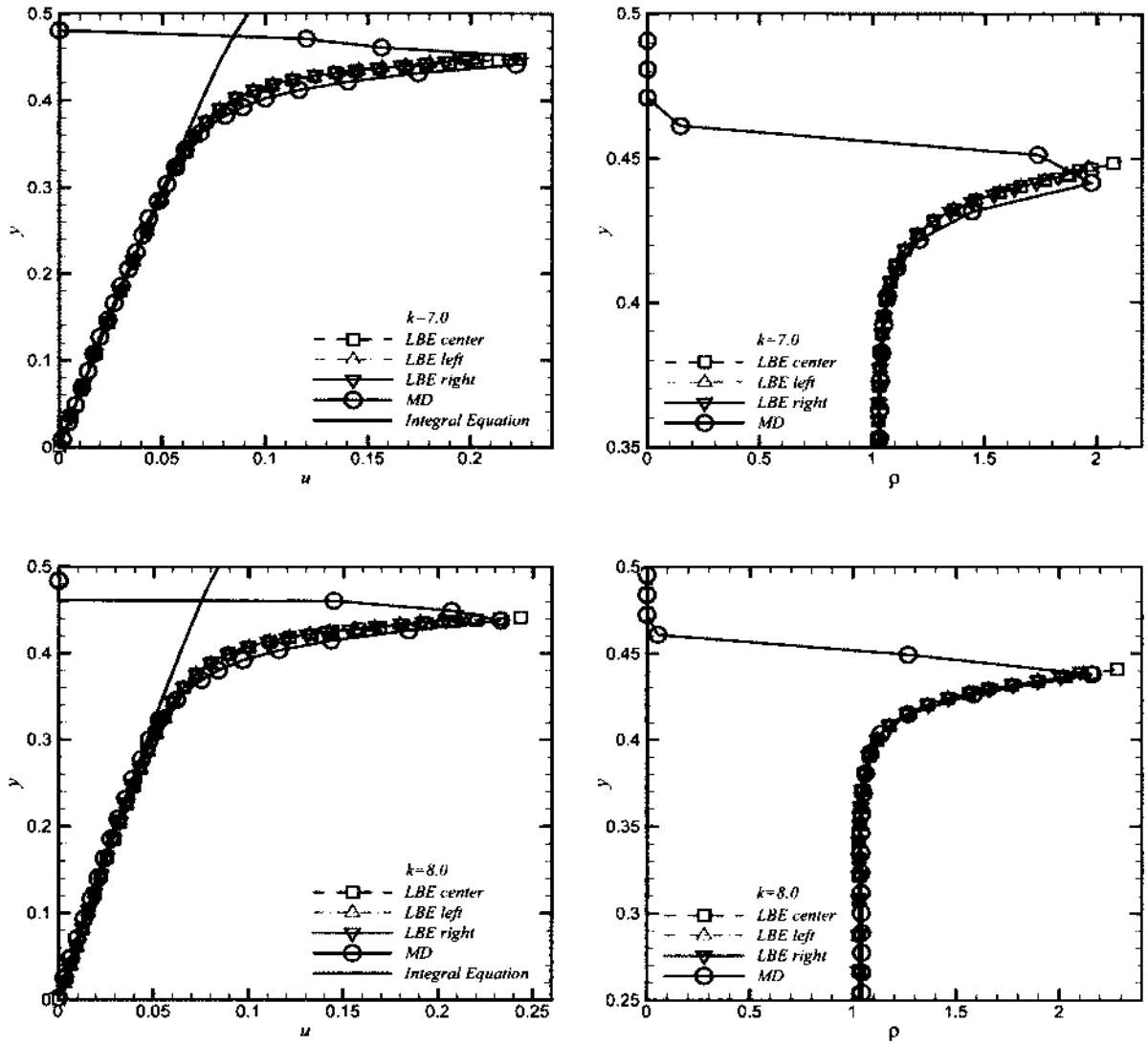

FIG. 49: Comparison of the streamwise velocity profiles (left) and the comparison of the density profiles (right) for Knudsen number $k = 7$ and 8: from the 2D wall-gas interaction TRT-LBE simulation at three positions (left $x = l/6$, center $x = l/2$ and right $x = 5l/6$) along x-axis, the MD simulation and the high precision solution of the integral equations for velocity.

simulation with 1D and 2D wall-gas interactions as we have run LAMMPS. The simulating times of the 1D wall-gas interaction TRT-LBE simualtions with three sets of nonuniform mesh, the 2D wall-gas interaction TRT-LBE simulations with the coarse

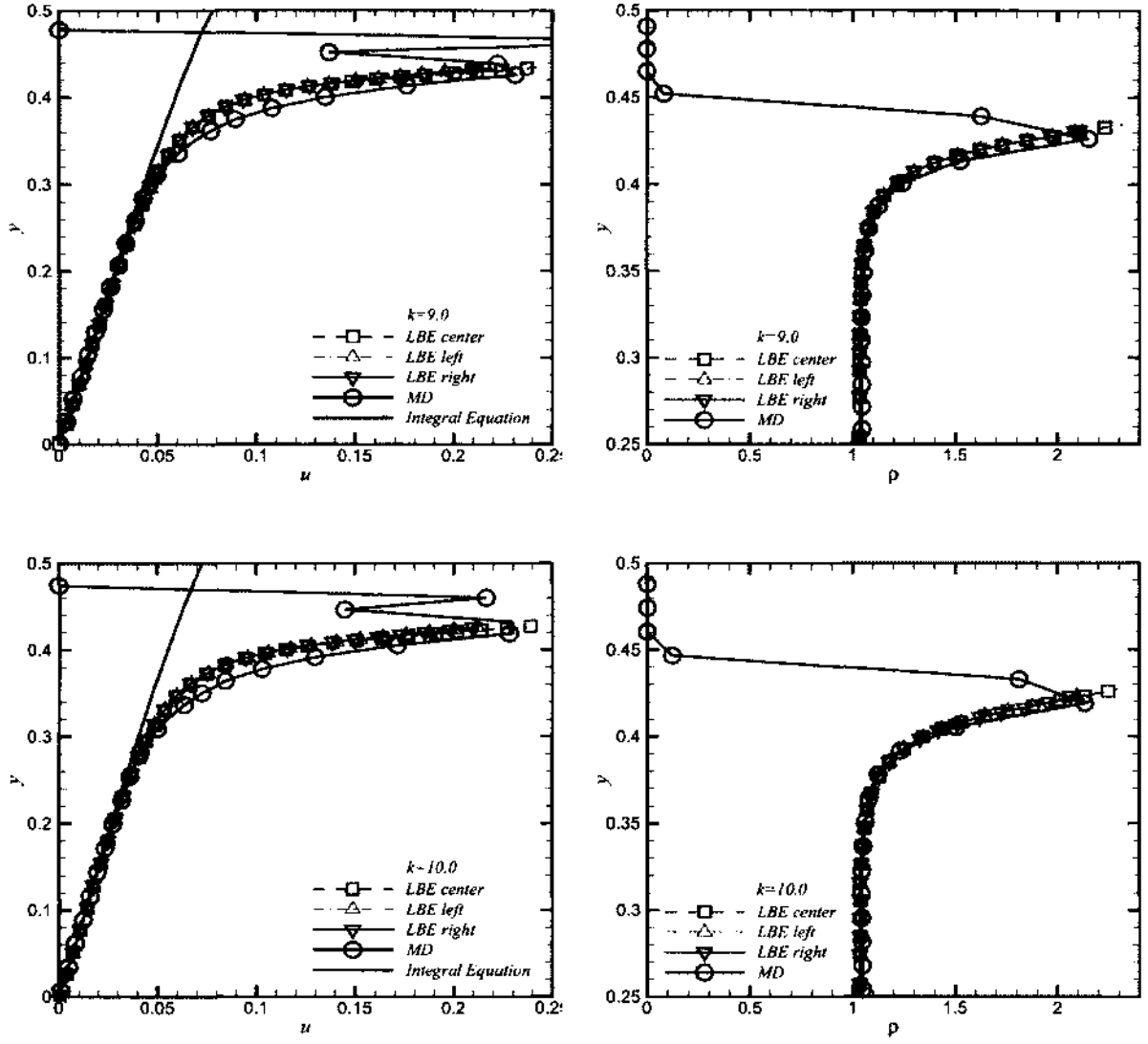

FIG. 50: Comparison of the streamwise velocity profiles (left) and the comparison of the density profiles (right) for Knudsen number $k = 9$ and 10: from the 2D wall-gas interaction TRT-LBE simulation at three positions (left $x = l/6$, center $x = l/2$ and right $x = 5l/6$) along x-axis, the MD simulation and the high precision solution of the integral equations for velocity.

nonuniform mesh and the MD simulations are compared and tabulated in Table 48.

From Table 48, we see the TRT-LBE simulations with 1D wall-gas interaction in the finest nonuniform mesh are over one hundred times faster than the corresponding

TABLE 48: The simulating times (in seconds) of the 1D wall-gas interaction TRT-LBE simualtions with three sets of nonuniform mesh, the 2D wall-gas interaction TRT-LBE simulations with the coarse nonuniform mesh and the MD simulations

k	corase mesh (1D)	corase mesh (2D)	finer mesh (1D)	finest mesh (1D)	MD
1.0	53.50	35.64	239.57	862.21	132012
2.0	48.78	28.28	198.16	762.20	124406
3.0	36.14	25.89	226.18	766.39	122045
4.0	49.74	24.13	248.27	767.21	134353
5.0	81.40	27.27	225.56	774.78	224641
6.0	61.47	26.49	214.03	771.98	250251
7.0	74.28	23.44	207.47	777.16	222935
8.0	69.66	24.92	263.15	786.08	365924
9.0	36.80	26.93	179.54	776.56	364996
10.0	62.22	25.53	202.30	757.50	326142

MD simulations. The TRT-LBE simulations with 2D wall-gas interaction are even faster than the corresponding LBE simulations with 1D wall-gas interaction. This may be because the 2D wall-gas interaction model is more compatible with the effective viscosity, which accelarates the convergence.

CHAPTER 6

CONCLUSION

We first summarize the thesis and then discuss future work as an extension of this thesis.

In Chapter two, we deduced a detailed derivation of the integral equations for velocity with arbitrary accommodation ratio at the boundary from the BGK equation for the harmoneous-oscillating Couette flow problem, the Kramers problem and the planar Poiseuille flow problem. The integral equation for the oscillating Couette flow contains four parameters: the Knudsen number k, the normalized relaxation time τ and the accomodation ratio $\alpha^{\pm}$ at the upper and lower walls, repectively. The integral equation for the Kramers problem has only one parameter, the accommodation ratio α at the wall. The integral equation for planar Poiseuille flow has three parameters: the Kunsen number k and the accomodation ratio $\alpha^{\pm}$ at the upper and lower walls. These derived integral equations provide relatively simpler and high quality models for studying the velocities and stresses of rarified isothermal shear driven flows and pressure gradient driven flows, which take Maxwell type boundary condition into account.

In Chapter three, we use two methods to solve the integral equations derived in Chapter two with high precision. The first method is our Chebyshev collocation method. The main idea of this method is to use two truncated Chebyshev series to approximate the solution of the integral equation. The first series is an approximation of the solution in the bulk region. The other series is an approximation of the solution in the near boundary regions. By using a subset of the Chebyshev collocation points, we substitute the first truncated Chebyshev expansion at the chosen collocation points into the integral equation to derive a linear system for the coefficients of the Chebyshev expansion. Solving the linear system, we obtain a solution to the integral equation in the bulk region. Due to the boundary singularities of the solution, this solution is not as accurate near the boundary as it is in the bulk region. To improve the rate of convergence of the solution at the boundaries, we introduce another truncated Chebyshev series to approximate the solution near the

boundaries. We use the Chebyshev collocation method to solve the integral equation for the steady Couette flow problem with purely diffusive boundary condition. The error analysis is given. Our solutions for various Knudsen numbers are shown to have at least 11 digits of precision. The second method is the chunk based collocation method. This method, instead of cutting the whole domain into the bulk region and the near boundary region, divides the domain into many more nonuniform subintervals with finer subintervals near the pre-estimated singularities. On each of the subintervals, the solution of the corresponding integral equation is approximated by a low degree Gauss-Legendre expansion. We choose Gauss-Legendre collocation points of corresponding degree on each subinterval and then substitute the piecewise Gauss-Legendre expansions at the chosen collocation points into the integral equation to derive a linear system for the expansion coefficients for all subintervals. We do not directly solve this linear system, instead, we implement a linear transform to convert the linear system for the expansion coefficients into a linear system for the solutions on all collocation points. The converted linear system is a strong diagonal dominant dense linear system, which is solved efficiently by the generalized minimal residual (GMRES) algorithms with high precision. The expansion coefficients on each subinterval is obtained by using inverse linear transform and the solution at an arbitrary position is evaluated easily. We use the chunk base collocation method to solve the integral equations for the steady Couette flow problem and the planar Poiseuille flow problem with a wide range of Knudsen numbers and the Kramers problem with various accommodation ratios at the upper and the lower walls. The error analysis is given. Our solution of the integral equations have at least 13 digits of precision.

In Chapter four, we analyze the velocity profile of the steady Couette flow problem with purely diffusive boundary condition at the upper wall and the lower wall. We derive an approximation of the velocity in terms of Abramowitz functions of order 0 and order 1. We compute the L_2 error of the approximation and compute the shear stress from the approximated solution. We reproduce Cercignani's variational approach for the linear and the cubic approximation of the velocity and find out typoes in their results. We derive a fifth degree approximation of the velocity by using a variational approach. We compare the errors of the linear, cubic and the fifth degree approximation of the velocity in term of the procision in computing the shear stress.

The comparison shows cubic approximation is an effective and cheaper approximation. We derive two more cubic approxiamtions to the velocity, one by fixing the coefficient of the linear term and fitting the cubic coefficient, the other by fixing both the linear and cubic coefficients according to accurate shear stress and half channel mass flow rate. The L_2 errors the two cubic approximation are also computed. We analyze the Knudsen number dependent velocity defect, slip velocity and half channel mass flow rate. By using least square fitting and the asymptotic behaviors of Abramowitz functions of order $-1, 0, 1$ and 2, we derive several approximations of the velocity defect, the microscopic slip velocity and the macroscopic slip velocity, and the half channel mass flow rate in terms of functions of the Knudsen number k. The fitting errors of these approximations are all discussed, showing the good performances of these approximations. The analysis of the velocity profile of the steady Couette flow gives insights into the Knudsen layer of the shearing flows, which can be used to remodel the rarefied shear flows in a Navier-Stokes framework. We show a simple example of how we use one of the velocity approximations to model the effective viscosity in the Navier-Stokes equation. By solving this Navier-Stokes equation one can reproduce the velocity profile. We validate this idea by using lattice Boltzmann equation with Dirichlet boundary condition to solve the Navier-Stokes equation with effective viscostiy.

In Chapter five, we implement the molecular dynamics simulation of the planar steady gaseous Couette flow in micro channels with Knudsen number ranging from 1.0 to 10.0 by using the open source package LAMMPS [18]. We model the streamwise velocity profiles and the density profiles from the MD simualtions. By using the same wall-gas interaction as MD simulation and the effective viscosity derived from our velocity and density models, we reconsider the molecular Couette flow in the Navier-Stoke equation framework. We use nonuniform mesh TRT-LBE simulation [48] with diffusive and speculative reflection combined boundary condition to solve the Navier-Stokes equation with one dimensional wall-gas interaction and two dimensional wall-gas interaction, respectively. The produced velocity profiles and the density profiles show convincing agreement in the bulk region with the high precision solution of the integral equation with purely diffusive boundary condition, and in both the bulk region and the near wall attractive wall-gas interaction region with the MD simulation.

In Chapter two, we derived the integral equation for the harmoneous-oscillating Couette flow. However, we haven't solved the integral equation numerically. This is because, at the moment, we are not able to precisely evaluate the Abramowitz function with the argument in the fourth quadrant of the complex plane. Specifically, we recall the integral equation for the harmoneous-oscillating Couette flow with pure diffusive boundary condition:

$$\begin{aligned} u(y)-&\frac{1}{\pi^{1/2}k}\int_{-1/2}^{1/2} u(s)I_{-1}\left(\frac{1-i\tau}{k}|y-s|\right)\mathrm{d}s \\ =&\frac{1}{2\pi^{1/2}}\left[I_0\left(\frac{1-i\tau}{k}(1/2-y)\right)-I_0\left(\frac{1-i\tau}{k}(y+1/2)\right)\right],\ y\in[-1/2,1/2]. \end{aligned}$$

To solve this equation, we need to evaluate the Abramowitz functions I_n with complex argument $z=x-yi,(x,y>0)$ precisely. These Abramowitz functions have complex values and can be split into a real part and an imaginary part:

$$I_n(z)=I_n(x-yi)=A_n(x,y)+iB_n(x,y),$$

where

$$\begin{aligned} A_n(x,y)&=\int_0^\infty t^n e^{-t^2-x/t}\cos(y/t)\,\mathrm{d}t, \\ B_n(x,y)&=\int_0^\infty t^n e^{-t^2-x/t}\sin(y/t)\,\mathrm{d}t. \end{aligned}$$

Due to the oscillating terms $\cos(y/t)$ and $\sin(y/t)$, the real part $A_(x,y)$ and the imaginary part $B_n(x,y)$ are hard to approximate. In the future, we are going to study high precision approximation of $A_n(x,y)$ and $B_n(x,y)$. Up to know, we have known, for fixed value of y, $A_n(x,y)$ and $B_n(x,y)$ are the solutions to the regular singular IVP in x,

$$\begin{aligned} xA_n'''+yB_n'''-A_n''+2A_n&=0, \\ xB_n'''-yA_n'''-B_n''+2B_n&=0, \end{aligned} \tag{186}$$

subject to the initial conditions,

$$A_n(0,y) = \int_0^\infty t^n e^{-t^2} \cos(y/t)\,\mathrm{d}t,$$
$$B_n(0,y) = \int_0^\infty t^n e^{-t^2} \sin(y/t)\,\mathrm{d}t,$$
$$A'_n(0,y) = -A_{n-1}(0,y) = -\int_0^\infty t^{n-1} e^{-t^2} \cos(y/t)\,\mathrm{d}t,$$
$$B_n(0,y) = -B_{n-1}(0,y) = -\int_0^\infty t^{n-1} e^{-t^2} \sin(y/t)\,\mathrm{d}t,$$
$$A''_n(0,y) = A_{n-2}(0,y) = \int_0^\infty t^{n-2} e^{-t^2} \cos(y/t)\,\mathrm{d}t,$$
$$B''_n(0,y) = B_{n-2}(0,y) = \int_0^\infty t^{n-2} e^{-t^2} \sin(y/t)\,\mathrm{d}t.$$

The initial conditions are discuss by Kruse *et al* [21]. We can use Macleod's [1] method of Chebyshev expansion to obtain the initial values. However, we still need a substantial breakthrough to precisely solve the system of Equation (186).

In Chapter five, we use the TRT-LBE simulation with bounce back speculative reflection combined boundary condition to reproduce the density profiles and streamwise velocity profiles of the steady Molecular Couette flows with Knudsen number $1.0 \leq k \leq 10.0$. The accommodation ratio β indicating the fraction of bounce back for cases of different Knudsen numbers are obtained by trial and error. We are going to discover the relationship between the Knudsen number and the accommodation ratio in the future.

As a more challenging future work, we plan to implement high quality molecular dynamics simulations for the molecular planar Poiseuille flow with a wide range of Knudsen numbers. This is a body force driven flow. The magnitude of the force added to each molecule at every time step and time step size need to be chosen delicately. The main difficulty of the MD simulation is that the rarity of the flow makes the system hard to relax to equilibrium. When we obtain quality MD data for the molecular planar Poiseuille flow, we are going to model the density profiles and the velocity profiles of the flow. Then, we can discuss the molecular plannar Poiseuille flow in the Navier Stokes equation framework by modeling the corresponding stress tensor according to the modeled density profiles and velocity profiles. Finally, we will reproduce the density and the velocity of the molecular planar Poiseuille flow by LBE simulation. The study of molecular planar Poiseuille flows will give us insights into the Knudsen layer of body force driven flow in microscale channnels.

BIBLIOGRAPHY

[1] Macleod AJ. Chebyshev expansion for Abramowitz functions. Appl Numer Math 1992;10:129-37.

[2] Abramowitz M, Stegun IA, editors. Handbook of mathematical functions with formulas, graphs, and mathematical tables. Washington, DC: National Bureau of Standards; 1964.

[3] Lether F. On the construction of Gauss-Legendre quadrature rules. J Comput Appl Math 1978;4(1):47-52.

[4] Cercignani C. Rarefied gas dynamics: from basic concepts to actual calculations. Cambridge, UK: Cambridge University Press; 2000.

[5] Cercignani C. The Kramers problem for a not completely diffusing wall. J Math Anal Appl 1965;10:568-86.

[6] Loyalka SK, Tompson RV. The velocity slip problem: accurate solutions of the BGK model integral equation. Eur J Mech B/Fluids 2009;28:211-13.

[7] Cercignani C, Pagani CD. Variational approach to boundary-value problems in kinetic theory. Phys Fluids 1966;9:1167-73.

[8] Gross EP, Jackson EA, Ziering S. Boundary value problems in kinetic theory of gases. Ann Phys 1957;1:141-67.

[9] Gibelli L. Velocity slip coefficients based on the hard-sphere Boltzmann equation. Phys Fluids 2012;24:022001.

[10] Einzel D, Panzer P, Liu M. Boundary condition for fluid flow: curved or rough surfaces. Phys Rev Lett 1990;64:2269-72.

[11] Lockerby DA, Reese JM, Emerson DR, Barber RW. Velocity boundary condition at solid walls in rarefied gas calculations. Phys Rev E 2004;70:017303.

[12] O'Hare L, Lockerby DA, Reese JM, Emerson DR. Near-wall effects in rarefied gas micro-flows: some modern hydrodynamic approaches. Int J Heat Fluid Flow 2007;28:37-43.

[13] Cercignani C, Lorenzani S. Variational derivation of second-order slip coefficients on the basis of the Boltzmann equation for hard-sphere molecules. Phys Fluids 2010;22:062004.

[14] Zhang WM, Meng G, Wei X. A review on slip models for gas microflows. Microfluid Nanofluid 2012;13:845-82.

[15] Guo ZL, Qin JH, Zheng CG. Generalized second-order slip boundary condition for nonequilibrium gas flows. Phys Rev E 2014;89:013021.

[16] Lockerby DA, Reese JM, Gallis MA. The usefulness of high-order constitutive relations for describing the Knudsen layer. Phys Fluids 2005;17:109902.

[17] Ginzburg I, d'Humières D. Multireflection boundary conditions for lattice Boltzmann models. Phys Rev E 2003;68:066614.

[18] Plimpton SJ. Fast parallel algorithms for short-range molecular dynamics. J Comp Phys 1995;117:1-19.

[19] Magda JJ, Tirrell M, Davis HT. Molecular dynamics of narrow, liquid-filled pores. J Chem Phys 1985;83:1888.

[20] Guo ZL, Zheng CG. Analysis of lattice Boltzmann equation for microscale gas flows: relaxation times, boundary conditions and the Knudsen layer. Int J Comput Fluid Dyna 2008;22:465-73.

[21] Kruse UE, Ramsey NF. The integral $\int_0^\infty y^3 \exp\left(-y^2 + i\frac{x}{y}\right) \mathrm{d}y$. J Math Phys 1951;30:40.

[22] Fujikawa S, Yano T, Watanabe M. Vapor-liquid interfaces, bubbles and droplets. Berlin Heidelberg, New York: Springer-Verlag; 2011.

[23] Bhatnagar PL, Gross EP, Krook M. A model for collision processes in gases. I. small amplitude processes in charged and neutral one-component systems. Phys Rev 1954;94(3):511-25.

[24] Sone Y, Takata S, Ohwada T. Numerical analysis of the plane Couette flow of a rarefied gas on the basis of the linearized Boltzmann equation for hard-sphere molecules. Eur J Mech B/Fluids 1990;9(3):273-88.

[25] Siewert CE. Generalized boundary conditions for the S-model kinetic equations basic to flow in a plane channel. J Quant Spectros Radiat Transfer 2002;72:75-88.

[26] Williams MMR. Boundary-value problems in the kinetic theory of gases Part I. slip flow. J Fluid Mechs 1969;36:145-59.

[27] Siewert CE. Poiseuille, thermal creep and Couette flow: results based on the CES model of the linearized Boltzmann equation. Eur J Mech B/Fluids 2002;21(5):579-97.

[28] Maxwell JC. On stresses in rarefied gases arising from inequalities of temperature. Phil Trans Roy Soc London 1879;170:Appendix 231-56.

[29] Cercignani C, Lampis M. Kinetic model for gas-surface interaction. Transp Theory Stat Phys 1971;1:101-14.

[30] Cercignani C. Plane Couette flow according to the method of elementary solutions. J Math Anal Appl 1965;11:93-101.

[31] Cercignani C. The method of elementary solutions for kinetic models with velocity-dependent collision frequency. Ann Phys 1966;40:469-81.

[32] Willis DR. Comparison of kinetic theory analyses of linearized Couette flow. Phys Fluids 1962;5:127-135.

[33] Loyalka SK, Petrellis N, Storvick TS. Some exact numerical results for the BGK model: Couette, Poiseuille and thermal creep flow between parallel plates. ZAMP 1979;30(3):514-21.

[34] Siewert CE. The linearized Boltzmann equation: concise and accurate solutions to basic flow problems. ZAMP 2003;54:273-303.

[35] Siewert CE. The linearized Boltzmann equation: concise and accurate solution of the temperature-jump problem. J Quant Spectrosc Radiat Transfer 2003;77:417-32.

[36] Barichello LB, Siewert CE. A discrete-ordinates solution for a non-grey model with complete frequency redistribution. J Quant Spectrosc Radiat Transfer 1999;62:665-75.

[37] Yap YW, Sader JE. High accuracy numerical solutions of the Boltzmann Bhatnagar-Gross-Krook equation for steady and oscillatory Couette flows. Phys Fluids 2012;24:032004.

[38] Jiang SD, Luo LS. Private communications; 2013.

[39] Helsing J, Ojala R. Corner singularities for elliptic problems: integral equations, graded meshes, quadrature, and compressed inverse preconditioning. J Comput Phys 2008;227:8820-40.

[40] Bremer J, Rokhlin V. Efficient discretization of Laplace boundary integral equations on polygonal domains. J Comput Phys 2010;229:2507-25.

[41] Bremer J, Rokhlin V, Sammis I. Universal quadratures for boundary integral equations on two-dimensional domains with corners. J Comput Phys 2010;229:8259-80.

[42] Ma J, Rokhlin V, Wandzura S. Generalized Gaussian quadrature rules for systems of arbitrary functions. SIAM J Numer Anal 1996;33:971-96.

[43] Yarvin N, Rokhlin V. Generalized Gaussian quadratures and singular value decompositions of integral operators. SIAM J Sci Comput 1998;20:699-718.

[44] Barisik M, Kim B, Beskok A. Smart wall model for molecular dynamics simulation of nanoscale gas flows. Commun Comput Phys 2010;7(5):977-93.

[45] Barisik M, Beskok A. Molecular dynamics simulations of shear-driven gas flows in nano-channels. Microfluid Nanofluid 2011;11:611-22.

[46] Dadzie SK, Meolans JG. Anisotropic scattering kernel: generalized and modified Maxwell boundary conditions. J Math Phys 2004;45:1804-19.

[47] Oliver J. An error analysis of the modified Clenshaw method for evaluating Chebyshev and Fourier series. J Inst Math Appl 1977;20:379-91.

[48] Luo LS, Liao W, Chen XW, Peng Y, Zhang W. Numerics of the lattice Boltzmann method: effects of collision models on the lattice Boltzmann simulations. Phys Rev E 2011;83:056710.

[49] Arnold VI. Mathematical Methods of Classical Mechanics (2nd Edition). New York: Springer-Verlag; 1989.

APPENDIX A

THE PROPERTIES AND THE APPROXIMATIONS OF ABRAMOWITZ FUNCTIONS

In this section, we summarize the properties of Abramowitz functions $I_n(x)$ and the approximation formulae to $I_n(x)$. The properties and formulae can be found in the work of Macleod [1] and the Handbook of Mathematical Functions edited by Abramowitz and Stegun [2].

The n^{th} order Abramowitz function I_n defined in equation (28) satisfies the following differential equation and recurrence relations,

$$xI_n''' - (n-1)I_n'' + 2I_n = 0, \tag{187}$$

$$I_{n+1}' + I_n = 0, \tag{188}$$

$$2I_n = (n-1)I_{n-2} + xI_{n-3}. \tag{189}$$

The first order Abramowitz function I_1 has the series expansion:

$$I_1 = \sum_{i=0}^{\infty}(a_i \ln x + b_i)x^i \tag{190}$$

with $a_0 = a_1 = 0, a_2 = -1, b_0 = 1, b_1 = \pi^{1/2}, b_2 = 3(1-\gamma)/2$, where $\gamma = 0.57721566490153286060\cdots$ is the Euler's constant. For $i \geq 3$,

$$a_i = -\frac{2a_{i-2}}{i(i-1)(i-2)},$$

$$b_i = -\frac{2b_{i-2} + (3i^2 - 6i + 2)a_i}{i(i-1)(i-2)}.$$

Thus, the first few terms of I_1 read

$$\begin{aligned} I_1(x) =& \frac{1}{2} + \frac{3}{4}(1-\gamma)x^2 + \frac{1}{188}(18\gamma - 3)x^4 + \cdots \\ & - \pi^{1/2} x \left(\frac{1}{2} - \frac{1}{6}x^2 + \frac{1}{180}x^4 - \cdots \right) \\ & - x^2 \ln x \left(\frac{1}{2} - \frac{1}{24}x^2 + \frac{1}{1440}x^4 - \cdots \right). \end{aligned} \tag{191}$$

In general, I_n can be approximately by the following asymptotic formulas

$$I_n(x) \sim \begin{cases} \pi^{(1-\sigma)/2} f_n(t) - \pi^{\sigma/2} g_n(t) + (-1)^n h_n(t) x^{n+1} \ln x, & 0 \le x \le 2, \\ (\pi/3)^{1/2} (\nu/3)^{n/2} e^{-\nu} q_n(\nu), & x > 2, \end{cases} \tag{192}$$

where $t = x^2/2 - 1, \nu = 2(x/2)^{2/3}, \sigma = |\lfloor (n+1)/2 \rfloor - \lfloor n/2 \rfloor|$ and the symbol $\lfloor \cdot \rfloor$ is the largest integer less than or equal to the given quantity. The functions f_n, g_n, h_n and q_n are analytic functions. When $n = 0, 1, 2$, Macleod [1] obtained accurate Chebyshev expansions $\sum' d_i T_i(t)$ for f_n, g_n, h_n and $\sum' d_i T_i(\nu)$ for q_n. $\sum'$ means the first term in the summation is halved. The coefficients of the Chebyshev expansion for f_n, g_n, h_n and q_n with $n = 0, 1, 2$ are tabulated in Table 49-Table 51, respectively.

TABLE 49: Coefficients of Chebyshev expansions for f_0, g_0, h_0 and q_0

f_0	d_0	-0.68121	92709	35494	69816	10^{0}	q_0	d_0	1.97755	49972	38930	67407	10^{0}
	d_1	-0.78867	91981	61492	52495	10^{0}		d_1	-0.10460	24792	00481	9485	10^{-1}
	d_2	0.51215	81776	81881	9543	10^{-1}		d_2	0.69680	79025	39253	66	10^{-3}
	d_3	-0.71092	35289	45412	96	10^{-3}		d_3	-0.58982	98299	99659	9	10^{-4}
	d_4	0.36868	18085	04287		10^{-5}		d_4	0.57716	44553	05320		10^{-5}
	d_5	-0.91783	23372	37		10^{-8}		d_5	-0.61523	01336	5756		10^{-6}
	d_6	0.12702	02563			10^{-10}		d_6	0.67853	96884	767		10^{-7}
	d_7	-0.10768	88			10^{-13}		d_7	-0.72306	25379	07		10^{-8}
	d_8	0.599				10^{-17}		d_8	0.63306	62736	5		10^{-9}
g_0	d_0	-0.60506	03943	08682	73190	10^{0}		d_9	-0.98945	3793			10^{-11}
	d_1	-0.41950	39816	32017	79803	10^{0}		d_{10}	-0.16819	80530			10^{-10}
	d_2	0.17032	65125	19037	0333	10^{-1}		d_{11}	0.67379	9551			10^{-11}
	d_3	-0.16938	91784	24913	97	10^{-3}		d_{12}	-0.20099	7939			10^{-11}
	d_4	0.67638	08951	9710		10^{-6}		d_{13}	0.54055	903			10^{-12}
	d_5	-0.13572	35362	55		10^{-8}		d_{14}	-0.13816	679			10^{-12}
	d_6	0.15629	7065			10^{-11}		d_{15}	0.34222	05			10^{-13}
	d_7	-0.11288	7			10^{-14}		d_{16}	-0.82668	6			10^{-14}
	d_8	0.55				10^{-18}		d_{17}	0.19456	6			10^{-14}
h_0	d_0	1.38202	65523	05749	89705	10^{0}		d_{18}	-0.44268				10^{-15}
	d_1	-0.30097	92907	39749	04355	10^{0}		d_{19}	0.9562				10^{-16}
	d_2	0.79428	88093	64887	241	10^{-2}		d_{20}	-0.1883				10^{-16}
	d_3	-0.64319	10276	84756	3	10^{-4}		d_{21}	0.301				10^{-17}
	d_4	0.22549	83068	4374		10^{-6}		d_{22}	-0.19				10^{-18}
	d_5	-0.41220	96619	5		10^{-9}		d_{23}	-0.14				10^{-18}
	d_6	0.44185	282			10^{-12}		d_{24}	0.11				10^{-18}
	d_7	-0.30123				10^{-15}		d_{25}	-0.4				10^{-19}
	d_8	0.14				10^{-18}		d_{26}	0.2				10^{-19}
								d_{27}	-0.1				10^{-19}

Apart from $I_0(x), I_1(x)$ and $I_2(x)$, we also need to compute $I_{-1}(x)$. $I_{-1}(x)$ is

TABLE 50: Coefficients of Chebyshev expansions for f_1, g_1, h_1 and q_1

f_1	d_0	1.47285	19257	79788	07369	10^{0}	q_1	d_0	2.13013	64342	90655	49448	10^{0}
	d_1	0.10903	49757	01689	56257	10^{0}		d_1	0.63715	26795	21853	9933	10^{-1}
	d_2	-0.12430	67536	00565	69753	10^{0}		d_2	-0.12933	49174	77510	647	10^{-2}
	d_3	0.30619	79468	53493	315	10^{-2}		d_3	0.56783	28753	22826	5	10^{-4}
	d_4	-0.22184	10323	07651	1	10^{-4}		d_4	-0.27943	49391	77646		10^{-5}
	d_5	0.69899	78834	451		10^{-7}		d_5	0.56002	14736	787		10^{-7}
	d_6	-0.11597	07644	4		10^{-9}		d_6	0.23920	09242	798		10^{-7}
	d_7	0.11389	776			10^{-12}		d_7	-0.75098	48650	09		10^{-8}
	d_8	-0.7173				10^{-16}		d_8	0.17301	53307	76		10^{-8}
	d_9	0.3				10^{-19}		d_9	-0.36648	87795	5		10^{-9}
g_1	d_0	0.39791	27794	90545	03528	10^{0}		d_{10}	0.75207	58307			10^{-10}
	d_1	-0.29045	28522	64547	20849	10^{0}		d_{11}	-0.15179	90208			10^{-10}
	d_2	0.10487	84695	46536	3504	10^{-1}		d_{12}	0.30171	3710			10^{-11}
	d_3	-0.10249	86952	26913	36	10^{-3}		d_{13}	-0.58596	718			10^{-12}
	d_4	0.41150	27939	9110		10^{-6}		d_{14}	0.10914	455			10^{-12}
	d_5	-0.83652	63894	0		10^{-9}		d_{15}	-0.18705	36			10^{-13}
	d_6	0.97862	595			10^{-12}		d_{16}	0.26254	2			10^{-14}
	d_7	-0.71868				10^{-15}		d_{17}	-0.14627				10^{-15}
	d_8	0.35				10^{-18}		d_{18}	-0.9500				10^{-16}
h_1	d_0	0.84150	29215	22749	47030	10^{0}		d_{19}	0.5873				10^{-16}
	d_1	-0.77900	50698	77414	3395	10^{-1}		d_{20}	-0.2420				10^{-16}
	d_2	0.13399	24558	78390	993	10^{-2}		d_{21}	0.868				10^{-17}
	d_3	-0.80850	39071	52788	3	10^{-5}		d_{22}	-0.290				10^{-17}
	d_4	0.22618	58281	728		10^{-7}		d_{23}	0.93				10^{-18}
	d_5	-0.34413	95838			10^{-10}		d_{24}	-0.29				10^{-18}
	d_6	0.31598	58			10^{-13}		d_{25}	0.9				10^{-19}
	d_7	-0.1884				10^{-16}		d_{26}	-0.3				10^{-19}
	d_8	0.1				10^{-19}		d_{27}	0.1				10^{-19}

TABLE 51: Coefficients of Chebyshev expansions for f_2, g_2, h_2 and q_2

f_2	d_0	1.03612	16280	42437	13846	10^{0}	q_2	d_0	2.46492	32530	43348	56893	10^{0}
	d_1	0.19371	24662	67945	70012	10^{0}		d_1	0.23142	79742	22489	05432	10^{0}
	d_2	-0.72587	58839	23300	7378	10^{-1}		d_2	-0.94068	17301	00857	73	10^{-3}
	d_3	0.17479	05908	64327	399	10^{-2}		d_3	0.82902	70038	08973	3	10^{-4}
	d_4	-0.12812	23233	75654	9	10^{-4}		d_4	-0.88389	47042	45866		10^{-5}
	d_5	0.41150	18153	651		10^{-7}		d_5	0.10663	85435	67985		10^{-5}
	d_6	-0.69710	47256	4		10^{-10}		d_6	-0.13091	12853	8529		10^{-6}
	d_7	0.69901	83			10^{-13}		d_7	0.19397	93208	445		10^{-7}
	d_8	-0.4492				10^{-16}		d_8	-0.27704	99383	75		10^{-8}
	d_9	0.2				10^{-19}		d_9	0.39590	68718	6		10^{-9}
g_2	d_0	1.46290	15719	86367	41150	10^{0}		d_{10}	-0.54083	54342			10^{-10}
	d_1	0.20189	46688	31540	14317	10^{0}		d_{11}	0.63554	6076			10^{-11}
	d_2	-0.29082	92087	99712	9022	10^{-1}		d_{12}	-0.38461	613			10^{-12}
	d_3	0.47061	04903	52700	50	10^{-3}		d_{13}	-0.11696	067			10^{-12}
	d_4	-0.25792	20803	59333		10^{-5}		d_{14}	0.68966	71			10^{-13}
	d_5	0.65613	37129	46		10^{-8}		d_{15}	-0.25031	13			10^{-13}
	d_6	-0.91411	0203			10^{-11}		d_{16}	0.78558	6			10^{-14}
	d_7	0.77427	6			10^{-14}		d_{17}	-0.23033	4			10^{-14}
	d_8	-0.429				10^{-17}		d_{18}	0.64914				10^{-15}
h_2	d_0	0.30117	22501	09104	88881	10^{0}		d_{19}	-0.17797				10^{-15}
	d_1	-0.15886	67818	31762	3783	10^{-1}		d_{20}	0.4766				10^{-16}
	d_2	0.19295	93693	55845	26	10^{-3}		d_{21}	-0.1246				10^{-16}
	d_3	-0.90199	58784	9300		10^{-6}		d_{22}	0.316				10^{-17}
	d_4	0.20610	50418	37		10^{-8}		d_{23}	-0.77				10^{-18}
	d_5	-0.26511	1806			10^{-11}		d_{24}	0.18				10^{-18}
	d_6	0.21086	4			10^{-14}		d_{25}	-0.4				10^{-19}
	d_7	-0.111				10^{-17}		d_{26}	0.1				10^{-19}

computed in three intervals. In the first interval $0 < x \leq \epsilon$, we use the following formula,

$$I_{-1}(x) = I_1''(x)$$

which is derived from equation (188). For $x > \epsilon$, we use the following formula,

$$I_{-1}(x) = \frac{2I_2(x) - I_0(x)}{x}$$

where both $I_0(x)$ and $I_2(x)$ are given by the first and second asymptotic formula in equation (192) for the second interval $\epsilon < x \leq 2.0$ and the third interval $x > 2.0$, respectively. Hence, $I_{-1}(x)$ is computed with the following formula:

$$I_{-1}(x) \sim \begin{cases} -\frac{3\gamma}{2} + \pi^{1/2}x + \left(\frac{54}{47}\gamma - \frac{1903}{1128}\right)x^2 - \left(1 - \frac{x^2}{2}\right)\ln x, & 0 < x \leq \epsilon, \\ \frac{\pi^{1/2}[2f_2(t) - f_0(t)]}{x} - [2g_2(t) - g_0(t)] + [2x^2 h_2(t) - h_0(t)]\ln x, & \epsilon < x \leq 2.0, \\ (\pi/3)^{1/2} e^{-\nu}\left[\frac{2\nu}{3}q_2(\nu) - q_0(\nu)\right], & x > 2.0, \end{cases} \tag{193}$$

where $t = x^2/2 - 1, \nu = 2(x/2)^{2/3}$ and $\epsilon = 1.5 \times 10^{-8}$.

APPENDIX B

NONEXISTENCE OF THE DERIVATIVE OF VELOCITY AT THE BOUNDARIES FOR THE STEADY COUETTE FLOW PROBLEM WITH PURE DIFFUSIVE BOUNDARY CONDITION

In this section, we prove $\lim_{y\to 1/2-} u'(y) \to \infty$ for the steady Couette flow problem with pure diffusive boundary condition.
Differentiation of equation (72) leads to the following equation

$$u'(y) - \frac{1}{\pi^{1/2}k}\int_{-1/2}^{1/2} \frac{\mathrm{d}}{\mathrm{d}y} I_{-1}\left(\frac{|y-s|}{k}\right) u(s)\,\mathrm{d}s = \frac{1}{2\pi^{1/2}k} G_{-1}(y,k). \tag{194}$$

Because

$$\begin{aligned}\int_{-1/2}^{1/2} \frac{\mathrm{d}}{\mathrm{d}y} I_{-1}\left(\frac{|y-s|}{k}\right) u(s)\,\mathrm{d}s &= -\int_{-1/2}^{1/2} \frac{\mathrm{d}}{\mathrm{d}s} I_{-1}\left(\frac{|y-s|}{k}\right) u(s)\,\mathrm{d}s \\ &= -G_{-1}(y,k)u(1/2) + \int_{-1/2}^{1/2} I_{-1}\left(\frac{|y-s|}{k}\right) u'(s)\,\mathrm{d}s,\end{aligned}$$

equation (194) becomes

$$u'(y) - \frac{1}{\pi^{1/2}k}\int_{-1/2}^{1/2} I_{-1}\left(\frac{|y-s|}{k}\right) u'(s)\,\mathrm{d}s = \frac{1-2u(1/2)}{2\pi^{1/2}k} G_{-1}(y,k). \tag{195}$$

With $y \to 1/2-$, equation (195) leads to

$$u'(1/2-) = \frac{1-2u(1/2)}{2\pi^{1/2}k}[I_{-1}(0+) - I_{-1}(1/k)] + \frac{1}{\pi^{1/2}k}\int_{-1/2}^{1/2} I_{-1}\left(\frac{1-2s}{2k}\right) u'(s)\,\mathrm{d}s.$$

Since $I_{-1}(y)$ is decreasing, with the fact that $u(y) < 1/2$ and $u'(y) > 0$, we have

$$u'(1/2-) = \infty.$$

Now we prove $u(y) < 1/2$ and $u'(y) > 0$.

From equation (72) we get

$$\begin{aligned} u(y,k) &\le \frac{\max u}{\pi^{1/2}k}\int_{-1/2}^{1/2} I_{-1}\left(\frac{|y-s|}{k}\right)\mathrm{d}s + \frac{1}{2\pi^{1/2}}F_0(y,k) \\ &\le \frac{\max u}{\pi^{1/2}}[\pi^{1/2} - G_0(y,k)] + \frac{1}{2\pi^{1/2}}F_0(y,k). \end{aligned}$$

Thus

$$\max u = u(y^*) \le \frac{\max u}{\pi^{1/2}}[\pi^{1/2} - G_0(y^*,k)] + \frac{1}{2\pi^{1/2}}F_0(y^*,k)$$

and we have

$$u(y) \le \max u \le \frac{F_0(y^*,k)}{2G_0(y^*,k)} \le \frac{F_0(1/2,k)}{2G_0(1/2,k)} < 1/2.$$

From equation (195) we have

$$\begin{aligned} & u'(y) - \frac{\min u'}{\pi^{1/2}k}\int_{-1/2}^{1/2} I_{-1}\left(\frac{|y-s|}{k}\right)\mathrm{d}s \\ \ge & u'(y) - \frac{1}{\pi^{1/2}k}\int_{-1/2}^{1/2} I_{-1}\left(\frac{|y-s|}{k}\right)u'(s)\,\mathrm{d}s \\ = & \frac{1-2u(1/2)}{2\pi^{1/2}k}G_{-1}(y,k). \end{aligned}$$

Assuming $\min u' = u'(y_*)$, one comes to

$$\begin{aligned} & \min u'\left[1 - \frac{1}{\pi^{1/2}k}\int_{-1/2}^{1/2} I_{-1}\left(\frac{|y_*-s|}{k}\right)\mathrm{d}s\right] \\ = & \min u' G_0(y_*,k)\pi^{-1/2} \\ \ge & \frac{1-2u(1/2)}{2\pi^{1/2}k}G_{-1}(y_*,k). \end{aligned}$$

Thus, we have

$$u'(y) \ge \min u' \ge \frac{1-2u(1/2)}{2kG_0(y_*,k)}G_{-1}(y_*,k) > 0.$$

This completes the proof.

APPENDIX C

LINEAR TRANSFORM AND INVERSE TRANSFORM BETWEEN GAUSS-LEGENDRE POLYNOMIAL EXPANSION COEFFICIENTS AND THE APPROXIMATED FUNCTION VALUES AT THE CORRESPONDING GAUSS-LEGENDRE ABSCISSAS

In this section, we establish the relation between the expansion coefficients and the nodal function values of the Legendre polynomial expansion of the function. Let $L_m(x)$ be the m^{th} degree Gauss-Legendre polynomial and $\tilde{L}_m(x)$ be the shifted and rescaled m^{th} degree Gauss-Legendre polynomial on the interval $[a, b]$. Then, the $(M-1)^{th}$ order Legendre polynomial expansion of $u(x)$ on the interval $[a, b]$ is written as

$$u(x) = \sum_{m=1}^{M} c_m \tilde{L}_{m-1}(x),$$

where c_m is the m^{th} coefficient. Let $\{x_m\}_{m=1}^{M}$ and $\{\tilde{x}_m\}_{m=1}^{M}$ be the finite sequence of M^{th} order standard Gauss-Legendre quadrature abscissas and the corresponding shifted and rescaled Gauss-Legendre abscissas on the interval $[a, b]$, respectively. Then, by using $\tilde{L}_{j-1}(\tilde{x}_i) = L_{j-1}(x_i)$, the values of $u(x)$ on the shifted and rescaled abscissas can be computed by $\boldsymbol{Qc} = \boldsymbol{u}$, where

$$Q = \begin{pmatrix} L_0(x_1) & L_1(x_1) & \cdots & L_{M-1}(x_1) \\ L_0(x_2) & L_1(x_2) & \cdots & L_{M-1}(x_2) \\ \cdots & \cdots & \cdots & \cdots \\ L_0(x_M) & L_1(x_M) & \cdots & L_{M-1}(x_M) \end{pmatrix},$$

$$\boldsymbol{c} = (c_1\, c_2\, \cdots\, c_M)^T, \quad \boldsymbol{u} = (u(\tilde{x}_1)\, u(\tilde{x}_2)\, \cdots\, u(\tilde{x}_M))^T.$$

Let $\{\omega_m\}_{m=1}^{M}$ and $\{\tilde{\omega}_m\}_{m=1}^{M}$ be the weights of the M^{th} order standard Gauss-Legendre quadrature and the shifted and rescaled Gauss-Legendre quadrature on $[a, b]$, respectively. Then $\tilde{\omega}_i = \frac{\omega_i(b-a)}{2}$. Since M^{th} order Gauss-Legendre quadrature is exact for

the integration of polynomials up to $(2M-1)^{th}$ degree, by using the orthogonality of the Legendre polynomial, we have

$$\begin{aligned}\|\tilde{L}_{j-1}\|_2^2 c_j &= \int_a^b \tilde{L}_{j-1}(x)\sum_{i=1}^{M} c_i \tilde{L}_{i-1}(x)\,\mathrm{d}x \\ &= \int_a^b \tilde{L}_{j-1}(x)u(x)\,\mathrm{d}x \\ &= \sum_{i=1}^{M} \tilde{\omega}_i \tilde{L}_{j-1}(\tilde{x}_i)u(\tilde{x}_i) \\ &= \frac{b-a}{2}\sum_{i=1}^{M} \omega_i L_{j-1}(x_i)u(\tilde{x}_i),\end{aligned}$$

where

$$\|\tilde{L}_{j-1}\|_2^2 = \frac{b-a}{2j-1},$$

Thus,

$$c_j = \frac{2j-1}{2}\sum_{i=1}^{M} \omega_i L_{j-1}(x_i)u(\tilde{x}_i).$$

Then, the Legendre polynomial expansion coefficients $\boldsymbol{c}$ of $u(x)$ can be computed by $P\boldsymbol{u} = \boldsymbol{c}$, where

$$P = \begin{pmatrix} \frac{2\cdot 1-1}{2}L_0(x_1)\omega_1 & \frac{2\cdot 1-1}{2}L_0(x_2)\omega_2 & \cdots & \frac{2\cdot 1-1}{2}L_0(x_M)\omega_M \\ \frac{2\cdot 2-1}{2}L_1(x_1)\omega_1 & \frac{2\cdot 2-1}{2}L_1(x_2)\omega_2 & \cdots & \frac{2\cdot 2-1}{2}L_1(x_M)\omega_M \\ \cdots & \cdots & \cdots & \cdots \\ \frac{2\cdot M-1}{2}L_{M-1}(x_1)\omega_1 & \frac{2\cdot M-1}{2}L_{M-1}(x_2)\omega_2 & \cdots & \frac{2\cdot M-1}{2}L_{M-1}(x_M)\omega_M \end{pmatrix},$$

$$\boldsymbol{u} = (u(\tilde{x}_1)\, u(\tilde{x}_2) \cdots u(\tilde{x}_M))^T, \quad \boldsymbol{c} = (c_1\, c_2 \cdots c_M)^T.$$

Obviously,

$$Q = P^{-1}.$$

APPENDIX D

GAUSS-LEGENDRE QUADRATURE

In this section, we explain how we compute the abscissas and weights of the M^{th} order Gauss-Legendre quadrature. The Gauss-Legendre abscissas are obtained by Newton's iteration,

$$x_{n+1} = x_n - \frac{L_M(x_n)}{L'_M(x_n)}. \tag{196}$$

We choose the M^{th} order Gauss-Chebyshev abscissas $\{\cos\frac{2m-1}{2M}\pi\}_{m=1}^{M}$ as the initial guess. The value of M^{th} degree Legendre polynomial is obtained by the Bonnet's recursion formula:

$$\begin{aligned} L_0(x) &= 1 \\ L_1(x) &= x \\ mL_m(x) &= (2m-1)xL_{m-1}(x) - (m-1)L_{m-2}(x),\ m = 2, 3, \cdots, M. \end{aligned} \tag{197}$$

The value of derivative of M^{th} degree Legendre polynomial is computed by

$$L'_M(x) = \frac{M[L_{M-1}(x) - xL_M(x)]}{1-x^2}. \tag{198}$$

Once the abscissas is at hand we can compute the corresponding weights. A frequently used formula for the weights of the M^{th} order Gauss-Legendre quadrature is

$$\omega_m = \frac{2}{(1-x_m^2)[L'_M(x_m)]^2}. \tag{199}$$

However, when M is big, the points in the abscissas will accumulate near ± 1. This will cause severe cancellation error when computing $1 - x_m^2$. An alternative formula for the weights is given by Frank Lether[3] without proof:

$$\omega_m = \frac{2}{\sum_{j=0}^{M-1}(2j+1)L_j^2(x_m)}. \tag{200}$$

Now, we prove it. By using equation (197), for any n, we have

$$\begin{aligned}
&nL_n(x)(n-1)L_{n-2}(x) - (n-1)^2L_{n-1}^2(x) \\
&- 2(n-1)xL_{n-1}(x)L_{n-2}(x) + (2k-3)L_{n-2}^2(x) \\
=&nL_n(x)(n-1)L_{n-2}(x) - (n-1)L_{n-1}(x)[(2n-3)xL_{n-2}(x) - (n-2)L_{n-3}(x)] \\
&- 2(n-1)xL_{n-1}(x)L_{n-2}(x) + (2n-3)L_{n-2}^2(x) \\
=&(n-1)L_{n-2}(x)[nL_n(x) - (2n-3)xL_{n-1}(x) - 2xL_{n-1}(x)] \\
&+ (n-1)L_{n-1}(x)(n-2)L_{n-3}(x) + (2n-3)L_{n-2}^2(x) \\
=&-(n-1)^2L_{n-2}^2(x) + (2n-3)L_{n-2}^2(x) + (n-1)L_{n-1}(x)(n-2)L_{n-3}(x) \\
=&(n-1)L_{n-1}(x)(n-2)L_{n-3}(x) - (n-2)^2L_{n-2}^2(x). \qquad (201)
\end{aligned}$$

Denote $L_{-1}(x) = 0$, then using equation (198), equation (201) and the fact $L_M(x_m) = 0$, we have

$$\begin{aligned}
&(1-x_m^2)\sum_{j=0}^{M-1}(2j+1)L_j^2(x_m) \\
=&\sum_{j=0}^{M-1}\{(2j+1)L_j^2(x_m) - x_mL_j(x_m)[(j+1)L_{j+1}(x_m) + jL_{j-1}(x_m)]\} \\
=&-x_mL_{M-1}(x_m)ML_M(x_m) + (2M-1)L_{M-1}^2(x_m) \\
&+\sum_{j=0}^{M-2}[-2(j+1)x_mL_{j+1}(x_m)L_j(x_m) + (2j+1)L_j^2(x_m)] \\
=&(M-1)L_{M-2}(x_m)ML_M(x_m) - (M-1)^2L_{M-1}^2(x_m) \\
&+\sum_{j=0}^{M-2}[-2(j+1)x_mL_{j+1}(x_m)L_j(x_m) + (2j+1)L_j^2(x_m)] + M^2L_{M-1}^2(x_m) \\
=&M^2L_{M-1}^2(x_m) \\
=&M^2[L_{M-1}(x_m) - x_mL_M(x_m)]^2 \\
=&(1-x_m^2)^2[L_M'(x_m)]^2. \qquad (202)
\end{aligned}$$

From equation (202), we have

$$\begin{aligned}
\omega_m &= \frac{2}{(1-x_m^2)[L_M'(x_m)]^2} \\
&= \frac{2}{\sum_{j=0}^{M-1}(2j+1)L_j^2(x_m)}.
\end{aligned}$$

We use equation (200) to compute the weights of the M^{th} order Gauss-Legendre quadrature.

APPENDIX E

VELOCITY OF FREE MOLECULAR COUETTE FLOW WITH ARBITRARY ACCOMMODATION RATIOS

In this section, we derive the velocity of free molecular flow with Couette flow setup and arbitrary accommodation ratios at upper and lower walls.
The steady collisionless Boltzmann equation is

$$\boldsymbol{\xi} \cdot \nabla f = 0, \tag{203}$$

where $f = f(\boldsymbol{r}, \boldsymbol{\xi})$ is the distribution function. $\boldsymbol{r}$ and $\boldsymbol{\xi}$ are the position and the velocity of the particle, respectively. With same setup and process of normalization as the Couette flow problem, we can write

$$f = \pi^{-3/2} \rho \xi_m^{-3} e^{-|\boldsymbol{\xi}|^2} \left(1 + \frac{U_0}{\xi_m} g\right),$$

with $g = g(y, \xi_x, \xi_y)$. Hence, equation (203) can be rewritten as

$$\frac{\partial g}{\partial y} = 0,$$

leading to $g = g(\xi_x, \xi_y)$. Denoting

$$\phi(\xi_y) = \pi^{-1/2} \int_{-\infty}^{\infty} \xi_x e^{-\xi_x^2} g \, \mathrm{d}\xi_x,$$

the velocity of the free molecular flow is

$$\begin{aligned} u &= \pi^{-1/2} \int_{-\infty}^{\infty} \phi(\xi_y) e^{-\xi_y^2} \, \mathrm{d}\xi_y \\ &= \pi^{-1/2} \int_{0}^{\infty} [\phi(\xi_y) + \phi(-\xi_y)] e^{-\xi_y^2} \, \mathrm{d}\xi_y. \end{aligned} \tag{204}$$

Recalling the boundary condition equations (22)-(23) for the Couette flow problem, the boundary condition for the current case due to independence of ϕ with y is

$$\begin{aligned} \phi(\xi_y) &= -(1 - \alpha^-)/2 + \alpha^- \phi(-\xi_y) \\ \phi(-\xi_y) &= (1 - \alpha^+)/2 + \alpha^+ \phi(\xi_y), \end{aligned}$$

where $\xi_y > 0$. We have constant solution of $\phi(\xi_y)$ and $\phi(-\xi_y)$,

$$\begin{aligned} \phi(\xi_y) &= \frac{(1-\alpha^-)+\alpha^-(1-\alpha^+)}{2(1-\alpha^-\alpha^+)}, \\ \phi(-\xi_y) &= \frac{(1-\alpha^+)-\alpha^+(1-\alpha^-)}{2(1-\alpha^-\alpha^+)}. \end{aligned}$$

Substituting them into equation (204), we have

$$u = \frac{\phi(\xi_y) + \phi(-\xi_y)}{2} = \frac{\alpha^- - \alpha^+}{2(1-\alpha^-\alpha^+)}.$$

VITA

Wei Li
Department of Computational and Applied Mathematics
Old Dominion University
Norfolk, VA 23529

PREVIOUS DEGREES:
B.S. in Computing Science at Wuhan University of Technology, China, June 2004,
M.S. in Applied Mathematics at Wuhan University of Technology, China, December 2006.

Typeset using LaTeX.